IFT - UNESP
INSTITUTO DE FÍSICA TEÓRICA

Femtoscopy with Strange Particles in pPb Collisions at $\sqrt{s_{\mathrm{NN}}} = 8.16$ TeV at CMS
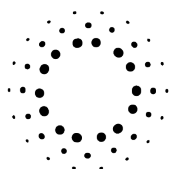
Dener de Souza Lemos

Advisor

Dra. Sandra dos Santos Padula

Co-Advisor:

Dr. César Augusto Bernardes

November of 2021

IFT - UNESP
INSTITUTO DE FÍSICA TEÓRICA

Femtoscopia com Partículas Estranhas em Colisões pPb a $\sqrt{s_{\mathrm{NN}}} = 8.16$ TeV no CMS

Dener de Souza Lemos

Orientadora

Dra. Sandra dos Santos Padula

Co-Orientador:

Dr. César Augusto Bernardes

Novembro de 2021

I dedicate this thesis to my parents
Maria Terezinha de Souza Lemos
and Rudimar José Morais de Lemos

Acknowledgments

I would like to thank:

- first, my advisor Sandra dos Santos Padula, for all the fruitful discussions, advices and for the friendship, being fundamental to the development of this work and for my academic carrier. I have no words to say how thankful I am and I will always be proud to call you as my "scientific mother".

- my co-advisor César Augusto Bernardes, for being a great friend, for teaching me so much about the CMS stuff and constantly willing to help me.

- to Syndell Fernandes, for always encouraging me with a lot of love, affection and patience. Thank you for stay on my side and make me so happy.

- my parents Rudimar Lemos, Maria Terezinha Lemos, my grand mother Deni Lemos and my godparents Janete Lemos e Claudeci Costa, for all the support that you gave to me during my life.

- to professor Sérgio Novaes, first for accepting me as a member of the SPRACE group and also for all the advices and teachings. I would also like to thank the other members of SPRACE, the professors: Eduardo Gregores, Pedro Mercadante and Thiago Tomei; the postdocs: Sudha and Sunil; and the students: Ana, Breno, Felipe, João, Isabela and Tulio; for all the useful discussions and great moments.

- my friend Rafael Reimbrecht, for ever stay on my side even with the distance.

- to professor Otavio Socolowski Jr., for introduce me to the heavy ion world. Thanks for all the discussions and for the friendship.

- the friends, from NCC: Allan, André, Jeff, Luigi, Ricardo and Sidney. From IFT: Anacé, Felippe, Gabriel, Jogean and Rafael. And from CMS heavy ion group. Thanks for all the moments and coffee's.

- to the IFT-UNESP professors and secretaries, for the support, kindness and friendship towards me. An special thank you to Dona Jô for the affection.

- to Fernandes family for the support.

- to São Paulo Research Foundation (FAPESP) for the financial support. This material is based upon work supported by the FAPESP grants No. 2017/02675-6 vinculated to the process No 2013/01907-0. Any opinions, findings, and conclusions or recommendations expressed in this material are those of the Author(s) and do not necessarily reflect the views of FAPESP.

"I would rather have questions
that can't be answered than
answers that can't be questioned."

Richard P. Feynman

Resumo

A femtoscopia é um método utilizado para investigar as dimensões espaço-temporais da fonte emissora de partículas criada em colisões a altas energias, através de correlações entre elas. Tais correlações são sensíveis à estatística quântica obedecida pelas partículas idênticas envolvidas, assim como à interação forte sentida pelos hádrons, sejam eles idênticos ou não-idênticos. O presente trabalho apresenta resultados de correlações femtoscópicas de partículas para todas as combinações de pares de K_S^0, Λ e $\overline{\Lambda}$, com dados do Run 2 do LHC coletados pelo experimento Compact Muon Solenoid (CMS) em colisões próton-chumbo (pPb) a $\sqrt{s_{NN}} = 8.16$ TeV. Neste trabalho, as correlações femtoscópicas são medidas utilizando a técnica de *single ratio* para partículas do mesmo evento em relação a partículas de eventos diferentes, juntamente com outros métodos baseados nos dados, empregados para extrair as informações desejadas. O modelo Lednicky-Lyubolshitz é aplicado para parametrizar as interações fortes entre hádrons, permitindo obter tanto os observáveis de espalhamento, quanto o tamanho da fonte emissora de partículas. A presente análise é realizada usando eventos com ampla variação de multiplicidades de partículas carregadas e momento transversal médio do par. Esse é a primeira medida de correlações femtoscópica de $K_S^0 K_S^0$ em colisões pPb e a primeira de correlações de $\Lambda\overline{\Lambda}$ e $K_S^0\Lambda \oplus K_S^0\overline{\Lambda}$ em colisões de sistemas pequenos. No estudo das fortes utilizando a femtoscopia de pares bárion-antibárion, observa-se uma anticorrelação, enquanto o comportamento oposto é visto no caso de correlações de pares bárion-bárion, sendo ambos consistentes com resultados de outros experimentos. Além disso, os parâmetros de espalhamento para pares bárion-antibárion mostraram independência em relação à multiplicidade de partículas carregadas.

Palavras Chaves: Femtoscopia; Partículas estranhas; Interação forte; Sistemas pequenos de colisão;

Áreas do conhecimento: Física; Física de Partículas Experimental; Física Nuclear de Altas Energias.

Abstract

Femtoscopy is a powerful method for probing the space-time dimensions of particle emitting sources created in high energy collisions through particle correlations. Such correlations are sensitive to the quantum statistics obeyed by the identical particles involved, as well as to the strong interaction felt by hadrons, for both identical or non-identical pairs. This work presents results of femtoscopic correlations for all pair combinations of K^0_S, Λ and $\overline{\Lambda}$ with data from the LHC Run 2 collected by the Compact Muon Solenoid (CMS) experiment in proton-lead collisions at $\sqrt{s_{NN}} = 8.16$ TeV. Detailed studies of the femtoscopic correlations are performed employing the single ratio technique of particles from the same event to those from different events, together with other data driven methods employed to extract the desired information. The Lednicky-Lyubolshitz model is used to parametrize the strong interactions, allowing to obtain the scattering observables, as well as the size of the particle emitting region. The present analysis is performed using samples of events in a wide range of charged particle multiplicities and pair average transverse momenta. This is the first femtoscopic correlation measurement of $K^0_S K^0_S$ in pPb collisions and the first $\Lambda\overline{\Lambda}$ and $K^0_S\Lambda \oplus K^0_S\overline{\Lambda}$ correlation results in small colliding systems. In the study of the strong interactions using femtoscopy of baryon-antibaryon pair, an anticorrelation is observed, whereas the opposite behavior is seen in the case of baryon-baryon pair correlations, both observations being consistent with previous measurements. Furthermore, the baryon-antibaryon scattering parameters showed an independent behavior with respect to charged particle multiplicity.

Keywords: Femtoscopy; Strange particles; Strong interaction; Small colliding systems;

Knowledge Areas: Physics; Experimental Particle Physics; High-energy Nuclear Physics.

Contents

Conventions

In this work we adopt the system of natural units, $\hbar = c = k_B = 1$, where $\hbar$ is the normalized Planck constant, c is the speed of light, and k_B the Boltzmann constant. The Minkowski metric $(+, -, -, -)$ is employed throughout this work.

Chapter 1

Introduction

One of the main goals of modern physics is to understand the elementary structure of matter and the fundamental laws that govern the Universe. In nature there are four well-known interactions: strong, weak, electromagnetic and gravitational. The strong force describes the interactions between partons (quarks and gluons), which are normally confined inside hadrons. However, at very high energy densities and temperatures, partons are no longer confined in hadronic bound states, but may form a novel state of matter called quark-gluon plasma.

This hot and dense medium is believed to have been present during the first microseconds after the Big Bang and may be part of the core of neutron stars. The possibility of creation of such a state of matter in the laboratory was first proposed in the seventies. One way to recreate the QGP in the laboratory is by using relativistic heavy ion collisions, that has been extensively studied experimentally and theoretically over the years. Since this novel state of matter could exist only for a short period of time, its direct observation would not be possible. Nevertheless, a few indirect probes have been suggested to investigate its formation. Such signatures were observed and measured at the Relativistic Heavy Ion Collider (RHIC) in gold-gold collisions at nucleon pair center-of-mass energy $\sqrt{s_{\mathrm{NN}}} = 200$ GeV [1]. However, different than the initial expectations, a strongly-coupled matter was observed, behaving more like a perfect fluid than a gas. Since then, the study of the properties of the hot and dense medium has been fundamental to allow a better understanding of the strong interactions. In 2010, the Large Hadron Collider (LHC) also measured hints of a QGP-like behavior in events with large number of charged particles produced in proton-proton collisions [2], generating more and more questions about the formation of this state of matter and opening an entire new world of study with the so-called small colliding systems.

The usage of two-particle correlations in the low relative momentum of the pair to estimate the space-time dimensions of the particle emitting source, the so called femtoscopy, is a tool that has been largely employed in high energy collision measurements during several decades. This effect in high energy collisions was first

observed, accidently, in the search for the ρ meson decaying into opposite-charged pions, in proton-antiproton collisions [3]. The experiment observed that identically charged pions followed an angular distribution different from the oppositely charged ones, which could only be explained by considering the symmetrization of their wave-function (Bose-Einstein quantum statistics). In the seventies, such correlations were also suggested as one of the possible QGP signatures. Over the years, the study of femtoscopy has allowed several measurements, from estimation of the volume (multidimensional) and lifetime of the system formed in high energy collisions, as well as the effects of Coulomb or strong final state interactions.

This thesis presents the first study of femtoscopic correlations of $K_S^0 K_S^0$, $K_S^0 \Lambda \oplus K_S^0 \overline{\Lambda}$, $\Lambda\Lambda \oplus \overline{\Lambda}\,\overline{\Lambda}$ and $\Lambda\overline{\Lambda}$ recorded by the Compact Muon Solenoid (CMS) experiment [4] at the LHC in proton-lead (pPb) collisions at $\sqrt{s_{\text{NN}}} = 8.16$ TeV using events in a wide range of charged particle multiplicities. The data used in the analysis that lead to this thesis was collected in the Heavy Ion Run that happened in November and December of 2016. The aim of this work is the measurement of the source size and the strong final state interactions scattering parameters, where the knowledge of such interactions is lacking. The measurements are performed as functions of charged particle multiplicity ($K_S^0 K_S^0$ and $\Lambda\overline{\Lambda}$) and of the pair transverse mass (only for $K_S^0 K_S^0$).

This work is structured as follows. In Chapter 2, we present a review of quantum chromodynamics and the quark-gluon plasma, including history, signatures and some interesting results, also for small colliding systems. Chapter 3 contains a theoretical approach of femtoscopic correlations and previous experimental measurements of the correlations of interest. Chapter 4 gives an overview of the LHC and outlines the CMS experiment. The complete data analysis procedure, including a detailed discussion about background estimation and systematic uncertainties are presented in Chapter 5. The results for all pair correlations are presented in Chapter 6. The conclusions and outlook are given in Chapter 7. In addition to the regular chapters, this thesis includes four appendices. Definitions and concepts used in the text are described in more details in Appendix A. Appendix B presents information about the thermodynamic and hydrodynamic description of the quark-gluon plasma. The derivation of the Lednicky-Lyubolshitz model is described in Appendix C. At the end, Appendix D briefly describes activities performed in the CMS collaboration.

Chapter 2

Strong Interactions and the Quark-Gluon Plasma

Particle physics is the scientific field responsible for studying the building blocks of matter (elementary particles) and their interactions. This field of physics was born in the 1880s and the first elementary particle discovered was the electron, in 1897, by J. J. Thomson [5]. Since then, several studies have been performed until reaching the current form of the Standard Model (SM) of particle physics [6, 7, 8, 9, 10] and other discoveries happened. The SM is a quantum field theory based on the symmetry group SU(3)×SU(2)×U(1), which describes the properties of elementary particles and the interactions among them. The SU(2)×U(1) is related to the electroweak[1] sector, whereas SU(3) refers to the strong sector that describes the colored constituents, i.e., the quarks and gluons. These constituents compose the hadrons: bosons (integer spin particles) and fermions (half-integer spin particles). The fourth force, gravity, is not yet included in the SM, however, in the energy scale currently accessed at accelerators, this interaction is extremely weak when compared to the other forces and can be neglected.

The general structure of Standard Model is shown on Fig. 2.1. According to the SM, there are three generations of fermions containing 12 particles (plus their respective antiparticles) divided equally in species classified as *leptons* and *quarks*. Leptons are particles that feel only electroweak interactions, the six leptons are: *electron (e^-)*, *electron neutrino (ν_e)*, *muon (μ^-)*, *muon neutrino (ν_μ)*, *tau (τ^-)* and *tau neutrino (ν_τ)*. Quarks are particles that, besides the electroweak force, are also sensitive to strong interactions. They carry an additional quantum number called *color charge* (see more at Sec. 2.1), and the quarks are six: *up (u)*, *down (d)*, *strange (s)*, *charm (c)*, *bottom (b)* and *top (t)*. The first generation of fermions, constitutes the everyday matter, i.e., composes the visible matter of the universe. In the

---

[1]The weak and electromagnetic interactions can be unified and described by the so-called electroweak theory developed by S. L. Glashow [11], M. A. Salam [12] and S. Weinberg [13], independently, and is also called Glashow-Weinberg-Salam model.

SM, interactions are mediated by the exchange of bosons: the electromagnetic force, that describes the interaction between electrically charged particles and is mediated by the *photon (γ)*; the weak force, responsible for flavor changing and process that includes neutrinos, are mediated by the $W^{\pm}$ and Z^0 bosons; the strong nuclear force that describes the interaction between particles which contain color charge, are mediated by the *gluon (g)*. The *graviton (G)* is the hypothetical boson that mediates the gravitational force and which is outside the SM. The last ingredient of the SM was theorized in 1964 by P. Higgs [14], F. Englert and R. Brout [15] for explaining the mass generation of elementary particles, called the *Higgs mechanism* (or Brout-Englert-Higgs mechanism). According to this mechanism the elementary particles obtain their mass by the interaction with the Higgs field (the heavier the particle, the more strongly it couples to the field) and the quantum excitations of this field correspond to a new particle: the *Higgs boson (H)*. The discovery of the Higgs boson happened in 2012 (∼50 years after the theoretical proposal), at the Large Hadron Collider (LHC), with the simultaneous measurements performed by the Compact Muon Solenoid (CMS) [16] and by the A Toroidal LHC ApparatuS (ATLAS) [17] collaborations. The Higgs boson mass was measured to be around 125 GeV. Nowadays, the SM is the one of the most successful theoretical models in the history of physics, with many predictions (including the Higgs boson) and precise agreements with experimental data.
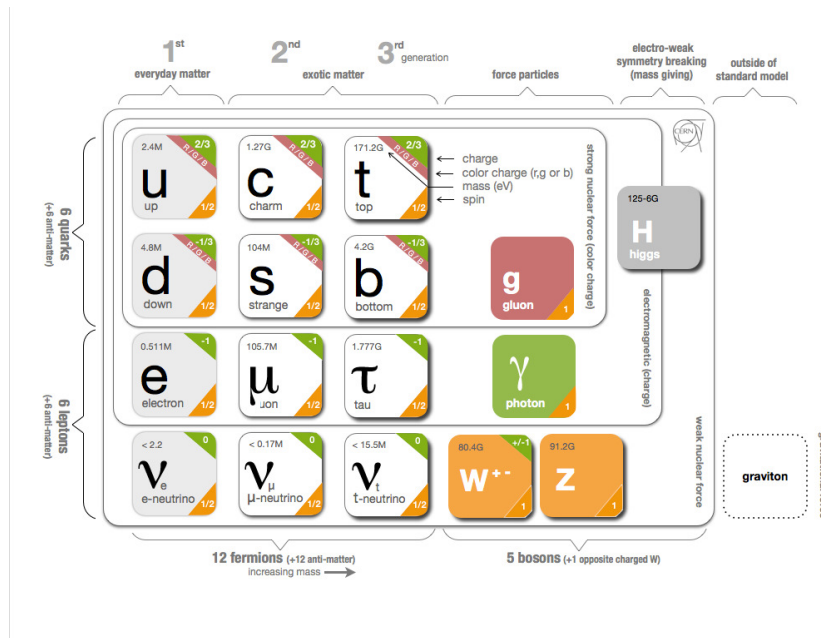
Figure 2.1: Sketch of the Standard Model structure. Extracted from CERN website https://cds.cern.ch/record/1473657 [last access on 13/Mar/2021].

In this work, we focus on the study of strong interactions between quarks, gluons and hadrons. Based on that, this chapter starts with a brief overview of strongly interacting particles, followed by the theory of strong interactions and the description of a state of matter called quark-gluon plasma.

2.1 Strongly interacting particles

Partons (quarks, antiquarks and gluons) are the only elementary particles that interact strongly. However, these particles are not observed in isolation in nature, but are grouped into particles called hadrons. When produced in high energy collisions, quarks and gluons hadronize[2] into narrow cones of particles in a certain phase-space region (along the direction of the original parton) that are called jets.

The first known hadrons were the proton, discovered by E. Rutherford in 1919 [18], and the neutron, discovered by J. Chadwick in 1932 [19]. In 1947, C. M. G. Lattes, H. Muirhead, G. P. S. Occhialini and C. F. Powell discovered the pion [20]. After this, a multitude of hadrons was discovered, and later they were classified in two categories (based on their masses): baryons, like protons and neutrons, and mesons, like pions.

In December of 1947, the first two strange particles were observed: the neutral and charged kaons ($K^0 \rightarrow \pi^+ \pi^-$ and $K^\pm \rightarrow \mu^\pm \nu_\mu$), in cosmic ray experiments performed by G. D. Rochester and C. C. Butler [21]. Later, in 1950, also with cosmic rays, the group of Armeteros et al., from Caltech, announced the observation of a neutral strange baryon decaying into a proton and a pion, called lambda (Λ) [22, 23]. One similarity between the decays of neutral kaons and lambdas is that their decays form a "V", and then that particles receive the name of V^0 particles.

With the progress in cosmic ray studies and the advent of particle accelerators, new hadrons were discovered, such as Δ's, Ξ's, Σ's and others. In the beginning, all these hadrons were believed to be elementary particles and the scientific community was looking for a unified model capable of describing the great variety of strongly interacting particles. The first attempt of an elementary particle classification was described by S. Sakata [24] in 1956 and expanded by the Nagoya model [25, 26]. These studies encouraged the search for a model where hadrons are not elementary particles, but instead, they are composed of more fundamental

---

[2]The hadronization is the process where partons group together into final state particles due the color confinement effect (see Sec. 2.2.2).

objects.

In 1964, M. Gell-Mann and G. Zweig proposed the quark model [27, 28]. According to this model, hadrons have an internal structure and are composed of elementary particles, called *quarks (q)* and *antiquarks (q̄)*. Initially, it was believed that there were three species of quarks, called *up (u)*, *down (d)*, *strange (s)* and respective antiquarks. These quarks should have the following characteristics: i) be fermions with spin 1/2; ii) have fractional electric charge; and iii) should have isospin and strangeness, in order to compose all the particles known at the time. In this model, baryons (antibaryons) are composed of three quarks (antiquarks), such as the proton (antiproton), which has an electrical charge equal to 1 (-1) and baryonic number[3] equal to 1 (-1), being composed of *uud* ($\overline{uu}\overline{d}$). Mesons are composed of a quark and an antiquark, such as π^+, which is composed of *ud̄*. However, this model failed to explain particles like Δ^{++}, which has spin 3/2, and would violate the Pauli exclusion principle[4] since their composition must be *uuu*. To solve the problem, O. W. Greenberg [29], M. Y. Han and Y. Nambu [30] created an additional quantum number called *color charge* so that the Pauli exclusion principle could be re-established. Therefore, each quark must assume a state of color, for instance the primary colors: *green*, *red* and *blue*; analogously, the antiquarks should carry the anticolors: *antigreen*, *antired*, and *antiblue*. Gluons are also colored, carrying an equal number of colors and anticolors, and the type of gluon is determined by this charge. Inside the hadrons, the combination of valence quarks must form a white object, that is, the total amount of color charge must be zero or all color charges must be present in equal quantity. This implies that each of the three quarks (antiquarks) inside the baryons (antibaryons) must have a color (anticolor) different from the other two. Similarly, the quark-antiquark pair inside the mesons must have a quark containing a certain color charge and an antiquark with an opposite color charge.

The quark model was only validated in the 1970s, when deep inelastic scattering (DIS)[5] experiments results established quarks as real objects [31]. The fourth quark flavor, called *charm (c)*, was discovered by the measurement of J/ψ bound state (formed by *cc̄*) simultaneously at Brookhaven National Laboratory (BNL) [32] and at Stanford Linear Accelerator Center (SLAC) [33]. The quark *bottom (b)* was discovered at Fermi National Laboratory (Fermilab) in 1977 by

---

[3]Each quark (antiquark) has fractional baryonic number equal to 1/3 (-1/3).

[4]According to the Pauli exclusion principle: two fermions cannot be in the same quantum state simultaneously.

[5]DIS uses leptons to probe the structure of hadrons.

measuring the Υ resonance (formed by $b\bar{b}$) [34]. Two years later, the existence of the *gluon (g)*, was established at Positron-Electron Tandem Ring Accelerator (PETRA) by the measurement of electron-positron interactions going in 3 jets ($q\bar{q}g$) in three different experiments [35, 36, 37]. In parallel, a strong evidence of the color charge was obtained by measuring the ratio of the cross-section of the process $e^+e^- \rightarrow$ hadrons, by the cross-section of $e^+e^- \rightarrow \mu^+\mu^-$. This experimental ratio could only be explained by considering the number of colors is equal to three [38]. The sixth, the heaviest and last quark from Standard Model, called *top (t)*, was discovery in 1995 by the DØ [39] and the Collider Detector at Fermilab (CDF) [40] collaborations, operating at the Fermilab Tevatron, by using proton-antiproton collisions at center-of-mass energy of 1.8 TeV (see beam energy definition at Sec. A.1 of Appendix A). Recent results also show the measurement of top quarks in heavy ion collisions [41, 42]. Years after the discovery of quarks and gluons, new exotic hadrons composed by four quarks, called *tetraquarks* have been observed by Belle [43], Beijing Spectrometer III (BES III) [44] and by the Large Hadron Collider beauty (LHCb) [45, 46, 47, 48] collaborations. LHCb also observed candidates of another species of exotic particles made by five quarks, called *pentaquarks* [49, 50].

After a very brief history of hadrons, quarks, gluons and colors, now it is possible to move to the theory used to describe the strong interactions.

2.2 Quantum Chromodynamics

Quantum ChromoDynamics (QCD) is a quantum field theory founded on first principles that describes the strong interactions between quark and gluon fields. QCD is a non-abelian[6] gauge theory based on the symmetry group SU(3) with 8 generators corresponding to the gluons. The Lagrangian density of QCD is written as [51, 52, 53]

$$\mathcal{L} = \sum_{\text{flavors}(f)} \overline{\psi}_i^f \left(i\gamma^\mu D_\mu - m_f \right)_{ij} \psi_j^f - \frac{1}{4} G_{\mu\nu}^a G^{a,\mu\nu}, \qquad (2.1)$$

where the first part of the lagrangian is the quark term and the second part represents the gluon term. The sum, on the left part, runs over the number of quark flavors (f). The ψ_j^f ($\overline{\psi}_i^f = \psi_i^{f\dagger}\gamma^0$) is the quark (antiquark) field with color j (i). The factors γ^μ are the Dirac matrices (see Sec. A.2 of Appendix A) and m_f is the

---

[6]Gauge theories are called non-abelian if the generators associated to the symmetry group anticommute.

mass of the quark with flavor f. Assuming the Einstein convention, i.e., repeated indices are implicitly summed, where $\mu, \nu = 0, 1, 2, 3$ are the spacetime indices, i, $j = 1, 2, 3$ represent the color indices in the quark field and $a = 1, ..., 8$ are the color indices of the gluon field. The covariant derivative is given by

$$D_\mu = \partial_\mu - i\frac{g_s}{2}\lambda^a A_\mu^a, \tag{2.2}$$

where ∂_μ is the partial derivative, g_s is the coupling of the strong interactions that can be written in terms of the so-called running coupling constant (α_s) as $4\pi\alpha_s = g_s^2$. λ^a are the Gell-Mann matrices (see Sec. A.2 of Appendix A) which are associated with the generators of SU(3) group as $T^a = \lambda^a/2$. A_μ^a is the gluon field. The gauge invariant gluonic field strength tensor is give by

$$G_{\mu\nu}^a = \partial_\mu A_\nu^a - \partial_\nu A_\mu^a + g_s f^{abc} A_\mu^b A_\nu^c, \tag{2.3}$$

where f^{abc} is the structure constants of SU(3) group defined through $[\lambda^a, \lambda^b] = 2if^{abc}\lambda^c$ (see Sec. A.2 of Appendix A).

Expanding the QCD Lagrangian 2.1, is possible to obtain the vertices of gluon self-interaction as a consequence of the non-abelian nature of QCD[7]:

$$\text{3-gluon vertex:} \quad \frac{g_s}{2}f^{abc}\left(\partial^\mu A^{a,\nu} - \partial^\nu A^{a,\mu}\right)A_\mu^b A_\nu^c, \tag{2.4}$$

$$\text{4-gluon vertex:} \quad -\frac{g_s}{4}f^{abc}f^{ade}\left(A^{b,\mu}A^{c,\nu}A_\mu^d A_\nu^e\right), \tag{2.5}$$

which are represented graphically in Fig. 2.2: a 3-gluon vertex (left) and a 4-gluon vertex (right). These self-interactions and the non-abelian behavior are crucial ingredients to study the nuclear aspects of QCD at high energies.
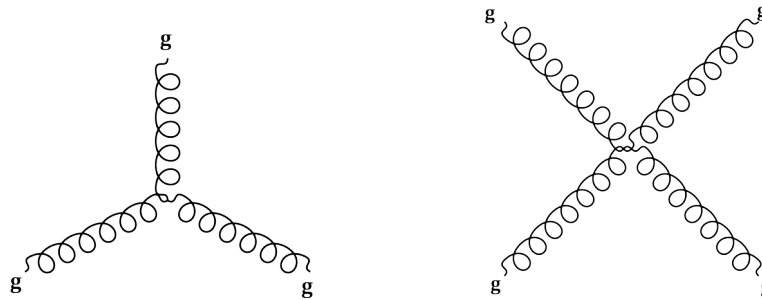
Figure 2.2: QCD Feynman diagrams for the self-interaction gluon vertices: 3-gluon (left) and 4-gluon (right).

---

[7]In the quantum electrodynamics (QED), the abelian quantum field theory that describes electromagnetism the mediator, the photon (γ), does not present self-interactions.

2.2.1 QCD running coupling constant

In QCD, as in most quantum field theories, the physical quantities are calculated by using perturbative expansions in terms of the coupling constant (α_s). The so-called Leading Order (LO) is the first order of the perturbative expansion and the following orders are Next-to-LO (NLO), Next-to-NLO (NNLO), and so on. In higher orders of α_s, loop diagram integrals contain divergences because of the arbitrariness of the values of momentum in the loop, being necessary to integrate from zero to infinity, going to energy scales where the theory is not valid. These divergences can be handled by using the *regularization* and *renormalization* process[8] [54, 55]. After the renormalization, the β function, which describes the dependence of the coupling constant of the theory with the renormalization scale (μ) can be written as

$$\beta(\alpha_s) = \frac{\partial \alpha_s(\mu^2)}{\partial \ln \mu^2} = -\alpha_s^2(\mu^2) \left[\beta_0 + \beta_1 \alpha_s(\mu^2) + \beta_2 \alpha_s^2(\mu^2) + ... \right], \quad (2.6)$$

where β_i are the coefficients of the beta function for different number of loops (β_0 for one-loop, β_1 for two-loops, and so on). Adopting the one-loop approximation (i.e., neglecting $\mathcal{O}(\alpha_s^i)$ terms for $i > 3$), the running coupling constant is

$$\alpha_s(\mu^2) = \frac{\beta_0^{-1}}{\ln \left(\mu^2 / \Lambda_{\text{QCD}}^2 \right)}, \quad (2.7)$$

where β_0 can be written in terms of the number of quark flavors (N_f) and number of colors (N_c) as $\beta_0 = (11 N_c - 2 N_f)/12\pi$ and $\Lambda_{\text{QCD}} \approx 200 - 300$ MeV [56] is the scale at which the coupling becomes infinite (called QCD Landau pole) extracted experimentally and depends on the regularization scheme [57].

In order to get a direct relation with the experimental data, one interesting choice is to consider the renormalization scale associated to the energy scale (Q) as $\mu^2 = Q^2$. Figure 2.3 shows the most recent measurements of $\alpha_s(Q^2)$ versus the energy scale Q for different orders of loop calculations summarized by the Particle Data Group (PDG) [10]. The latest world average value obtained at the mass of the Z^0 boson is $\alpha_s(M_{Z^0}^2) = 0.1179 \pm 0.0010$.

---

[8]The regularization procedure consists of replacing the basic physical parameters of the Lagrangian with finite regularized parameters and then treating the divergences by applying a renormalization scheme.
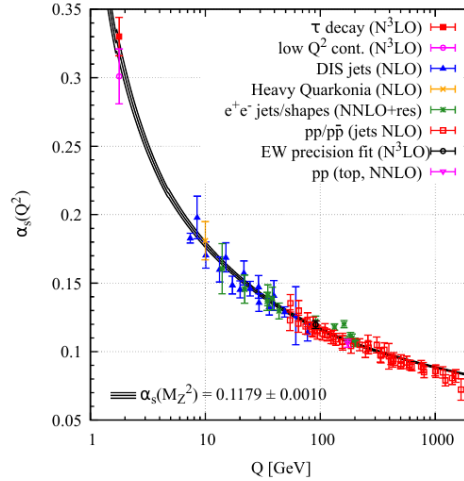
Figure 2.3: Particle Data Group summary of α_s measurements as a function of the energy scale Q. Extracted from [10].

The α_s behavior decreasing with Q^2 indicates that at high energies (small distances) the color field strength is reduced, allowing perturbative calculations (pQCD). On the other hand, at lower energies (large distances or small Q^2), α_s is large, thus accessing the non-perturbative regime, where the pQCD is not valid anymore. Such effects can be understood as interactions between the gluon field and the QCD vacuum: in large α_s, interactions with virtual quark-antiquark pairs acts as colour dipoles forming a color screening effect, while in small α_s, interactions with virtual gluons increases the net effect of the colour charge producing a called antiscreening effect.

One possible way to perform calculations in a non-perturbative regime is by using the so-called *lattice gauge theory* or *lattice QCD* (LQCD). The LQCD is a numerical approach which discretizes and solve the QCD equations in a grid with spacing a in both spatial and temporal dimensions. This formalism reproduces with an incredible precision a large number of experimental measurements (e.g., mass spectrum of light and heavy hadrons [58, 59]) and also has been largelly used to study QCD phase transition (see Sec. 2.3.2).

2.2.2 Color confinement and asymptotic freedom

The fact that quarks and gluons cannot be observed in isolation in nature is called *color confinement*. This picture corresponds to the fact that the intensity of the strong nuclear interaction between quarks increases with the distances between

them[9], in which case α_s is larger, leading to the non-perturbative regime as shown by Fig. 2.3. Mathematically, this effect is not yet completely understood and is one of the Clay Mathematics Institute's Millennium Problems [61].

One way to qualitatively understand the color confinement is by the illustration in Fig. 2.4. When two quarks from a baryon (or a quark-antiquark pair from a meson) are pulled apart, the intensity of the color field (represented by the strings) increases, until its energy is large enough ($E > 2m_q$) to create a new quark-antiquark pair out of the vacuum, so that the original baryon split into a baryon and a meson (or the original meson split into two mesons). This explains why it is not possible to observe particles with color charge different from white (color neutral) in the detectors. The color confinement mechanism is present in the hadronization process and jet production.
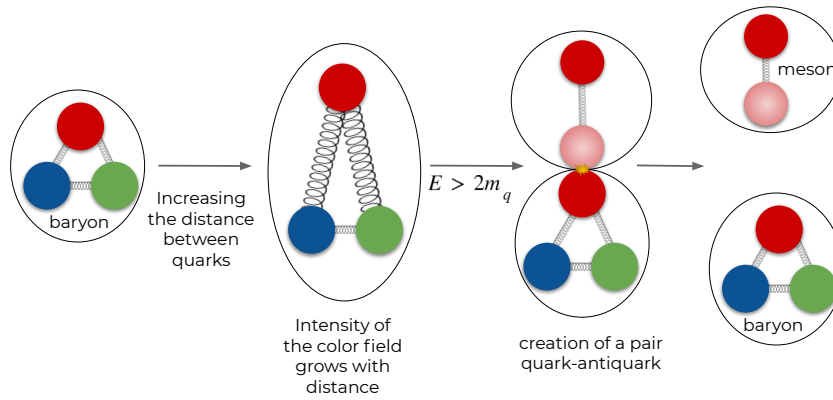
Figure 2.4: Sketch of a hypothetical tentative of removal of a quark from a baryon with subsequent creation of a meson (quark-antiquark pair) in association with the color confinement mechanism.

Another important property of QCD is the *asymptotic freedom*, discovered in 1973 by D. Gross, F. Wilczek [52] and D. Politzer [62] (Nobel Prize of Physics in 2004). The asymptotic freedom is a direct consequence of the non-abelian nature of QCD and, on the other side of color confinement, says that at high energies the separation distance between quarks is small and, consequently, the intensity of the strong interaction is reduced. This can be better understood by means of the plot in Fig. 2.3: for higher values of Q^2, α_s gradually decreases, that is, the greater the energy of the system, the more the quarks and gluons behave as free particles. The asymptotic freedom is the property which allows the study of QCD in the

---

[9]The potential of the field is proportional to the separation between the quarks r as $V(r) \sim kr$ ($k \sim 1 \, \text{GeV}/\text{fm}$), demanding more and more energy as the distance between them increases [60].

perturbative regime for small α_s. In the mid-seventies, this property also lead to the conjecture of the existence of a new state of matter called quark-gluon plasma, which is discussed in the next section.

2.3 Quark-Gluon Plasma

The Quark-Gluon Plasma (QGP), name given by E. V. Shuryak [63], is the QCD phase of matter created at extremely high temperatures (order of 10^{12} K) and energy densities (higher than 1 GeV/fm^3). In this system quarks and gluons are no longer confined into hadronic bound states. This state of matter is believed to have been present at the beginning of the universe, around 10^{-5} seconds after the Big Bang [64].

Historically, the idea of the study of matter in extreme conditions was first suggested by T. D. Lee in 1974 [65, 66, 67]. W. Greiner et. al. [65, 67, 68] pointed out that these conditions could be achieved by using nucleus-nucleus (AA) collisions. In 1975, J. C. Collins and M. J. Perry [69], based on the QCD asymptotic freedom property, suggested that the QGP should behave like an ideal gas composed of quarks and gluons and, since then, microscopic models was largely applied to study this state of matter. In the 1980s, many possible experimental signatures of QGP were proposed (see Sec. 2.3.3). In 1982, J. D. Bjorken [70] proposed the relativistic hydrodynamic description (first studied by Landau [71, 72]) to describe the matter formed in nucleus-nucleus collisions. However, the microscopic models were largely used for that description, until the QGP was discovered experimentally in 2005. After that, the hydrodynamical model (a brief description of this model can be found at Sec. B.2 of Appendix B) was adopted, studied, improved and simulations performed by different codes (CHESS [73, 74, 75], SPHERIO [76, 77], MUSIC [78, 79], SONIC [80], iEBE-VISHNU [81] and others) are still being used today for studying the properties of the QGP (equation of state, viscosity, ...).

Experimentally, studies of heavy ion collisions (HIC) starts in the 1970s at Bevalac[10] located at Lawrence Berkeley National Laboratory (LBNL). Bevalac performed collisions using Carbon, Neon and Argon against a fixed target with energies from 0.2 to 2.6 GeV per nucleon in order to investigate the equation of state (EoS) of QCD at high densities [82, 83] (see Sec. 2.3.2). They observed that a possible compressed nuclear matter was created, confirming the prediction

---

[10]Bevalac is a combination of the Bevatron (synchrotron that accelerated protons) and the SuperHILAC (linear accelerator that injected heavy ions into the Bevatron) accelerators.

from W. Greiner et. al.; the Bevalac was decommissioned in 1993. In the 1980s the Alternating Gradient Synchrotron (AGS) at Brookhaven National Laboratory (BNL), was also adapted to collide ions of gold (Au) and silicon (Si), with center-of-mass energy up to $\sqrt{s_{NN}} \sim 5$ GeV per nucleon, against fixed targets (made of Au or beryllium (Be) or aluminum (Al)). The AGS operated HIC for 12 years (later becoming part of the Relativistic Heavy Ion Collider complex) delivering analyses from several experiments as E802, E810, E814, E858 and others, they observed some signatures, but could not establish the existence of the QGP. Towards the mid-eighties HIC have been studied also at the Super Proton Synchroton (SPS) accelerator at Conseil Europen pour la Recherche Nuclaire (CERN)[11], producing collisions of lead (Pb) against fixed-targets of Pb or Au with a center-of-mass energy per nucleon up to $\sqrt{s_{NN}} \sim 17$ GeV. Seven large experiments were used to collect data from SPS: NA44, NA45, NA49, NA50, NA52, NA57/WA97 and WA98. Based on the compiled results from these experiments, at the end of 1999, when it was about to be decommissioned, the SPS announced the discovery of a new state of matter consistent with QGP [84, 85], showing a good agreement with microscopic models, which considers the QGP as a gas-like matter. The SPS fixed-target program is still active with the NA61/SHINE experiment, in order to study hadron production and neutrinos in nucleus-nucleus, hadron-nucleus and hadron-proton collisions [86].

In the year 2000, the Relativistic Heavy Ion Collider (RHIC), started to operate at BNL using AGS as a pre-accelerator, with the main plan to search for the QGP formation. Different from its predecessors, RHIC is a collider, which means that the collisions are performed with a beam of particles against another particle beam and, not against fixed targets. Proton-proton (pp), gold-gold (AuAu) and copper-copper (CuCu) collisions were delivered at different center-of-mass energies. The data from RHIC collisions were collected and analysed by four main experiments: BRAHMS, PHOBOS, PHENIX and STAR. The two-last ones are still operational, however PHOBOS and BRAHMS, completed their operations in 2005 and 2006, respectively. In 2005, researchers from RHIC, after the measurements of many signatures, officially announced the discovery of the QGP [1] in AuAu collisions. Differently than early expectations, RHIC showed that this matter is strong-coupled, behaving not as a gas, but rather more like an almost perfect fluid (low viscosity). After that, RHIC conducted several measurements in order to better understand the QGP properties for different collision systems (pAl, dAu,

---

[11]In english: European Organization for Nuclear Research.

CuAu, and others) and later, by varying a large range of center-of-mass energy (with $\sqrt{s_{\mathrm{NN}}}$ from 7.7 to 200 GeV), to search for a possible critical point in the QCD phase diagram (see Sec. 2.3.2). The RHIC program is still active and a bit about its future plans are presented in the Sec. 4.1.3 of Chapter 4.

At the moment, the most powerful heavy ion collider is the Large Hadron Collider (LHC) at CERN, which uses SPS as a pre-accelerator. The LHC heavy ion program started in 2010 with lead-lead (PbPb) collisions at $\sqrt{s_{\mathrm{NN}}}$ = 2.76 TeV, allowing to study the QGP at the TeV scale. Nowadays, this program counts with measurements for the four mains experiments with studies in lead-lead, proton-lead and xenon-xenon collisions at different energies. More detail about LHC and the collisions performed there are described at Chapter 4. The QGP signatures observed at RHIC was confirmed at LHC and also new surprising results have been observed, as the collectivity behavior of the system produced in events with high multiplicity[12] in proton-proton collisions (see Sec. 2.3.4).

2.3.1 Heavy ion collision evolution

After years of study and measurements previously mentioned, nowadays the evolution of heavy ion collisions can be described as shown by the Fig. 2.5.
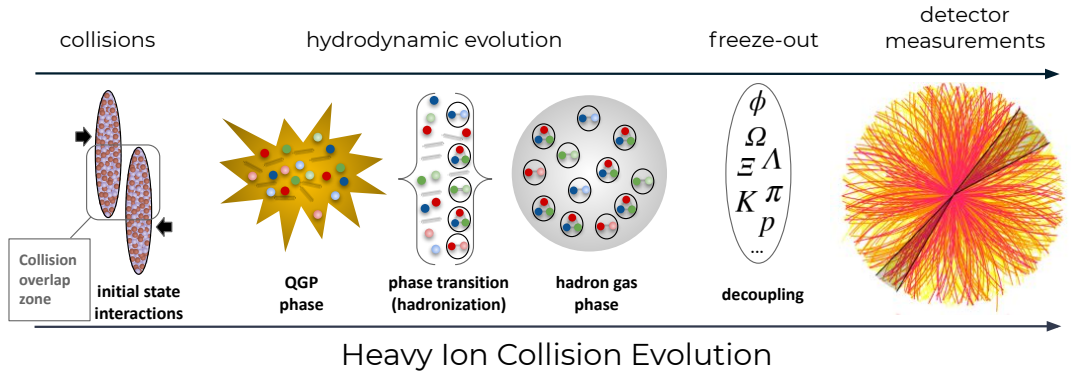
Figure 2.5: Schematic view of the heavy ion collision evolution. The detector image was extracted from https://cms.cern/news/jet-quenching-observed-cms-heavy-ion-collisions [last access on 13/Mar/2021].

According to Fig. 2.5, two nuclei accelerated at velocities close to speed of light in the vacuum (*c*), are contracted by the Lorentz factor in the longitudinal direction.

---

[12]The multiplicity is defined as the number of charged particles produced per collision.

The region of interaction (the overlap of the two nuclei) defines the centrality[13] of the collision (see Sec. A.3 of Appendix A). When the collision happens, a large deposition of energy occurs forming an initial system. After a complex process involving microscopic collisions between the constituents of this system, a hot and dense matter (QGP) is formed in local thermal equilibrium[14]. From this moment, the hydrodynamical model can be applied. As the space-time evolution of the system occurs, the matter formed in the collision expands and cools down. During this process, partons begin to regroup into hadrons. After a certain time, all matter formed in the collision will be in the hadronic phase. When the mean free path of hadrons in the system is in the order of the characteristic dimension of the system, the thermal equilibrium hypothesis is no longer valid and the hydrodynamic model can no longer be used. In this stage, the system decouples (freezes-out) and the hadrons formed in the collision and their decay products moves freely to the detector.

2.3.2 QCD phase diagram

In the 1960s Rolf Hagedorn studied the thermodynamical proprierties of hadronic matter, proposing the so-called *statistical bootstrap model* [87]. In his studies, Hagedorn considered that at high energies the matter can be described as a hadron gas (HG) and can be treated by using statistical mechanics. He observed that the density of the known hadrons increases exponentially, and diverges at a temperature of 158 MeV. At the time, this value was interpreted as a limiting temperature and received the name of *Hagedorn temperature* (T_H). Nowadays, the Hagedorn temperature can be interpreted as the critical temperature around which a phase transition occurs between the QGP phase and hadron gas. Calculations of the QCD phase transition are harder because in this region the critical temperature (T_c) is in the order of Λ_{QCD}, than α_s becomes large and pQCD cannot be used, showing the need for theoretical calculations in order to describe the phase transition.

Initially, it was believed that a first order phase transition would happen between the QGP and HG [88], that is, there would be a mixed phase during which both the QGP and the HG coexisted. This was first calculated by considering the

---

[13]Centrality is the quantity which estimates the overlap region between the nuclei, with 0% corresponding to a complete overlap (head on) and 100% to the case that the nuclei barely touch each other.

[14]Local thermal equilibrium means that every small part of the system can still be roughly described by the thermal equilibrium laws.

QGP to a gas composed of free quarks (u, d, s), antiquarks ($\bar{u}, \bar{d}, \bar{s}$) and gluons. Using statistical mechanics, it is possible to estimate the thermodynamic quantities for the hadron gas at low temperatures and for the QGP at high temperatures (see more details in Sec. B.1 of Appendix B). However, the interactions and the confinement of quarks and gluons at lower temperatures should also be taken into account, which can be done by means of the MIT bag model [89]. According to this model, a constant energy density $\mathcal{B}$ is postulated, called bag constant, which is adjusted to make the pressure in the QGP phase coincident with the pressure of the hadron gas at a certain T_c ($P_{HG}(T_c) = P_{QGP}(T_c)$). All uncertainties in the calculations are associated with $\mathcal{B}$. For $\mathcal{B} = 380$ MeV and zero baryon density, we have a critical phase transition temperature of $T_c \approx 162$ MeV.

With the improving precision of LQCD calculations, it became possible to estimate more accurately the thermodynamic quantities in the phase transition at zero baryon density. The results from LQCD showed that this phase transition would be a *crossover*[15] between the HG and the QGP. Figure 2.6 shows a comparison between the energy density, ε, divided by temperature, T, to the fourth power versus T for the EoS with first order phase transition (continuous blue line) and for the parametrization of LQCD results from HOTQCD collaboration [90] (dashed red line). Is possible to observe that the two EoS are identical in the hadron gas phase. The EoS with first order phase transition shows an abrupt change at T_c, corresponding to the mixed phase between the QGP and hadrons gas phase, whereas the LQCD presents a smooth transition. According to this LQCD EoS, the critical temperature is situated at $T_c = 154 \pm 9$MeV, in agreement with the Hagedorn temperature estimate. Based on these results, the hypothesis of a critical point (circle), where a second order phase transition is expected, arises on the transition curve: at high temperatures (T) and low baryon chemical potential (μ_B)[16] a crossover phase transition is expected (dashed line); at high-μ_B and lower T the phase transition is of first order (continous line) as illustrated in Fig. 2.7. This diagram can be divided in two parts: at high-T ($> T_c$) the QGP can be accessed and at low-T ($< T_c$) the other states of matter are expected. The point $(0,0)$ is the vacuum. For high-T and $\mu_B \sim 0$ stands the situation corresponding to the early universe, i.e., soon after the Big Bang. By increasing μ_B and decreasing in T regions accessible by the accelerators is indicated: LHC, RHIC, NICA and FAIR.

---

[15]Crossover is a smooth phase transition that ends at the critical end point, where the phase transition is of a second-order.

[16]μ_B can be understood as the excess of matter compared to antimatter.

The usual nuclear matter exists at lower temperatures and for μ_B around 900 MeV. Increasing μ_B a state of matter called neutron gas (a degenerate fermionic gas) is expected at the interior of neutron stars [91]. And, for higher values of μ_B and higher T it is possible to access a theoritized state of matter called color superconductor [92].
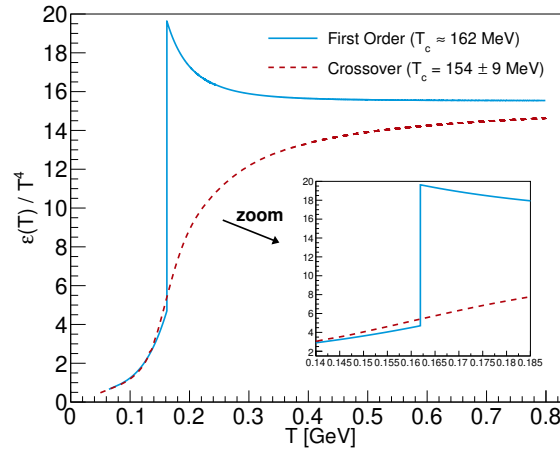
Figure 2.6: Energy density (ε) divided by temperature (T) to the fourth potence (ε/T^4) in arbitrary units versus temperature for a first order phase transition (solid blue line) and for a crossover phase transition from LQCD calculations [90] (dashed red line) . See text for more information.
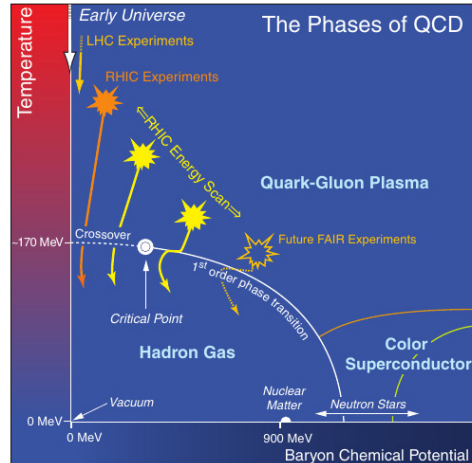
Figure 2.7: QCD phase diagram showing the temperature as function of the baryon chemical potential. The lines represent the phase transition boundaries, the circle represents the possible critical point, colored arrows represent the regions accessible by accelerators. See more information in the text. Extracted from [93].

2.3.3 QGP signatures

The direct observation of the QGP is not possible because this system, created in high energy collisions, lasts for a very short period of time in the deconfined phase, and only its hadronized products are detected. However, the study of this state of matter can be done indirectly through characteristic signatures that are observed as final state particles at the detector, that were affected by the presence of QGP. Some of these QGP signatures are described below.

Collective behavior

One of the strongest evidences of the quark-gluon plasma formation is the collective behavior observed in heavy ion collisions. The collective evolution of the system is described by the anisotropic flow. We can understand the production of this flow with the help of Fig. 2.8. After a non-central heavy ion collision, the participants[17], form a region corresponding to the volume of interaction between the nuclei, represented by the ellipsoid in Fig. 2.8, left, that is spatially anisotropic. With the evolution of the system, this spatial anisotropy is transferred to the momentum space, due to the difference between the pressure gradients in the major and minor axes of the ellipsoid, as shown in the Fig. 2.8 (top right). This behavior indicates that the evolution of the system is also anisotropic. We can say that the system has a very high energy density in the reaction region, decreasing gradually towards the edges of the system, more quickly in the direction x than in the direction y of the figure.

This anisotropy is reflected in the azimuthal (ϕ) distributions of the particles final state, as shown in Fig. 2.8 (bottom right), and can be expressed by a Fourier expansion, as [94]

$$\frac{dN}{d\phi} \propto 1 + 2 \sum_{n=1}^{\infty} v_n \cos\left[n\left(\phi - \psi_{EP}\right)\right] \tag{2.8}$$

where v_n and ψ_{EP} are the Fourier coefficients (also called harmonics) and the azimuthal angle with respect to the event plane, respectively[18]. The event plane is the closest experimental realization of the reaction plane, which is not accessible to experiments, since it uses the impact parameter (distance between the center of the nuclei) in its definition. The v_1 coefficient is related with the energy momentum

---

[17]The participants are the nucleons that interact at the moment of the collision, the other nucleons are called spectators. See Sec. A.3 of Appendix A.

[18]The event plane is one of the possible methods which are used to estimate v_n, other methods also used are: cumulants, scalar product and Lee-Young Zeros [94].

conservation, while the second-order coefficient (v_2), called elliptic flow, reflects the lenticular shape of the interaction area formed in non-central collisions and is dominant over the others. The higher-order coefficients, particularly the odd indices n, come from fluctuations in the positions of the nucleons in the initial conditions. The fact that these coefficients are non-zero is an indicative of the system collectivity. For the studies of the QGP, the elliptic flow is important, since this quantity is directly affected by the medium properties (equation of state, viscosity and others). Figure 2.9 shows the elliptic flow as a function of the transverse momentum (p_T) measured by STAR and PHENIX collaborations in AuAu collisions at $\sqrt{s_{NN}}$ = 200 GeV for different particle species, compared to ideal hydrodynamical simulations [95]. A good agreement between data and simulations can be observed at low-p_T. For higher-p_T, viscosity or jets effects can contribute to this disagreement. Another interesting result observed in this figure is the mass ordering (heavier particles shown lower v_2); this effect was predicted by hydrodynamics and is clearly present in the data. Later, it was observed that v_2 also shows a scaling with the number of constituent quarks (n_q), which means that, if we measure the elliptic flow for baryons and mesons and divide by the respective n_q, the resulting v_2 values will be in agreement with each other, which can be interpreted as these hadrons flowing together [96]. The detailed experimental studies of the elliptic flow at RHIC and the good agreement with the ideal hydrodynamical model were essential ingredients to demonstrate that the produced QGP as a nearly perfect fluid. At the LHC, similar measurements have been performed, thus confirming the results and behaviors observed at RHIC. In addition, among a pletora of new experimental results, the LHC presented surprisingly results, such as the flow measurements in small colliding systems (see Sec. 2.3.4).
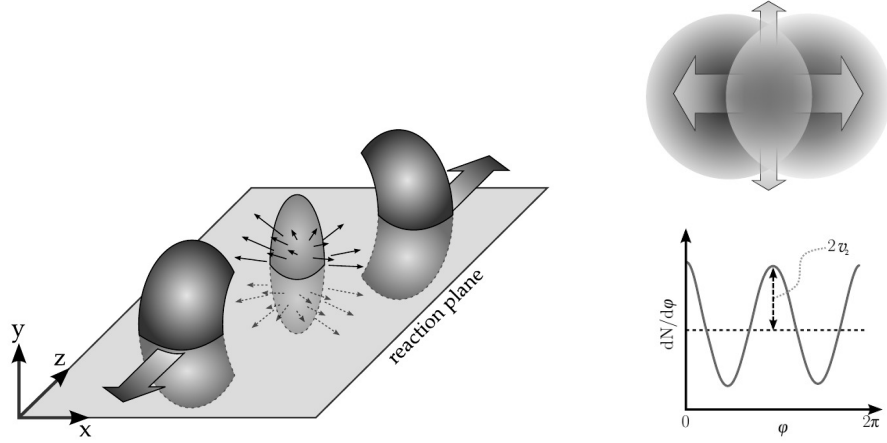
Figure 2.8: Schematic view of the interaction volume between two nuclei. The anisotropy observed in the *xy* plane generates the anisotropic flow. On the left a 3-dimensional representation is shown, on the top right the same idea is presented in the *xy* plane, on the bottom right an example of the azimuthal distribution is shown. Extracted from [97].
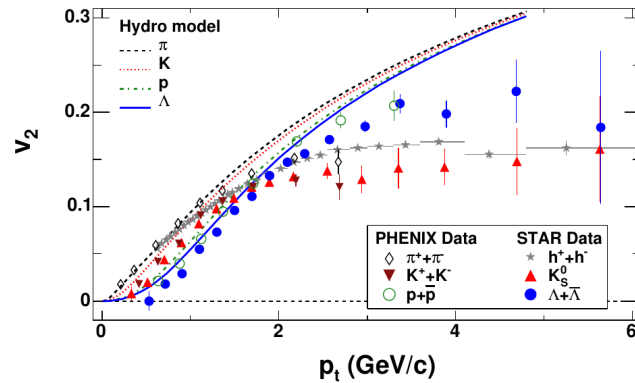
Figure 2.9: Elliptic flow (v_2) as a function of transverse momentum (p_T) measured by STAR and PHENIX collaborations (markers) for different species of particles compared to ideal hydrodynamical simulations (lines). Extracted from [95].

Strangeness enhancement

The strangeness enhancement was proposed as a QGP signature by J. Rafaelski and B. Muller [98]. The production of strange quarks can happen through three different ways: i) gluon splitting ($g \rightarrow s\bar{s}$); ii) gluon fusion $gg \rightarrow s\bar{s}$; iii) quark-antiquark annihilation ($q\bar{q} \rightarrow s\bar{s}$). In proton-proton interactions, the production of hadrons composed by strange quarks are usually suppressed when compared to hadrons containing light quarks (u and d), because of the higher mass of the strange quark (which requires higher energies). According to J. Rafaelski and

B. Muller, if a dense and hot matter is formed, a very large gluon density and energy is present, therefore, the gluon fusion process will be favored energetically, which should not occur in a scenario without the QGP medium. As the system evolves, the strange quarks created in the QGP, start to group with other quarks of the medium, producing bound states which are the strange hadrons. This enhancement was observed first at the AGS [99] by the measurement of the K/π ratio, later this was also observed at SPS [100], RHIC [101] and LHC [102]. Figure 2.10 shows the production yield of protons and strange hadrons (Λ, $\overline{\Lambda}$, Ξ^-, $\overline{\Xi}^+$ and $\Omega^- + \overline{\Omega}^+$) performed in HIC relative to pp collisions at RHIC at $\sqrt{s_{NN}}$ = 200 GeV (solid markers) and to pBe collisions at SPS at $\sqrt{s_{NN}}$ = 17.3 GeV (open markers) as a function of the number of participants, N_{part} (higher N_{part}, most central is the collision). The results show a clear enhancement, increasing with N_{part}, for the strange hadrons (even in different energies), which cannot be seen for protons. And these results are in agreement with thermal models (arrows) which suggest the presence of the dense medium.
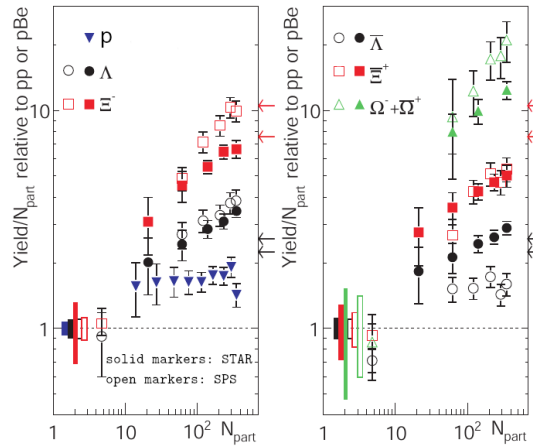
Figure 2.10: Production yield of protons and strange baryons (Λ, $\overline{\Lambda}$, Ξ^-, $\overline{\Xi}^+$ and $\Omega^- + \overline{\Omega}^+$), measured by STAR collaboration in AuAu collisions at $\sqrt{s_{NN}}$ = 200 GeV (solid markers) relative to the same yield in pp collisions and for NA57 collaboration in PbPb collisions at $\sqrt{s_{NN}}$ = 17.3 GeV (open markers) relative to the same yield in pBe collisions as function of N_{part}. Extracted from [101].

Jet quenching

In 1982, J. D. Bjorken proposed the idea of the jet quenching phenomena [103]. High energy jets are produced by the fragmentation of partons produced at the beginning of the collisions. In the case where a quark-gluon plasma is formed, these partons should feel the hot and dense medium, losing their energy by

interactions with the QGP constituents or by medium-induced gluon radiation. According to the original idea by Bjorken, if two jets are produced back-to-back and one of them goes through the QGP, at the end one jet will be measured with high energy and the other will be quenched. Figure 2.11, shows a schematic view of back-to-back jets produced at proton-proton collisions (top) and in the case idealized by Bjorken's (bottom).
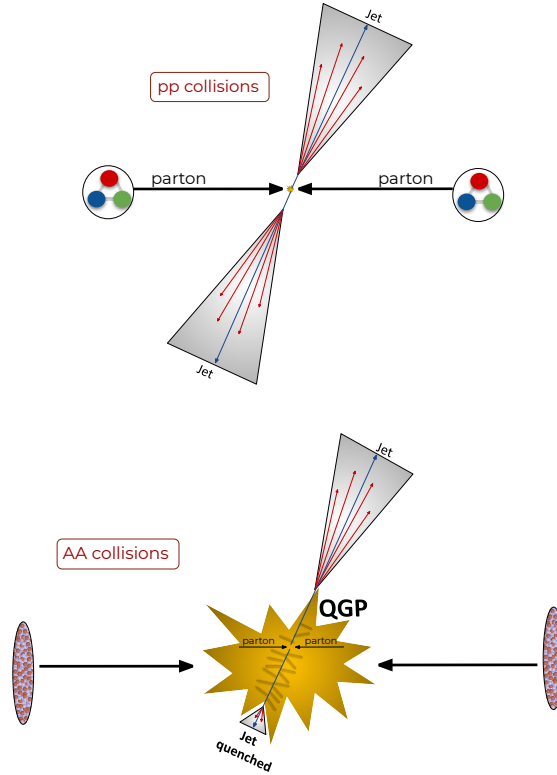
Figure 2.11: Sketch of the back-to-back dijet production in proton-proton (top) and heavy ion (bottom) collisions.

The first experimental evidence of this effect was observed by STAR collaboration at RHIC in the measurement of the di-hadron azimuthal correlations ($\Delta\phi$) [19] between low-p_T and high-p_T particles at $\sqrt{s_{NN}}$ = 200 GeV comparing pp (black line), central dAu (red circles) and central AuAu (blue stars) collisions [104], shown in Fig. 2.12. Their results show that, at $\Delta\phi \sim 0$, the peak coming from the jets is present in all the colliding systems, however, the back-to-back correlations disappears in the case of gold-gold collisions, similarly to the Bjorken's idea. Later, this effect was observed and largely scrutinized at the LHC [105, 106].

---

[19]$\Delta\phi$ is the azimuthal angle (in the transverse plane) difference between the two particles (see more at Chapter 4).
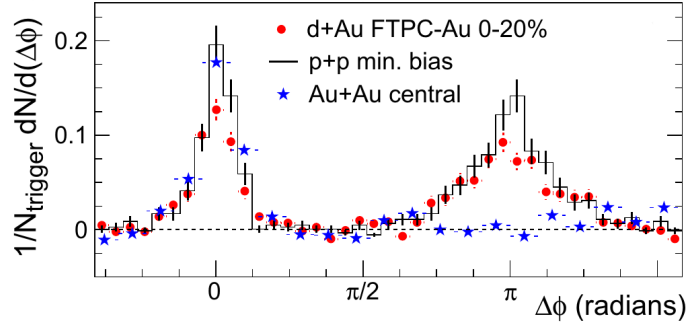
Figure 2.12: Di-hadron $\Delta\phi$ correlations for pp (black line), central dAu (red circles) and central AuAu (blue stars) collisions. Extracted and adapted from [104].

Production of high-p_T particles

High-p_T hadrons are expected to be produced by hard scatterings in the initial stages of the heavy ion collisions, therefore could be sensitive to entire evolution process of the system and, consequentelly, could be used as QGP probes. To quantify such effect, one observable called *nuclear modification factor* (R_AA) is used, which is defined as

$$R_\mathrm{AA} = \frac{N_\mathrm{AA}}{\langle N_\mathrm{coll} \rangle N_\mathrm{pp}},$$

(2.9)

where, N_AA is the particle yield measured in nucleus-nucleus (AA) collisions, where the QGP is expected, $\langle N_\mathrm{coll} \rangle$ is the average number of binary nucleon collisions happening in AA collisions, estimated by centrality models (e.g., Glauber model [107, 108]), and N_pp is the same yield measured in proton-proton collisions, that is used as a reference, where the QGP is not expected. The case R_AA less than the unity is associated with a suppression, i.e., the yield is reduced by the interaction of the particles with the medium, similarly to jet quenching, nowadays the R_AA is also used to observe and explore jet suppression in different kinematical windows. Figure 2.13 shows an example of R_AA for high-p_T hadrons as function of the number of participants in different collision centralities, as measured by the ALICE collaboration for PbPb collisions at $\sqrt{s_\mathrm{NN}}$ = 2.76 TeV, for π (green triangles) and D mesons (black squares). For both particle species it is possible to see that the suppression is strongest for most central collisions than in peripheral ones. This is expected, since the system formed will be larger and will survive for a longer time interval in central events, thus increasing the number of interactions, which is translated into a stronger suppression.
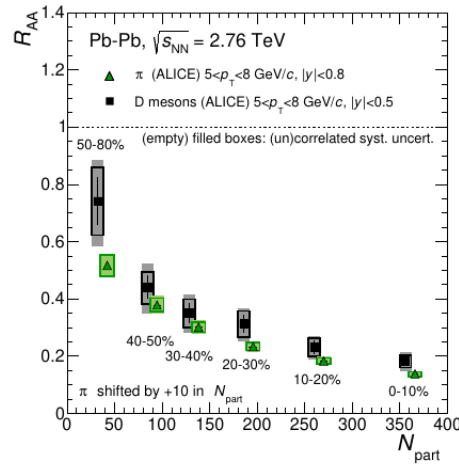
Figure 2.13: R_{AA} for PbPb collisions at $\sqrt{s_{NN}} = 2.76$ TeV as a function of the number of participants and centrality, for π (green triangles) and D (black squares) mesons measured by ALICE collaboration. Extracted from [109].

Quarkonium suppression

Quarkonium is a bound state composed of a heavy quark and its antiquark, therefore being a neutral particle and its own antiparticle. They are basically classified in two species: charmonium, formed by a $c\bar{c}$ pair (e.g., J/ψ) and bottomonium, formed by $b\bar{b}$ (e.g., Υ). The suppression of quarkonium states in QGP matter was first proposed for J/ψ particles by T. Matsui e H. Satz [110], in 1986. According to them, the J/ψ binding potential is screened by the interactions with the constituents of the hot and dense medium. This happen because the Debye colour screening potential increases with the temperature of the medium, and above certain temperature, the binding potential cannot hold the two quarks together, and the bound is dissociated in a c and a $\bar{c}$ in the plasma. Besides, if the QGP initial temperature is high enough, the $c\bar{c}$ pair may not form a bound state. After that, these quarks will combine with lighter quark flavors (u and d) increasing the production of open-charm mesons (e.g., D, which is composed by $c\bar{u}$) and reducing the production of J/ψ mesons. For larger binding radius, the potential of the quarkonium states become weaker and for that reason, the most excited quarkonium states are expected to be more loosely bounded and to dissociated at lower temperature as compared to the ground state, leading to a sequential suppression. This means that, for the charmonium states, $\psi(2S)$ would be more suppressed than J/ψ and, for the bottomonium states, $\Upsilon(3S)$ would be more suppressed than $\Upsilon(2S)$, which would be more suppressed than $\Upsilon(1S)$. The

first evidence of this suppression was found at SPS [111], and nowadays this is still extensively studied at RHIC and LHC [112, 113, 114].

Figure 2.14, on the left, shows the R_{AA} p_T dependence of the $J/\psi \to e^+e^-$ (green solid circles) and $J/\psi \to \mu^+\mu^-$ (yellow open circles), as measured by PHENIX collaboration at RHIC, in central (0-20%) AuAu collisions at $\sqrt{s_{NN}} = 200$ GeV [112]. From this plot it is possible to see the clear suppression in the all p_T range investigated. On the right, the dimuon invariant mass distribution measured by CMS collaboration [113] is shown in the range 8-14 GeV. The comparison between PbPb and pp collisions (normalized by the $\Upsilon(1S)$ mass peak in PbPb) shows a clear sequential suppression for the higher excited states of bottomonium ($\Upsilon(2S)$ and $\Upsilon(3S)$).
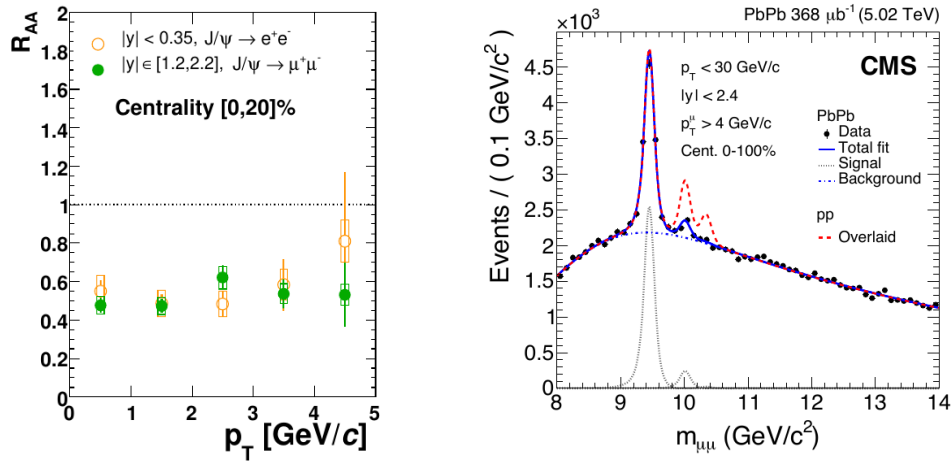
Figure 2.14: Left: R_{AA} of J/ψ particles decaying into pairs of muons (yellow open circles) and electrons (green solid circles) measured by PHENIX collaboration at RHIC in central (0-20%) AuAu collisions at $\sqrt{s_{NN}} = 200$ GeV. Extracted from [112]. Right: Dimuon invariant mass distribution, measured by CMS collaboration in the range of $\Upsilon(nS)$ production for PbPb collisions (0-100%) at $\sqrt{s_{NN}} = 5.02$ TeV. The black points are the data, the solid blue line is the total fit, the dotted-dashed blue line is the combinatorial background, the dotted blue line shows the signal only (total $-$ background) and the dashed red line shows the pp signal shapes added on top of the PbPb background and normalized by the $\Upsilon(1S)$ mass peak in PbPb. Extracted from [113].

Electroweak probes

The usage of electromagnetic particles to investigate the QGP formation was first proposed by E. Shuryak in 1978 [115]. Photons and dileptons are good probes because they can be produced by interactions in different stages of the system

evolution, not been affected by interactions with the medium since they only interact electromagnetically. These probes can be used to obtain information about the temperature and energy density of the system. In the QGP phase, photons are mainly produced by Compton effect ($qg \to q\gamma$) and by annihilation process ($q\bar{q} \to g\gamma$), whereas the main source of dileptons is the Drell-Yan process ($q\bar{q} \to l^+l^-$). In the hadronic phase, photons are produced by Compton effect ($\pi\rho \to \gamma\rho$) and pion annihilation ($\pi\pi \to \gamma\rho$), dileptons are mainly coming from the interactions between π's and ρ's, and also by Drell-Yan process (at high invariant mass). Besides all these processes, dileptons and photons can also be produced in the early stages of the collision (hard scattering) and by hadronic decays (e.g., $\pi^0 \to \gamma\gamma$, $J/\psi \to e^+e^-$ and others).

Experimentally, the above effects are studied in different ways. Dileptons are investigated by measuring their invariant mass and, for photons, the transverse momentum yield can be used as a thermometer for studing the QGP temperature. In both cases, the results compared with models, are in favor of the formation of the QGP. However, the background observed in this kind of measurements is huge, making it difficult to draw final conclusions. Figure 2.15 (left) shows the invariant mass distribution for electron pairs measured by PHENIX collaboration at RHIC [116]. Their results show a discrepancy in the region between 0.1 and 0.7 GeV for most central collisions for data (full markers) as compared to the cocktail model in which the QGP is not taken into account (lines). However, this excess disappears in peripheral AuAu collisions and is not present in pp collisions. This enhancement can be described by models that assume the QGP formation [117]. Figure 2.15 (right) shows the yield of photons as function of their transverse momentum measured by PHENIX collaboration [118]. The spectra can be described/modeled by the sum of the contributions shown as the blue line in the plot, from thermal photons, produced considering a QGP with an initial temperature of 370 MeV shown by the red line, and from prompt photons, from hard process, shown by the black line.

Nowadays, the production of weak bosons ($W^\pm$ and Z^0) are also investigated for being used as reference since these bosons are not modified by QGP effects and should not be affected by flow. The experimental measurements show involving the $W^\pm$ and Z^0 bosons that $R_{AA} \approx 1$ and v_2 consistent with zero, as expected [114, 119, 120].
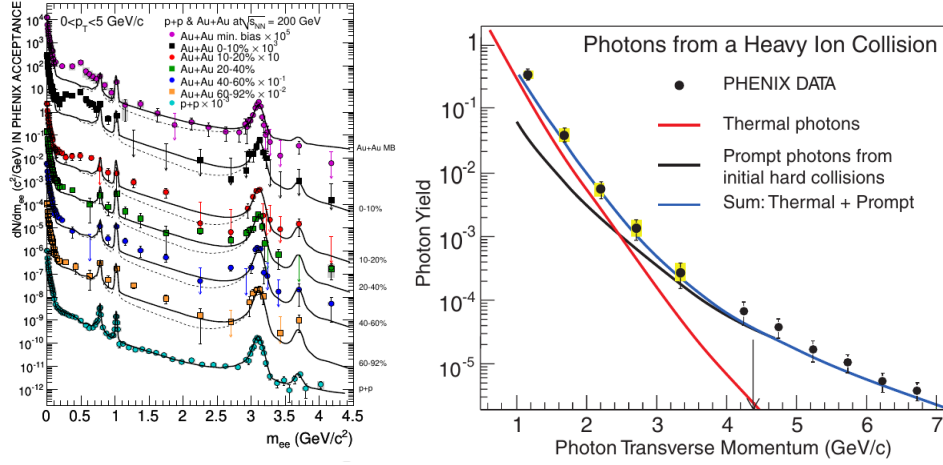
Figure 2.15: Left: dielectron invariant mass distribution measured by PHENIX collaboration [116] in AuAu collisions in different centralities, as compared to pp collisions. Extracted from [112]. Right: photon spectra as a function of transverse momentum measured by PHENIX collaboration in AuAu collisions, the blue line is the sum of thermal photons (red) and prompt photons (black) produced by models considering QGP formation with an initial temperature of 370 MeV. Extracted from [118].

Femtoscopy

The femtoscopic correlations (or HBT effect, as called in earlier times) of particles pairs is a method used to estimate the space-time dimensions of the system and/or final-state interactions felt by particles produced in high-energy collisions. This method can be used in any colliding system (e^-e^+, $p\bar{p}$, pp and others) and has a long tradition in high energy heavy ion collisions, being extensively studied along decades mainly used for studying correlations between identical pions [121, 122, 123, 124]. Femtoscopy is the main theme of this thesis, therefore, a more detailed description (history, connection with QGP and theoretical studies) is presented in the Chapter 3 and the experimental procedure used in this analysis is discussed in Chapter 5.

2.3.4 Small colliding systems

In 2010 a new chapter of history began to be written, as the CMS collaboration performed a measurement of two-particle $\Delta\eta - \Delta\phi$ [20] correlations of charged

---

[20]$\Delta\eta$ is the pseudorapidity (η) difference between the two particles in the correlation. The pseudorapidity is defined as $\eta = -\ln(\tan(\theta/2))$, where θ is the scattering angle with respect to the collision axis (see more in Chapter 4).

hadrons in proton-proton collisions at $\sqrt{s} = 7$ TeV [2]. The study was performed using collision events with no requirement in the number of produced charged particles (tracks), called minimum bias events, and specially selected events with more than 110 charged particles, called high multiplicity[21]. Figure 2.16 (top panel), shows the results obtained by CMS in 2010, for minimum bias (left) and for high multiplicity (right) events. Surprisingly, an enhancement around $\Delta\phi \sim 0$ for all $\Delta\eta$ range of the correlation was observed for high multiplicity events. This effect is called *ridge* and was first observed in heavy ion collisions at RHIC [125, 126], and have a direct relationship with the collective behavior of the system (v_n), being a typical QGP signature, and was unexpected in small colliding systems. These results were very exciting in the heavy ion community and small colliding systems started to be extensively studied. Later, a similar collective behavior was observed in proton-lead collisions [127], as shown in Fig. 2.16 (middle panel) for high multiplicity events (right), but not seen for events with less than 35 particles produced (left). Figure 2.16 (bottom panel) shows a comparison between elliptic flow using different methods for pp at $\sqrt{s} = 13$ TeV (left), pPb at $\sqrt{s_{NN}} = 5.02$ TeV (middle) and PbPb collisions at $\sqrt{s_{NN}} = 2.76$ TeV (right) measured by CMS in similar multiplicity ranges [128]. In all cases a non-zero v_2 was observed presenting similar trends. CMS also measured a significant v_2 for different particle species and non-zero v_3 [128, 129]. In LHC, ATLAS [130], ALICE [131, 132] and LHCb [133, 134] collaborations have also measured such effects in pp and pPb collisions. At RHIC, flow measurements were performed by PHENIX [135] and STAR [136] collaborations for pAu, dAu, and ^{3}HeAu collisions, observing also significant flow coeficients, v_n.

The ATLAS and CMS also investigate the possibility of collective behavior by using ultra peripheral collisions (UPC)[22]. ATLAS collaboration has performed the analysis in PbPb collisions at $\sqrt{s_{NN}} = 5.02$ TeV [139] and measured the elliptic flow of the photo-nuclear interaction (the photon is emitted from one lead and interact with the other lead). Their measurements shows a non-zero v_2 with similar dependence in multiplicity and transverse momentum (but smaller magnitude) as pp and pPb collisions (minimum bias). CMS collaboration performed the UPC analysis in proton-lead collisions at $\sqrt{s_{NN}} = 8.16$ TeV [140], searching for

---

[21]The selection of minimum bias or high multiplicity events is made by event selections (called triggers). More details about that can be found in Sec. 5.1 of Chapter 5. The CMS trigger system is presented in Sec. 4.2.7 of Chapter 4.

[22]UPC is a name given to collisions where the nucleon/nuclei interact only with a photon emitted by the other nucleon/nuclei. More details can be found in Refs. [137, 138].

v_2 of photon-proton interaction (photon is emitted from the lead and interact with the proton) and the results show a v_2 coefficient different than zero with bigger magnitude as compared to v_2 from pPb collisions (minimum bias) in the same multiplicity range. This results were first interpreted as possible jet-like correlations and further studies are still needed to understand such behavior.

The ridge-like structure was also searched experimentally by using high multiplicity e^+e^- collisions (in this case, multiplicity greater than 35) at $\sqrt{s} = 91$ GeV with archived data collected by ALEPH experiment at LEP [141] and ep collisions (DIS) with $\sqrt{s} = 318$ GeV in two multiplicity ranges (2 to 10 and 15 to 35), performed by ZEUS collaboration at HERA [142]. In both analyses, their results do not show any structure around $\Delta\phi \sim 0$ and are in agreement with Monte Carlo (MC) simulations that does not include QGP formation.

Phenomenological studies provided another big surprise: the hydrodynamical model shows a very good agreement with experimental data for v_n coefficients in small colliding systems [135, 143, 75]. This is unexpected, because the mean free path in those collisions should already be of the order of the characteristic dimension of the system[23]. Figure 2.17 (top panel) shows the comparison of v_n results from hydrodynamical simulations using the `iEBE-VISHNU` code (with different input parameters) and the data from CMS [2] and ATLAS [130] for proton-proton collisions at $\sqrt{s} = 13$ TeV: v_n dependence on multiplicity is show on the left and v_2 as a function of p_T, on the right [143]. In both plots it is possible to see a good agreement of data and model. The plot on the left also show the predictions for the multiplicity dependence of v_4. Figure 2.17 (bottom panel) shows the results for v_2 and v_3 from hydrodynamical predictions (red curve for `iEBE-VISHNU` simulations and blue curve for `SONIC` simulations) and the color glass condensate (CGC)[24] model posdiction calculations compared to the data collected by PHENIX experiment, collected in pAu (left), dAu (middle), and ^{3}HeAu (right) collisions, for the events with highest centrality/multiplicity $(0-5\%)$ at $\sqrt{s_{NN}} = 200$ GeV [135]. All the models can describe the data, however the hydrodynamical calculations are in better agreement with the experimental measurements, especially for v_3.

The second QGP signature observed in small colliding systems was the strangeness enhancement, measured by ALICE collaboration in 2016 [102], for proton-proton collisions at $\sqrt{s} = 7$ TeV and proton-lead collisions at $\sqrt{s_{NN}} = 5.02$ TeV,

---

[23]The applicability of hydrodynamics in small colliding systems is still an open question.

[24]The CGC is a theory which considers that a state of high density gluonic matter is created in the initial state of very high energy collisions, whose dynamics can be described by QCD evolution equations [144, 145, 146].

selecting high multiplicity events. Figure 2.18 shows the ratio between the yields from particles composed by strange quarks, $2K_S^0$ (the factor 2 appears because the K_S^0 is its own antiparticle), $\Lambda + \overline{\Lambda}$, $\Xi^- + \overline{\Xi}^+$, $\Omega^- + \overline{\Omega}^+$ and pions ($\pi^+ + \pi^-$) which are composed by usual matter (quarks up and down). ALICE results show a clear enhancement with multiplicity from small colliding systems to nucleus-nucleus collisions, for all particle species, following the order: proton-proton to proton-lead to lead-lead. Comparison with Monte Carlo event generators (`PYTHIA8` [147], `EPOS-LHC` [148] and `DIPSY` [149]) for proton-proton collisions at $\sqrt{s}$ = 7 TeV are also shown, none of these MC's considers the QGP formation. According to ALICE conclusions, more studies are needed in order to understand the mechanism of strangeness production in high multiplicity events. Recently, hydrodynamical simulations was performed by using the `CHESS` code [73, 74, 75] (more details at Sec. B.2 of Appendix B) for ideal and viscous (including both shear and bulk) cases and compared with particle yield from ALICE measurements [102]. Figure 2.19 shows the comparison between data and simulations for K_S^0's (top left), Λ's (top right) and Ξ's (bottom left) in four multiplicity ranges. Hydrodynamics shows a good agreement with data for all particle species in all multiplicity ranges for both ideal (red solid line) and viscous (blue dashed line) cases with a freeze-out temperature of $T_{fo} = 145$ MeV. These results show that the hydrodynamical model is also a good tool to study strange particle production and could also be applied to study events with lower multiplicity although further studies are still needed.

Many other experimental measurements were performed before writing this thesis and some of the other signatures presented in Sec. 2.3.3 were found in small colliding systems (e.g., quarkonia suppression). However, these results are in agreement with models that not include QGP effects [150, 151, 152], and in other cases (e.g., suppression of high-p_T particles) the signatures was not observed yet [153, 154, 155]. The small colliding systems are still an open question and efforts are needed in order to understand such effects. Interesting studies and discussions about this theme can be found in Refs. [156, 157, 158, 159, 160, 161]. This thesis is focused to obtain a better understanding of small colliding systems by using femtoscopy measurements with strange particles (K_S^0, Λ and $\overline{\Lambda}$). The physics of femtoscopic correlations is presented in the next chapter.
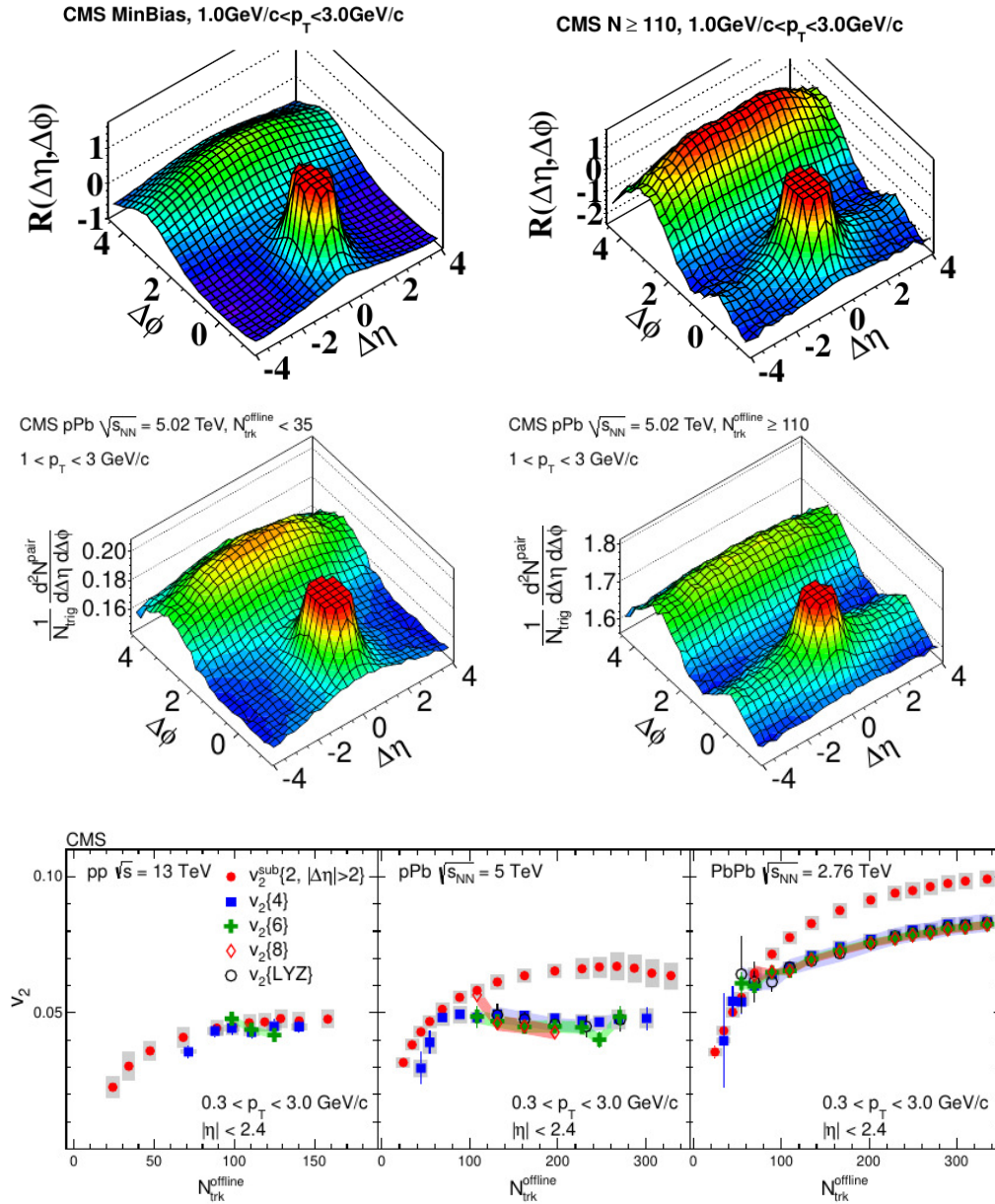
Figure 2.16: CMS measurements of the collective behavior in small colliding systems. Top panel: $\Delta\eta$ and $\Delta\phi$ dependence of two-particle correlation in proton-proton collisions at $\sqrt{s} = 7$ TeV, for minimum bias (left) and high multiplicity (right) events. Extracted from [2]. Middle panel: $\Delta\eta$ and $\Delta\phi$ dependence of two particle correlations in proton-lead collisions at $\sqrt{s_{\mathrm{NN}}} = 5.02$ TeV, for minimum bias (left) and high multiplicity (right). Extracted from [127]. Bottom panel: multiplicity dependence of elliptic flow (v_2) for different methods (different markers) and for different systems, proton-proton at $\sqrt{s} = 13$ TeV (left), proton-lead at $\sqrt{s_{\mathrm{NN}}} = 5.02$ TeV (middle) and lead-lead at $\sqrt{s_{\mathrm{NN}}} = 2.76$ TeV (right). Extracted from [128]. In the bottom plot, the fact that the different v_n coefficients overlap (mainly for $n > 2$) is an additional indication of the system collectivity. It can be seen that this behavior is present in all three colliding systems investigated.
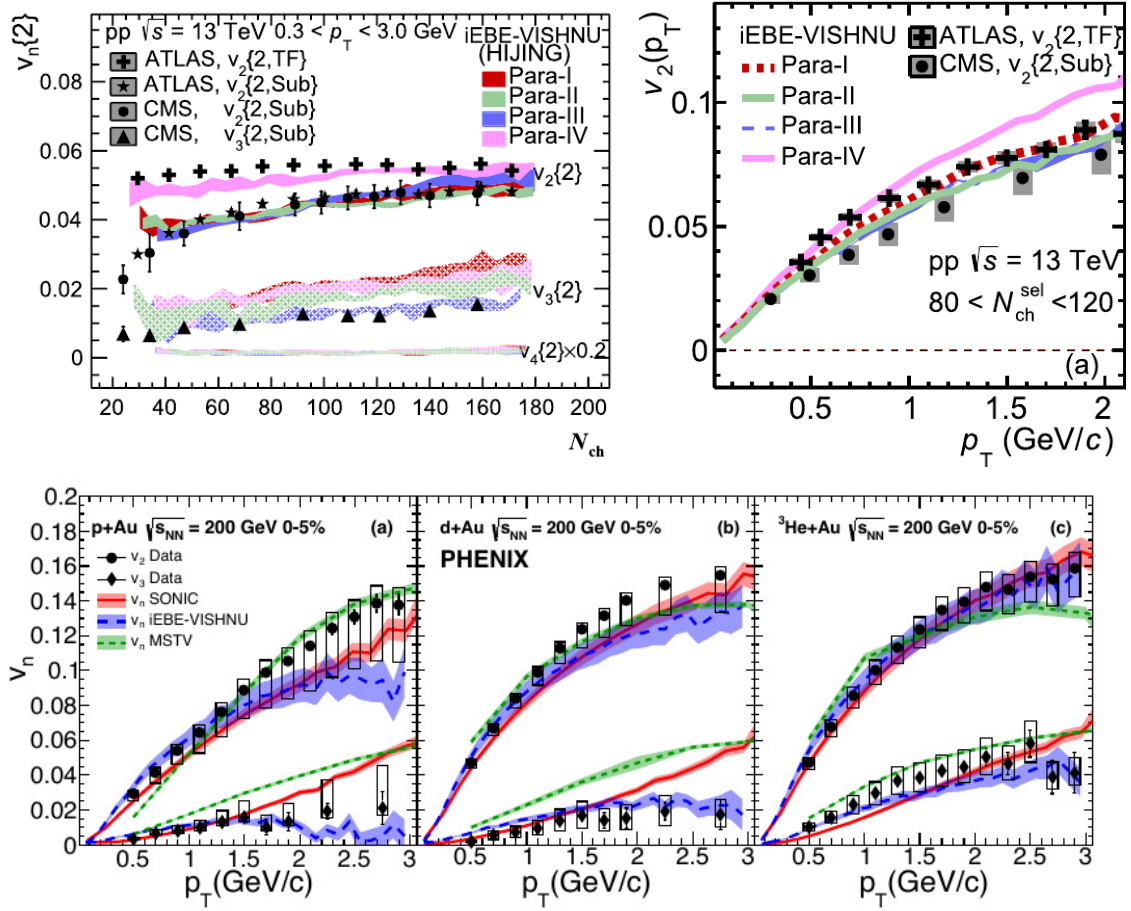
Figure 2.17: Top panel: flow harmonics (v_n) from hydrodynamical calculations for proton-proton collisions at $\sqrt{s}$ = 13 TeV compared with the data from CMS and ATLAS, showing the dependence on multiplicity (left) and on transverse momentum (right). Extracted from [143]. Bottom panel: v_2 and v_3 measured by PHENIX collaboration in proton-gold (left), deuteron-gold (middle) and helium³-gold at $\sqrt{s_{NN}}$ = 200 GeV, for the events with highest multiplicities (0-5%). Blue (from iEBE-VISHNU) and red lines (from SONIC) correspond to hydrodynamical predictions from different models and the green line is for the CGC model posdiction. Extracted from [135].
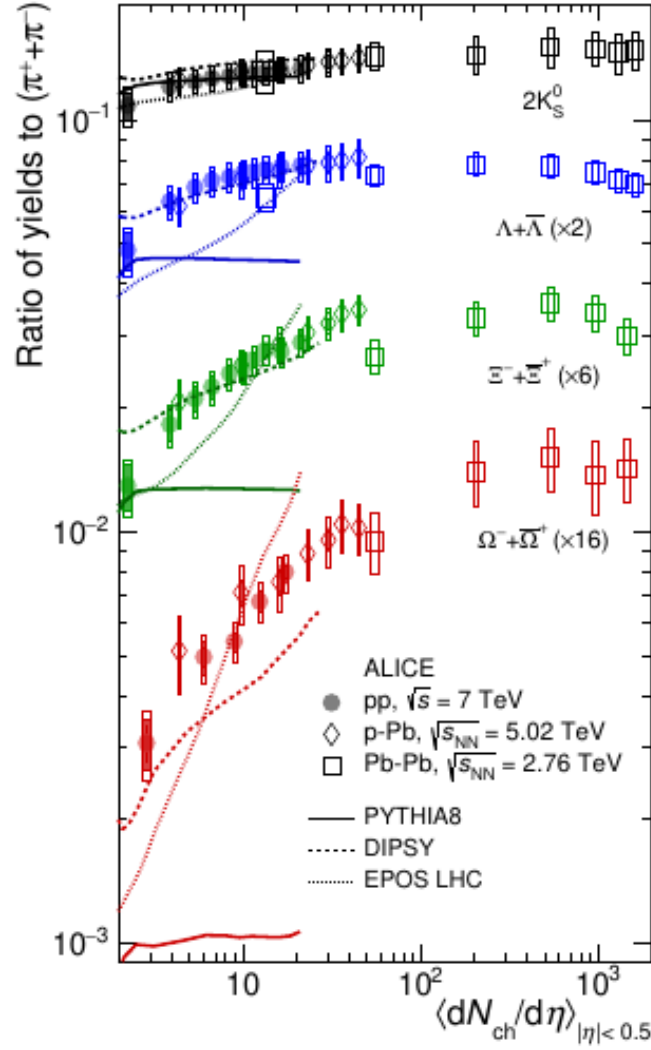
Figure 2.18: Experimental ratio of the yields of strange particles $2K_S^0$ (black), $\Lambda + \overline{\Lambda}$ (blue), $\Xi^- + \overline{\Xi}^+$ (green), $\Omega^- + \overline{\Omega}^+$ (red) to pions ($\pi^+ + \pi^-$) versus multiplicity, measured by ALICE for proton-proton (circles), proton-lead (diamond) and lead-lead (squares) collisions. Lines represent Monte Carlo simulations: `EPOS-LHC` (dotted line), `PYTHIA8` (full line) and `DIPSY` (dashed line). Extracted from [102].
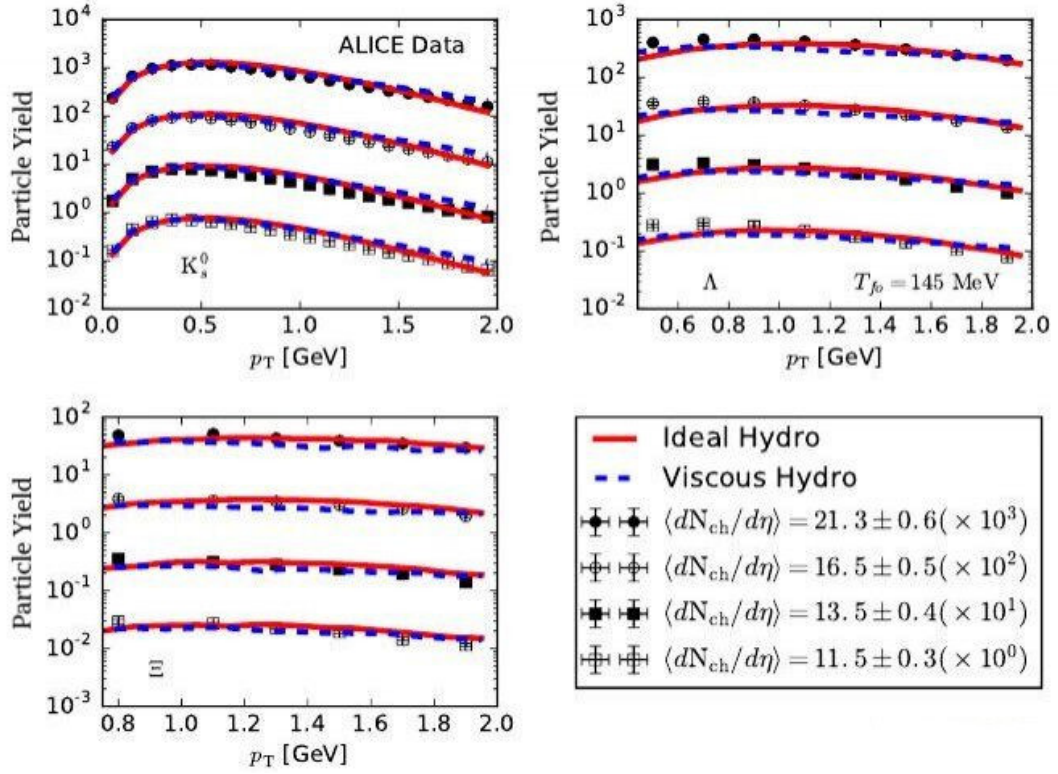
Figure 2.19: Particle yield versus p_T of strange particles: K_S^0 (top left), $\Lambda + \overline{\Lambda}$ (top right) and $\Xi^- + \Xi^+$ (bottom left) as measured by ALICE collaboration [102] (markers), compared with hydrodynamical simulations from the CHESS code [75] in four ranges of multiplicity, as shown in the legend. Lines represent hydrodynamical calculations for ideal (red solid line) and viscous (blue dashed line) cases with freezeout temperature of $T_{fo} = 145$ MeV.

Chapter 3

Femtoscopy

Femtoscopy is the study of multi-particle correlations in low relative momentum, used to investigate physical quantities in the order of femtometers/fermis (10^{-15} m). Such femtoscopic correlations are a powerful method for probing the space-time dimensions of the particle emitting source created in high-energy collisions. These correlations are sensitive to the quantum statistics (QS) obeyed by the identical particles produced in the collisions (Bose-Einstein for bosons or Fermi-Dirac for fermions), as well as of the underlying interactions among the particles. The QS effect can be used to estimate the apparent particle emitting source size. The method is also sensitive to the final-state interactions (FSI), i.e., those to which the particles may be submitted after their emission, such as Coulomb, in the case of charged particles, or strong interactions, between hadron pairs. Therefore, the FSI may provide information about such scattering effects.

This chapter begins with a historical overview about femtoscopy, followed by the description of quantum statistical effects for identical particles. Then the final-state interaction studies are presented, including the model used to measure scattering quantities from strong FSI, and a brief description of the Coulomb effect[1]. At the end, highlights of previous results on correlations measurements from other experiments are shown.

3.1   Historical overview

The original idea of using correlations to estimate the source sizes was idealized in the 1950s by the engineer and astronomer Robert Hanbury Brown, and later elaborated theoretically in collaboration with the mathematician Richard Quentin Twiss, in radio astronomy, as an improvement of the techniques known at that time to measure angular diameter of stars (θ) [162]. Besides the studies with radio sources, they proved that it was possible to extend its concept to the optical

---

[1]The Coulomb FSI is presented by completeness, since this work considers only neutral particles.

domain, first performing a successful laboratory experiment using an artificial light source coming from a mercury arc lamp with two photomultiplier tubes [163] and later with an experimental apparatus used to determine the size of stellar sources, based on photon coincidence measurements [164]. With the help of the physicist E. M. Purcell, they showed that the simultaneous detection phenomenon stems from the fact that photons tend to arrive together in the detectors due to Bose-Einstein statistics [165], and also mentioned that identical fermions should present an anticorrelation, following the Fermi-Dirac statistics. This method received the name *intensity interferometry*, but it became known as *HBT (Hanbury-Brown Twiss) effect*.

The first angular diameter of a star using intensity interferometry was performed by Hanbury Brown and Twiss for measuring Sirius (α Canis Majoris), in 1956 [162, 164]. To carry out this measurement, they adapted two army search-light projectors with diameter of 1.56 m using mirrors, as shown in Fig. 3.1 (left). These mirrors collected the photons emitted from the star and focused them to photomultiplier detectors. The signal generated passed through a noise filter and was routed to a coincidence circuit called *correlator* (electronic counter circuit). The measurement was performed for 5 months in four different baselines (distance between the detectors), d = 2.56 m, 5.35 m, 6.98 m and 8.93 m. The probability to detect both photons simultaneously (number of coincidences or correlation function), $\Gamma^2(d)$, as a function of baseline measured by Hanbury Brown and Twiss for the Sirius star is shown in Fig. 3.1 (right). The intensity of the observed correlation decreased as the baseline was increased, showing the effect of the Bose-Einstein statistics.

Using the approximation of considering the star emission as a luminous disk, the data was fitted by the function

$$\Gamma^2(d) = \left[\frac{2J_1(\pi\theta d/\lambda)}{\pi\theta d/\lambda} \right]^2, \tag{3.1}$$

where θ is the angular diameter of the star, λ the detected photon wave length and J_1, the Bessel function (see Chapter 11 of Ref. [166]). In this way, was possible to estimate the angular diameter, θ, from Sirius star as 6.3 ± 0.5 milli arcsec [162, 164], as compared to the currently accepted value is 5.936 ± 0.016 milli arcsec [167].
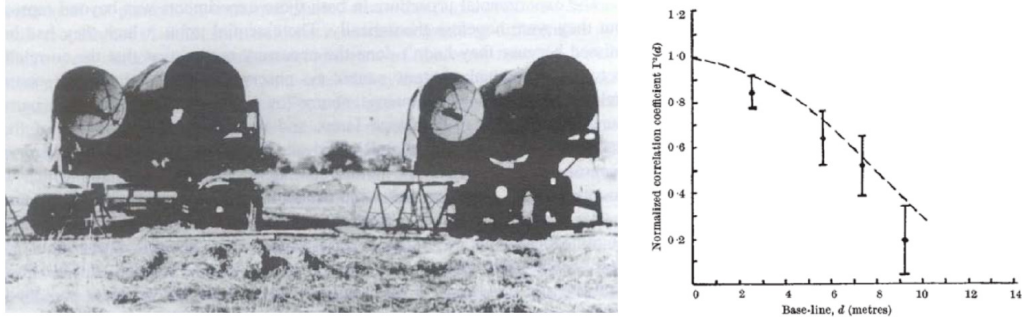
Figure 3.1: First optical intensity interferometer apparatus adapted by Hanbury Brown and Twiss at Jodrell Bank Experimental Station, University of Manchester, London (left), and the measurement of the correlation as a function of the baseline (right), for Sirius star. The line on the right plot is the fit used by Hanbury Brown and Twiss from Eq. (3.1). Extracted from [162].

In the 1960s, the Narrabri Stellar Intensity Interferometry (NSII) was built in collaboration by the Manchester and Sydney Universities, based on Hanbury Brown's design and ideas [162]. The NSII was located near the Narrabri, in the north-central New South Wales, Australia. The apparatus consisted of two parabolic reflectors with a diameter of 6.5 m composed of 252 hexagonal mirrors, each with a photoelectric detector. The reflectors were placed on a circular railway track with a diameter of 188 m, which was used to change the distance between the two reflectors and increase or decrease the baseline. The reflectors were connected by cables to the control building, which was built at the center of the circular railway track. A garage was built to store the reflectors when NSII was not taking data. In total, the angular diameters of 32 stars were measured at NSII [168], from June 1964 to February, 1972, when the program was closed. After NSII, the intensity interferometry was no longer used in astronomy due new methods and advances in technology. In 2017, experimental results were obtained by the Observatoire de la Côte d'Azur, located in Nice, France. They measured the angular diameter of 6 stars and the results were in agreement with those obtained at the NSII [169, 170, 171]. This experiment was performed with the itention to revive the usage of intensity interferometry in astronomy, specially by using the Cherenkov Telescope Array (CTA) [172], which is composed of more than 100 telescopes, allowing precise measurements and studies, including higher order (> 2) correlations.

In the field of particle physics, the HBT effect was first observed in 1959 by

G. Goldhaber, S. Goldhaber, W. Y. Lee e A. Pais[2] [3] (later called GGLP effect), without previous knowledge of the HBT experiment. Their experiment aimed at the search for the ρ meson decaying into opposite-charged pions, in proton-antiproton (p$\bar{\text{p}}$) collisions at $\sqrt{s} = 2.1$ GeV, performed at the Bevalac, LNBL, USA. The amount of data they collected was not enough to establish the existence of ρ meson. Nevertheless, in their measurements they found that identically charged pions followed a distribution different from the oppositely charged ones, which could only be described by considering the symmetrization of their wave function. They then observed correlations that led to an enhancement of the number of identical bosons with respect to that of non-identical bosons, when the two particles are close to each other in phase space. The observed distribution was them fitted by a Gaussian, $1 + \exp[-q^2 R^2]$, where $q = p_1 - p_2$ is the relative momentum and R is the inverse of the Gaussian width in fm, interpreted as the system size. These measurements reflect the sensitivity of particle momentum correlations to the space-time separation of the particle emitters, due to the effects of quantum statistics. Therefore, by measuring the relative momentum distribution of identical particles as a function of their relative momentum the information about the emitting source size could be accessed. Since then, these correlations started to be extensively studied in particle colliders, mainly using pions, and for different colliding systems as $\text{e}^+\text{e}^-, \text{pp}, \text{p}\bar{\text{p}}$, heavy ions and others. In the mid-seventies, these correlations were suggested as a signal of the quark-gluon plasma formation, following the idea that a possible phase transition to a QGP state could be formed in heavy ion collisions. At that time, such state was considered to be a gas of non-interacting quarks and gluons and the phase transition was of first order, suggesting that the QGP would live long and the measured HBT radio would be much larger than the nuclear size.

In parallel to experimental advances, theory and phenomenology were extensively investigated and refined methods were created in order to study such correlations, as for example: multidimensional analyses, the effect of final state interactions, connections with flow behavior, and so on [121, 173, 174]. The name *femtoscopy* was given by Richard Lednicky [173, 175, 176, 177] as a generalization of the study of particle correlations in low relative momentum to non-identical particles. Therefore, the same nomenclature can be used to study correlations of identical (QS+FSI) and/or non-identical particles, reflecting their final-state interaction. Finally, besides the application in astronomy and particle physics, the

---

[2]At this time, the group does not know about the work from Hanbury Brown and Twiss.

study of these correlations have also been performed in other fields of physics as, for example, in quantum optics [178].

3.2 Quantum statistics

The function that describes the correlation between two particles, emitted chaotically, and relate it to the dimensions and dynamics of the emitting source, as well as the underlying events, is called *correlation function* (CF). Theoretically, this CF can be written as the ratio between the joint probability of detecting both particles, $\mathcal{P}_2(p_1^\mu, p_2^\mu)$, by the probability of detecting each particle individually, $\mathcal{P}_1(p_i^\mu)$, as

$$C(p_1^\mu, p_2^\mu) = \frac{\mathcal{P}_2(p_1^\mu, p_2^\mu)}{\mathcal{P}_1(p_1^\mu)\mathcal{P}_1(p_2^\mu)} \qquad (3.2)$$

where p_1^μ and p_2^μ are the four-momenta of the two particles. From now on, the four-vector indexes ($\mu, \nu, ...$) will be omitted to simplify the notation.

The quantum statistical effect is present in correlations between identical particles, and can be described by the symmetrization (Bose-Einstein) or antisymmetrization (Fermi-Dirac) of their wave function. One way to understand such an effect and construct the correlation function is by using the simple picture shown in Fig. 3.2. Consider that two identical particles (bosons or fermions) emitted from points 1 and 2 are detected at A and B with four-momentum p_1 and p_2, respectively. Using plane waves, i.e., neglecting final-state interactions, the generalized probability amplitude for an individual particle, with momentum p (p_1 or p_2), emitted at certain point x (1 or 2) of the source to reach the point x' (A or B) is given by [88]

$$\psi_{x \to x'}(p) = A(x, p)\, e^{i\alpha(x)} e^{ip \cdot (x - x')}, \qquad (3.3)$$

where $A(x, p)$ and $\alpha(x)$ are the magnitude and the random phase (independent in each emission) of this amplitude.
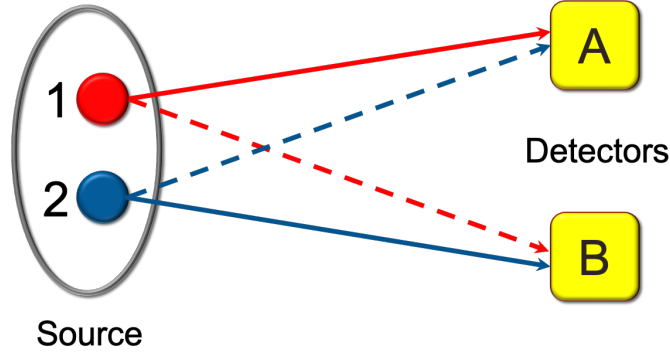
Figure 3.2: Simplified illustration of a particle emitting source. One particle is emitted from the source at the point 1 (red), with four-position x_1, and another, identical to the first, is emitted from the point 2 (blue), at space-time position x_2. Two detectors A, located at x_A, and B, located at x_B, measure the particles with momentum p_1 and p_2. Since they are indistinguishable, there are two ways to detect these particles as represented by the continuous and dashed lines.

Therefore, the probability amplitude for detecting one particle, emitted from 1, with momentum p_1 in A and, detect an identical particle, from 2, with momentum p_2 in B (represented by the continuous lines at Fig. 3.2) can be written as the product of individual amplitudes, as [88, 179]:

$$
\begin{aligned}
\Psi_{1,2 \to A,B}(p_1, p_2) &= \psi_{x_1 \to x_A}(p_1)\psi_{x_2 \to x_B}(p_2), \\
&= A_{1,1}e^{i\alpha_1}e^{ip_1 \cdot (x_1 - x_A)}A_{2,2}e^{i\alpha_2}e^{ip_2 \cdot (x_2 - x_B)},
\end{aligned} \tag{3.4}
$$

where $A_{i,j} = A(x_i, p_j)$ and $\alpha_i = \alpha(x_i)$ are used to simplify the notation. We consider that the probability of measuring two particles emitted from the same source point can be neglected. Furthermore, here the simplest case is assumed, where the source is static, chaotic, the emitted particles do not interact (no final state interactions) or decay (come from the decays of other particles) after the emission and the effect of higher order (three, four, ..., N particles) correlations is negligible.

Since the detected particles are indistinguishable, the cross-term, represented by the dashed lines in Fig. 3.2, must also be considered: particle emitted from 1, with momentum p_2, arrive in B and the particle emitted from 2, with momentum p_1, is detected in A; in this case:

$$
\begin{aligned}
\Psi_{2,1 \to A,B}(p_1, p_2) &= \psi_{x_2 \to x_A}(p_1)\psi_{x_1 \to x_B}(p_2), \\
&= A_{2,1}e^{i\alpha_2}e^{ip_1 \cdot (x_2 - x_A)}A_{1,2}e^{i\alpha_1}e^{ip_2 \cdot (x_1 - x_B)}.
\end{aligned} \tag{3.5}
$$

Thus, the total probability amplitude is written as

$$\Psi(p_1, p_2) = \frac{1}{\sqrt{2}} \left[\Psi_{1,2 \to A,B}(p_1, p_2) \pm \Psi_{2,1 \to A,B}(p_1, p_2) \right], \tag{3.6}$$

where the signal is related with the wave function symmetrization $(+)$, for bosons, or antisymmetrization $(-)$, for fermions.

In a more realistic case, the pair of particles can be emitted from any other two points of the extended source. This is taken into account by summing all possible combinations of producing pairs of particles from two distinct points. Then, Eq. (3.6) can be rewritten as

$$
\begin{aligned}
\Psi_\Sigma(p_1, p_2) &= \sum_{x_1, x_2} \Psi(p_1, p_2) = \sum_{x_1, x_2} \frac{1}{\sqrt{2}} \left[\Psi_{1,2 \to A,B}(p_1, p_2) \pm \Psi_{2,1 \to A,B}(p_1, p_2) \right] \\
&= \frac{1}{\sqrt{2}} \sum_{x_1, x_2} e^{i\alpha_1} e^{i\alpha_2} \left[A_{1,1} A_{2,2} e^{ip_1 \cdot (x_1 - x_A)} e^{ip_2 \cdot (x_2 - x_B)} \right. \\
&\quad \left. \pm A_{1,2} A_{2,1} e^{ip_1 \cdot (x_2 - x_A)} e^{ip_2 \cdot (x_1 - x_B)} \right],
\end{aligned}
\tag{3.7}
$$

where we assume that the random phases, α_i, depend on the emission point, but not on the momentum of the emitted particles.

The probability distribution for a joint observation of two identical particles with four-momentum p_1 and p_2, $\mathcal{P}_2(p_1, p_2)$, is defined as

$$\mathcal{P}_2(p_1, p_2) = \frac{1}{2!} |\Psi_\Sigma(p_1, p_2)|^2, \tag{3.8}$$

where the factor $1/2!$ is included to avoid double counting. Using the Eqs. (3.7) and (3.8), we obtain

$$
\begin{aligned}
\mathcal{P}_2(p_1, p_2) &= \frac{1}{2} \sum_{x_1, x_2} \left\{ |A_{1,1}|^2 |A_{2,2}|^2 + |A_{1,2}|^2 |A_{2,1}|^2 \right. \\
&\quad \left. \pm A_{1,1} A_{2,2} A_{1,2} A_{2,1} \left[e^{i(p_1 - p_2) \cdot (x_1 - x_2)} + e^{-i(p_1 - p_2) \cdot (x_1 - x_2)} \right] \right\} \\
&\quad \times \left\langle e^{i(\alpha_1 + \alpha_2 - \alpha_1' - \alpha_2')} \right\rangle.
\end{aligned}
\tag{3.9}
$$

Once the emitting source is considered chaotic, the random phases fluctuate rapidly. Therefore, it is necessary to consider an average over the phases, where

the only non-null terms are [174]

$$\left\langle e^{i(\alpha_1+\alpha_2-\alpha_1'-\alpha_2')} \right\rangle = \delta_{\alpha_1\alpha_1'}\delta_{\alpha_2\alpha_2'} + \delta_{\alpha_1\alpha_2'}\delta_{\alpha_2\alpha_1'}. \tag{3.10}$$

Replacing Eq. (3.10) into Eq. (3.9), it turns possible to assume the exchange (anti)symmetry between the positions of the two identical particles, so we can write: $A(p_1, x_1) = A(p_1, x_2)$ and/or $A(p_2, x_1) = A(p_2, x_2)$; leading to

$$
\begin{aligned}
\mathcal{P}_2(p_1, p_2) &= \sum_{x_1, x_2} |A_{1,1}|^2 |A_{2,2}|^2 \left\{ \left[1 \pm e^{i(p_1-p_2)\cdot(x_1-x_2)} \pm e^{-i(p_1-p_2)\cdot(x_1-x_2)} \right] \right\} \\
&= \sum_{x_1, x_2} |A_{1,1}|^2 |A_{2,2}|^2 \left\{ 1 \pm \frac{1}{2} \left[e^{iq\cdot x} + e^{-iq\cdot x} \right] \right\} \\
&= \sum_{x_1, x_2} |A_{1,1}|^2 |A_{2,2}|^2 \left[1 \pm \cos(q\cdot x) \right]. \tag{3.11}
\end{aligned}
$$

where $q = p_1 - p_2$ and $x = x_1 - x_2$ are the relative momentum and relative separation, respectively. The sum in Eq. (3.11) can be rewritten, in the continuous limit, as an integral by introducing a source density function, $\rho(x)$. Substituting $\sum_{x_1, x_2} \to \int dx_1 dx_2 \rho(x_1)\rho(x_2)$, it returns

$$
\begin{aligned}
\mathcal{P}_2(p_1, p_2) &= \int dx_1 \, dx_2 \, \rho(x_1) \, \rho(x_2) |A_{1,1}|^2 |A_{2,2}|^2 \left[1 \pm \cos(q\cdot x) \right] \\
&= \int dx_1 \, dx_2 \, s(x_1, p_1) \, s(x_2, p_2) \left[1 \pm \cos(q\cdot x) \right] \\
&= \mathcal{P}_1(p_1)\mathcal{P}_1(p_2) \pm \int dx_1 dx_2 s(x_1, p_1) s(x_2, p_2) \cos(q\cdot x) \tag{3.12}
\end{aligned}
$$

where s is the emission function, defined as $s(x_i, p_j) = |A(x_i, p_j)|^2 \rho(x_i)$. The probability to detect an individual particle emitted from any point of the extended source is given by

$$\mathcal{P}_1(p) = \int dx \, s(x, p). \tag{3.13}$$

Using Eqs. (3.12), (3.13) and Eq. (3.2), the correlation function is written as

$$C(p_1, p_2) = \frac{\mathcal{P}_2(p_1, p_2)}{\mathcal{P}_1(p_1)\mathcal{P}_1(p_2)} = 1 \pm \frac{\int dx_1 \, dx_2 \, s(x_1, p_1)s(x_2, p_2)\cos(q\cdot x)}{\int dx_1 \, s(x_1, p_1) \int dx_2 \, s(x_2, p_2)}, \tag{3.14}$$

or[3],

$$C(p_1, p_2) = 1 \pm \frac{\left| \int dx \; \sqrt{s(x, p_1) \, s(x, p_2)} \; e^{iq \cdot x} \right|^2}{\int dx \, s(x, p_1) \int dx \, s(x, p_2)}. \qquad (3.15)$$

Besides the relative momentum of the pair, $q = p_1 - p_2$, the average momentum of the pair is also defined as $k = 1/2(k_1 + k_2)$. Furthermore, Eq. (3.15) can be reduced to a simplified form by imposing the so-called *smoothness approximation*, which assumes that the emission function has a sufficiently weak dependence on the relative momentum q [180, 181]. Using this approximation, $s(x, p_i)$ is expanded with respect to $s(x, \mathrm{k})$ as

$$s(x, p_1) = s(x, \mathrm{k}) + \frac{q}{2} \left. \frac{\partial s(x, p')}{\partial p'} \right|_{p'=\mathrm{k}} + \mathcal{O}(q^n, \text{ for } n > 1),$$

and

$$s(x, p_2) = s(x, \mathrm{k}) - \frac{q}{2} \left. \frac{\partial s(x, p')}{\partial p'} \right|_{p'=\mathrm{k}} + \mathcal{O}(q^n, \text{ for } n > 1),$$

where the momentum of the particles are written as $p_1 = \mathrm{k} + q/2$ and $p_2 = \mathrm{k} - q/2$.

Taking the product of the emission functions, we have

$$s(x, p_1)s(x, p_2) = s^2(x, \mathrm{k}) + \frac{q}{2} s(x, \mathrm{k}) \left[\left. \frac{\partial s(x, p')}{\partial p'} \right|_{p'=\mathrm{k}} - \left. \frac{\partial s(x, p')}{\partial p'} \right|_{p'=\mathrm{k}} \right]$$
$$+ \mathcal{O}(q^n, \text{ for } n > 1). \qquad (3.16)$$

Replacing Eq. (3.16) in Eq. (3.15), and neglecting the contribution from higher order powers of q, i.e. $\mathcal{O}(q^n, \text{ for } n > 1)$, the two-particle correlation function is rewritten as

$$C(q = p_1 - p_2) = 1 \pm \left| \frac{\int dx \, s(x, \mathrm{k}) \, e^{iq \cdot x}}{\int dx \, s(x, \mathrm{k})} \right|^2. \qquad (3.17)$$

The equation above shows that, in the case of identical particles, the two-particle correlation function, considering only quantum statistical effects, is directly related to the Fourier transform of the emission function. Therefore, the width of this correlation signal can be associated with the space-time dimensions of the emitting source. The description above was derived assuming static source.

---

[3]The following property was used here: $f(x_i, p_i) + f^*(x_i, p_i) = 2\Re[f(x_i, p_i)]$.

However, a dependence on the average momentum of the pair, $k_T = |\mathbf{p}_{1,T} + \mathbf{p}_{2,T}|/2$ is observed in high energy collisions, which is directly related to the dynamics of the system, indicating the expansion of the source [174].

In addition, it is useful to rewrite Eq. (3.14) in the reference frame of interest. For a pair of on-shell identical particles[4], the so-called *mass-shell constraint* holds [183], that is, the product between q and k is, by construction,

$$q \cdot k = (p_1 - p_2) \cdot \frac{1}{2}(p_1 + p_2) = \frac{1}{2}(p_1^2 - p_2^2) = \frac{1}{2}(m_1^2 - m_2^2) = 0, \qquad (3.18)$$

then

$$q \cdot k = (q_0, -\mathbf{q}) \cdot (k^0, \mathbf{k}) = 0, \text{ implying that } q_0 = \frac{1}{k^0}\mathbf{k} \cdot \mathbf{q}. \qquad (3.19)$$

According to Eq. (3.19), q_0 shows a dependence on $\mathbf{k}$, which can be eliminated by adopting the pair rest frame (PRF), where $\mathbf{k} = \frac{1}{2}(\mathbf{p}_1 + \mathbf{p}_2) = 0$, therefore,

$$q \cdot x = (q_0, -\mathbf{q}) \cdot (x^0, \mathbf{r}) = -\mathbf{q} \cdot \mathbf{r}, \qquad (3.20)$$

where $\mathbf{r} = \mathbf{x_1} - \mathbf{x_2}$. Using the above result, together with the smoothness approximation, Eq. (3.14) can be rewritten, in the PRF, as

$$C(q) = \frac{\int dx_1\, dx_2\, s\,(x_1, k)\, s\,(x_2, k)\, [1 \pm \cos(\mathbf{q} \cdot \mathbf{r})]}{\int dx_1\, s\,(x_1, k) \int dx_2\, s\,(x_2, k)}. \qquad (3.21)$$

The source function, $S(\mathbf{r}, t)$, is defined as

$$S(\mathbf{r}, t) = \frac{\int dx_1\, dx_2\, s(x_1, k)\, s\,(x_2, k)\, \delta^4(x - x_1 + x_2)}{\int dx_1\, s\,(x_1, k) \int dx_2\, s\,(x_2, k)}, \qquad (3.22)$$

that can be simplified using the *equal time approximation* [173] in the PRF, which assumes that both particles are emitted at the same time, removing the time dependence, as $S(\mathbf{r}) = \int S(\mathbf{r}, t)\delta(t)$. Thus, it is possible to rewrite Eq. (3.21) as follows

$$\begin{aligned} C(q) &= \int d\mathbf{r}\, S(\mathbf{r})\, [1 \pm \cos(\mathbf{q} \cdot \mathbf{r})] \\ &= \int d\mathbf{r}\, S(\mathbf{r}) \left[1 \pm \frac{e^{i\mathbf{q} \cdot \mathbf{r}} + e^{-i\mathbf{q} \cdot \mathbf{r}}}{2}\right], \end{aligned} \qquad (3.23)$$

---

[4]The mass-shell constraint is still valid for non-identical particles by redefining the relative momentum as $q = (p_1 - p_2) - (p_1 - p_2)(m_1^2 - m_2^2)/(p_1 + p_2)^2$ [182]. If the particles are identical, $m_1 = m_2$, $q = p_1 - p_2$ is restored.

where the term within brackets can be identified as the (anti)symmetrized free wave function, given by

$$\Psi(\mathbf{q}, \mathbf{r}) = \frac{1}{\sqrt{2}} e^{2i\mathbf{k} \cdot \mathbf{R}} \left(e^{i\frac{\mathbf{q} \cdot \mathbf{r}}{2}} \pm e^{-i\frac{\mathbf{q} \cdot \mathbf{r}}{2}} \right), \tag{3.24}$$

where $\mathbf{R} = (\mathbf{x}_1 + \mathbf{x}_2)/2$ is the center-of-mass vector. Therefore, the correlation function can be written only in terms of the source and wave functions, i.e.,

$$C(q) = \int d\mathbf{r} \, S(\mathbf{r}) \, |\Psi(\mathbf{q}, \mathbf{r})|^2. \tag{3.25}$$

The equation above is called *Koonin-Pratt formula* [184, 185], where all of the information about the quantum statistics effect and final state interactions are included in the wave function[5]. This formalism is general and can be applied in all cases (identical and non-identical particles), being specially useful for studies involving FSI (see Sec. 3.3 and Appendix C). In addition, Eq. (3.25) shows that the parametrization of the source function is a key ingredient to describe the correlations, which is briefly discussed in the next section.

3.2.1 Source function parametrization

The theoretical modeling of the correlation function depends on the source function adopted, which cannot be directly obtained experimentally. Because of its simplicity, a Gaussian-like function was assumed along the years to represent this source [186], and is given by

$$S(r) = \frac{e^{-r^2/4R^2}}{(4\pi R^2)^{3/2}}, \tag{3.26}$$

being normalized to unity, i.e., $\int S(\mathbf{r}) d\mathbf{r} = 1$. Therefore, in the case of identical particles and neglecting FSI, the correlation function can be obtained by using Eq. (3.23), as follows

$$
\begin{aligned}
C(q) &= 1 \pm \int_0^{2\pi} \int_0^{\infty} \int_0^{\pi} d\phi d\theta dr \, r^2 \sin\theta \frac{e^{-r^2/4R^2}}{(4\pi R^2)^{\frac{3}{2}}} \cos\left(qr\cos\theta\right) \\
&= 1 \pm e^{-q^2 R^2}.
\end{aligned}
\tag{3.27}
$$

---

[5]In the case of non-identical particles with negligible FSI, $|\Psi(\mathbf{q}, \mathbf{r})|^2 = 1$, and assuming a normalized source function, i.e. $\int S(\mathbf{r}) d\mathbf{r} = 1$, we obtain $C(q) = 1$.

However, as the accelerators reached higher collision energies and different colliding systems, it was experimentally observed that the correlation is better adjusted by an exponential-type form [187, 188, 189, 190, 191], mainly in small colliding systems. In this case, the source function is better described by a Cauchy-Lorentz function [186] (also normalized to unity, i.e., $\int S(\mathbf{r})d\mathbf{r} = 1$),

$$S(r) = \frac{R}{\pi^2 (r^2 + R^2)^2},$$ (3.28)

that leads to

$$
\begin{aligned}
C(q) &= 1 \pm \int_0^{2\pi} \int_0^\infty \int_0^\pi d\phi d\theta dr \, r^2 \sin\theta \frac{R}{\pi (r^2 + R^2)^2} \cos\left(qr\cos\theta\right) \\
&= 1 \pm e^{-|qR|}.
\end{aligned}
$$ (3.29)

Figure 3.3 shows a comparison between the Gaussian (red solid lines), Eq. (3.26), and the Cauchy-Lorentz (dashed blue lines), Eq. (3.28), source distributions (multiplied by $4\pi r^2$), as a function of the particle pair separation, r, for $R = 1.5$ fm (left) and $R = 4.0$ fm (right). A clear difference between the shapes can be observed; for comparing the corresponding radii parameters, we should take into account the conversion factors, i.e. $R_{\text{Cauchy-Lorentz}} \sim \sqrt{\pi}\, R_{\text{Gaussian}}$ [190].
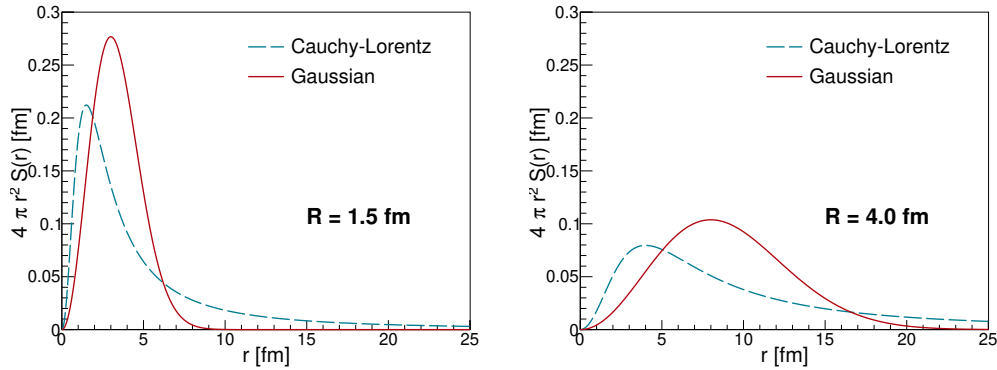

Figure 3.3: Normalized source distributions as a function of r for $R = 1.5$ fm (left) and $R = 4.0$ fm (right). The different lines represent the Gaussian (red solid) and Cauchy-Lorentz (blue dashed) shapes.

In order to study the CF shape experimentally and theoretically, Csörgő, Hegyi and Zajc [186, 192] proposed an additional degree of freedom, α, called *Levy index*

or *index of stability*, in which case the correlation is be fitted by the function

$$C(q) = 1 \pm e^{-|qR|^{\alpha}}. \tag{3.30}$$

Figure 3.4 shows the effect of this parameter in the correlation function for identical bosons (left) and fermions (right) with $R = 1.5$ fm. For $\alpha = 2$ (red solid line) the Gaussian-like behavior is recovered, while $\alpha = 1$ (blue dashed line) stands for the Cauchy-Lorentz case, and an intermediate value $\alpha = 1.5$ (purple dot-dashed line) is also shown.
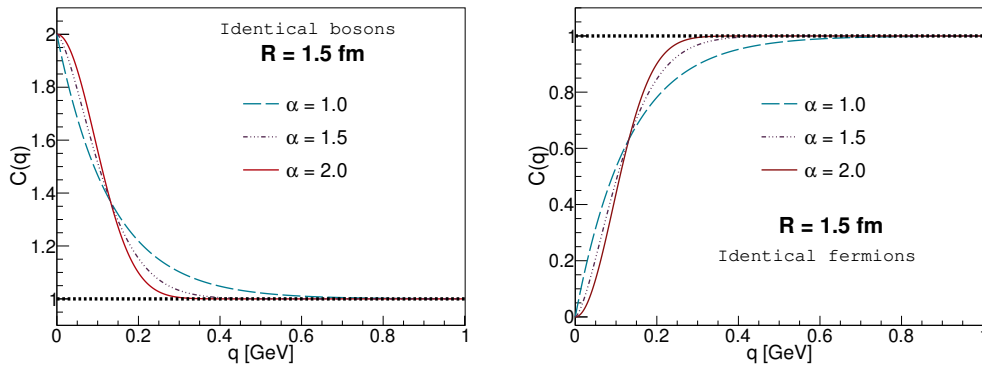
Figure 3.4: Correlation as a function of q with $R = 1.5$ fm for identical bosons (left) and identical fermions (right). The different lines show the α values: 2.0 (red solid), 1.5 (blue dashed) and 1.0 (purple dot-dashed).

Measurements conducted by PHENIX collaboration in $0 - 30\%$ central AuAu collisions at $\sqrt{s_{NN}} = 200$ GeV using correlations between identical pions in one and three dimensions indicate $\alpha \approx 1.2$ [193, 194], far from the Gaussian case ($\alpha = 2$). This parameter was also measured (in one dimension) by STAR collaboration, in the same centrality and collision system, resulting in $\alpha \approx 1.4$ (preliminary) [195]. More recently, the NA61/SHINE collaboration obtained $\alpha \approx 1.2$ in $0 - 20\%$ central BeBe collisions with 150 GeV per nuclei [196], being consistent with PHENIX results. Further studies in both experimental and theoretical sides are still needed in order to understand the real correlation function shape and possible distortion effects. Furthermore, a dependence of the type of colliding system may also be related to the value of α.

In this thesis, since we are also interested in studying the strong final state interactions, besides the quantum statistic effects, the Lednicky-Lyuboshits model [175] (see Sec. 3.3 and Appendix C) is applied, which is derived by assuming a Gaussian-shape for the source function. Therefore, from now on, only the Gaussian source

function ($\alpha = 2$) will be used in our studies.

3.2.2 Spin dependence

In the description above, the correlations between identical fermions or identical bosons were differentiated by the sign corresponding to the effects of antisymmetrization or symmetrization of their wave functions. However, the spin of the correlated particles also plays an important role and must be considered. The spin dependence can be introduced as

$$C(q) = \sum_S \rho_S C_S(q), \tag{3.31}$$

where $S = |s_1 - s_2|, ..., s_1 + s_2$ is the total spin of the pair, written in terms of the individual particle spin, s_i, the sum taking into all possible combined states. For an unpolarized source, the statistical weight is given by $\rho_S = \frac{(2S+1)}{(2s_1+1)(2s_2+1)}$. The Eq. (3.31) is general and also valid for correlations between non-identical particles (see Appendix C).

For pairs of identical spin zero mesons, as $K_S^0 K_S^0$, the total wave function is symmetric and there is only one possible spin state, $S = 0$ and $\rho_S = 1$, thus the correlation function for identical bosons is given by Eq. (3.27) with positive sign, i.e., $C(q) = 1 + e^{-q^2 R^2}$.

In the case of identical spin half baryons, such as $\Lambda\Lambda$ and $\overline{\Lambda}\overline{\Lambda}$, the total spin of the pair can be either a singlet ($S = 0$) or triplet ($S = 1$), and both contributions must be considered:

- the singlet state, written as $\frac{1}{\sqrt{2}} [|\uparrow\downarrow\rangle - |\downarrow\uparrow\rangle]$, contributes with $\rho_{S=0} = 1/4$ (even) and returns a symmetric spatial wave function, thus the same expression as for spin zero mesons can be applied, i.e., $C_{S=0}(q) = 1 + e^{-q^2 R^2}$;

- the triplet state has $\rho_{S=1} = 3/4$ (odd) and contain three configurations: $|\uparrow\uparrow\rangle$, $|\downarrow\downarrow\rangle$ and $\frac{1}{\sqrt{2}} [|\uparrow\downarrow\rangle + |\downarrow\uparrow\rangle]$. In this case the spatial pair wave functions is antisymmetric, that leads to $C_{S=1}(q) = 1 - e^{-q^2 R^2}$.

Consequently, the two-particle correlation function for spin half baryons is given by the sum of the contributions from singlet and triplet states with the corresponding statistical weights, as

$$C(q) = \frac{1}{4}C_{S=0}(q) + \frac{3}{4}C_{S=1}(q) = 1 - \frac{1}{2}e^{-q^2 R^2}. \tag{3.32}$$

Therefore, we can write the correlation function for the case of considering QS only, as

$$C(q) = 1 + C_{QS}(q) = 1 + Ae^{-q^2R^2},\tag{3.33}$$

where $C_{QS}(q)$ represents the quantum statistics part. The Eq. (3.33) will be used in this thesis, with factor A defined as: $A = 1$ for $K_S^0 K_S^0$, $A = -1/2$ for $\Lambda\Lambda$ and/or $\overline{\Lambda}\overline{\Lambda}$ and $A = 0$ for the case of non-identical particles, i.e., $\Lambda\overline{\Lambda}$, $K_S^0\Lambda$ and $K_S^0\overline{\Lambda}$. Figure 3.5 shows the behavior of the quantum statistics contribution in the two-particle correlation function for identical spin zero bosons (red solid line) and for identical spin half baryons (blue dashed line). The case without QS effect (non-identical particles) is shown by the constant black dotted line at unity. In experimental analyses, the so-called invariant quantities are commonly used, which means $q_{inv} = q_{PRF} = \sqrt{-q^\mu q_\mu} = \sqrt{(\mathbf{p}_1 - \mathbf{p}_2)^2 - (E_1 - E_2)^2} = q$ and $R_{inv} = R_{PRF} = R$, called "lengths of homogeneity", which is the inverse of the Gaussian width that can be measured and is interpreted as the source size at the freeze-out. To keep the consistency, we will use the notation q and R along this chapter and use the notation q_{inv} and R_{inv} only in Chapter 5.
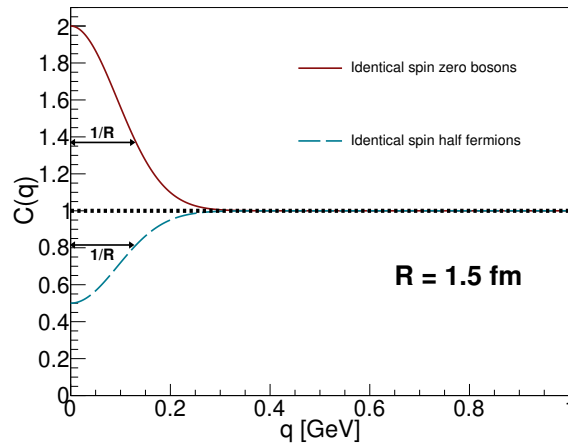
Figure 3.5: Correlation as a function of q with $R = 1.5$ fm for identical spin zero bosons (red solid line) and identical spin half fermions (blue dashed line). The arrows show R as the inverse of the Gaussian width.

3.2.3 λ parameter

In the early eighties, a new parameter, called λ, was introduced by Deutschmann et al. [197] to reduce systematic uncertainties in the experimental fits of the correlation function. The discrepancies and large systematic uncertanties observed were

associated with the Gaussian fit used, which has its maximum at 2 for $q = 0$ GeV and such behavior was not observed in the data points, due to effects of bin width, resonances, among others. The easiest way to solve this inconsistency was to add an extra degree of freedom, λ, later called *incoherence* or *chaoticity* parameter, in the correlation function as $C(q) = 1 + \lambda C_{QS}(q)$, that describe better the intensity of the correlation at $q = 0$ GeV, thus reducing the systematic uncertanties. Figure 3.6, shows the correlation function considering only quantum statistics effects: identical spin zero bosons (left) and identical spin half fermions (right); for $\lambda = 1$ (red solid line), 0.7 (blue dashed line) and 0.4 (purple dot-dashed line) and $R = 1.5$ fm. The $\lambda = 1$ is the case where the Gaussian maximum is equal to 2, while for small values of λ the intensity is reduced. Nowadays, λ is also used to take into account uncorrelated effects, as for example particles coming from decays (called non-prompt) [198, 199]. In this thesis, the λ parameter follows the original idea and is used as a free fit parameter and an observable.
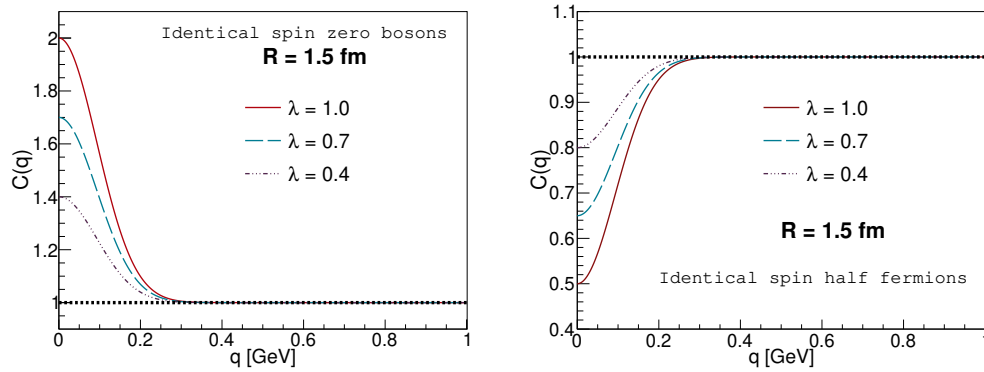
Figure 3.6: Correlation as a function of q using different λ values: 1 (red solid line), 0.7 (blue dashed line) and 0.4 (purple dot-dashed line) for quantum statistics cases: bosons with spin zero (left) and fermions with spin half (right).

3.3 Final state interactions

In addition to the study of quantum statistical effects, femtoscopic correlations also allow to extract information about the final state interactions felt between the correlated particles in high energy collisions. A brief description of the most common FSI (strong and Coulomb) is presented below.

3.3.1 Strong interactions

The application of two-particle correlations to study the strong final state interactions and scattering observables was first studied by R. Lednicky and R. Lyuboshits in the eighties [175]. They developed an analytical model (called Lednicky-Lyuboshits, or LL, model)[6], derived using the Koonin-Pratt equation, Eq. (3.25), considering a Gaussian-type, Eq. (3.26), for the emitting source, and assuming that only the s-wave (spherical) part is affected by the interaction. In this approach, the total wave function is given by [175, 200, 201]

$$\Psi\left(\mathbf{q},\mathbf{r}\right) = e^{i\frac{\mathbf{q}\cdot\mathbf{r}}{2}} + \phi(q,r), \tag{3.34}$$

where the exponential part represents the plane wave function and $\phi(q,r)$ the scattered wave that contains information about the scattering amplitude, $f(q)$, and consequently the strong FSI. In the limit of $q \to 0$, the scattering amplitude is related to the total cross section of the interaction, by [202] (see also Chapter 6 of Ref. [200])

$$\sigma(q) = 4\pi|f(q)|^2. \tag{3.35}$$

The scattering amplitude, $f(q)$, is theoretically modeled in a different way for the case of $K_S^0 K_S^0$ as compared to the other correlations, to take into account the effects present and the knowledge acquired about each interaction [177, 203, 204]. For this reason, the $K_S^0 K_S^0$ correlation is discussed separately in the description below.

Neutral kaon pairs

Kaons were the first hadrons containing strange quarks that were observed experimentally [21], being composed as: $\left|K^0\right\rangle = \left|d\bar{s}\right\rangle$, $\left|\overline{K}^0\right\rangle = \left|\bar{d}s\right\rangle$, $\left|K^+\right\rangle = \left|u\bar{s}\right\rangle$ and $\left|K^-\right\rangle = \left|\bar{u}s\right\rangle$. Because of the different quark composition, the neutral kaons are ~ 4 MeV heavier than the charged ones. In addition, neutral kaons present an interesting property: they produce a $K^0 - \overline{K}^0$ mixed state originated from second order weak charged current interactions, as shown by the two Feynman diagrams in Fig. 3.7. In other words, K^0 can change into $\overline{K}^0$ via W boson exchange. Although the K^0 and $\overline{K}^0$ are strong interaction eigenstates, these particles are not normally observed through weak decay channels in the laboratory [205]. Instead, the measurable neutral kaon mass states that are observed through weak

---

[6]A more detailed derivation of this model for all of the correlations of interest is shown in Appendix C.

interaction are combinations of K^0 and $\overline{K}^0$, given as

$$|K_S^0\rangle = \frac{|K^0\rangle + |\overline{K}^0\rangle}{\sqrt{2}} = \frac{|d\overline{s}\rangle + |\overline{d}s\rangle}{\sqrt{2}} \qquad (3.36)$$

and

$$|K_L^0\rangle = \frac{|K^0\rangle - |\overline{K}^0\rangle}{\sqrt{2}} = \frac{|d\overline{s}\rangle - |\overline{d}s\rangle}{\sqrt{2}}. \qquad (3.37)$$
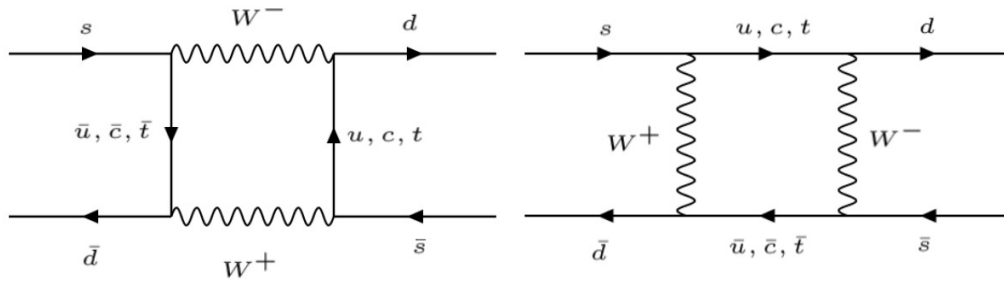
Figure 3.7: Feynman diagrams of $K^0 - \overline{K}^0$ mixing due second order weak interactions.

The sub-indices "S" and "L" stand for "Short" and "Long", related to the lifetimes of the state: $\sim 9 \times 10^{-11}$ and $\sim 5 \times 10^{-8}$ seconds, respectively, corresponding to decay lengths of ~ 3 centimeters and ~ 15 meters. The idea that neutral kaons have different lifetimes was predicted by M. Gell-Mann and A. Pais in 1955 [205].

Experimentally, the charged kaons are measured as tracks that leave signs in tracker (see next chapter), while neutral kaons must be measured using their decay products into charged particles (see Chapter 5). Because of the long lifetime of K_L^0, this particle cannot be measured in the main LHC detectors, since only the energy deposited in the calorimetry system (see next chapter) is observed as a signal, that cannot be distinguished from that of any other neutral particle. Consequently, the studies performed in this thesis consider only K_S^0 mesons, and from now on referring also to neutral kaons.

Using the definition from Eq. (3.36), the two identical K_S^0 state can be expressed as follows

$$|K_S^0 K_S^0\rangle = \frac{1}{2}\Big[|K^0 K^0\rangle + |\overline{K}^0\overline{K}^0\rangle + |K^0\overline{K}^0\rangle + |\overline{K}^0 K^0\rangle\Big],$$

where the states of identical kaons, $|K^0 K^0\rangle$ and $|\overline{K}^0\overline{K}^0\rangle$, contributes for the en-

hancement in low-q because of the Bose-Einstein quantum statistics, as consequence of the wave function symmetrization and present a negligible strong FSI effect. On the other hand, the states of non-identical kaons (no QS), $\left|K^0\overline{K}^0\right\rangle$ and $\left|\overline{K}^0K^0\right\rangle$, contain a significant effect of strong final state interactions and need to be considered [203, 204].

Therefore, the $K_S^0K_S^0$ correlation function can be parametrized using the Lednicky-Lyuboshits model, by [203, 204]

$$
\begin{aligned}
C(q) &= 1 + C_{QS}(q) + C_{SI}(q) \\
&= 1 + Ae^{-q^2R^2} + \frac{1}{2}\left[\frac{|f(q)|^2}{R^2} + \frac{4\Re f(q)}{\sqrt{\pi}R}F_1(qR) - \frac{2\Im f(q)}{R}F_2(qR)\right],
\end{aligned}
\tag{3.38}
$$

where $A = 1$ for identical spin zero bosons,

$$
F_1(qR) = \int_0^{qR} dx\frac{e^{x^2-(qR)^2}}{qR} \quad \text{and} \quad F_2(qR) = \frac{1-e^{(qR)^2}}{qR}.
\tag{3.39}
$$

The scattering amplitude, $f(q)$, for the case of neutral kaons (comming from $\left|K^0\overline{K}^0\right\rangle$ and $\left|\overline{K}^0K^0\right\rangle$) is dominated by the near threshold s-wave resonances $f_0(980)$ and $a_0(980)$, that can be written in terms of the masses of these resonances, m_i (for i equals to $f_0(980)$ or $a_0(980)$), and the couplings, γ_i, these being related with the first $\left(f_0(980), a_0(980) \to K^0\overline{K}^0\right)$ and second $\left(f_0(980) \to \pi\pi, a_0(980) \to \pi\eta\right)$ channels, as [203]

$$
f(q) = \frac{f_{f_0}(q) + f_{a_0}(q)}{2},
\tag{3.40}
$$

where

$$
f_{f_0}(q) = \frac{\gamma_{f_0 \to K^0\overline{K}^0}}{m_{f_0}^2 - s - i\gamma_{f_0 \to K^0\overline{K}^0}q/2 - i\gamma_{f_0 \to \pi\pi}p_{f_0 \to \pi\pi}}
\tag{3.41}
$$

and

$$
f_{a_0}(q) = \frac{\gamma_{a_0 \to K^0\overline{K}^0}}{m_{a_0}^2 - s - i\gamma_{a_0 \to K^0\overline{K}^0}q/2 - i\gamma_{a_0 \to \pi\eta}p_{a_0 \to \pi\eta}}.
\tag{3.42}
$$

Here, $s = 4m_{K^0}^2 + q^2$ and p is the momentum of the second decay channel in the pair rest frame, related to the corresponding partial width $\Gamma = \gamma p/m$ [206, 207],

e.g., $p_{a_0 \to \pi\eta} = \sqrt{(m_{a_0}^2 - (m_\eta - m_\pi)^2)(m_{a_0}^2 - (m_\eta + m_\pi)^2)}/2m_{a_0}$ assuming $m_\pi = 139.57$ MeV and $m_\eta = 547.86$ MeV from PDG [10]. In the literature [203, 204, 208, 209, 206, 207], the set of parameters associated with $f_0(980)$ and $a_0(980)$ are usually taken from several low energy experiments as listed in Table 3.1.

Table 3.1: Experimental mass and coupling parameters, in GeV, for $f_0(980)$ and $a_0(980)$ particles from the literature [208, 209, 206, 207].

Reference	m_{f_0}	$\gamma_{f_0 \to K^0\overline{K}^0}$	$\gamma_{f_0 \to \pi\pi}$	m_{a_0}	$\gamma_{a_0 \to K^0\overline{K}^0}$	$\gamma_{a_0 \to \pi\eta}$
Martin et. al. (a) [208]	0.978	0.792	0.199	0.974	0.333	0.222
Antonelli et. al. (b) [209]	0.973	2.763	0.528	0.985	0.404	0.371
Achasov et. al. (c) [206]	0.996	1.305	0.268	0.992	0.555	0.440
Achasov et. al. (d) [207]	0.996	1.305	0.268	1.003	0.836	0.458

Figure 3.8 shows the $K_S^0 K_S^0$ correlation function containing the contribution of strong final state interactions, for the different set of parameters listed in Table 3.1 (different line colors) for two different values of $R = 1.5$ fm (left) and 3.5 (right) fm. The complete correlation, from Eq. (3.38), is shown in the top panel plots and compared with the case of considering only quantum statistics $(1 + C_{QS}(q)$, in red), while the contribution for strong FSI only $(1 + C_{SI}(q))$ is presented in the bottom panel plots. From Fig. 3.8 it can be seen that the strong FSI includes a depletion in the low-q ($q < 0.5$ GeV) region, that is more pronounced for small values of R, due the $1/R^2$ dependence shown in Eq. (3.38). In terms of physics, this anticorrelation in femtoscopy corresponds to an "attractive" behavior of the final state strong interaction potential, and can also indicate an annihilation process, since with this effect coming basically from the non-identical $K^0\overline{K}^0$ interactions. In this thesis, the parameters from the reference named (a) in Table 3.1 are used as standard, while the others are employed as systematic studies.
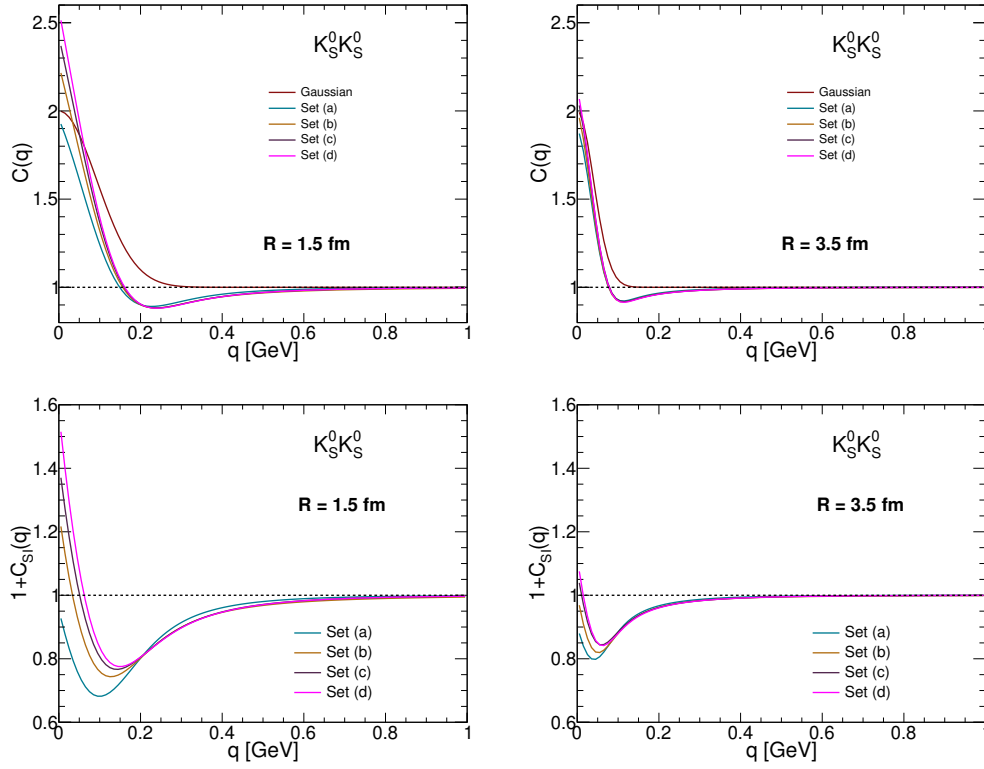
Figure 3.8: Examples of $K_S^0 K_S^0$ correlation function, from Eq. 3.38, using the strong FSI set of parameters from Table 3.1, for two different values of the radius parameter, $R = 1.5$ fm (left) and $R = 3.5$ fm (right) fm. Top panel: full correlation compared with the case without including strong FSI (Gaussian, $1 + C_{QS}$, in red). Bottom panel: contribution of strong FSI ($1 + C_{SI}(q)$) only. More information in the text.

Correlations involving Λ and $\overline{\Lambda}$

The spin half lambda baryons were the first observed three-quark state containing strange quarks in their composition: $|\Lambda\rangle = |uds\rangle$ and $|\overline{\Lambda}\rangle = |\bar{u}\bar{d}\bar{s}\rangle$ [22, 23]. As in the case of K_S^0, Λ's and $\overline{\Lambda}$'s can be reconstructed via their decay into charged particles. For the case of correlations involving lambdas, $\Lambda\Lambda$, $\overline{\Lambda}\overline{\Lambda}$, $\Lambda\overline{\Lambda}$, $K_S^0\Lambda$ and $K_S^0\overline{\Lambda}$, the contribution of possible spin states must be taken into account. Therefore, the LL model is written as [175]

$$
\begin{aligned}
C(q) &= 1 + C_{QS}(q) + C_{SI}(q) = 1 + Ae^{-q^2 R^2} \\
&+ \sum_S \rho_S \left[\frac{|f^S(q)|^2}{2R^2} \left(1 - \frac{d_0^S}{2\sqrt{\pi}R} \right) + \frac{2\Re f^S(q)}{\sqrt{\pi}R} F_1(qR) - \frac{\Im f^S(q)}{R} F_2(qR) \right],
\end{aligned}
$$

(3.43)

where ρ_S is the spin weight defined in the pervious section and the sum runs over all possible spin states. As mentioned earlier, $A = -1/2$ for $\Lambda\Lambda$ and $\overline{\Lambda}\,\overline{\Lambda}$ correlations and $A = 0$ for $\Lambda\overline{\Lambda}$, $K_S^0\Lambda$ and $K_S^0\overline{\Lambda}$ pairs.

The scattering amplitude, $f(q)$ from Eq. (3.43), can be parametrized in terms of the measurable quantities by using the *effective range expansion* (ERE) [201],

$$f(q) \approx \left[\frac{1}{f_0} + \frac{1}{8}d_0 q^2 - i\frac{q}{2} \right]^{-1}, \tag{3.44}$$

where f_0 and d_0 are the *scattering lenght*[7] and *effective range*, respectively; they are the physical observables that can be extracted by using the femtoscopic fit. Ideally, each spin state (singlet or triplet) is associated to different f_0 and d_0 parameters, however, it is not possible to measure the spin dependence in the current high energy experiments. Therefore, an average spin dependence is considered and a single set of f_0 and d_0 values are extracted from the fit.

In this thesis, the f_0 parameter is written using the femtoscopic convention[8] and can have real ($\Re f_0$) and imaginary ($\Im f_0$) parts. The $\Re f_0$ is related to the elastic interactions. If $\Re f_0 > 0$ a correlation above unity is seen ($C(q) > 1$) and, according to the femtoscopic convention, this means an "attractive" behavior, similarly to the identical bosons QS case (nevertheless, it corresponds to a repulsive strong interaction potential). On the other hand, if $\Re f_0 < 0$ and anticorrelation is expected ($C(q) < 1$), indicating a "repulsive" behavior, similarly to the identical fermion QS case, corresponding to an attractive strong interaction potential or the possibility of a bound-state formation. The $\Im f_0$ is related to inelastic interactions happening between the correlated particles and is expected to be always greater or equal to zero. For baryon-antibaryon pairs, this quantity is expected to be greater than zero because of the possibility of occurence of an annihilation process; for identical baryons this must be zero and for meson-baryon correlations it is not yet known. At last, the d_0 parameter enters into the wave function as a correction to the scattering amplitude, being related to the range achieved by this interaction, and is expected to be of the order of the source size, R, and greater or equal to zero. Also, d_0 can be used to differentiate between a repulsive behavior (anticorrelation), $d_0 > |f_0|/2$, or a possible bound state, $d_0 < |f_0|/2$, based on the binding energy defined in Refs. [210, 211].

In addition, the correction (negative) term in parentheses in Eq. (3.43) takes

---

[7]In the limit of $q \to 0$, the scattering amplitude and length are identical, i.e., $f(q) = f_0$.

[8]Note that, in the usual convention the scattering length is called a_0 and defined as $a_0 = -f_0$.

into account the effect of pair interactions that occur in the range of non-zero potential (i.e., non-asymptotic region). This correction implies an extra constraint to avoid negative (unphysical) correlations, where the d_0 value must be of the order of the radius parameter, R, specially for negative values of f_0.

Figure 3.9 shows the influence of each scattering observables on the correlation function: $\Re f_0$ (top left), $\Im f_0$ (top right), d_0 (bottom left), and radius R (bottom right) from Eq. (3.43), considering only the strong FSI, i.e., $C(q) = 1 + C_{\text{SI}}(q)$. It can be seen from Fig. 3.9 that, for positive $\Re f_0$, $C(q) > 1$ and following the femtoscopy convention, it implies an "attractive" behavior (repulsive strong interaction potential), while negative values of $\Re f_0$, $C(q) < 1$ (top left), reflect a "repulsive" behavior (attractive strong interaction potential). For the imaginary part of the scattering lenght, $\Im f_0$, it can be seen that the effect is small for $\Re f_0 < 0$, being more pronounced for $\Re f_0 > 0$ (top right). The d_0 parameter (bottom left) tends to reduce the strength of the correlation function for positive $\Re f_0$, while the opposite behavior can be seen for negative $\Re f_0$. In the case of the dependence on R (bottom right), the strength of the correlation is reduced for bigger R as expected, since the LL model, Eq. (3.43), goes with $1/R^2$. Although the correlation shows a dependence on R, it is expected that the scattering parameters are constant for different multiplicities or centralities, since these are final state interactions (after particle emission) [175, 177, 181, 212, 213]. A last and interesting observation for all plots is that the strong FSI has an influence in the region $q \leq 0.5$ GeV, an important effect to consider when estimating the non-femtoscopic background in our analysis (see Chapter 5).
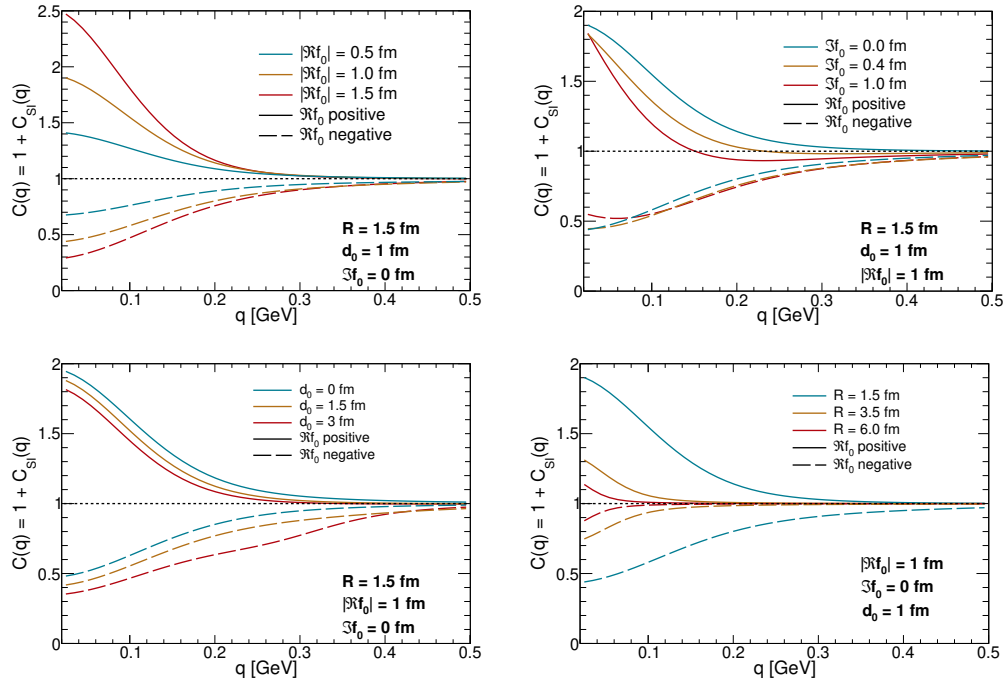
Figure 3.9: Example of the contribution of the strong FSI parameters using the LL model, in Eq. (3.43), in the correlation function $C(q) = 1 + C_{SI}(q)$, for different values (in different colors) of $\Re f_0$ (top left), $\Im f_0$ (top right), d_0 (bottom left) and R (bottom right). The plots show results for both $\Re f_0 > 0$ fm (solid lines), and $\Re f_0 < 0$ fm (dashed lines). More information in the text.

3.3.2   Coulomb interactions

Correlations between charged particles are also sensitive to Coulomb final state effects, where same-sign (SS) and opposite-sign (OS) particles experience repulsive and attractive interactions, respectively. Such behavior is also observed in the correlation function and affects especially the very low-q region. In this thesis, only neutral particles are considered, therefore, are not affect by these interactions. Nevertheless, to give a more complete picture of the effects observed in femtocopic correlations, a brief description of Coulomb FSI effect is presented below.

The Coulomb final state interactions observed in femtoscopic correlations is well studied and is used in experiments more as a correction, rather than to obtain additional informations [187, 188, 189, 214]. To take this effect into account, the Bowler-Sinyukov formula is traditionally applied [215, 216, 217],

$$C(q) = \mathcal{N} \left\{ 1 - \lambda + \lambda K(q) \left[1 + C_{QS}(q) \right] \right\}. \tag{3.45}$$

Assuming the ideal case, $\mathcal{N} = \lambda = 1$, and considering opposite-sign particles, where no QS ($C_{QS}(q) = 0$) and no strong FSI are present, we have $C(q) = K(q)$. Therefore, all the information about the Coulomb FSI is contained in correction factor, $K(q)$, which can be written as [217]

$$K(q) = \int d\mathbf{r}\, S(\mathbf{r})\, |\Psi(\mathbf{q}, \mathbf{r})|^2, \tag{3.46}$$

where the source and wave functions, correspond to those in the Koonin-Pratt formula, Eq. (3.25).

The Coulomb wave function is given by [217]:

$$\Psi(\mathbf{q}, \mathbf{r}) = e^{-\frac{\pi\zeta}{2}} \Gamma(1 + i\zeta) e^{i\frac{\mathbf{q}\cdot\mathbf{r}}{2}} {}_1F_1(-i\zeta; 1; i(qr - \mathbf{q}\cdot\mathbf{r})/2), \tag{3.47}$$

where $\zeta = \pm m\alpha/q$, m is mass of the particles, $\alpha = 1/137$ is the fine structure constant, Γ and ${}_1F_1$ are the gamma and hypergeometric functions (see Chapters 8 and 13 of Ref. [166]), respectively. The signal $+$ or $-$, in ζ, is related to the pair interaction, being positive for repulsion, SS ($++$, $--$), and negative for attraction, OS ($+-$). The Eq. (3.47) is valid for pairs of particles where the Coulomb effect is the dominant FSI term, e.g. $\pi\pi$; however, in cases where both strong and Coulomb FSI are expected to play important roles, e.g. $p\Xi^-$, this equation is no longer valid and the two-particle wave function must include the scattering quantities. More information about that can be found in Refs. [177, 181].

For a point-like source, $S(r) = \delta(r)$ and $r = 0$, the Coulomb correction factor is given by the Gamov factor, $G(q)$, written as [217]

$$K(q) = G(q) = |\Psi(q, r = 0)|^2 = \frac{2\pi\zeta}{e^{2\pi\zeta} - 1}, \tag{3.48}$$

in which the effects of repulsion or attraction are included in the sign of ζ. This is a reasonably good approximation for pp collisions at the LHC energies, as shown in Refs. [187, 188, 189, 214].

However, in the case of extended sources, like in heavy ion collisions, the Gamov approximation is not enough and a more elaborate treatment is needed [217]. In this case, the correction depends on the shape chosen for the source function, as shown by Eq. (3.46). Assuming a Gaussian shape as in Eq. (3.26), the integral used to obtain the Coulomb correction factor can only be calculated numerically,

but it can be approximate by the expression [217]

$$K(q) = G(q) \left[1 + \frac{4R_{\text{eff}}}{\sqrt{\pi}} {}_2F_2 \left(\frac{1}{2}, 1; \frac{3}{2}, \frac{3}{2}; -q^2 R_{\text{eff}}^2 \right) \right], \tag{3.49}$$

where ${}_2F_2$ is another hypergeometric function (see Chapter 13 of Ref. [166]) and R_{eff} is the effective size of the Coulomb interaction, which is usually taken to be proportional to R.

Recently, an approximation for $K(q)$ considering a Cauchy-Lorentz source function, as in Eq. (3.28), was derived by the CMS Collaboration resulting in the following expression [189]

$$K(q) = G(q) \left[1 + \pi \zeta \frac{qR_{\text{eff}}}{1.26 + qR_{\text{eff}}} \right]. \tag{3.50}$$

This function was used in measurements of charged pions and kaons in pp, pPb and peripheral PbPb collisions at $\sqrt{s_{\text{NN}}} = 0.9 - 7$ TeV, returning similar results for pp collisions as considering Gamov correction.

A comparison between the Coulomb correction factors, $K(q)$, as a function of q, for two different effective sizes, $R_{\text{eff}} = 1.5$ (left), 4.0 (right) fm, considering Gamov (blue) from Eq. (3.48), for Gaussian (red), Eq. (3.49), and Cauchy-Lorentz (yellow), Eq. (3.50), source functions, are shown in Fig. 3.10 for same-sign (dashed lines, repulsive interaction) and opposite-sign (solid lines, attractive interaction) pion pairs ($m_\pi = 139.7$ MeV). The Coulomb correction, $K(q)$, affect mainly the $q < 0.1$ GeV region and show similar shapes for different R_{eff}. As expected, the discrepancy between Gamov and the cases considering extended sources is larger for higher R_{eff} values, however, for small R_{eff}, as shown for 1.5 fm, the Gamov shows a similar behavior when compared to the proper Coulomb correction.
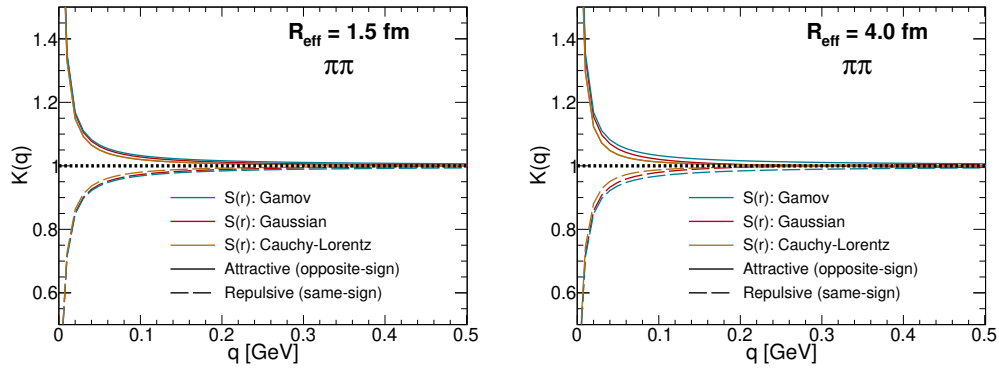
Figure 3.10: Coulomb correction factor, $K(q)$, as a function of q considering a pair of pions for attractive (solid lines), $\pi^+\pi^-$, and repulsive (dashed lines), $\pi^+\pi^+$ and/or $\pi^-\pi^-$, interactions by considering different sources: i) Gamov (blue), described by Eq. 3.48; ii) Gaussian (red), from Eq. 3.49; and iii) Cauchy-Lorentz (yellow), from Eq. 3.50; for R_{eff} equal to 1.5 (left) and 4.0 (right) fm.

3.4 Highlights of previous measurements

The experimental measurements of femtoscopic correlations have been extensively studied along the years in particle accelerators [121, 174, 122, 123, 124, 218], specially using pions, since they are the most abundant hadrons produced.

The results presented in this thesis are the first correlation measurements of $K_S^0 K_S^0$, $K_S^0 \Lambda \oplus K_S^0 \overline{\Lambda}$, $\Lambda\Lambda \oplus \overline{\Lambda}\,\overline{\Lambda}$ and $\Lambda\overline{\Lambda}$ pairs[9] employing data collected by the CMS experiment in small colliding systems, which is used to study the source size as well as the strong FSI. The analysis methods are described in detail in Chapter 5. This section shows a brief overview of the experimental results for each correlation of interest as measured by other experiments.

3.4.1 $K_S^0 K_S^0$

The femtoscopic correlations between neutral kaons is one of the most studied among the correlations of interested. The first measurement of $K_S^0 K_S^0$ correlations was performed in $p\overline{p}$ annihilations at $\sqrt{s_{\text{NN}}} = 0.76$ GeV at PS/CERN[10] in 1978, with

---

[9]The symbol $\oplus$ implies that the correlations are combined to increase the data sample used in the analysis.

[10]This CERN program was called THRESH-GRIND-SLICE and the experimental analysis was done for 1.4 million pictures from the exposure of the 81 cm Saclay hydrogen bubble chamber (see cds.cern.ch/record/763448 and cds.cern.ch/record/2010847) to an antiproton beam of 0.76 GeV momentum.

the multiplicity of produced particles being less than 5, resulting in $R = 0.9 \pm 0.2$ fm [219]. In the LEP era, experimental measurements of $K_S^0 K_S^0$ were performed in e^+e^- collisions at $\sqrt{s} = 91$ GeV by OPAL [220], ALEPH [221] and DELPHI [222], in 1993 and 1994, with an average multiplicity of about 2 produced particles per event. The parameter R was measured with values between 0.5 and 0.8 fm, while λ lied between 0.6 and 1.2. The results obtained were in agreement, within uncertainties, in all three experiments.

The first attempt to measure $K_S^0 K_S^0$ correlations in heavy ion systems was made in 1999 by the WA97 Collaboration at SPS/CERN, in PbPb collisions at $\sqrt{s_{NN}} = 158$ GeV [223]. However, only about two thousand pairs were analyzed, which did not allow to extract a conclusive information about the source. In 2005, the STAR Collaboration measured the one-dimensional neutral kaon correlations in AuAu collisions at $\sqrt{s_{NN}} = 200$ GeV with a centrality window of $0 - 80\%$ [203]. In this analysis a very detailed study about strong final state interactions was performed applying the Lednicky-Lyuboshitz model, using different set of parameters coming from other experiments (A,B, c and d lines in the plot, see Sec. 3.3), but not including strong FSI (only Gaussian), as shown by the fits in Fig. 3.11 (left). The R extracted do not present a strong dependence on the scattering parameters and is shown in Fig. 3.11 (right) as a function of the transverse mass (m_T), and compared with results from $\pi^+\pi^+$, $\pi^-\pi^-$, $p\Lambda$, $\overline{p}\Lambda$, $\overline{p}\overline{\Lambda}$ and $p\overline{\Lambda}$ correlations, suggesting a possible scaling in m_T. In 2007, neutral kaon correlations were also measured in Neutron-Carbon (nC) interactions at average neutron energy of 51 GeV by the EX-CHARM spectrometer [224] at U-70 accelerator (proton-syncronton) [225] located in Russia, with charged particle multiplicity in a range of 4 to 9. Such correlation were studied considering the strong FSI and not; the final results for the radius parameter were compatible with the ones measured by the LEP experiments.

At LHC, only ALICE Collaboration has already measured neutral kaon correlations. The first result obtained was measured in pp collisions at $\sqrt{s} = 7$ TeV [226] in two bins of multiplicity (1 to 11 and > 11) and two bins of average transverse momentum, k_T, (0 to 0.85 GeV and > 0.85 GeV), as shown in the top panel of Fig. 3.12: the correlations as a function of q (four left plots), fitted with (solid line) and without (dashed line) the LL model to study the effect of strong FSI; the extracted R as a function of transverse mass (right plot), and comparing the $K_S^0 K_S^0$ measurements with previous results from charged pions in the same multiplicity ranges. These observations show that the inclusion of strong FSI leads to a better description of the data. ALICE also performed measurements

of $K_S^0 K_S^0$ correlations in one and three spatial dimensions in PbPb collisions at $\sqrt{s_{NN}}$ = 2.76 GeV [204, 227, 228], including the centrality dependence; this was the latest experimental result available before writing this thesis. An example of the one dimensional correlation function measured using the LL fit (solid line) by ALICE Collaboration in central PbPb collisions ($0 - 10\%$) and $0.2 < k_T < 0.6$ GeV is shown in Fig. 3.12 (bottom left), while the extracted R as a function of m_T, for different pairs and centralities, is presented in Fig. 3.12 (bottom right). As expected, the lengths of homogeneities increase from peripheral to central collisions. Also, it is possible to observe that the R values measured show a similar behavior (scaling) when compared with measurements from other particle species.

This thesis shows the first analysis of $K_S^0 K_S^0$ correlations in proton-lead collisions.
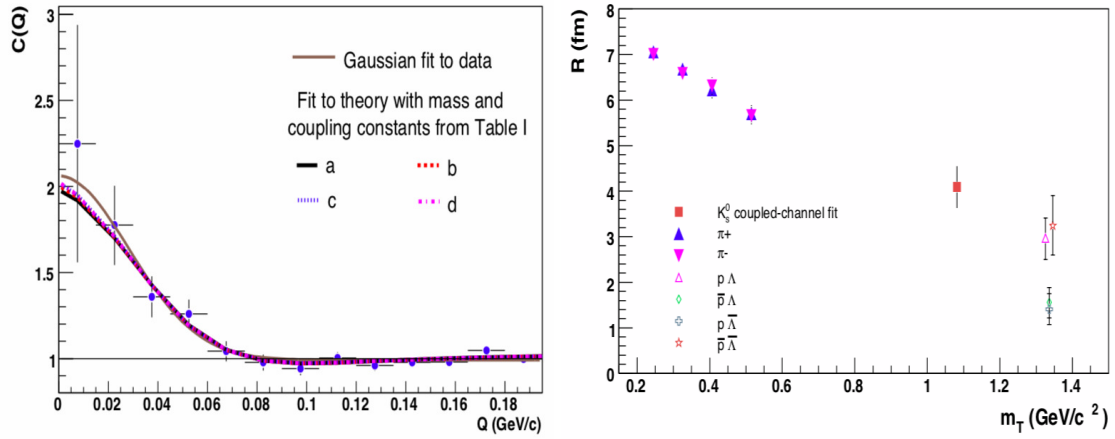
Figure 3.11: Measurement of $K_S^0 K_S^0$ femtoscopic correlations from STAR Collaboration in AuAu collisions with $\sqrt{s_{NN}}$ = 200 GeV. More information in the text. Extracted from [203].
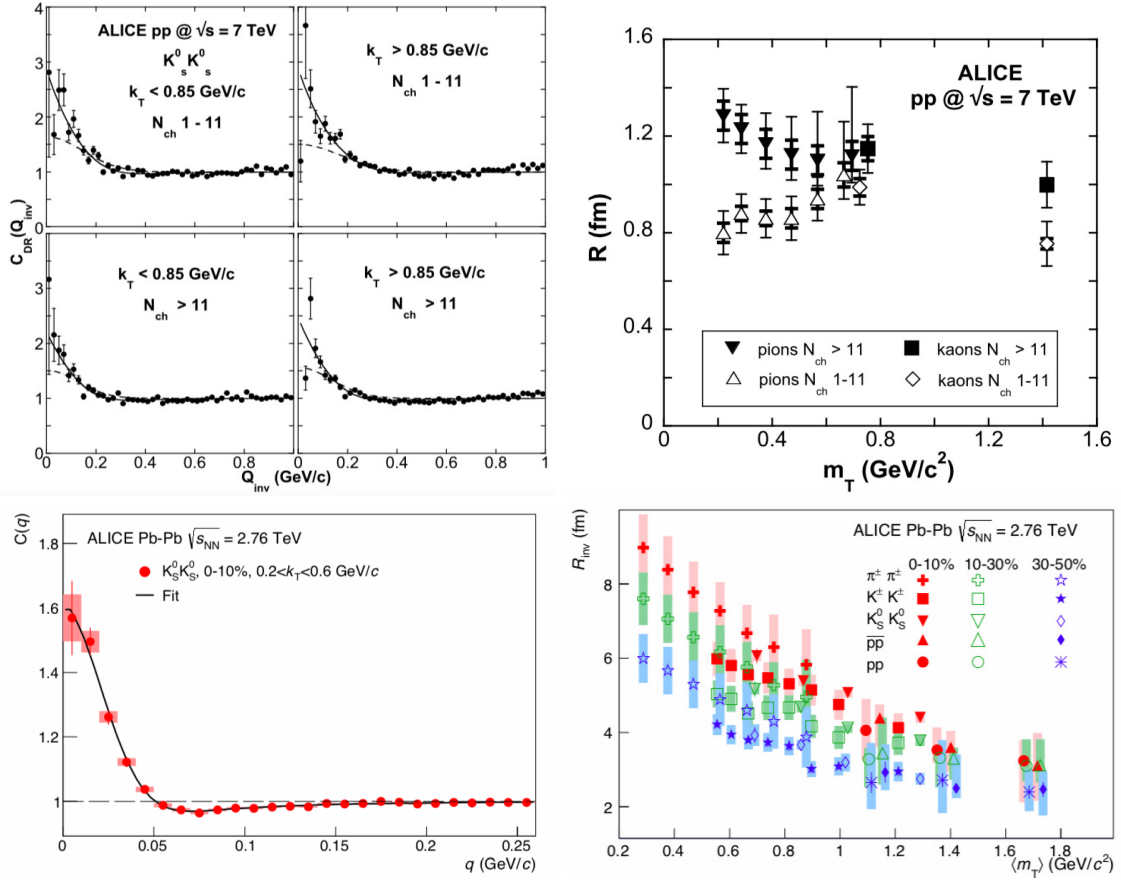
Figure 3.12: Summary of one dimensional results measured by ALICE Collaboration for $K_S^0 K_S^0$ correlations in pp collisions at $\sqrt{s} = 7$ TeV (top panel) and PbPb collisions at $\sqrt{s} = 2.76$ TeV (bottom panel). More information in the text. Extracted from [226, 227].

3.4.2 $K_S^0 \Lambda \oplus K_S^0 \overline{\Lambda}$

From an experimental point of view, the meson-baryon femtoscopic correlations started to be studied only recently, having collected a small amount of results so far. Initially these correlations were used to study the relative space-time asymmetries in the production of different particle species (e.g., relative time delays or spatial shifts due to collective flow) [182, 229, 230, 231]. Because they are non-identical particles, only final state interactions (strong and/or Coulomb) are present and the Lednicky-Lyuboshits model can be applied to extract the scattering parameters.

In the case of the correlations that are relevant for this analysis, $K_S^0 \Lambda \oplus K_S^0 \overline{\Lambda}$, the only measurement was performed by the ALICE Collaboration in PbPb collisions at $\sqrt{s_{NN}} = 2.76$TeV [181, 232], as shown in Fig. 3.13: for the correlation function

(top panel) in different centralities (0-10%, 10-30% and 30-50%), using $K\Lambda$ in different pair configurations, including fits and systematic uncertainties; for the scattering ($\Re f_0$, $\Im f_0$ and d_0) and source (λ and R) parameters (bottom panel). Note that the fits to extract the scattering quantities are performed simultaneously for different centralities, i.e., single values for $\Re f_0$, $\Im f_0$ and d_0 are obtained for all centrality windows. The λ parameter is nearly constant (within the uncertainties) and R increases for more central collisions, as expected, since larger values of R could correspond to higher number of produced particles. For $K_S^0\Lambda \oplus K_S^0\overline{\Lambda}$, the obtained results for the scattering quantities indicate a slightly attractive interaction (although the null result is not excluded, considering the uncertainties), $\Re f_0 \geq 0$, while the imaginary part is greater than zero ($\Im f_0 > 0$), implying that the inelastic process is dominant. These results are close to the values from theory, where $q \to 0$ is assumed, within the ERE ($f(q) = f_0$). Also, an "attractive" behavior (repulsive strong interaction potential) was measured in $K_S^0\Lambda \oplus K_S^0\overline{\Lambda}$ and $\Lambda K^- \oplus \overline{\Lambda}K^+$, while for $\Lambda K^+ \oplus \overline{\Lambda}K^-$ a "repulsive" behavior (attractive strong interaction potential) was obtained. A negative, unphysical, d_0 value was extracted by the ALICE fits in $K_S^0\Lambda \oplus K_S^0\overline{\Lambda}$. One possible interpretation for this result is that the ERE used in the LL model to describe these correlations might not be applicable in this case[233], and a more complex description is required[11].

Other measurements were performed by the ALICE Collaboration in meson-baryon correlations, focusing mainly in the strong FSI study of $p\phi$ [234] in pp collisions at $\sqrt{s}$ = 13 TeV, also for pK in pp at $\sqrt{s}$ = 5, 7 and 13 TeV [235], and more recently in PbPb collisions at $\sqrt{s_{NN}}$ = 2.76 GeV [213]. In all the measurement using the LL model, a positive d_0 result was observed.

This thesis shows the first $K_S^0\Lambda \oplus K_S^0\overline{\Lambda}$ measurement in small colliding systems and the first meson-baryon correlations with CMS data.

---

[11]Probably due the small signal observed when compared to the background.
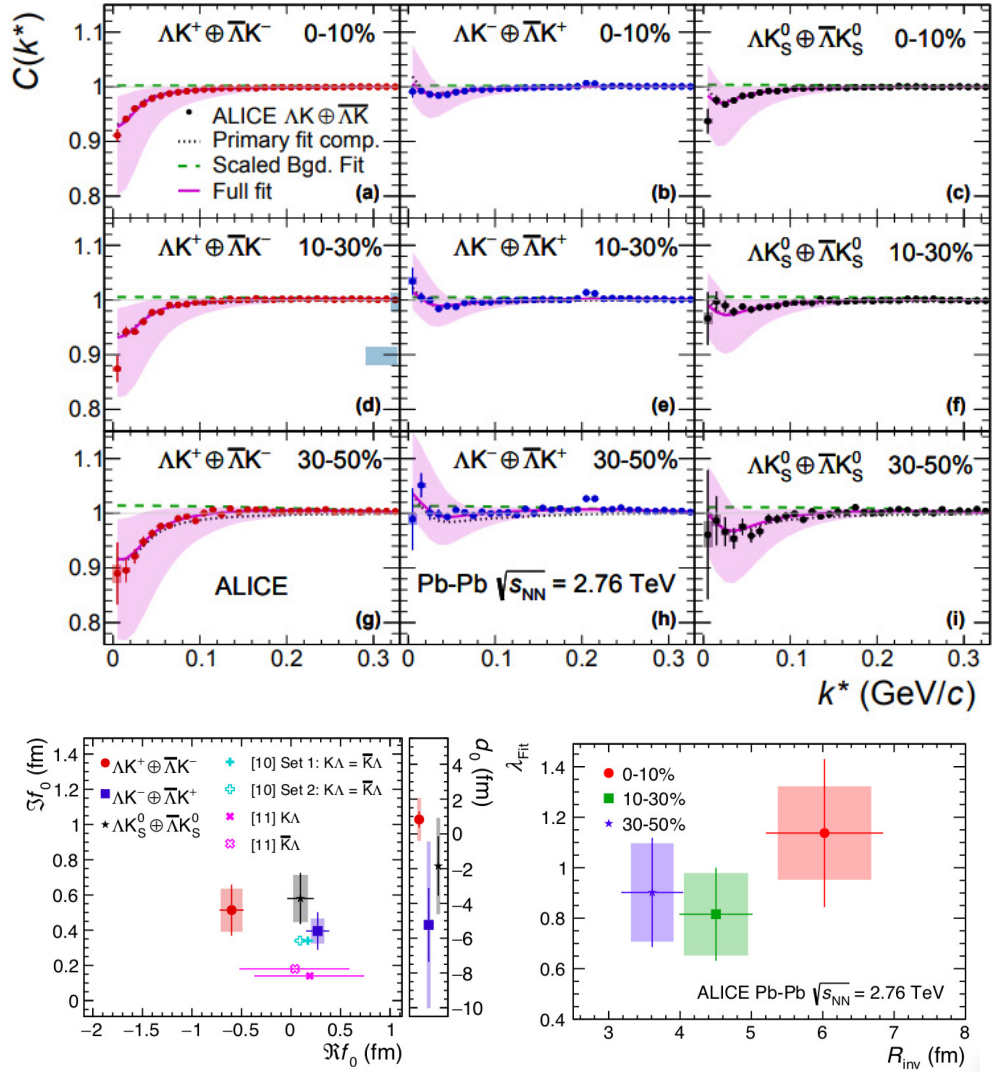
Figure 3.13: Top panel: measured correlation as a function of k^* $(q/2)$ for different $K\Lambda$ pairs (solid circles) in PbPb collisions at $\sqrt{s_{NN}}$ = 2.76 TeV, in three different centralities: 0-10% (top), 10-30% (middle) and 30-50% (bottom). The fit results (pink solid line), background (green dashed line), strong FSI only (black dotted line) and systematic uncertainties (pink band) are also shown. Bottom panel: the scattering quantities ($\Re f_0$, $\Im f_0$, d_0) measured using the LL fit are shown on the left, while the λ versus R_{inv} results are shown on the right. Extracted from [232].

3.4.3 $\Lambda\Lambda \oplus \overline{\Lambda}\overline{\Lambda}$

Only a small number of experimental results on femtoscopic correlations of identical Λ baryons is available, with first measurements from LEP experiments in the nineties. This measurement was conducted by the ALEPH experiment at e^+e^- at $\sqrt{s}$ = 91 GeV [236] in 1999, resulting in $R = 0.12 \pm 0.15$ (stat.) ± 0.08 (syst.) fm.

In this analysis, the effect of strong final state interaction was not considered. In heavy ion collisions, the first femtoscopic measurement was performed in 1999 by WA97 Collaboration at SPS/CERN [223], but only $\sim$ 1200 pairs of Λ's were analyzed, being not possible to obtain informations about the source size or the strong FSI.

The strong final state parameters were analyzed for the first time for $\Lambda\Lambda \oplus \overline{\Lambda}\overline{\Lambda}$ interactions in the early 2000 years, based on the double-hypernucleus events, called NAGARA [237], measured in low energy nuclear scattering experiments. In this case, theoretical calculations were compared to the data in order to extract the observables, indicating that an "attractive" behavior ($\Re f_0$ positive) was obtained: $\Re f_0 = 0.575$ fm, $d_0 = 6.45$ fm [238] and $\Re f_0 = 0.77$ fm, $d_0 = 6.59$ fm [239].

Later, in 2015, $\Lambda\Lambda \oplus \overline{\Lambda}\overline{\Lambda}$ scattering observables were measured for the first time using femtoscopic correlations. The analysis was performed by the STAR collaboration in AuAu collisions at $\sqrt{s_{\mathrm{NN}}}$ = 200 GeV [240] at RHIC. Figure 3.14 shows the correlation as a function of q (left) and the scattering parameter plot of $r_{\mathrm{eff}} = d_0$ (effective range) versus $1/|a_0| = 1/|f_0|$ (scattering length). The data points (black circles with systematic uncertainties as a blue band) were fitted including the strong final state interactions from the LL model. In addition, an extra term, based on phenomenology, was included to model possible residual (non-prompt) effects. Different than the expectations and other baryon-baryon interactions, the scattering parameters obtained by STAR indicated a "repulsive" behavior (negative $\Re f_0$) with the following fit parameters: $\Re f_0 = -1.10 \pm 0.37(\mathrm{stat.})^{+0.68}_{-0.08}(\mathrm{syst.})$, $d_0 = 8.52 \pm 2.56(\mathrm{stat.})^{+2.09}_{-0.74}(\mathrm{syst.})$, $R = 2.96 \pm 0.38(\mathrm{stat.})^{+0.96}_{-0.02}(\mathrm{syst.})$ fm and $\lambda = 0.18 \pm 0.05(\mathrm{stat.})^{+0.12}_{-0.06}(\mathrm{syst.})$. In the same year, however, STAR data was re-analyzed by K. Morita et. al. [241] by fixing the intensity parameter $\lambda \sim 0.445$, based on the prompt fraction of Λ and $\overline{\Lambda}$ from phenomenological models. By using this method, they estimated a range for the observables, where an "attractive" behavior (positive $\Re f_0$) was observed: $1.25 < \Re f_0 < 0.55$ fm and $3.5 < d_0 < 7$ fm. In addition, a comparison with different potential models was performed, beint the data better described by the models with positive $\Re f_0$.

In 2019, ALICE Collaboration at the LHC performed a measurement of $\Lambda\Lambda \oplus \overline{\Lambda}\overline{\Lambda}$ correlations in pp at $\sqrt{s}$ = 7 and 13TeV, and pPb collisions at $\sqrt{s_{\mathrm{NN}}}$ = 5.02 TeV [210, 242]. The signal observed in their correlation measurement was small, as can be seen in Fig. 3.15 for pp (left) and pPb (right) collisions. Due to the small signal, a scan in f_0 and d_0 was performed (fixing R, based on pp correlation results) and compared to the data (bottom plot in Fig. 3.15). In this way, ALICE could

establish exclusion regions with 3σ significance for the scattering observables, with a very small probability to obtain a "repulsive" behavior (or bound state), $\Re f_0 < 0$, which favors the "attractive" behavior (repulsive strong interaction potential). Note that the dashed area in ALICE's plot returns unphysical results (negative correlations), and excludes the result from the STAR measurement, but not that from the re-analysis).

In addition, $\Lambda\Lambda \oplus \overline{\Lambda}\,\overline{\Lambda}$ correlations also have been used to search for a hypothetical exotic H-dibaryon state that could be composed of six (anti)quarks, *uuddss* ($\bar{u}\bar{u}\bar{d}\bar{d}\bar{s}\bar{s}$), containing strangeness $-2(2)$ and baryon number equals to 2. This exotic particle was predicted in 1977 by Jaffe [243] with an expected mass of ~ 81 MeV, below the two lambda mass threshold. Calculations from LQCD suggested the possibility of H-dibaryon to exist as a bound state or resonance pole [244, 245]. Experimentally, searches for this exotic state performed in the nineties reported negative results [246, 247, 248]. In 2001, the analysis of NA-GARA events reduced the binding energy, from Jaffe's estimate, to 7.13 ± 0.87 MeV with 90% of confidence level. In 2007, the KEK$-$E522 collaboration observed an enhancement with 2σ significance at 15 MeV above the $2m_\Lambda$ threshold (but bellow Ξn threshold) using the invariant mass spectrum from $^{12}C(K^-, K^+ \Lambda\Lambda\, X)$, indicating that the effects of FSI for pairs of identical Λ baryons are attractive [241]. Later, in 2013, the H-dibaryon was searched by Belle collaboration in [249]$e^+e^- \rightarrow Y(1S), Y(2S) \rightarrow HX \rightarrow \Lambda p\pi^- X$, and by ALICE collaboration in 2015, with the measurement of the invariant mass spectrum of $H \rightarrow \Lambda p\pi^-$ in central PbPb collisions [250]. In the same year STAR collaboration also searched for H-dibaryons using $\Lambda\Lambda \oplus \overline{\Lambda}\,\overline{\Lambda}$ correlations in AuAu collisions [240]. More recently, in 2019, new results were obtained by the ALICE Collaboration, this time employing the femtoscopic technique in pp and pPb collisions [210]. All these results are in favor of the non-existence of an exotic H-dibaryon state[12]. The main focus of this thesis is to study the strong final state interactions by using $\Lambda\Lambda \oplus \overline{\Lambda}\,\overline{\Lambda}$ correlations, but a quick check using the two lambda's invariant mass was performed with no sign of a H-dibaryon. Also, our $\Lambda\Lambda \oplus \overline{\Lambda}\,\overline{\Lambda}$ results are consistent with previous measurements.

The previous measurements could not establish the nature of the $\Lambda\Lambda \oplus \overline{\Lambda}\,\overline{\Lambda}$ strong final state interaction, however the data and phenomenology indicates an attractive strong FSI in this case. This thesis shows the first analysis using

---

[12]The most recent binding energy for a possible $\Lambda\Lambda \oplus \overline{\Lambda}\,\overline{\Lambda}$ state (if it exists) was measured by ALICE Collaboration as $3.2^{-2.4}_{+1.6}(\text{stat.})^{-1.0}_{+1.8}(\text{syst.})$ MeV.

$\Lambda\Lambda \oplus \overline{\Lambda}\,\overline{\Lambda}$ correlations at the top LHC energy for proton-lead collisions with a larger data sample.
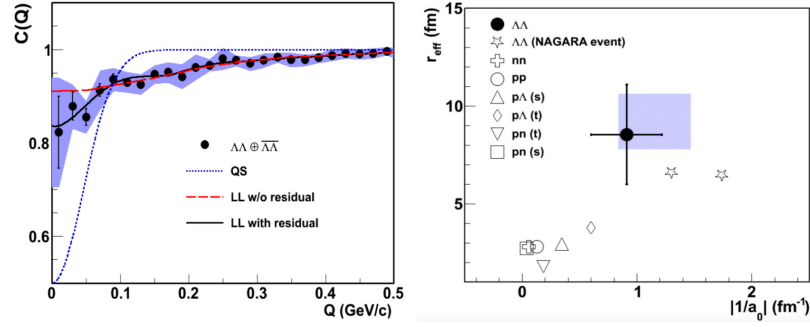
Figure 3.14: STAR Collaboration measurements in AuAu collisions (0-80% centrality) at $\sqrt{s_{\mathrm{NN}}} = 200$ GeV for $\Lambda\Lambda \oplus \overline{\Lambda}\,\overline{\Lambda}$ correlation function (left) and scattering parameters (right): $r_{\mathrm{eff}} = d_0$ versus $1/|a_0| = 1/|f_0|$. Extracted from [240].
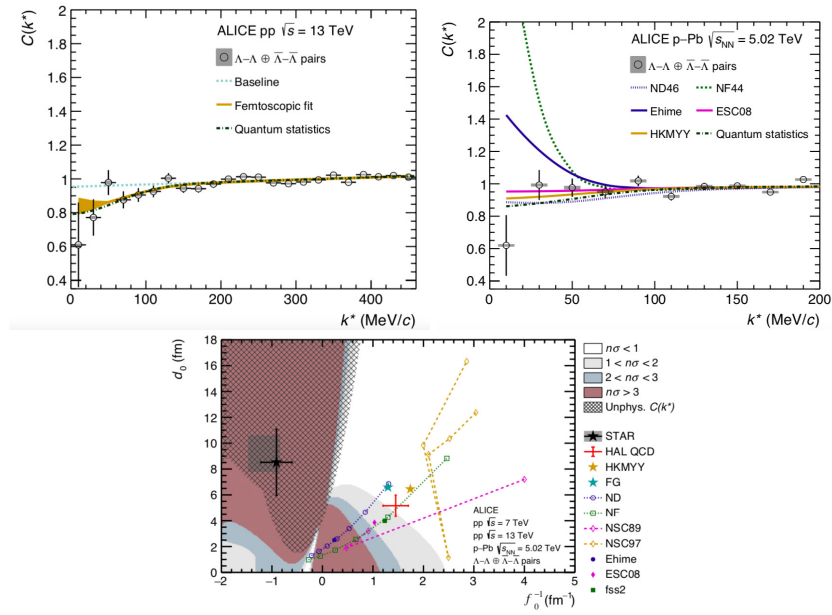
Figure 3.15: ALICE Collaboration measurement of $\Lambda\Lambda \oplus \overline{\Lambda}\,\overline{\Lambda}$ correlations in pp collisions at $\sqrt{s} = 7$ and 13 TeV and pPb collisions at $\sqrt{s_{\mathrm{NN}}} = 5.02$ TeV. Top panel: $C(k^*)$ as a function of k^* ($q/2$) in pp collision at $\sqrt{s} = 13$ TeV (left) for pPb collisions at $\sqrt{s_{\mathrm{NN}}} = 5.02$ TeV (right). Bottom panel: d_0 versus f_0^{-1} exclusion plot using the LL model. More information in the text. Extracted from [210].

3.4.4 $\Lambda\overline{\Lambda}$

In baryon-antibaryon and in meson-baryon correlations discussed here, only final state interactions are expected and the LL model can be used to estimate the scattering observables. The number of experimental results with such information is small and most of the measurements started in the 20th century in $p\overline{p}$ annihilation processes from lower energy scattering experiments [251, 252, 253, 254]. Later, $p\overline{p}$ femtoscopic correlations by STAR collaboration in AuAu collisions with $\sqrt{s_{NN}}$ between 7.7 and 200 GeV [255] and from ALICE collaboration in PbPb collisions with $\sqrt{s_{NN}}$ = 2.76 TeV [256] became available. For pairs with non-zero strangeness content, the femtoscopic correlations started to be studied with $p\Lambda$ pairs by the STAR collaboration in 2006, [257] in AuAu collisions at $\sqrt{s_{NN}} = 200$ GeV, leading to a interesting discussion about the impact of resonance decays on the correlation function (see Sec. 5.3.3 of Chapter 5). In the case of $\Lambda\overline{\Lambda}$ correlations, the only measurement of the strong FSI quantities was performed by ALICE collaboration in PbPb collisions [212], and is shown in Fig. 3.16: the top panel shows the correlation, $C(k^*)$, as a function of k^* in $p\overline{p}$ (top), $p\overline{\Lambda} \oplus \overline{p}\Lambda$ (middle) and $\Lambda\overline{\Lambda}$ (bottom) for $\sqrt{s_{NN}}$ = 2.76 (right) and 5.02 (left) TeV. The bottom panel shows results for the scattering parameters ($\Re f_0$, $\Im f_0$ and d_0) extracted using the LL model for $p\overline{\Lambda} \oplus \overline{p}\Lambda$ (red marker), $\Lambda\overline{\Lambda}$ (pink marker) and combined baryon-antibaryon (green marker), $B\overline{B}$, results. The additional markers represent results from lower energy experiments, as described in the legend. According to ALICE results the baryon-antibaryon correlations indicate a "repulsive" behavior (attractive strong interaction potential), $\Re f_0 < 0$, and a significant non-zero imaginary part of the scattering length, $\Im f_0 > 0$, that can be interpreted as the presence of an annihilation process. This analysis presents physics results consistent with the previous baryon-antibaryon results from low energy experiments. Moreover, the behavior of the scattering parameters is similar compared to pairs of different particle species. This is in agreement with one of the possible scenarios implemented in microscopic models[13], indicating that $\Im f_0$ must be the same for all baryon-antibaryon pairs.

This thesis shows the first analysis using $\Lambda\overline{\Lambda}$ correlations in small colliding systems

---

[13]Such models describes the evolution of the system (or part of it) by considering it as a gas treated by the relativistic Boltzmann equation. More information can be found in Refs. [258, 259].
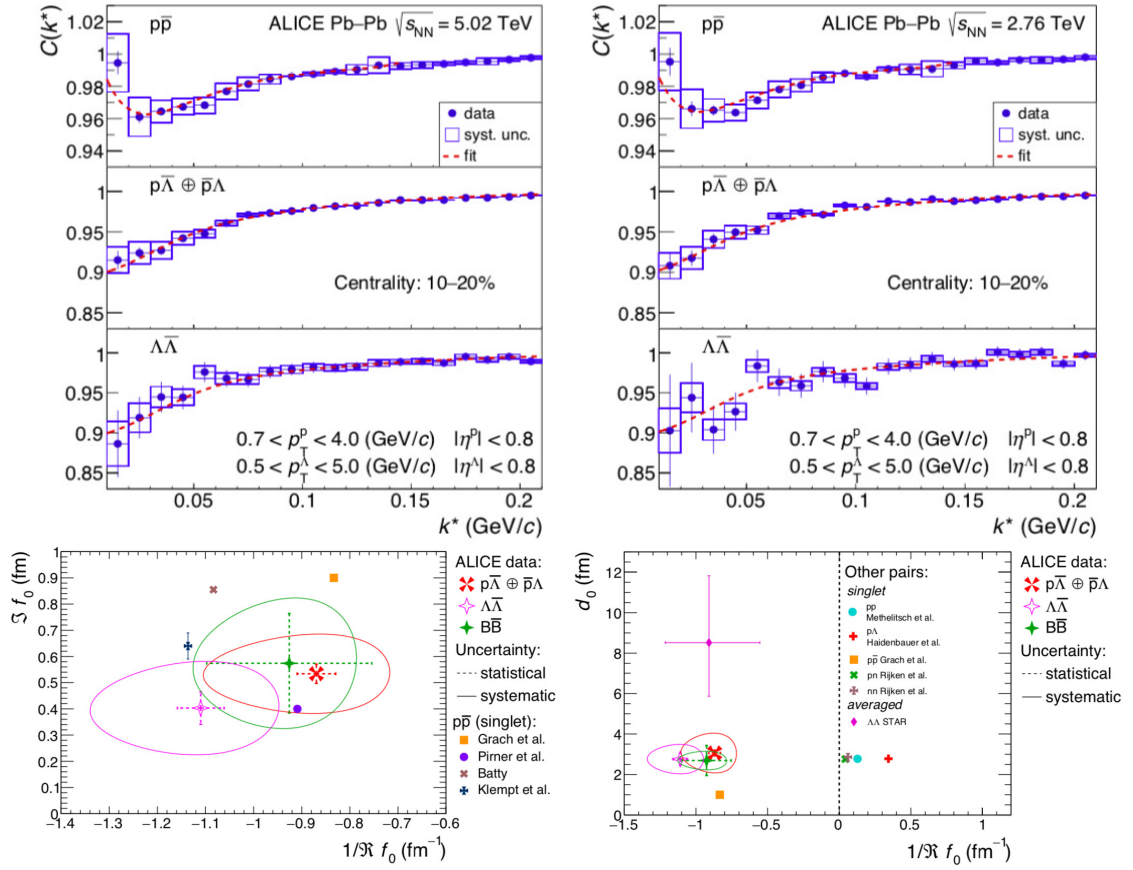
Figure 3.16: Baryon-antibaryon measurements performed by the ALICE collaboration in PbPb collisions. Top panel: $C(k^*)$ as a function of k^* for different pairs and energies. Bottom panel: scattering parameters ($\Re f_0$, $\Im f_0$ and d_0) extracted using the LL model. More information in the text. Extracted from [212].

Chapter 4

The CMS Experiment

Along the human history, the need for understanding what we are made of and the interactions that govern nature, led to the construction of experiments with which the study of the elementary structure of matter became possible. The first scattering experiment performed by E. Rutherford, colliding α particles against a gold foil, unveiled the existence of the atomic nucleus [18] and marked the start of that era.

Nowadays, one of the main tools created to investigate the structure of matter are the particle colliders. With the advancement of technology, several particle accelerators were built in order to understand different physical processes. In addition, accelerators are always on the frontier between science and technology, being directly or indirectly responsible for advances on both fields. Therefore, they are also considered to be an essential part in other areas of research such as medicine, computer science, biology and others.

This chapter describes an overview of the experimental setup used to collect the proton-lead data used in this thesis. Starting with a description of the LHC particle accelerator, followed by the description of the CMS detector.

4.1   Large Hadron Collider

The Large Hadron Collider (LHC) [260, 261] is the state of the art in particle accelerators, being the largest and most powerful collider experiment ever built. The LHC is a circular accelerator with 27 km of circumference installed in a tunnel 50 to 175 meters underground, (where the Large Electron-Positron Collider - LEP was installed before) located, at CERN, by the Swiss-French border. It was originally designed to collide protons at a centre-of-mass energy of 14 TeV with the

instantaneous luminosity (defined at Sec. A.4 of Appendix A) peak[1] of 10^{34}cm^{2}s^{-1} with the capability of colliding also heavy ions (lead (Pb) and more recently xenon (Xe)) in different configurations, which includes also proton-lead collisions.

The LHC ring is composed of two parallel beam pipes in which the particles are accelerated in opposite directions at velocities close to the speed of light ($\sim 99.99999991\%$ of c) in a nearly perfect vacuum. This beam intersects at four points (where the collision occurs), where the main detectors are located. The particles are accelerated by eight radio frequency superconducting cavities (per beam). Superconducting dipole magnets (cooled at ~2 K and producing magnetic fields greater than 8 T) are installed in many points of the ring in order to bend the particle's trajectory. Also, superconducting quadrupoles and auxiliary superconducting magnets are used to focus the beams and beam corrections, respectively. The LHC project was approved in 1994 and the construction took place from 1998 to 2008, motivated by open questions in physics, specially the search for the Higgs boson (predicted by the Higgs mechanism, responsible by the mass generation), that was discovered by ATLAS and CMS at the LHC in 2012 [16, 17].

The LHC started its activities in September 2008 with the first bunches of protons accelerated in both directions. However, a technical incident in the magnets caused a 14 month shutdown, necessary to repair and recalibrate the systems. The LHC beam activity was resumed in November of 2009 with proton-proton collisions at $\sqrt{s}$ = 900 GeV, starting the first run period (Run 1) that lasted until 2013. After that, the LHC stopped its operations for two years for upgrades, a period called long shut-down 1 (LS1). In 2015, the LHC started the second period of collisions (Run 2) that was concluded at the end of 2018. The second long shut-down (LS2) happened from December of 2018 up to 2021. Nowadays the LHC is in a period called hardware commissioning and magnet training, which was extended because of the COVID-19 pandemic. The Run 3 is expected to start in April of 2022.

During the Run 1 period, LHC had delivered proton-proton (pp) collisions at a nucleon-nucleon center-of-mass energy (see definition at section A.1 of Appendix A) of $\sqrt{s}$ = 900 GeV, $\sqrt{s}$ = 2.36 TeV, $\sqrt{s}$ = 7 TeV and $\sqrt{s}$ = 8 TeV. In the heavy ion program, the LHC performed proton-lead (pPb) collisions at $\sqrt{s_{\mathrm{NN}}}$ = 5.02 TeV and lead-lead (PbPb) collisions at $\sqrt{s_{\mathrm{NN}}}$ = 2.76 TeV. At Run 2, pp collisions

---

[1]This luminosity corresponds to beams of 2808 bunches (groups of particles that are accelerated) with approximately 10^{11} protons in each bunch and is related with the higher luminosity general purpose detectors at proton-proton collisions (CMS and ATLAS). Other detectors (e.g. LHCb) and the lead collisions require lower luminosity because of the physics process involved.

at $\sqrt{s}$ = 13 TeV (twice the nominal luminosity) and $\sqrt{s}$ = 5.02 TeV, Xenon-Xenon (XeXe) at $\sqrt{s_{NN}}$ = 5.44 TeV, pPb at $\sqrt{s_{NN}}$ = 8.16 TeV, as well as PbPb collisions at $\sqrt{s_{NN}}$ = 5.02 TeV happened at the LHC.

4.1.1 CERN accelerator complex

Before colliding, protons and ions need to reach their nominal collision energy. In order to reach such high energies, a complex with several lower energy accelerators is used. The CERN accelerator complex is shown by Fig. 4.1.
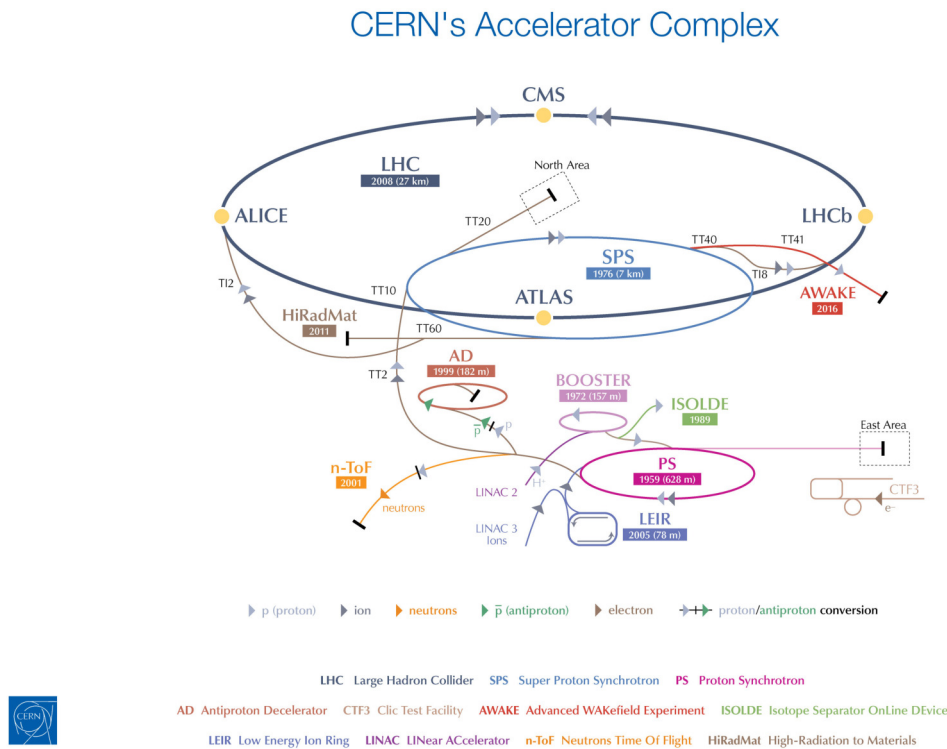
Figure 4.1: Schematic view of the CERN accelerator complex. Extracted from https://cds.cern.ch/record/1621583 [last access on 13/Mar/2021].

Proton beams are obtained by ionizing a hydrogen gas [262] then it is initially accelerated to an energy of 50 MeV by the Linear accelerator 2 (Linac-2)[2] [264]. Upon reaching this energy, these protons are transferred to the Proton Synchrotron Booster (PSB) [265], raising the energy to 1.4 GeV. After this, the protons are injected into Proton-Synchrotron (PS) [266] that increases the energy to 25 GeV and divides the beams in bunches of 25 ns of bunch spacing. Then, PS send these

---

[2]Linac-2 reached the end of its operational life and will be replaced by Linac-4 [263] for Run 3.

bunches to Super Proton Synchrotron (SPS) [267], which accelerated the beam to 450 GeV. At the end, SPS injects the proton beams into the LHC, where they will achieve the nominal energy and collide.

Heavy ions are collected from the electron cyclotron resonance[3] ion source [268]. After this process, the initial beams are not completely ionized, and in the case of lead, beams of Pb^{27+} are created. Once these beams are produced, they are accelerated to 4.2 MeV per nucleon at the Linac-3 [269] and then they are sent to the Low Energy Ion Ring (LEIR). During this process, the lead ions passes through a carbon foil (with thickness of 0.3 μm) which strips additional electrons, thus obtaining bunches of Pb^{54+} ions. At LEIR, the beam is accelerated to an energy of 72 MeV per nucleon and then transferred to PS, where they are accelerated to 5.9 GeV per nucleon with a bunch space of 75 or 100 ns. Next, this lead beams passes through another foil (now aluminium) where all the electrons are removed, getting a bunch of Pb^{84+} ions, which are then sent to SPS (the lead bunches not fully ionized are dumped). The SPS accelerates the lead ions to 177 GeV per nucleon and are then transferred to the LHC, which increases the energy before the collisions.

In the proton-lead collisions, studied in this thesis, bunches of protons are inserted in one direction and bunches of lead in the opposite direction, then the insertion is inverted during the Run, to check the consistency of the obtained data (since the physics should not depend on that).

4.1.2   LHC detectors

At the LHC, there are four main experiments with different proposals:

- A Large Ion Collider Experimet (ALICE) [270]: is a detector weighing ~10000 tons, located in St. Genis-Pouilly, France, with the following dimensions: length of 26 m, height of 16 m, width of 16 m. ALICE is specialized in measuring and analysing heavy ion collisions. This detector is specifically designed to study the quark-gluon plasma and its properties;

- A Toroidal LHC ApparatuS (ATLAS) [271]: is a detector weighing ~7000 tons, located in Meyrin, Switzerland (near the CERN site), with the following dimensions: length of 46 m, height of 25 m, width of 25 m (the largest one).

---

[3]The electron cyclotron resonance is a method of plasma heating. In this process, a plasma with very high density can be obtained by the usage of microwave frequencies, producing multi-charged ions.

ATLAS is one of the two general-purpose experiments at the LHC, being optimized to detect collisions with higher luminosity and study different physical processes;

- Compact Muon Solenoid (CMS) [4]: is a detector weighing ∼14000 tons, located in Cessy, France, with the following dimensions: length of 21 m, height of 15 m, width of 15 m. CMS is also a multi purpose detector, similar to ATLAS, with the possibility to perform measurements from Higgs bosons to quark-gluon plasma properties. The CMS is described in more details at section 4.2;

- Large Hadron Collider beauty (LHCb) [272]: is a detector weighing ∼5600 tons, located in Ferney-Voltaire, France, with the following dimensions: length of 21 m, height of 10 m, width of 13 m. Different from the others, this is a single-arm forward spectrometer with planar detectors originally projected to study the physics of particles composed by *b* quarks and matter-antimatter asymmetry. Nowadays LHCb is used to perform analyses in different research areas, including heavy ions, with the possibility to operate as a fixed-target.

In addition to the four experiments mentioned above, the LHC also counts with 3 smaller detectors, which are: the TOTal, Elastic and diffractive cross-section Measurement (TOTEM) [273], a forward experiment used to measure the total pp cross-section and study of elastic scattering and diffractive processes; Large Hadron Collider forward (LHCf) [274], a small experiment that uses particles measured in the forward direction of collisions as a source to simulate high-energy cosmic rays; and the Monopole and Exotics Detector at the LHC (MOEDAL) [275], which is the most recent experiment at LHC, being approved in 2010, whose main motivation is to search for the conjectured magnetic monopole. TOTEM is installed close to the CMS interaction point, LHCf is installed near ATLAS and MOEDAL near LHCb.

4.1.3 Future of LHC and ion colliders

The plans of LHC until 2036 are summarized in the sketch presented in Figure 4.2. Run 3 will probably start in April, 2022, and should last until December, 2024. During this period, pp (along the year) and heavy ion (end of the year) collisions are programmed, and it is expected that LHC will achieve its top

nominal energy ($\sqrt{s}$ = 14 TeV) in pp collisions. In the heavy ion program, pPb and PbPb are expected and the possibility of using collisions with oxygen atoms to investigate intermediate-size systems[4] are under discussion. In December, 2024, another long shut-down is programmed (LS3). During LS3 it is expected that the LHC and the experiments will undertake a profound upgrade aiming at the so-called High-Luminosity LHC (HL-LHC). In this process, the luminosity should increase by a factor of 5 to 7.5, as compared to the nominal, and expected to work at top the energy (14 TeV). Run 4 should start in 2027 with the first HL-LHC collisions, and continue until 2030. Looking at Fig. 4.2, Run 4 is the last run including heavy ion collisions in its schedule, however, in long term, this change. After that, two more long shut-downs (LS4 and LS5) and at least another run (Run 5) are expected.
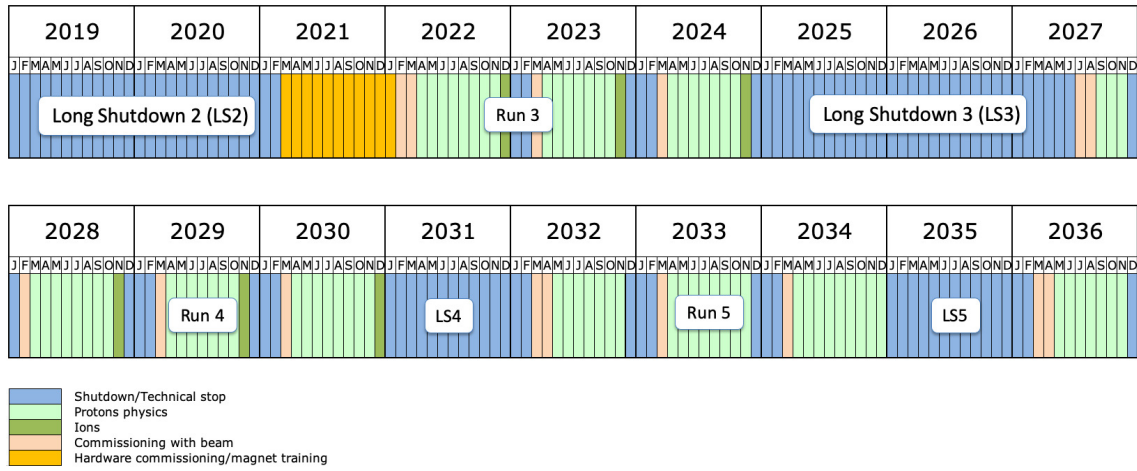
Figure 4.2: LHC long term schedule updated in September of 2020. Extracted from https://lhc-commissioning.web.cern.ch/schedule/LHC-long-term.htm [last access on 13/Mar/2021].

Besides the plans presented for the LHC, possible future applications has being studied:

- Extend the activities to the so-called High-Energy LHC (HE-LHC), which is an upgrade allowing to collide protons and ions with twice the current available center-of-mass energy [276];

- Use the LHC as a pre-accelerator for the Future Circular Collider (FCC), planned to be an accelerator with 100 km of circumference. The idea is to

---

[4]Since oxygen (O) atoms have only 16 nucleons, pO and OO collisions could be used as an intermediate-size system as compared to pp, pPb and XeXe systems.

start as an electron-positron collider [277] and then move to a hadron/ion collider [278, 279] (analogous to LEP and LHC). Is expected that the FCC should collide pp at $\sqrt{s}$ = 100 TeV, pPb at $\sqrt{s_{NN}}$ = 63 TeV, and PbPb at $\sqrt{s_{NN}}$ = 39 TeV.

- Upgrade the LHC colliding electrons against hadrons (deep inelastic scattering), called Large Hadron electron Collider (LHeC) [280];

The FCC is probably the successor of LHC [281, 282], however this was not confirmed yet. Besides the LHC, other experimental programs are ongoing or planned for the future of heavy ion physics. At the Relativistic Heavy Ion Collider (RHIC), the STAR and PHENIX (which will be called sPHENIX) collaborations are upgrading their detectors to perform the second beam energy scan (BESII), for covering the center-of-mass energy range from 3.5[5] to 19.6 GeV with higher statistics, in order to search for the possible QCD critical point. A new ion collider under construction is the Nuclotron-based Ion Collider fAcility (NICA) at Joint Institute for Nuclear Research (JINR) - Russia [283, 284]. The collider is designed to collide heavy and light ions at center-of-mass energies from 4 to 11 GeV, with the main focus on the study of the QGP at high baryon density, search for the critical point, and others. It is planned to start its activities in 2022. Another ion facility under construction that will be used to investigate the QCD phase diagram in the energy range from 10 to 40 GeV per nucleon is the Facility for Antiproton and Ion Research (FAIR) at GSI, Germany, with the possibility to study also electron-ion (eA) interactions by using ELectron-Ion Scattering in a Storage Ring (ELISe) [285]. The first collisions are planned for 2025. About eA interactions, another facility is planned to investigate such collisions, the successor of RHIC, called eRHIC or Electron-Ion Collider (EIC) [286] in the USA. At last, but not least, the Super proton-proton Collider (SPPC) [287], a collider proposed by the Chinese particle physics community, being similar to FCC, with 100 km of circumference and similar energy scale. This collider will be installed in the same tunnel as the Circular Electron Positron Collider (CEPC, planned to be concluded in 2030) [288] and the construction is expected to be concluded in 2042.

---

[5]The energy of 3.5 GeV is for fixed-target mode only, while the minimum for collider mode is 7.7 GeV.

4.2 Compact Muon Solenoid

The Compact Muon Solenoid (CMS) [4] is a general-purpose detector and one of the main experiments at the LHC. The CMS project was approved in 1995 and the construction of the surface building started in 1998. In 2000, when the LEP was decommissioned, the cavern (100 m underground) construction started, and was completed in 2004. After that, the main components of the detectors were installed in the cavern. In September 2008, the first beams circulated in the LHC and collide at CMS. However, due to problems in the magnet alloys, the operations were suspended and the first collisions only happened in 2009. Since then the CMS is operational, collecting data from pp and heavy ion collisions.

The central feature of the CMS apparatus, shown in Fig. 4.3, is a superconducting solenoid magnet of 6 m internal diameter, providing a magnetic field of 3.8 T. Inside the solenoid volume, there are four primary sub detectors including: a tracker detector system (divided in pixels and strips), used to measure the trajectory of the charged particles; a lead tungstate crystal electromagnetic calorimeter used to measure the energy of electrons, positrons and photons; a brass and plastic scintillator hadron calorimeter, responsible for the measurement of the energy deposited by the hadrons. Muons are measured in gas-ionization detectors embedded in the steel flux-return yoke outside the solenoid. The geometry of the solenoid is reflected in the design of the entire detector, given the cylindrical shape, there is a natural division of geometry into barrel and endcaps (disks closing the barrel region) that provides almost 4π coverage ($\sim 98\%$) of the solid angle around the interaction region.

The CMS uses a right-handed coordinate system with the origin positioned at the center of the detector, called the *interaction point* (IP), as shown in Fig. 4.4. In cartesian coordinates, the z-axis is defined along the beam pipe, the x-axis points to the center of the LHC ring and the y-axis is vertical and points upward. Adopting the cylindrical coordinate system, the radial distances (r) can be determined in the transverse (xy) plane as $r = \sqrt{x^2 + y^2}$, the azimuthal angle (ϕ) can be measured from the x-axis also in the xy plane, $\phi = \arctan(y/x)$, as shown in Fig. 4.4 (left) and the polar angle (θ) is measured from the $+z$ axis in the rz plane as shown in Fig. 4.4 (right). Different than r and ϕ, the polar (scattering) angle is not Lorentz invariant under longitudinal boosts, but this can be solved by replacing θ by another quantity called pseudorapidity (η), defined as $\eta = -\ln\left[\tan\left(\theta/2\right)\right]$, which, for massless particles or at the high-energy limit, coincides with the rapidity that is

Lorentz invariant over z-axis transformations. The particle transverse momentum (p_T) is defined as $p_T = \sqrt{p_x^2 + p_y^2} = p \sin\theta$, where p is the measured particle momentum.
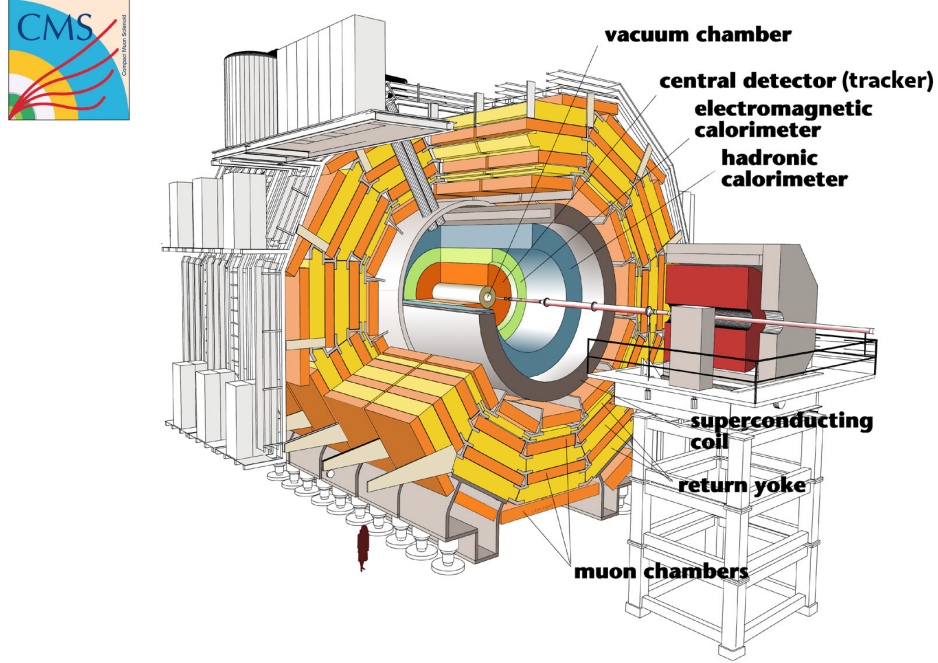
Figure 4.3: Cutaway view of the CMS showing the main components of the detector. Extracted and adapted from https://cds.cern.ch/record/39040 [last access on 13/Mar/2021].
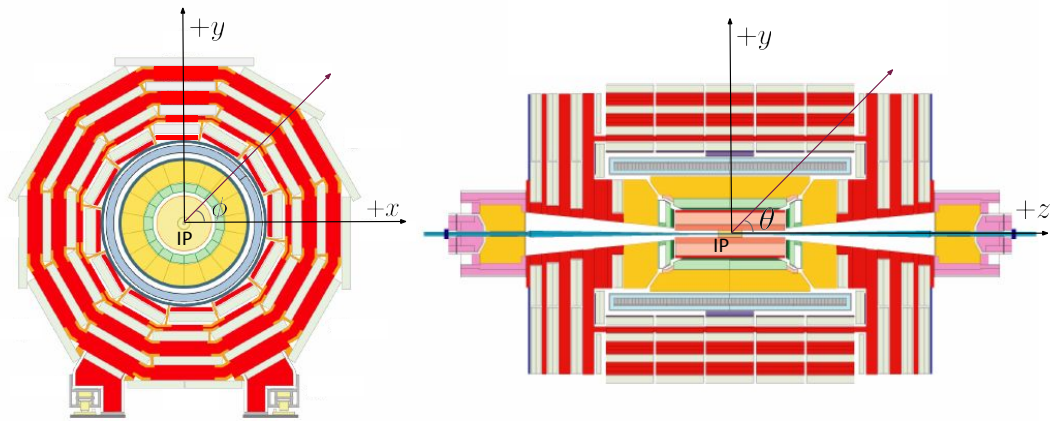

Figure 4.4: CMS coordinate system in the transverse plane (xy) on the left and in the zy plane on the right. Extracted and adapted from https://twiki.cern.ch/twiki/bin/view/CMSPublic/MuonDPGPublic180622 [last access on 13/Mar/2021].

Besides the main detectors, the CMS also has two very forward sub detectors specialized in studies of diffractive effects:

- Centauro and Strange Object Research (CASTOR) [289] is a calorimeter based on Cherenkov radiation detection, composed of quartz and tungsten plates connected to photomultipliers, installed at 14.38 m from the IP on the negative z coordinate. It was projected to cover a pseudorapidity range of $-6.6 < \eta < -5.2$ and are used in both pp and heavy ion collisions;

- Zero Degree Calorimeter (ZDC) [290] are two calorimenters composed of tungsten and quartz fibers, divided in two sections: an electromagnetic section and a hadronic section. This detector are installed in the opposite directions in order to measure the energy deposited by neutral particles in the region $|\eta| > 8.3$. The ZDC can be used to determine centrality (see Sec. A.3 of Appendix A) in heavy ion collisions by means of the nucleon spectators (which are not present in the overlap region).

Another forward detector constructed by CMS and TOTEM collaboration is the so-called CMS-TOTEM Precision Proton Spectrometer (CT-PPS). This sub detector consists of a silicon tracker system and a set of timing counters installed between 200 and 220 m from the IP on both sides of CMS, allowing to perform high precision studies with a proton tracking and timing in the very forward region. This can be used to investigate high energetic processes from QCD and electroweak, and possible search for beyond standard model physics. The first CT-PPS data was collected in 2016. More information can be found at Ref. [291].

In addition to all of these sub detectors, there are a number of subsystems, with functions of collecting, organizing and monitoring data. In parallel to the hardware part, the CMS SoftWare (`CMSSW`) is the framework responsible to perform both the *online* (during the data-taking process) and *offline* (reconstruction and subsequent data analysis) functions (see more at Sec. 4.2.7). The `CMSSW` is an open source framework available at Github [292] written in C++ and Python languages and contains the ROOT Data Analysis Framework (`ROOT`) [293] integrated, which provides essential tools for data format, reconstruction and analyses.

4.2.1 General view

A simple way to understand the CMS particle detection is using a transverse slice of the detector as represented by Fig. 4.5. The particles (represented by lines)

are emitted by the collision point in the center of the detector. Charged particles leave curved trajectories on the silicon tracker system because of the magnetic field effect; in the case of neutral particles this trajectory is not observed. The electrons (solid red line) and photons (dashed blue line) deposit all their energy in the electromagnetic calorimeter, the electrons are descrimited by the tracker system. Similarly, charged and neutral hadrons are stopped by the hadronic calorimeter, where their total energy is measured. Muons fly crossing the entire detector and their measurement is made by the trajectory given in both tracker and muon detectors. Neutrinos are not detected, however these particles are inferred from an imbalance in the transverse energy (called missing transverse energy).
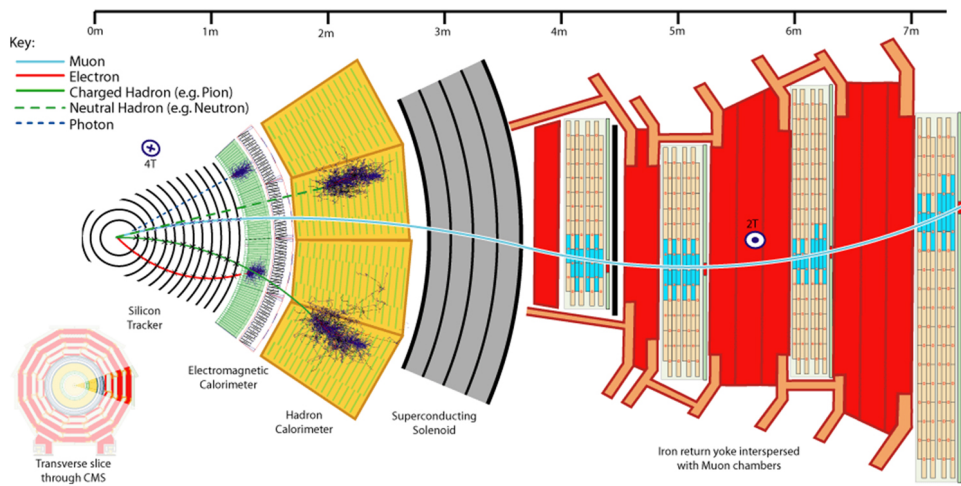
Figure 4.5: Sketch of transverse CMS slice including the particle detection scheme. Extracted from https://cds.cern.ch/record/2205172 [last access on 13/Mar/2021].

A detailed description of the CMS experiment, sub detectors and detection methods can be found in Ref. [4]. A brief overview of each of CMS components are shown below.

4.2.2 Tracker system

The CMS tracker system is a unique instrument, in both complexity and size, positioned closer to the interaction point, used to measure the signals given by the trajectory of the charged particles that pass through it. The trajectories of the particles are bent by the magnetic field, leaving signals in the material which are later connected by the reconstruction algorithms, producing a track. With the informations of the charge, magnetic field and the curvature radius it is possible to estimate the particle transverse momentum (more about the reconstruction is

shown at Sec. 4.2.9). This sub detector is made of silicon sensors that provide a very good spatial resolution, allowing a precise map of the trajectories. The silicon detectors present resistance to radiation, high granularity and works efficiently in the region of strong magnetic fields. Once the tracks are obtained, it is possible to identify the three dimensional vertex positions[6] for primary interactions (initial interaction between the protons or heavy ions) called *primary vertex* and those corresponding to the decays of unstable particles (e.g. K_S^0) produced by the primary interaction, called *secondary vertex*.

This tracker is composed of two different technologies, installed as shown in Fig. 4.6:

- The silicon pixel detector (in blue) is made of silicon pixels with high granularity, each pixel with $100 \, \mu$m $\times$ $150 \, \mu$m of area and $320 \, \mu$m of thickness. This detector is installed close to the beam pipe, totally covering the region of $|\eta| < 2.4$ and receiving a large dose of radiation. This sub detector is also divided in two regions: the barrel (BPix) which was initially composed by three cylindrical layers with ~ 55 cm in the longitudinal direction (z) with radii of 4.4, 7.3 and 10.2 cm from the beam; and the endcap (FPix), composed by two disks at each extremity of BPix with a diameter of 30 cm located at specific distances at the z-axis (± 34.5 and ± 46.5 cm). The spatial resolution for position measurements in this detector is in the order of $20 \, \mu$m in the longitudinal direction and $10 \, \mu$m in the transverse direction, this good resolution is important for the track reconstruction and for the primary and secondary vertex estimative. Figure 4.7 (top panel) shows an artistical view of the pixel tracker, with dimensions included, which was used to collect the 2016 proton-lead data, analyzed in this thesis. Due the large radiation received, the pixel detector was completely replaced during an upgrade made between 2016 and 2017 (end of the year shutdown), by including a four layer BPix detector (radii of 2.9, 6.8, 10.9 and 16.0 cm) and a FPix detector composed by three concentric disks installed on each side. A comparison between the pixel detector before and after the upgrade is show in Fig. 4.7 (bottom panel);

- The silicon strip tracker (in red) are made by silicon microstrips positioned just after the pixels, in the radial region between ~ 20 cm and ~ 116 cm, designed to measure the tracking quantities over a much larger volume.

---

[6]The vertex are the points in the detector where the particles are emitted.

This sub detector is divided in four main subsystems: the tracker inner barrel (TIB), tracker outer barrel (TOB), tracker endcaps (TEC) and tracker inner disks (TID). TIB, TID and TOB are located in the barrel and TEC is placed in the endcaps. The TIB consists of four concentric cylinders made by strips sensors with 320 μm of thickness and $80-120$ μm of spacing, installed surrounding BPix. It covers the longitudinal region of $|z| < 60$ cm, with the radii between 25 and 50 cm. The TOB extends the TIB range to $|z| < 110$ cm, by employing sensors with 500 μm-depth and pitches between $120-183$ μm. This subsystem is made of six cylindrical layers with a radius from 55 to 116 cm. The TEC is the only component installed at the endcaps and consists in 9 concentric disks in each side of the detector, covering the ranges $22-114$ cm in r and $124-282$ cm in $|z|$. The sensors used in the TEC have 320 and 500 μm of thickness and $96-184$ μm of spacing. The TID is installed in a small gap region between the TIB and the TEC ($20 < r < 50$ cm and $80 < |z| < 90$ cm); this subsystem is composed of three disks on each extremity, with sensor thick of 320 μm and strip pitch between $100-141$ μm. The sub detectors located close to the IP (where the particle flux is higher), i.e., the TIB and the TID, have a spatial resolution in the range of $23-25$ μm, while the TOB and the TEC have a resolution of the order of $35-53$ μm.

The detection principle is the same in both pixels and strips: when the charged particle traverses the sensitive medium of the detector, it ionizes the material creating electron-hole pairs. These pairs move in opposite directions due to an electric field applied to the silicon. Later, the electrons will be attracted by cathodes and the holes by anodes, generating an electric current that is measured by the electronic system.

In total, the tracker cylinder has an active area of ~ 198 m^2 and the temperature inside is controlled to be around -20 °C, to obtain an optimal performance of the silicon sensors and electronic components.
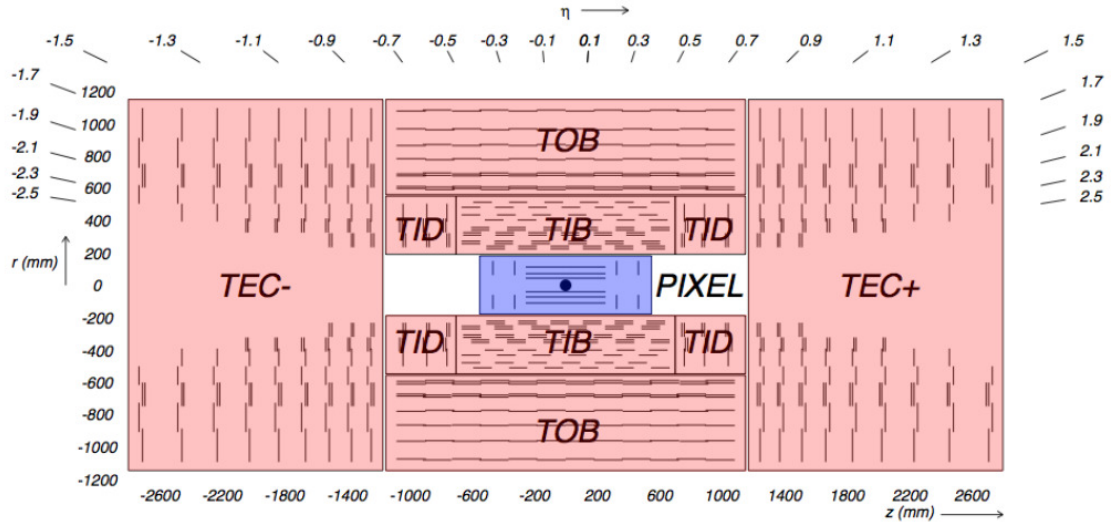
Figure 4.6: Geometrical view of CMS tracker systems in the *zr* plane with pixel (blue) and strip (red) components with lines representing the layers. The pseudo-rapidity range is also shown. Extracted from [4].
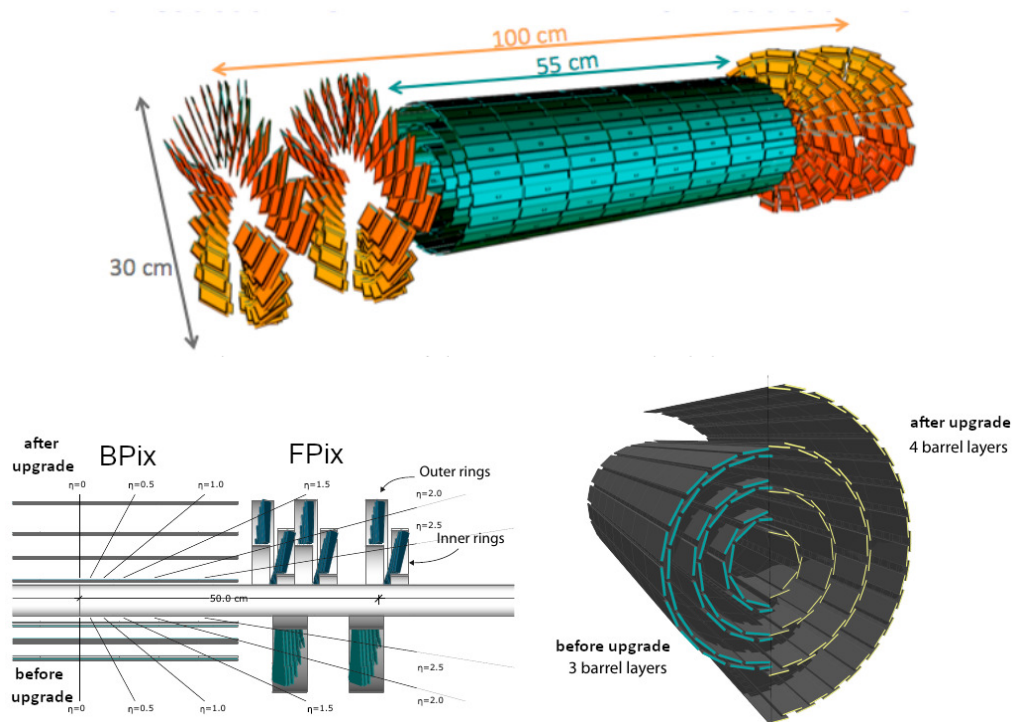
Figure 4.7: Top panel: artistic view of the silicon pixel tracker, before the upgrade, including the respective dimensions. Extracted from [294]. Bottom panel: comparison between the pixel detectors before and after the upgrade with pseudorapidity ranges (on the left) and barrel layers (on the right). Extracted and adapted from [295].

4.2.3   Electromagnetic calorimeter

The electromagnetic calorimeter (ECAL) is a hermetic and homogeneous calorimeter positioned just after the tracker and before the hadronic calorimeter, used to measure the energy of electrons, positrons and photons. This sub detector is mainly composed of crystals of lead-tungstate ($PbWO_4$), used to convert the energy deposited by incident particles into scintillation light (mostly via Bremsstrahlung effect of electrons/positrons and pair production of photons), which are transformed into electronic signals by photodetectors placed in the back of each crystal. The crystals are dense enough to stop a shower initiated by an electron/positron or a photon and the intensity of the signal measured is proportional to the energy of the incident particle.

The $PbWO_4$ material was chosen because of its high density (8.28 g/cm^3), short radiation length (0.89 cm) and small Molière radius (2.19 cm)[7], resulting in a fine granularity and a compact calorimeter. Also, this material is resistant to radiation, transparent to their own scintillation light, and it is also a fast scintillator with 80% of the photons emitted within 25 ns, allowing the separation between bunch crossings.

The geometry of ECAL is divided in three sections as shown in Fig. 4.8:

- The ECAL Barrel (EB) has a cylindrical shape and covers the $|\eta| < 1.479$ region. It is composed of 61200 crystals of $PbWO_4$ grouped into 36 units of 1700 crystals called supermodules;

- The ECAL Preshower (ES) has 20 cm of total thickness and covers the fiducial region of $1.653 < |\eta| < 2.6$. The ES is divided in two layers: i) two lead disks that initiate the electromagnetic showers from incoming particles; and ii) silicon sensors (137216 in total), similar to those used in the tracker, for measuring the energy deposition and the transverse shower profiles. The main goal of ES is to identify high energetic neutral pions that decays into pairs of photons, however it can be used for other purposes (e.g. position determination of electrons and photons with high granularity). The ES plays an important role during the Higgs boson measurement ($H \rightarrow \gamma\gamma$), since one of the main components of the background is $\pi^0 \rightarrow \gamma\gamma$ (due the π^0 short lifetime);

---

[7]The radiation length is related to the material stopping power. The Molière radius is the space region where the electromagnetic showers will be contained.

- The ECAL Endcaps (EE) is placed at the endcaps, just after the ES, increasing the pseudorapidity range to $1.479 < |\eta| < 3.0$. Each endcap is composed of two semicircles called *Dees* (in allusion to the format of letter D), the Dees being composed of 3662 crystals of $PbWO_4$.
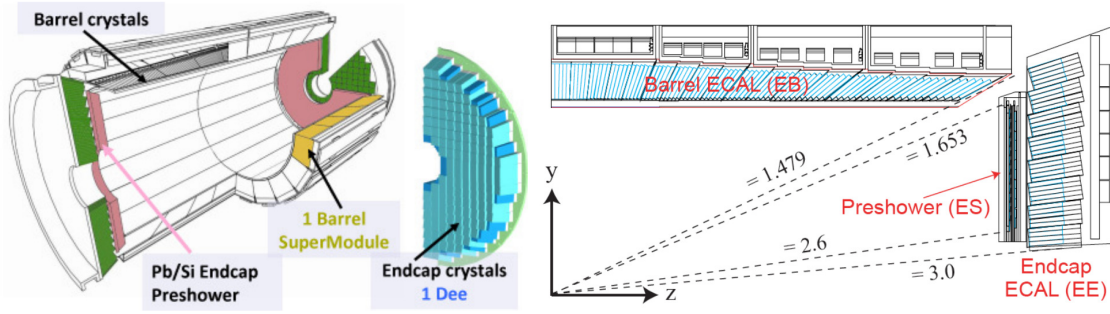
Figure 4.8: Representation of the ECAL sections, on the left. Extracted from [296]. Geometrical view of the ECAL in the *zy* plane with η ranges included, on the right. Extracted from [297].

The ECAL energy resolution[8] is parametrized by [4]

$$\left(\frac{\sigma_E}{E}\right)^2 = \left(\frac{2.8\%}{\sqrt{E}}\right)^2 + \left(\frac{12\%}{E}\right)^2 + (0.3\%)^2 , \qquad (4.1)$$

where E is the deposited energy. The first component is the stochastic term related to event-by-event fluctuations and photodetector gain; the second is the noise term that depends on electronics and digitalization noise, as well as on additional particles causing signals that overlap in time, called pileup (PU); and the last part is a constant term that depends on the detector intercalibration error, non-uniformities of the longitudinal light collection and leakage of energy from the back of the crystal. This constant term is also sensitive to the temperature stability of the crystals, which is optimized by maintaining the temperature at 18.00 ± 0.05 ºC. The values presented at Eq. 4.1 were obtained by a fit to data from an electron test beam for $0 < E < 250$ GeV.

4.2.4   Hadronic calorimeter

The hadronic calorimeter (HCAL) is the second detector in the CMS calorimetry system, located surrounding the ECAL. It is used to measure the energy deposited

---

[8]The energy resolution is defined as the detector ability to accurately determine the energy of the incoming radiation.

by hadrons (mainly pions and kaons). Hadrons interact strongly and are much more massive than electrons (the light stable hadron, $\pi^{\pm}$ is ~ 280 times heavier than the electron). Because of that, they are not stopped by ECAL, requiring another sub detector made by a material with high atomic number. At CMS, the HCAL is basically composed of layers interspersed with an absorbent (first and last layers) and scintillating media. Due to radiation, the choice of material and technology depend on the region in which the sub detectors are installed, as will be shown later.

The detection principle is similar to that of the ECAL: when a hadron interacts with matter (absorbent medium), it produces a shower of particles coming from complex processes (mostly by inelastic interactions and sequential decays). These showers pass through the layers of the detector interacting with the scintillators, producing light that is transformed in electronical signals by photodetectors. The total amount of light (summing over layers) in a given region receives the name of *towers*, which are the signals proportional to the energy of the incident hadron.

The HCAL geometry is divided in four regions, as shown by Fig. 4.9:

- The HCAL Barrel (HB) is positioned in the barrel, in the region between EB and the solenoid magnet and covers the pseudorapidity range $|\eta| < 1.3$. It is made of brass plates to absorb the particles, alternated with scintillator layers that generate signals associated with the energy deposition;

- The HCAL Endcaps (HE) is similar to HB in function and composition, but placed at the endcaps between the EE and the steel return yoke, covering a total region of $1.3 < |\eta| < 3.0$;

- The HCAL Forward (HF) is a detector close to the beam pipe, covering the $3.0 < |\eta| < 5.0$ region, composed mainly by quartz fiber that is resistant to high radiation, combined with a steel absorver. This sub detector uses Cherenkov radiation to measure the energy deposited by the particles and is important in CMS, since at least one energy tower at HF is required for the trigger system to select minimum bias events (more details at Sec. 5.1.1 of Chapter 5). In heavy ion analyses, this detector is also used to determine the centrality of the collisions (see Sec. A.3 of Appendix A);

- The HCAL Outer (HO) is located between the solenoid and the steel return yoke, covering the region of $|\eta| < 1.26$. This sub detector is made by scintillator material distributed in five rings, without the presence of absorver

elements. The HO position is strategically chosen to measure high energetic jets that cross HB.

In total the HCAL covers a region of $|\eta| < 5$, presenting an approximately energy resolution of [4, 298]:

$$\left(\frac{\sigma_E}{E}\right)^2 = \left(\frac{120\%}{\sqrt{E}}\right)^2 + (5\%)^2, \tag{4.2}$$

where the terms are the same as in Eq. 4.1. The noise term in the present case is small and can be neglected. The values presented at Eq. 4.2 were obtained by a fit to data from test beams with energies of $30 < E < 1000$ GeV.

The full CMS calorimetry system (ECAL + HCAL) is projected to stop all the particles, with the exception of neutrinos[9] and muons, the latest being measured by the muon system presented in Sec. 4.2.6. This system is an important component on the Level-1 trigger (see Sec. 4.2.7)
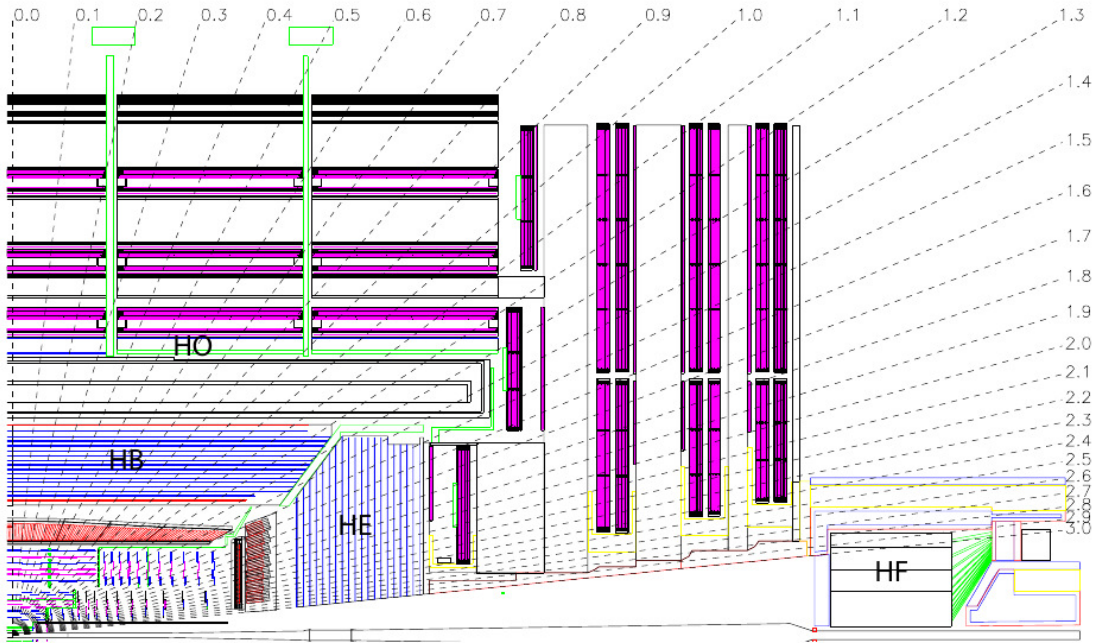

Figure 4.9: Schematic view of the CMS hadronic calorimeter components: HB, HE, HF and HO. The pseudorapidity ranges are shown by the dashed lines. Extracted from [4].

---

[9]The HCAL is the main detector used to estimate the missing transverse energy because of the high η coverage.

4.2.5 Superconducting Solenoid

The superconducting solenoid magnet is one of the main parts of the detector, it weighs 12000 tons with 6 meters of diameter and 12.5 meters of length, positioned between HB and HO, being large enough to encompass the tracker system and calorimeters. The solenoid, whose the artistical view is shown in Fig. 4.10 (left), is composed by a superconducting niobium titanium (NbTi) material cooled at ∼4 K. The magnet's characteristics were chosen in order to generate a magnetic field of 3.8 T at the center of CMS, as shown by the field map (and lines) in Fig. 4.10 (right). A field of this magnitude allows the estimation of the charge and momentum of high energetic particles. In the external area of the solenoid, a steel return yoke is installed, consisting of five three-layer dodecagonal wheels on the barrel and three disks at each extremity of the endcaps. This yoke is responsible for the magnetic field homogeneity (2 T in opposite directions) and also gives mechanical support to the muon system, which is described in the next section.
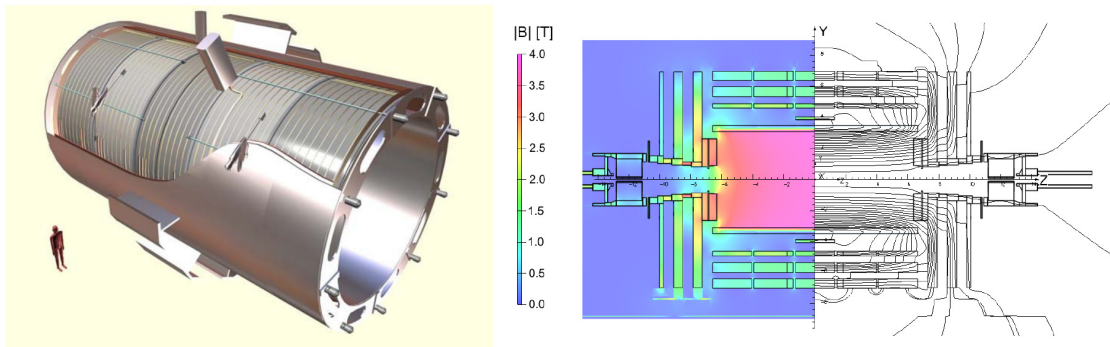
Figure 4.10: Left: artistical view of the CMS solenoid. Extracted from [4]. Right: map of the magnetic field in the CMS detector. Extracted from [299].

4.2.6 Muon system

Muons are important objects of analysis in almost all LHC experiments. Since electrons, positrons, photons and hadrons will be stopped by their respective calorimeters and the neutrinos are not detected, the CMS muon system is installed outside the solenoid with a detection area of $\sim$ 25000 m^2, located between the layers of the steel return yoke in the barrel and endcaps, as shown in Fig. 4.11. This sub detector is strategically positioned in this place because muons are massive leptons ($\sim$ 105.7 MeV) with a long mean lifetime ($\sim$ 2.2 μs) and do not interact strongly, passing directly through ECAL and HCAL, losing only a small amount of energy. This system was developed employing gas detectors for identifying

the vertices and trajectories of the muons with high spatial resolution and low response time, being possible to be used in momentum measurements with high accuracy and it is also used in the trigger system (see Sec. 4.2.7).

The CMS muon chambers are composed of three distinct gaseous technologies, installed in the detector as shown in Fig. 4.11:

- The Drift Tubes (DT) are placed in the barrel region ($|\eta| < 1.2$), providing high spatial resolution (approximately 100 μm) for position measurements. The DT consists of a 50 μm-diameter anode wire placed inside a rectangular tube connected to two cathode strips. The tubes are filled with a mixture of 85% argon (Ar) and 15% carbon dioxide (CO_2);

- The Cathode Strip Chambers (CSC) are installed in the endcaps ($0.9 < |\eta| < 2.4$), with a spatial resolution of 50 μm and specifically designed to work more efficiently in the region of non-uniform magnetic fields. This detector consists of a plane made by anode wires crossed by a plane of orthogonal cathode strips within a gas volume composed of 40% Ar, 50% CO_2 and 10% tetrafluorometano (CF_4);

- The Resistive Plate Chambers (RPC) are located in both barrel and endcaps ($|\eta| < 1.6$), helping the DT's and CSC's with trajectory reconstruction and by providing a high time resolution of the order of 5 ns. RPC's are formed by two parallel plates (anode and cathode), both made with high resistivity plastic material, separated by a gas volume composed of 95.2% Freon ($C_2H_2F_4$), 4.5% isobutene ($iC_2H_2F_4$) and 0.3% sulfur hexafluoride (SF_6).

The basic detection principle is the same in all these three technologies. When a muon or any charged particle passes through the gas volume, it ionizes the atoms releasing the electrons. Anodes and cathodes (positive ions are attracted by the anode and the electrons attracted by the cathode) with a specific potential difference generate an electric field used to accelerate the electrons from the gas ionization. These electrons also ionize the other atoms in the gas, because of the energy gain from the electromagnetic field, resulting in an avalanche effect that is recorded by the electronic system, allowing for the position and/or time measurement. The DT's measure the position based on the electron time of flight, CSC's based on the coordinates of the cathode plane and RPC's based on the timing related to the small distance between the plates.

The choice of detector technologies in CMS was made because of the large surface to be covered, the uniformity/non-uniformity of the magnetic field and the different radiation environments. There are in total 1400 muon chambers composed of 250 DT's, 540 CSC's and 610 RPC's. These sub detectors, working together with the tracker, guarantee the identification of muons and the measurement of their position and momentum with high reconstruction efficiency [4]. The reconstruction of muons are done in three different ways: i) tracker muons, which are trajectories measured at tracker system, containing at least one single signal in the muon system; ii) standalone muons, tracks reconstructed using informations coming from the muon system only; and iii) global muons, in which the muons are reconstructed by matching the track from the tracker with a track from standalone muons.
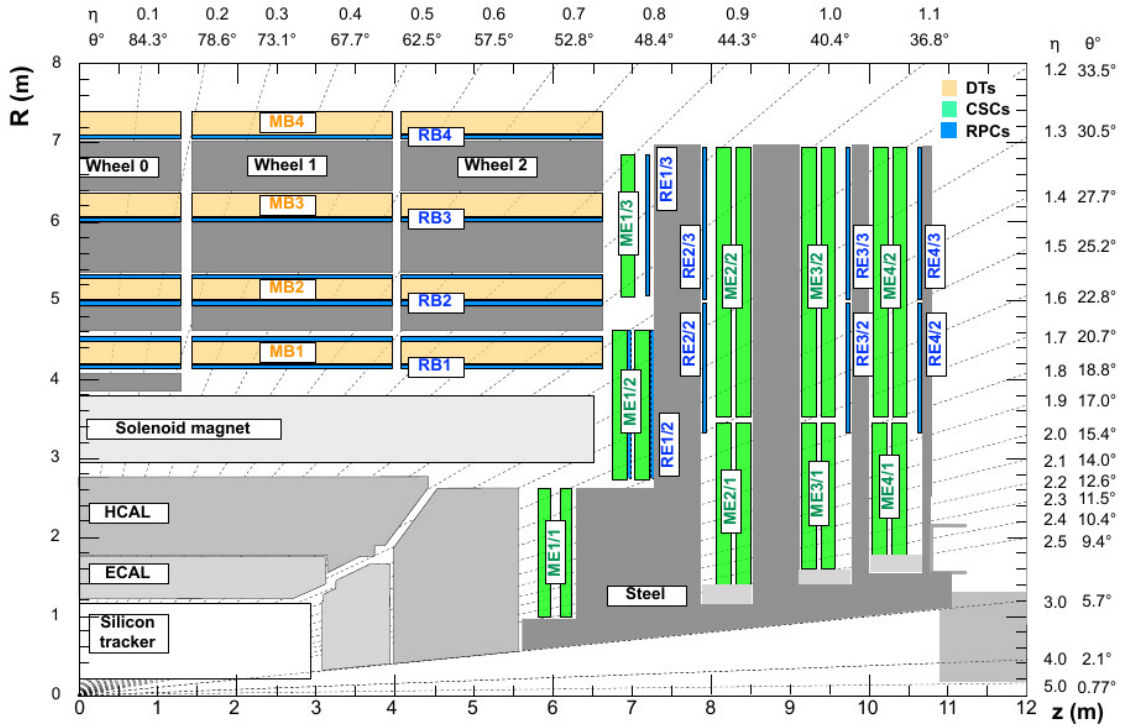

Figure 4.11: Layout of one quarter of the CMS detector (transversal *r* versus longitudinal *z*) showing the technologies used for the muon system: DT's in yellow, CSC's in green and RPC's in blue. The interaction point is positioned at (0,0) and the pseudorapidity dependence is also shown by the dashed lines. Extracted from [300].

4.2.7 Trigger system and data acquisition

The CMS experiment collects large amounts of data produced by the LHC collisions (crossing frequency of 40 MHz for pp collisions) and, unfortunately, it is not possible to process and/or save all the data produced (~ 1 Pb/s). In order to deal with that, a trigger system is necessary to select fast and precisely the events of interest, among all the produced ones (the events not selected are lost forever). The CMS trigger system was developed to be processed in two stages as shown in Fig. 4.12:

- The Level-1 Trigger (L1T) is a hardware-based trigger used to select or discard the events coming from the detector, a set of selections is implemented by the users in a so-called trigger menu and are applied directly to the firmware. L1T comes into action just after the collisions and takes a maximum of 3.2 μs[10] to process a single event (the logical decision takes less than 1 μs, and most of the time is used by the transit of signals from the electronic systems). The L1T uses the information of energy tower deposited in the calorimetry system (ECAL and HCAL) and signals from the muon system to find the objects (e, μ, jets,...) and take the decisions. L1T is designed to reduce the event rate from 40 MHz to less than 100 kHz;

- The High-Level trigger (HLT) is a software-based trigger that uses the output from L1T as an input and works as another event filtering. It is performed using sophisticated computer algorithms executed in a so-called processor farm composed by multicore computers. These algorithms are similar to those used for the physical analysis themselves, employing `CMSSW` (including the possibility of specific requirements in the objects, e.g., jets with energy higher than 20 GeV), although optimized to increase the running speed. The HLT is designed to process the pp events in $\sim$250 ms and heavy ion events in $\sim$350 ms (it depends on the number of tracks and/or centrality, since the track reconstruction is the most time consuming) and to reduce the event rate from 100 kHz to less than 100 Hz, after which only 100 MB/s is stored.

After the trigger selection (L1T+HLT), the online reconstruction is done and the events selected are stored in a format called RAW data, saved at the computational infrastructure used by CMS (shown in Sec. 4.2.8). The RAW data contain all

---

[10]The system allocates the data in a temporary area for a maximum of 3.2 μs, after this time interval the events are overwritten.

the information coming from the detector with a size of ~ 1 MB per event. To allow the physicists/users (also called analyzers) to perform analysis, an offline reconstruction is performed over the RAW files by using `CMSSW`, producing a new data format called RECO (~ 3 MB/ev), where the physical objects (tracks, jets, ...) are available. The final data format used by the CMS Heavy Ion Group is the analysis object data (AOD)[11], which is a subset of RECO (just removing some objects) and has the information needed for all the analysis with a reduced size (~ 0.5MB/ev).
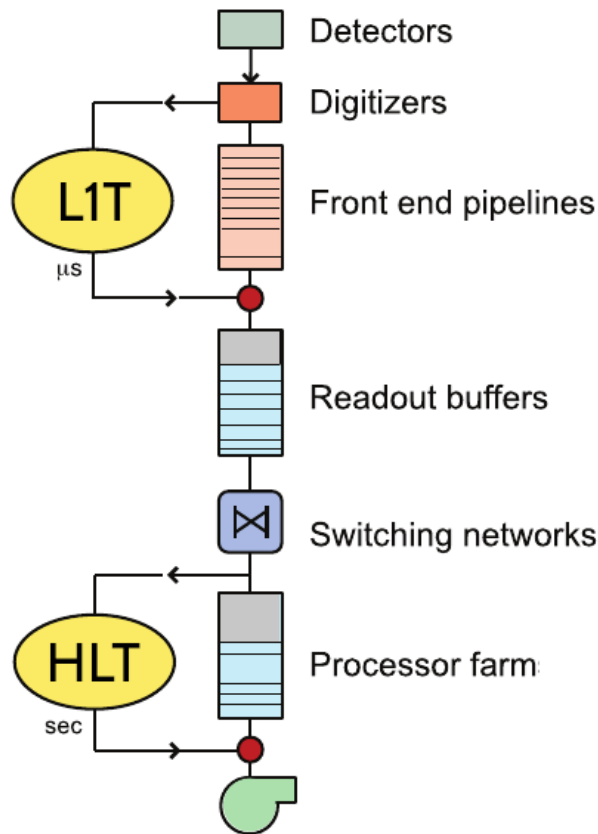
Figure 4.12: Schematical view of the CMS trigger system. Extracted from [301].

In the case of Monte Carlo (MC) simulations, the AOD samples are produced with the same reconstruction procedure (including the same detector conditions) as used for real data via `CMSSW`. First, the events are generated by a specific MC

---

[11]This format was also used in pp collisions during Run 1. However, another two reduced formats (obtained basically by removing some physical objects), MiniAOD and NanoAOD, have been used in pp collisions during Run 2, with the sizes of $30-50$ kB/event and $1-2$ kB/event respectively. The MiniAOD was implemented and adopted by the CMS Heavy Ion Group in 2020 and will be used for the next Run and also for the data collected during 2018 PbPb run (which are already produced).

model (e.g., `EPOS-LHC` [148]) containing the physics and/or background of interest. The objects produced at this step are called GEN (e.g., GEN jets). Later this events passes through the detector simulation using GEometry ANd Tracking 4 [302] (`GEANT4`)[12] . Once the detector conditions was simulated, the reconstruction is processed by `CMSSW` and the RAW and AOD samples for MC are created (containing exactly the same content as in data). The objects present in the AOD are called RECO (e.g., RECO tracks). Usually these MC's are generated by the CMS Heavy Ion Monte Carlo Group and accessed by the analyzers.

In this thesis, we performed the analysis by using data and MC from the AOD files. The data are collected by triggers for different multiplicities. In the MC related studies (only for minimum bias), we have used both GEN and RECO objects, in order to study backgrounds and detector effects. More details about data, MC and the analysis are presented at Chapter 5.

4.2.8 Computational infrastructure

The CMS counts with a large and hierarchical computational infrastructure that uses a grid of computers connected around the world (more than 170 computing centers in 42 countries sharing their resources) to process and save all the data collected by the experiment, Monte Carlo simulations and physics analyses. This structure is called Worldwide LHC Computing Grid (WLCG), and the cluster of computers are called *Tiers*, which are classified according to their storage capacity and computing power. There are four types of Tiers:

- Tier-0 (T0) is located at CERN, the first and only site at this level of the hierarchy. It is responsible by the acquisition of the RAW information coming from the detector, initial storage on magnetic tape, first offline reconstruction (called Prompt) of the data and distribution to Tier-1 centers with a transition tax of 10 Gb/s. Recently, the Tier-1 from Budapest is used as mirror of CERN T0 with a connection of 100 Gb/s between them;

- Tier-1 (T1) are large centers in CMS collaborating countries, usually in large national laboratories (e.g., Fermilab). There are 14 T1 sites around the globe, each of them stores a copy of a portion of the data received from the T0 (safety copy). The T1 provides substantial computing power for further

---

[12]`GEANT4` models the geometry and simulates the response of the detector. Basically, all the physical processes happening for each event are simulated as, for example, the passage of particles through the detector layers or the radiation-matter interaction.

reconstructions (re-reconstruction) of the RAW data, after improvements or changes in the reconstruction algorithms, and is used to distribute the reconstructed data to Tier-2 sites to perform the physics analyses. Also, each T1 provides storage for the MC simulations generated by Tier-2 sites;

- Tier-2 (T2) are medium-size centers associated with research groups (e.g. SPRACE). Nowadays there are in total 155 Tier-2 sites in the world used for physics analyses, calibration studies and MC production for the entire experiment;

- Tier-3 (T3) are small clusters of computers or even individual desktops located in universities vinculated to the CMS experiment, providing local access to the Grid. There is no formal engagement between WLCG and T3 resources.

The São Paulo Research and Analysis Center (SPRACE) [303] was deployed in 2003, to provide the necessary means for the participation of researchers from the State of São Paulo in high energy experiments. In the beginning, SPRACE started to process data and Monte Carlo generation from the DØ experiment at Fermilab, in the USA. Later, SPRACE joined the CMS collaboration at CERN, hosting a Tier-2 of WLCG structure, called BR-SP-SPRACE, linked to the Fermilab Tier-1. Nowadays, the SPRACE cluster has 128 servers with 1792 CPU cores and 2000 TB of storage. In this thesis, the SPRACE resources were extensively used for data analysis and Monte Carlo production.

4.2.9   Track and vertex reconstruction

As in this thesis we are interested in measuring strange particles (and later, their correlations), reconstructed by their decays into stable charged particles (tracks); the main sub detector used is the tracker system. After the reconstruction, these tracks are saved in AOD files as a collection called *generalTracks* containing tracks coming from pixels and strips. The calorimetry information is used only to validate the charged hadron measured by the tracker, which means that, if the track candidate reconstructed is real, it should leave a large amount of energy in both ECAL and HCAL. If this requirement is not met, these tracks are not added to this collection. In the context of this work, the important physical objects are the tracks, as well as the primary and secondary vertices. The track and primary

vertex reconstruction are presented briefly in this Sec., while the secondary vertex (or K_S^0, Λ and $\overline{\Lambda}$) reconstruction is presented in more detail at Sec. 5.2 of Chapter 5.

Track reconstruction

As charged particles fly through the tracker, electronic signals, called *hits*, are measured in different positions of the silicon sensors, which can be combined to reconstruct the particle trajectories (and momentum). In the case of an homogeneous magnetic field in a cylindrical detector, the particle trajectories are helix-shaped and can be used to relate the curvature radius in the transverse plane to the transverse momentum of the particle as

$$R \approx \frac{p_T}{0.003qB} \tag{4.3}$$

where R is the curvature radius of the helix (in cm), p_T is the transverse momentum (in GeV), q is the elementary electric charge (in units of e) and B is the magnetic field (3.8 T for CMS). Since p_T is estimated by Eq. 4.3, ϕ and η are measured and the mass of the particle is known[13], it is possible to obtain the particle four-vector.

The origin of the helix can be used to estimate the particle emission point/vertex, while the endpoint of the helix should match the deposit of energy (from the same particle) in the calorimetry system. Therefore, the process used to find tracks is similar to a very complex game of connecting-the-dots using the hits (from inner layer to outer layer of the tracker) left by the charged particles, as shown by the illustration in Fig. 4.13. The variables used to determine the trajectories at CMS are the helix curvature, distance in the transverse (d_{xy}) and longitudinal (d_z) directions (called distance of closest approach or impact parameters) compared to the center of the beam spot and the polar and azimuthal angles [305].

---

[13]CMS does not have a specific detector for particles identification yet, which means that the track measured cannot distinguish a pion or a kaon; because of that, most of the analyses refer to charged particles, considering the pion mass (because of their abundance). However, a new detector called Minimum Ionizing Particles Timing Detector (MTD) is under construction and will be installed in the barrel and endcaps for the HL-LHC, allowing to identify pions, kaons and protons based on their time of flight [304].
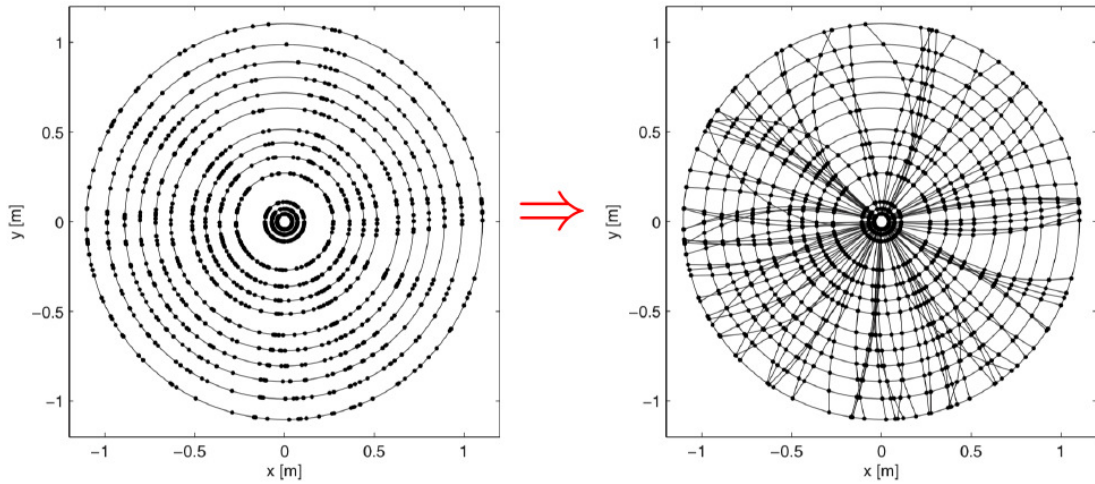
Figure 4.13: Illustrative representation of the hits left by the charged particles at the tracker detector in the transverse (*xy*) plane, before the reconstruction (left) and after the reconstruction (right). Extracted from http://journeys.ictp-saifr.org/wp-content/uploads/2019/07/ThiagoTomei_JourneysICTP2019_Lecture3-Reconstruction-1.pdf, [last access on 13/Mar/2021].

This "game" is a computational challenge and the most time-consuming process in the entire event reconstruction. In `CMSSW`, an specific software called *Combinatorial Track Finder* (CTF) [306] was developed to support the pattern recognition and track fitting in the same framework, based on an extension of the *Kalman Filter* algorithm (KF) [307, 308]. KF is mathematically equivalent to global least-square minimization, being an optimal solution for a discrete dynamic system that evolves linearly between the steps, making it a good option for hits left in the different layers of the tracker. The trajectories from given hits are reconstructed by several interactions of CTF in a process called *interactive tracking* (IT). The main idea of the IT is to search first for tracks that are effortless to identify (e.g. high-p_T tracks) and once this tracks are found, the corresponding hits are removed for the next interactions facilitating the identification of more complicated trajectories (e.g., low-p_T tracks).

The full track reconstruction can be summarized in five steps:

- *Hit reconstruction*: the hits left by the particles can be affected by detector inefficiencies like temperature variations, radiation damage or dead modules. To study such undesired effects, the observed hits are compared with simulations [309, 310] and, based on that, corrections are applied to those hits used in the track reconstruction;

- *Seed generation*: once the hits in the tracker are identified and corrected, the process of interactive tracking starts using them as input. First, an initial estimate of the trajectories, called *seed*, is generated by using 2 (pairs) or 3 (triplets) three-dimensional hits[14] usually obtained from the pixel detector (because of the high granularity and high resolution), however in cases of particle decay, seeds can be built by the strips to find tracks out of the pixel region. These seeds (or initial track candidates) provides the related initial track parameters and uncertainties;

- *Track finding*: for each seed supplied, the CTF extrapolates the trajectories interactively along the expected path given by the charged particle, searching for the adjacent hits from the next detector layer, in an interval where the width is related to the accuracy of the parameters. During this process a χ^2 compatibility check is performed between the hit and extrapolated trajectory. If a hit is founded in the expected position, this is assigned to the track candidate and the algorithm updates the respective trajectory parameters;

- *Track fitting*: once the hits are collected and a first estimative of the track parameters are given, the trajectory is fitted by using KF and smoother to obtain the final parameters at the interaction point exploiting the full track path [311]. First, the KF fit is initialized from the innermost hits on the track and corresponding covariance matrix scaled up by a large factor in order to limit the possible bias. After this process, the fit is then performed in an iterative way using the full list of hits (from the inside outwards), updating the trajectory estimate for each hit. This first filter/fit is followed by a second stage, called smoother, where another filter is initialized using the result of the first one and runs backward towards the beam line. Both KF and smoother uses a Runge-Kutta propagator [312] to extrapolate each trajectory from one hit to the next and to obtain the best possible estimate for the parameters;

- *Track selection*: in that last step, quality cuts are introduced to the track variables available to reduce the number of tracks produced by random combinations of hits. The selection is made by using a method called Boosted Decision Tree (BDT) [313] implemented using Toolkit for Multivariate Data

---

[14]After the pixel track upgrade it is possible to construct seeds with 4 hits as well.

Analysis (TMVA)[15] [314] at ROOT. In BDT a large set of variables are mapped into a one, called BDT variable, which returns values between -1 and 1. Applying cuts on BDT variables implies simultaneous selection over all the quantities used to produce this variable. As an artificial intelligence artefact, the BDT is first trained by using MC simulations to classify a track as good (high quality is close to 1) or bad (otherwise) and then is used in data. Based on BDT optimization, the tracks are then divided in three categories (flags): *loose*, *tight* and *highPurity*. Loose is the minimum requirement to keep a track in generalTracks collection, while tight and highPurity are increasingly stringent requirements optimized to obtain the maximum purity (number of real tracks) reducing the background (number of fake tracks) as much as possible. Trajectories that are not selected by any of these flags are discarded. In general, highPurity is adopted in most of the analyses and event selections, but the others flags can be used depending on the analysis goal. For example, in strange particle reconstruction the track loose selection is used to increase the statistics.

After all the above steps, additional selections based on kinematics (usually p_T and η), both transverse (d_{xy}/σ_{xy}) and longitudinal (d_z/σ_z) impact parameter significance and transverse momentum resolution (σ_{p_T}/p_T) are applied to select the offline reconstructed events with higher efficiency and lower number of fake tracks (in PbPb and XeXe collisions additional selections in track χ^2 and number of hits are used). The efficiency can be defined as the probability to obtain a track from a real charged particle, while the so-called fakes are the tracks reconstructed basically from random/wrong combinations of hits. The optimization of this selection is usually performed by the CMS Heavy Ion Tracking Group using Monte Carlo simulations wherever is possible to identify the track (RECO particle) by using the generated (GEN) particle. In that case, the efficiency is then defined as the distribution of RECO particles that matches with GEN particles in the same event, divided by the same distribution from GEN particles. The fake rate comes from the ratio between yield of RECO particles which does not match the GEN particles and the yield of all RECO particles. The selection applied in proton-lead collisions are shown at Sec. 5.1.3 of Chapter 5, together with efficiency and fake rate distributions. At CMS, the track reconstruction shows an efficiency between 70 and 90% in pp and pPb events with a fake fraction of less than 2% (it depends

---

[15]TMVA provides an artificial intelligence (machine learning) environment with different regression techniques focused in high-energy physics.

on p_T and η). In PbPb and XeXe, these quantities depend also on the centrality, since central events have a larger number of tracks, making reconstruction difficult and thus reducing the efficiency and increasing the fakes. For example, in 2018 PbPb collisions, the reconstruction had an efficiency between 50 and 60% for more central events (0-5% centrality) and $\sim 70\%$ for peripheral events (70-80% centrality). At the end, the efficiency and fake rate are corrected as weights at analysis level. More details about the track reconstruction can be found in Refs. [306, 315, 311].

Primary vertex reconstruction

After the reconstruction, the track information can be used to construct the vertices. In experimental high-energy physics, a vertex can be defined as a common origin for two or more tracks, indicating the spatial position (and related uncertainty) of the physical process. The vertex coming from the prompt interactions between collided particles (hard scattering), where many tracks/particles are produced, are called primary vertex (PV). Only one PV per collision is expected, however, some events present more than one PV due to pileup effects. This can affect the measurements and need to be treated as shown at Sec. 5.1.3 of Chapter 5.

The process of primary vertex reconstruction is performed in three steps:

- *Selection of tracks*: to obtain the PV reconstruction, the first step is to find the tracks coming from the primary interaction. This is initially performed by applying selections on the transverse distance of closest approach over its uncertainty (d_{xy}/σ_{xy}), the quality of the tracking fit (χ^2), and the number of hits in the pixel (N_{pixels}) and strips (N_{strips}) in the tracker. In pPb collisions (and also in pp) the following selections are applied: $d_{xy}/\sigma_{xy} < 5$, $\chi^2 < 20$, $N_{pixels} \geq 2$ and $N_{strips} \geq 5$ [306];

- *Track clustering*: the selected tracks are grouped into several primary vertex candidates that originate from the same interaction point, based on the informations from z-coordinate at their distance of closest approach. The clustering is performed in pPb collisions by using a deterministic annealing (DA) algorithm [306, 316]. This algorithm works to minimize a global χ^2 between vertices and tracks, by modeling them as a system with many degrees of freedom and treating them with statistical mechanics;

- *Vertex fitting*: once the clusters of tracks are produced, a three dimensional vertex fit is performed by using an adaptive vertex fitter method [317] (similarly to DA) to compute the best estimate of vertex parameters. In this

case, the χ^2 is taken between the cluster's tracks and the 3D vertex position, and weights between 0 and 1 are associated with the tracks, reflecting the probability of belonging to the vertex. Tracks that are more than a few standard deviations from the position of the reconstructed vertex receive small weights, while tracks that are compatible with the vertex position have a weight close to 1. At the end, the x, y and z positions are obtained, as well as fit quantities like normalized χ^2 (χ^2 divided by number of degrees of freedom) and covariance matrix.

At CMS, the PV reconstruction has an efficiency very close to 100% for events with more than 2 tracks in all of the colliding systems. An example of efficiency as a function of the number of tracks is shown at Fig. 4.14 for pp collisions at 7 TeV for data (in black) and MC (in red) samples. The small difference between data and simulation is due to the presence of PU effects (with a mean value of 8) present in data. In heavy ion collisions (PbPb and XeXe) the PU probability it is almost neglegible ($< 1\%$) while in for pPb collisions is estimated as 10-25% and is corrected as shown on Sec. 5.1.3 of Chapter 5.
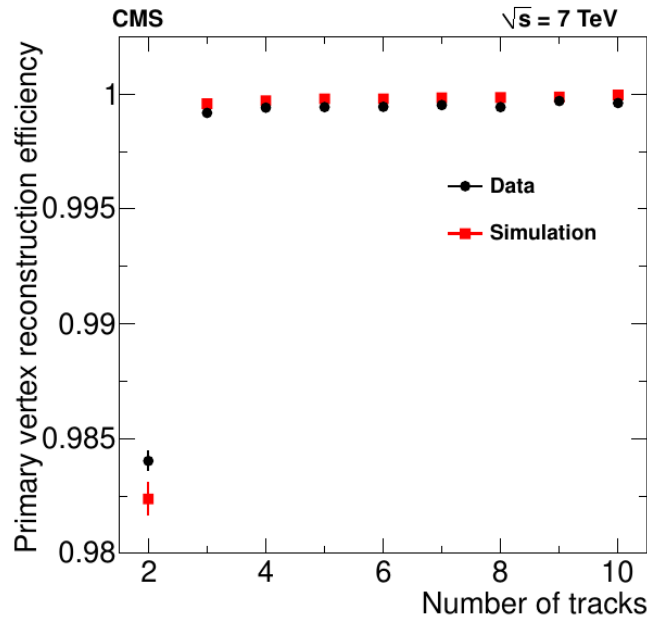

Figure 4.14: Primary vertex reconstruction efficiency as function of the number of tracks for pp collisions at $\sqrt{s} = 7$ TeV for data (in black) and for simulations (in red). Extracted from [306].

Chapter 5

Data Analysis

In this chapter, the data analysis procedure used in this thesis is discussed in detail. We start with the datasets, triggers, Monte Carlo simulation as well as event and track selections in proton-lead collisison, followed by the description of the strange particles (K_S^0, Λ and $\overline{\Lambda}$) reconstruction. The experimental method to measure the femtoscopic correlations is presented, including studies of strange particles purity corrections, non-femtoscopic effects, strange particles from heavy hadron decay (non-prompt) and fitting. At the end of this chapter, the summary of systematic uncertainties are presented.

5.1 Datasets, simulations and event selection

The analysis of femtoscopic correlations using K_S^0, Λ and $\overline{\Lambda}$ in proton-lead collisions at $\sqrt{s_{\mathrm{NN}}} = 8.16$ TeV is performed using data recorded by the CMS experiment in 2016, during the heavy-ion run (November/December) at CERN. The run was divided in two different beam configurations: p-going (proton in $+z$ direction) and Pb-going (lead in $+z$ direction), corresponding to a joint integrated luminosity of $L_{\mathrm{int}} \approx 180$ nb^{-1} (≈ 9 billion events). The AOD files were obtained from the data collected for different multiplicity triggers using `CMSSW` version CMSSW_8_0_X.

5.1.1 Trigger selection

The CMS experiment uses a complex trigger system composed by the L1T and HLT stages to select the events of interest (see Sec. 4.2.7 of Chapter 4). We are interested in studying femtoscopy using different multiplicity regions. The events analyzed in this thesis were recorded by using minimum bias (MB) and high multiplicity (HM) triggers. In this thesis, the datasets collected using MB trigger and HM triggers will be called MB and HM data samples, respectively. In pPb, the MB sample corresponds to the offline charged particle multiplicity,

$N_{trk}^{offline}$, in the range [0,120), while four HM triggers are used to select events in the range [120,400). These triggers are briefly described below.

Minimum Bias

Defined as the trigger with minimum requirements to select events with at least one collision. At CMS experiment, this is performed by L1T that collects events in which one tower with energy of at least 1 GeV is deposited at the HF detector (on one or both sides). Later, those events are filtered by the HLT to reduce the dataset size and remove undesired events. This is done by including track selections based on the tracker barrel acceptance ($|\eta| < 2.4$) and a requirement of at least one track with $p_T > 0.4$ GeV in the pixel detector. In proton-lead data at 8.16 TeV, two approaches were used to estimate the MB trigger efficiency (L1T+HLT):

- *based on data*: the efficiency is defined as the ratio of the number of events that fire (are accepted) the MB trigger over the number of zero bias events[1]. The minimum bias trigger is 100% efficient for events with more than 9 tracks. The integrated MB trigger efficiency for events with at least one track is found to be around 97%.

- *based on simulations*: the efficiency from MC events is defined as the ratio between the number of events that fire the trigger and the number of generated (GEN) events. The MB trigger efficiency studied using `EPOS-LHC` and `HIJING` (see Sec. 5.1.2) is between 93.8% and 98.7%.

The resulting trigger and online event selection efficiency was found to be about 98%. The MB is the highest statistic sample that we have, corresponding to ≈ 7.8 billion ($\approx 87\%$) events, analyzed in this thesis, with high efficiency in a multiplicity range between 0 and 120. The other 13% correspond to high multiplicity triggers, that are described below.

High Multiplicity

Events with multiplicity above 120 were selected using dedicated triggers with different multiplicity thresholds: 120, 150, 185 and 250. The first two (120 and 150) thresholds were obtained by using the same L1T as for MB, but including two additional selections at the HLT step: MinSepZ$_{pixel}$ < 0.12 and MinSepZ$_{full}$ < 0.15. These selections MinSepZ$_{pixel}$ and MinSepZ$_{full}$ represent the minimum separation

---

[1]Zero bias is a special trigger that requires at least one bunch crossing at the detector point.

in *z* between the track and the vertex for tracks reconstructed using only the pixel detector and using full tracker, respectively. The other two thresholds (185 and 250) are implemented employing the so-called energy tower count (TC) trigger at the L1T level, which uses information from the barrels of ECAL and HCAL detectors, where events were selected if pass a criterium in the number of active towers. An active tower is defined as a trigger tower (ECAL+HCAL) with a transverse energy greater than 0.5 GeV. The requirements TC > 115 or 120 were used for multiplicity between 185 and 250 and TC > 145 or 150, for multiplicity above 250 and below 400 [2]. At the HLT level, exactly the same selections as in 120 and 150 thresholds were applied.

To measure the total HM triggers efficiency (L1T+HLT) the minimum bias trigger is used as reference. The efficiency is then computed using the following expression:

$$\text{HM Trigger Efficiency} = \frac{\text{Number of events firing desired trigger and MB trigger}}{\text{Number of events firing only MB trigger}}.$$

In general, the efficiency shows a plateau above 95% in each multiplicity range, which corresponds to the performance target for the HM triggers. The total number of events recorded for each HLT trigger can be found in Table 5.1.

Table 5.1: Total number of HM events recorded during 2016 Heavy Ion Run for each HLT trigger, together with the multiplicity range where each trigger is efficient (> 95%).

HLT Trigger	$N_{trk}^{offline}$ range	Number of Events
HLT_PAFullTracks_Multiplicity120	[120,150)	286.51 million
HLT_PAFullTracks_Multiplicity150	[150,185)	216.14 million
HLT_PAFullTracks_Multiplicity185*	[185,250)	795.7 million
HLT_PAFullTracks_Multiplicity250	[250,400]	64 million

Reweighting

During the data-taking period it is possible to predefine the trigger event rate to save bandwidth and consequently storage. The so-called *"prescale"* can be used to select exactly the desired number of events to be collected by each trigger. The application of different prescales in distinct HLT triggers can interfere with

---

[2]The reason for adopting two TC thresholds for the same multiplicity range is related to the observation of a considerable variation in the noise level of HCAL during data-taking.

the measurement if the analysis requires that the data from those triggers to be combined (as in some of our cases). The effect of prescale on our multiplicity distribution, for all the triggers in different colors can be seen in Fig. 5.1 (top left). The $N_{trk}^{offline}$ distribution is expected to be smooth but, because of the prescale effect, it is possible to observe jumps in the trigger threshold regions. Those jumps can bias the analysis returning a wrong $N_{trk}^{offline}$ mean value. Two methods were developed to correct such effect, by calculating weights using the data sample from the unprescaled (no prescale applied) trigger as reference, as follows,

- *From Bits (FB)*: using the information of the triggers fired

$$w_{FB} = \frac{\text{Number of events that fire only the unprescaled trigger}}{\text{Number of events that fire the unprescaled and the prescaled triggers}}.$$

- *From Lumi (FL)*: scale factor from luminosity[3]

$$w_{FL} = \frac{\text{luminosity collected by the unprescaled trigger}}{\text{luminosity collected by the prescaled trigger}}.$$

In the above definitions, w_{FB} and w_{FL} are weights calculated for each method and applied in all the histograms used in our analysis. In pPb collisions at 8.16 TeV, only the `HLT_PAFullTracks_Multiplicity250` is unprescaled and this sample is used as reference. The weights are shown in Table 5.2 for p-going and Pb-going samples, with similar values between FB and FL. Figure 5.1 (top right) shows the comparison of $N_{trk}^{offline}$ distributions after applying the weights for FB, FL, and the case without the reweighting. Figure 5.1 (bottom panel) shows that both methods, FB on the left and FL on the right, return smooth $N_{trk}^{offline}$ distributions. The mean value of the reweighted histogram is $\langle N_{trk}^{offline} \rangle \sim 49$ by using both FB or FL methods, while the non-reweighted mean is $\langle N_{trk}^{offline} \rangle \sim 58$, showing a possible bias. No difference on the mean $N_{trk}^{offline}$ values was observed if calculated for each trigger individually. In this thesis, we have used FB as default and FL for systematic studies. In cases where it is possible to bin in different triggers, the results without the reweighting also checked as systematic.

---

[3]Calculated using `brilcal` [318], that is a command-line tool that returns the luminosity collected by each trigger.
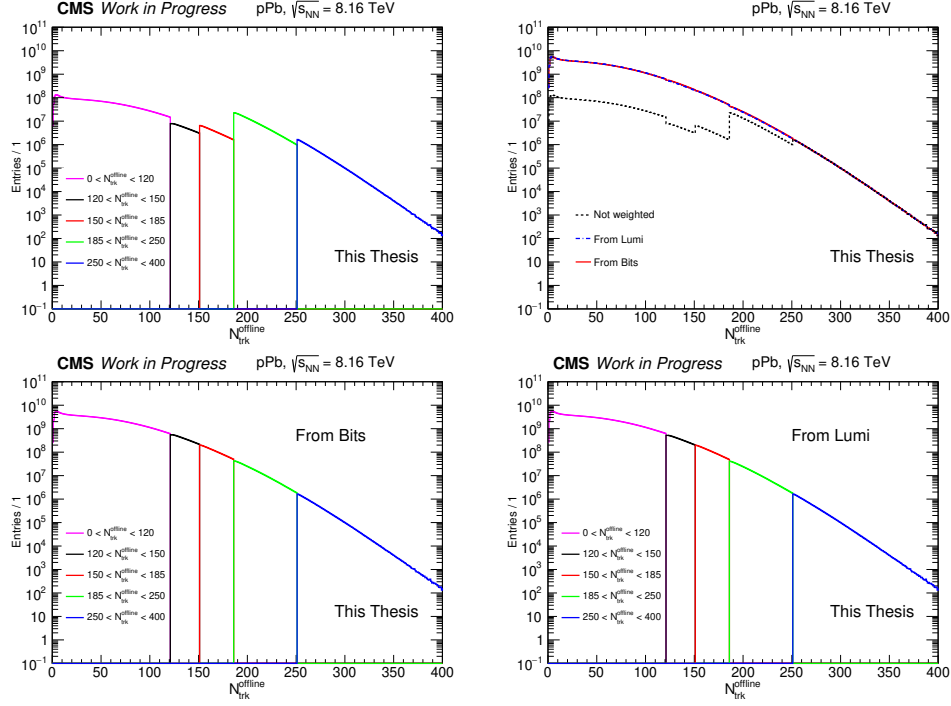
Figure 5.1: Offline multiplicity distributions in the range [0,400]. Top left: for all the triggers in different colors, without the reweighting procedure. Top right: Effect of the reweight using both weights, "From Lumi" (blue dashed-dotted line) and "From Bits" (red solid curve), compared to unweighted histogram (black dashed line). Bottom left: for all the triggers after applying w_{FB}. Bottom right: for all the triggers after applying w_{FL}.

Table 5.2: Weights used in the reweighting procedure for p-going and Pb-going in different multiplicity ranges/triggers. For the $N_{trk}^{offline}$ range [250,400), the weight is equal to unity because this sample is used as reference.

$N_{trk}^{offline}$ range	$w_{FB}^{\text{p-going}}$	$w_{FB}^{\text{Pb-going}}$	$w_{FL}^{\text{p-going}}$	$w_{FL}^{\text{Pb-going}}$
0 to 120	59.38	35.22	56.33	37.14
120 to 150	70.47	70.03	66.85	65.72
150 to 185	25.54	35.06	24.82	34.62
185 to 250	2.22	1.71	2.19	1.64
250 to 400	1.00	1.00	1.00	1.00

5.1.2 Monte Carlo simulations

In addition to the datasets collected by CMS during the 2016 run, MC simulation studies were performed, to investigate the non-femtoscopic background (see Sec. 5.3.2) and detector effects. The MC generators are computer programs based

on phenomenological and/or theoretical approaches with the goal of producing high energy collision events that can be directly compared to the experimental measurements and methods. For pPb collisions at $\sqrt{s_{\mathrm{NN}}} = 8.16$ TeV, there are samples available for reconstructed and generated levels, often produced by the CMS Heavy Ion MC Group[4], including the data-taking detector conditions for MB events only. The official MC samples used in this thesis are the EPOS-LHC [148] and HIJING [319] with ≈ 60 million events each, and AMPT [320] with ≈ 20 million events. Other two private GEN level samples were produced using PYTHIA8 (version 8.212) [147], considering pp collisions at 8.16 TeV, to investigate and better understand of the non-femtoscopic background, since PYTHIA8 allows studies at parton level. Those two samples were created with the same configuration as the official ones, but applying different selections on the transverse momentum of the scattered hard parton: i) $p_{\mathrm{T}}^{\mathrm{parton}} > 2$ GeV and ii) $p_{\mathrm{T}}^{\mathrm{parton}} > 20$ GeV. Each of these samples contains ≈ 60 million events[5]. A short description of the MC models used in this thesis are presented below:

- *EPOS-LHC* [148]: the physics of EPOS-LHC is based on a two-type core-corona model divided as: i) the "core" uses a particular flow parametrization that represents the region of high energy density and small volume from a thermalized matter; and ii) at low energy density, the "corona" is described by parton scattering processes. Based on that, the model scales from pp collisions, whose processes are mostly corona, to heavy ion collisions, where a large core is expected, due flow from the hydrodynamical expansion, and pPb is in the transition between the two regimes. Later, the system hadronizes and, at some freeze-out temperature, it decouples. The EPOS-LHC is an event generator tuned to reproduce observables at LHC energies and can be used for all colliding systems (pp, pPb and PbPb), showing a good performance for reproducing cross sections and strange hadron yields (which is also reflected in our q_{inv} distribution).

- *HIJING* [319]: is based on QCD-inspired models with the assumption that hard or semihard parton scatterings with low transverse momentum are expected to dominate high energy heavy ion collisions. The HIJING event generator simulates multiple parton scattering by using a model where

---

[4]The MC samples produced by this group are called official, while the produced by analyzers are called private.

[5]In the official CMS PYTHIA8 samples, only datasets with less than one million of events were available, which is not enough for V^0 femtoscopic studies.

each additional interaction modifies the parton's kinematics, resulting in a large number of minijets (defined as jets with low transverse momentum) produced. Those minijets still have enough energy to be described by perturbative QCD (pQCD) methods. In addition, the jet suppression effects due to the medium formed in heavy ion collision is also taken into account. The `HIJING` code can also be used for different colliding systems and over a large energy range, in agreement with data for spectra of many particle species.

- *AMPT* [320]: this model starts with the minijet partons produced in `HIJING` as an initial condition. The scattering between those partons are than modeled using a parton cascade model (considering two-body interactions) and cross sections from pQCD. Later, these partons hadronize and the dynamics of the hadronic matter formed is described by a hadronic cascade, which includes interactions between the particles (hadrons) and additional reactions that are important at higher energies. The `AMPT` describes the data from SPS to LHC energies for particle yields and flow measurements.

- *PYTHIA* [147]: this model simulates all steps of a hadron-hadron collisions at high energies, from the interaction between the initial partons, hard scattering, to the hadronization of the produced partons, including the possibility of multipartonic interactions, as well as initial and final state radiations. This is one of the most used MC generators in high energy physics, showing a very good description of the data in a wide range of energies for different colliding systems (e^+e^-, $p\overline{p}$, ...), including pp collisions at LHC. In this thesis we have used `PYTHIA8`, version 8.212, considering pp collisions at $\sqrt{s} = 8.16$ TeV, since the application of `PYTHIA8` in heavy ion collisions is still under discussion.

None of these MC generators has the femtoscopic effects implemented, neither quantum statistics, nor strong final-state interactions. However they still can be employed to study the track reconstruction performance, event selection efficiency, strange particle reconstruction, influence of jets, non-femtoscopic background effects, cross-checks, and other potential detector effects.

5.1.3 Event reconstruction and selection

After the trigger selection, several background sources not coming from hadronic collisions, such as beam-gas collisions and beam scraping events, remain in our

data. Furthermore, the datasets also may contain electromagnetic interactions from ultra-peripheral collisions (UPC). To extract a sample with pure hadronic collisions for the analysis, an offline selection criterion was studied and event filters were determinated by the CMS Heavy Ion Global Observables Group. Those selections are identical for all the analyses in a determinated system (pp, pPb, ...) with certain energy. In pPb collisions at $\sqrt{s_{\mathrm{NN}}} = 8.16$ TeV, the following event filters were applied [321]:

- *Beam-scraping filter*: used to avoid the "Previously Known As Monsters" (PKAM) background events, which are characterized by large multiplicities observed in the tracker without any sign of a common origin of the tracks within the CMS detector. To remove these large multiplicity events, this filter was developed for pp and later adapted for pPb analyses, being resposible to remove events where the number of reconstructed tracks is larger than a certain threshold but the fraction of good quality tracks is low. The requirement of this filter are:

  1. the good quality on the tracks is the highPurity requirement.
  2. the minimum number of tracks required to check the quality of the event is 10.
  3. the minimum fraction of good quality tracks in the event is required to be larger than 25%.

- *Primary vertex (PV) filter*: a valid reconstructed vertex is required to be within absolute z vertex position, $|v_z|$, less than 15 cm and the number of tracks associated with this vertex has to be greater than 2. This filter is used to confirm that the event has a valid vertex and is sufficient to reject all backgrounds from non-colliding bunches.

- *Hadron forward (HF) coincidence filter*: this filter requires at least 1 tower on each side of the interaction point in the HF calorimeter with an energy deposit above 3 GeV. This requirement removes more than 99% of UPC events.

In total, these selections remove less than 2% of the events.

Rejection of pileup events

As mentioned at Sec. 4.2.9 of Chapter 4, some events can contain more than one interaction per bunch crossing and this process is called *pileup* (PU). For the pPb data samples at 8.16 TeV, the probabitily that such multiple interactions occur is around 10-25%, depending on the instantaneous luminosity. In this thesis, the pileup is a secondary effect, since all the tracks used to measure the observables are reconstructed with respect to one primary vertex. However, to make a precise measurement, the effect from PU is also evaluated and a proper filter was created by CMS Heavy Ion Tracking Group, being applied to all the events. This PU filter are not intended to remove events with two collisions, but to only reject the events that are too close to each other spatially.

To obtain a balance between attaining good statistics and the PU contamination, one needs to look at the spatial distribution of the vertices. That can be studied by using the correlation between the number of tracks associated with the second populated vertex (N_{trk}^{vtx}) and the z distance between the most populated vertex and other vertices (dz); that correlation gives us information to come up with reasonable combinations for the pileup filter. In pPb collisions, the N_{trk}^{vtx} vs dz selections are optimized by using datasets for specific events with pileup averaged over time of 0.004, 0.04, 0.1 and 0.25 and using special `EPOS-LHC` simulated samples with exactly 1, 2 and 3 PU vertices. The final selection rejects or accepts events using different dz cuts according to the observed N_{trk}^{vtx}, e.g., for $N_{trk}^{vtx} = 5$, events with $dz > 4$ cm are rejected. As N_{trk}^{vtx} increases, dz cut decreases, removing all the events with $dz > 0$ cm for $N_{trk}^{vtx} > 20$. The overall efficiency of this selection can be estimated by the MC simulations, and is around 99.6%.

The available PU filters, in pPb collisions, are than divided in three, defined as:

- *pileupFilter_pPb8TeV_Gplus*: uses N_{trk}^{vtx} vs dz selection to accept or reject events.

- *olvFilter_pPb8TeV_dz1p0*[6]: accept events with two vertices based on N_{trk}^{vtx} vs dz, but the selection is applied only for dz values larger than 1 cm.

- *pileupFilter_pPb8TeV_vtx1*: accept events with only 1 reconstructed vertex (do not use the N_{trk}^{vtx} vs dz selection).

---

[6]olvFilter stands for "overlapping vertex filter", which only filters those events with 2 or more vertices that are too close to each other.

Following the instructions from CMS Tracking Group, our analysis uses the olvFilter_pPb8TeV_dz1p0 as default and the other filters, together with the case without filter, are used as systematics. The application of these filters removes between 2% and 8% of the events, depending on the filter applied.

Multiplicity definition and track performance

The charged particle multiplicity in a single event is defined as the sum of all the charged particles in that event with a certain criterion. In CMS, this criterion is determinated by an offline selection (see Sec. 4.2.9 of Chapter 4). This is studied by comparing the reconstructed tracking quantities between MC and data to reduce the fraction of fake tracks as much as possible, keeping a good agreement between data and the MC fraction of real tracks. Those selections are defined by the CMS Heavy Ion Tracking Group, being used for all the analyses with multiplicity dependence, which may change according to the colliding system and energy.

In pPb collisions at $\sqrt{s_{\mathrm{NN}}}$ = 8.16 TeV, highPurity tracks [306] are used for investigating $N_{\mathrm{trk}}^{\mathrm{offline}}$ dependence. For further selections, a reconstructed track is considered as a primary-track candidate, if the absolute impact parameter significance in the transverse and z separation between the track and the primary vertex, $|d_{xy}/\sigma_{xy}|$ and $|d_z/\sigma_z|$, are both less than 3. In order to remove tracks with poor momentum resolution, the relative uncertainty of the momentum measurement, $\sigma_{p_{\mathrm{T}}}/p_{\mathrm{T}}$, is required to be less than 10%. Primary tracks that fall in the kinematic range of $|\eta| < 2.4$ and $p_{\mathrm{T}} > 0.4$ GeV are selected to ensure a reasonable tracking efficiency and low fake rate. These cuts are applied in a consistent way in all the analyzed samples; events that do not have tracks within these conditions are not used.

Once the track selections and multiplicity are defined it is possible to estimate the efficiency and fake rate using the official MC samples (defined at Sec. 4.2.9 of Chapter 4). Figure 5.2 shows the efficiency (upper panel) and the fake rate (lower panel) of the reconstructed tracks as functions of η (left) and p_{T} (right). All plots are made using MC minimum bias samples from EPOS-LHC (open red circles) and HIJING (open black squares) for pPb collisions at 8.16 TeV. The fake fraction is estimated to be less than 2%, while the efficiency is between 70 to 90%.

After applying the filters and the track selection, between 10 and 20% of the total number of events are removed (not used) in our analysis.
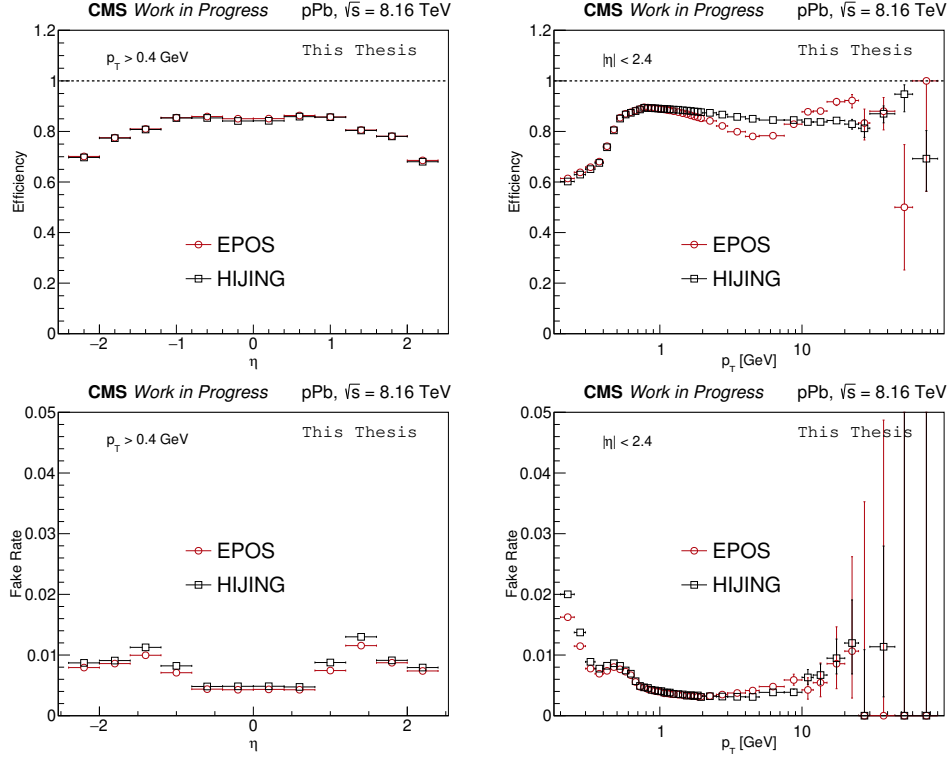
Figure 5.2: Proton-lead track efficiency (upper panel) and fake rate (lower panel) at $\sqrt{s_{\mathrm{NN}}}$ = 8.16 TeV with dependence on η (left), p_{T} (right) for: EPOS-LHC (open red circles) and HIJING (open black squares).

5.2 Reconstruction of strange particles

The reconstruction of $\mathrm{K}^0_{\mathrm{S}}$, Λ and $\overline{\Lambda}$ candidates (generally referred as V^0's) for pPb collisions used in this thesis is performed similarly to previous CMS analyses [322, 323]. In this method, variables of interest from the decay topology are studied and selections applied in order to optimize[7] the signal fraction, $s/(s+b)$, and signal significance, $s/\sqrt{s+b}$, where s and b are the signal and combinatorial background yields respectively. The V^0 decay topology is shown in Fig. 5.3. Since CMS has no specific detector to identify particles, the pair of tracks (usually called daughters) is assumed to be $\pi^+\pi^-$ in the $\mathrm{K}^0_{\mathrm{S}}$ reconstruction (branching ratio, BR, of $69.2 \pm 0.05\%$ [10]), while the assumption of being $\pi^- p$ ($\pi^+ \overline{p}$) is used in Λ ($\overline{\Lambda}$) reconstruction (BR: $63.9 \pm 0.5\%$ [10]). For $\Lambda/\overline{\Lambda}$ candidates, the lower-momentum track is assumed to be the pion. The mass of each track is assumed to depend on the invariant mass of the V^0 candidate.

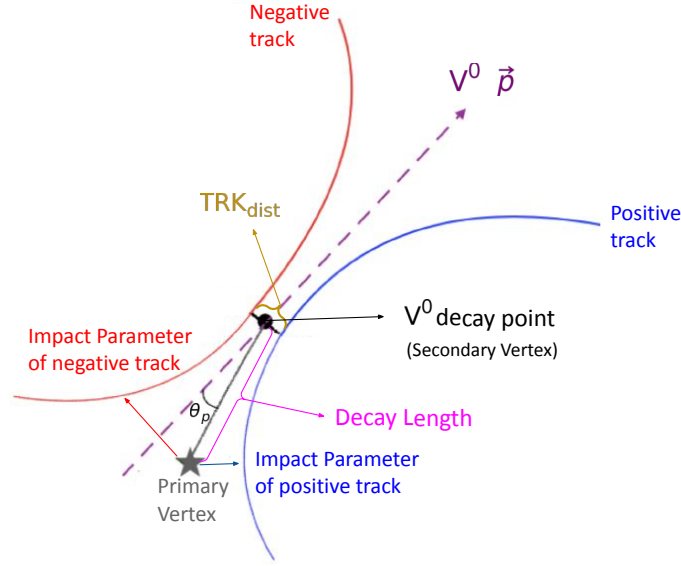[7]The optimization is first studied in MC simulations and later applied to the data.

Figure 5.3: Schematic view of the V^0 decay topology with the variables used to reconstruct the K^0_S, Λ and $\overline{\Lambda}$ candidates.

To increase statistics and the efficiency of tracks with low momentum and large impact parameters[8], characteristic of the V^0 decay products, the standard Loose selection of tracks [306] is used to reconstruct the V^0 candidates. Oppositely charged tracks with at least 4 hits in total and transverse (d_{xy}/σ_{xy}) and longitudinal (d_z/σ_z) impact parameter (see Fig. 5.3) significance greater than 1 are first selected to form a secondary vertex. The distance between the pair of tracks (TRK$_{\text{dist}}$, in yellow) is required to be less than 0.5 cm. The fitted vertex in x, y, z of each pair of tracks is required to have a χ^2 value normalized by the number of degrees of freedom less than 7. Those selections help to reduce the wrong combinations of tracks and, consequently, the combinatorial background. In addition, it is required for each track that at least one pixel layer has one valid hit. This requirement is defined in order to reduce the contamination from processes such as electron pairs from photon conversion and tracks from decay of long-lived resonances. For V^0's, the significance of the decay length (in pink), which is the three-dimensional distance between the primary and V^0 vertices divided by its uncertainty, is required to be greater than 5 to reduce background contributions. The angle θ_p between the V^0 momentum vector (in purple) and the vector connecting the primary and V^0 vertices is required to satisfy $\cos \theta_p > 0.999$. This reduces the effect of nuclear interactions, random combinations of tracks and $\Lambda/\overline{\Lambda}$ particles originating from

---

[8]The impact parameter can be understood as the distance between the extrapolated reconstructed track and the primary vertex.

weak decays of Ξ and Ω particles. To remove K_S^0 candidates misidentified as $\Lambda/\overline{\Lambda}$ particles and vice versa or V^0's produced by remnant electron pairs from photons conversion, a dedicated study is presented at Sec. 5.2.1.

In this work, tracks with $p_T > 0.2$ GeV and $|\eta| < 2.4$ are used to reconstruct V^0's. The K_S^0's are selected in the range $0.3 \leq p_T \leq 8.5$ GeV, Λ's and $\overline{\Lambda}$'s in the range $0.5 \leq p_T \leq 8.5$ GeV. The full pseudorapidity range is used ($|\eta| < 2.4$) for V^0's in order to increase the sample size. An additional, a requirement is applied to the χ^2 normalized by the number of degrees of freedom of tracks used to reconstruct the V^0's to avoid using the same track to reconstruct two V^0's (called duplicated tracks), an effect studied in detail on Sec. 5.2.2.

After all the selections presented, $\sim$22% of the events have at least one K_S^0, $\sim$3.5% one Λ, and $\sim$3.0% one $\overline{\Lambda}$. In the case of events with V^0 pairs: $\sim$5% have two K_S^0; $\sim$0.15% two Λ's; $\sim$0.12% two $\overline{\Lambda}$'s; $\sim$ 0.27% of Λ $\overline{\Lambda}$; $\sim$ 1.4% of K_S^0 Λ, and $\sim$ 1.3% with K_S^0 $\overline{\Lambda}$. These estimates include the contribution the contribution from combinatorial background. A total of $\sim 2.6 \times 10^9$ K_S^0's, $\sim 3.3 \times 10^8$ Λ's and $\sim 2.9 \times 10^8$ $\overline{\Lambda}$'s were analysed. The number of V^0's per event considering all MB and HM datasets, is shown at Fig. 5.4. As expected, it is possible to see a larger production of K_S^0 per event, with a maximum of twelve, when compared to Λ and $\overline{\Lambda}$, maximum of six.
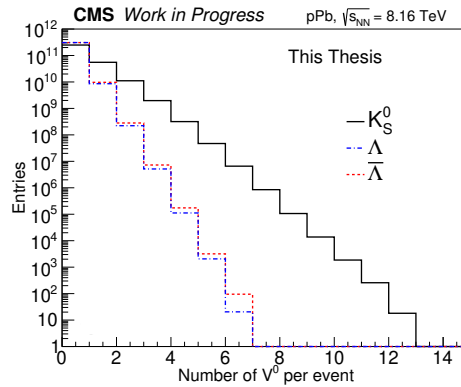
Figure 5.4: Number of V^0's per event for K_S^0 (black solid line), Λ (blue dashed-dotted line) and $\overline{\Lambda}$ (red dashed line) produced in pPb collisions using all MB and HM datasets. The first bin represent events with no V^0 candidates. More details in the text.

5.2.1 Removal of misidentified candidates

In the CMS experiment, the tracks cannot be identified as pions or protons and the mass of each track has to be assigned depending on the identity of V^0

candidates. Based on that, the K_S^0 candidates can be misidentified as Λ or $\overline{\Lambda}$ candidates and vice versa. In particular, there is high probability that a track assumed to be a proton in a Λ or $\overline{\Lambda}$ candidate is actually a pion (because of its abundance). To select clean samples of K_S^0, Λ and $\overline{\Lambda}$ the so-called Armenteros-Podolanski plot is investigated.

Armenteros-Podolanski (A-P) plot is a two dimensional plot, of the transverse momentum of the oppositely charged decay products with respect to the V^0 candidate, q_T, versus the longitudinal momentum asymmetry, $\alpha = (p_L^+ - p_L^-)/(p_L^+ + p_L^-)$, where $p_L^{\pm}$ is the longitudinal momentum with respect to the V^0 direction, of the positive $(+)$ and negative $(-)$ daughter particles. Examples of A-P plots from pPb data can be seeing in Fig. 5.5 for K_S^0 (upper panel) and $\Lambda/\overline{\Lambda}$ (bottom panel) candidates, for both minimum bias (left panel) and high multiplicity (right panel) datasets. The resulting distributions can be explained by the fact that pair of pions from K_S^0 decay have the same mass and, therefore, their momenta are distributed symmetrically, on average (top bands), while the proton (antiproton) in Λ $(\overline{\Lambda})$ decay takes, on average, a larger part of momentum and results in an asymmetric distribution (two lower bands). The misidentified candidates can be clearly observed and are shown by the arrows in those figures.
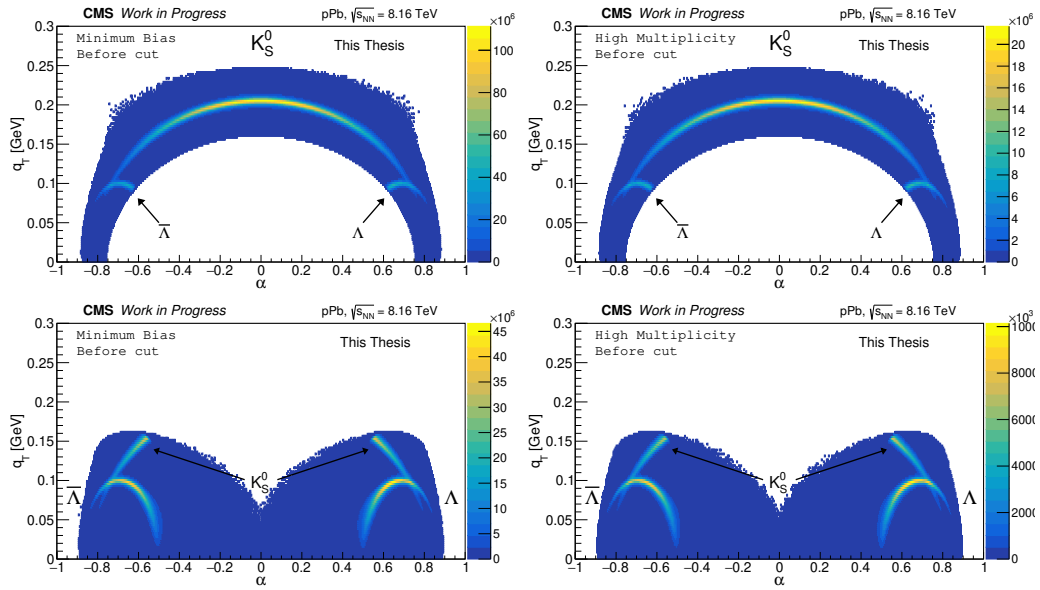

Figure 5.5: Armenteros-Podolanski (A-P) plots for K_S^0 (upper panel) and $\Lambda/\overline{\Lambda}$ (bottom panel) candidates in pPb collisions, for minimum bias (left panel) and high multiplicity (right panel) data samples before the cuts. The misidentified contamination is shown by the arrows.

In order to remove the misidentified K^0_S, the π-π hypothesis is applied to Λ and $\overline{\Lambda}$ candidates. This hypothesis assumes that both daughter tracks from a decay of Λ or $\overline{\Lambda}$ candidate are pions and recalculate the invariant mass of the decayed mother particle. A similar procedure is used to remove the misidentified Λ and $\overline{\Lambda}$ (p-π hypothesis), assuming that the K^0_S daughters are pion and proton. The recalculated invariant mass distribution for K^0_S (left), Λ and $\overline{\Lambda}$ (right) in pPb collisions are shown in Fig. 5.6 for both minimum bias (red open circles) and high multiplicity (black open squares) data samples. Clear peaks near K^0_S (Λ and $\overline{\Lambda}$) PDG mass value, 0.49763 (1.1156) GeV [10], can be seen for recalculated invariant mass of $\Lambda/\overline{\Lambda}$ (K^0_S) candidates. To remove those misidentified Λ and $\overline{\Lambda}$, recalculated mass of the K^0_S candidates are required to be 10 MeV (5 and 15 MeV for systematics) away from the $\Lambda/\overline{\Lambda}$ PDG mass value. To remove those misidentified K^0_S, recalculated mass of the Λ and $\overline{\Lambda}$ candidates are required to be 20 MeV (15 and 25 MeV for systematics) away from the K^0_S PDG mass value.

Figure 5.6: Re-calculated invariant mass for K^0_S (left) and $\Lambda/\overline{\Lambda}$ (right) in pPb collisions, for minimum bias (red open circles) and high multiplicity (black open squares) data samples. For K^0_S is assumed that the daughters are $p\pi$ and for $\Lambda/\overline{\Lambda}$ is assumed that the daughters are $\pi\pi$.

In addition, there is also a chance that both of the V^0 daughter tracks are in fact electrons coming from photon conversion and, in that case, the *e-e* hypothesis is applied, similarly to π-π and p-π hypotheses. A small peak can be seen in the *e-e* recalculated invariant mass distributions as shown by Fig. 5.7. To avoid such effect, a veto of *e-e* invariant mass less than 15 MeV (10 and 20 MeV as systematics) is also applied to remove misidentified photons.
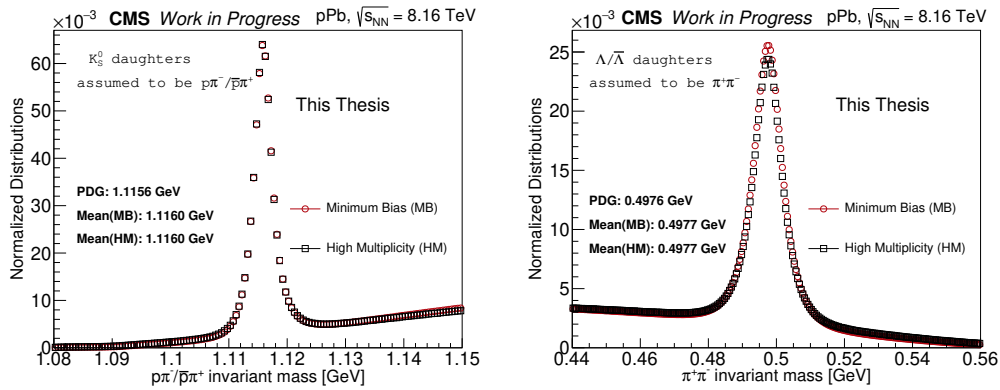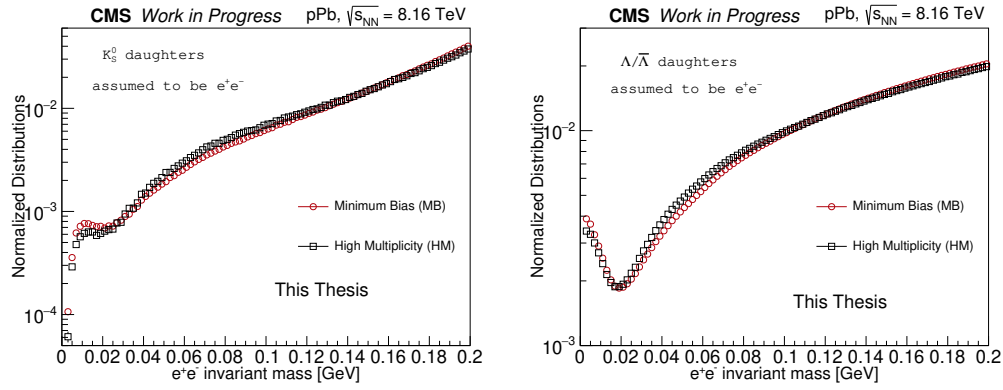
Figure 5.7: Re-calculated invariant mass for K_S^0 (left) and $\Lambda/\overline{\Lambda}$ (right) in pPb collisions, for minimum bias (red open circles) and high multiplicity (black open squares) data samples. In both cases is assumed that the daughters are electrons.

The effect of the cuts can be seen on A-P plots in Fig. 5.8 for K_S^0 (upper panel), Λ and $\overline{\Lambda}$ (bottom panel). Although a small fraction of the real candidates are removed, the misidentified band is completely removed by the cuts. And there are some candidates with very low q_T removed as misidentified photon conversion, which has small effect to our V^0 candidates.
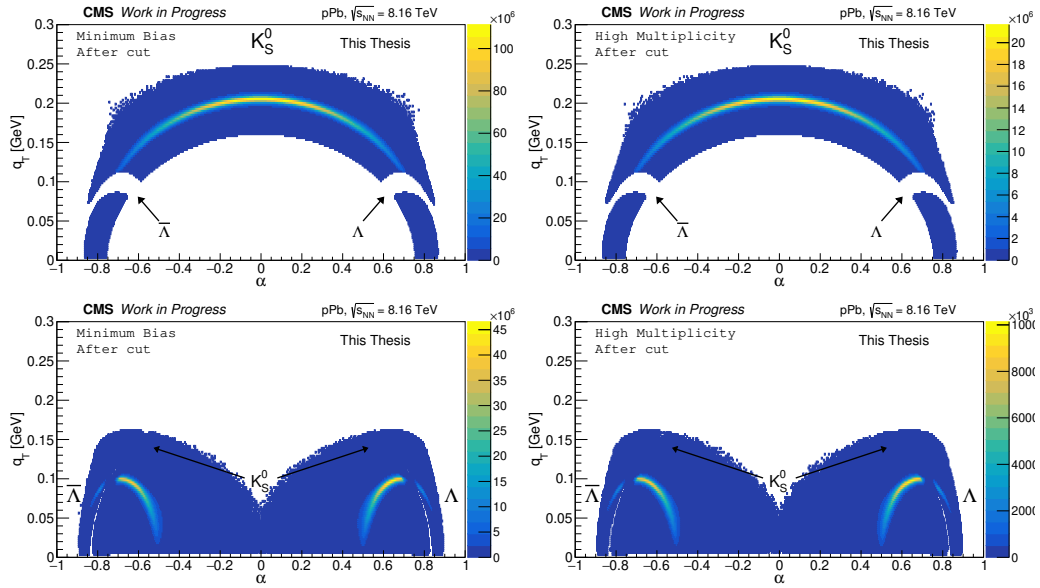

Figure 5.8: Armenteros-Podolanski (A-P) plot for K_S^0 (upper panel) and $\Lambda/\overline{\Lambda}$ (bottom panel) candidates in pPb collisions, for minimum bias (left panel) and high multiplicity (right panel) data samples after the cuts. The contamination is completely removed.

5.2.2 Duplicated tracks removal

A bump in the low-q_{inv} region was observed in correlations involving identical V^0's, which can be seen by the red solid lines in Fig. 5.9, for $K_S^0 K_S^0$ (top left) and $\Lambda\Lambda \oplus \overline{\Lambda}\overline{\Lambda}$ (bottom left). To investigate such effect, the q_{inv} distributions of GEN and RECO V^0's from official MC simulations were checked. For all the MC models (`EPOS-LHC`, `HIJING` and `AMPT`), the bump is present for RECO particles and is not seen in the case of GEN particles, what suggests a possible problem occured in V^0 reconstruction. Therefore, a good starting point is to study the tracks used to reconstruct those strange particles, which can be done by applying a matching procedure between V^0's from GEN (V_G^0) and RECO (V_R^0) levels. The matching consists to find the V_R^0 from the V_G^0, which is done by using their distance in phase-space, $\Delta R = \sqrt{(\eta_R - \eta_G)^2 + (\phi_R - \phi_G)^2} < 0.03$, and similar transverse momentum, $\Delta p_T^* = \left| (p_T^R - p_T^G)/p_T^G \right| < 0.03$ ($\Delta R, \Delta p_T^*$ less than 0.05 and 0.1 were also checked). Here, η, ϕ, and p_T are the pseudorapidity, azimuthal angle and transverse momentum for the GEN (sub-index G) and RECO (sub-index R) V^0's. Particles within these conditions are called matched (true), while the others are called unmatched (fake).
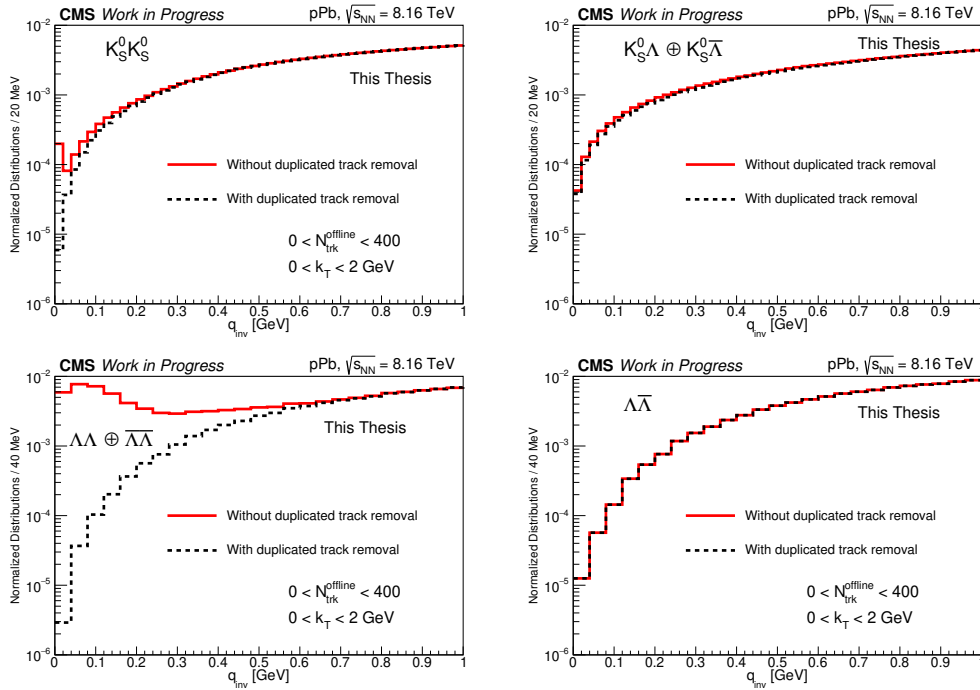

Figure 5.9: Normalized q_{inv} distributions with (black dashed line) and without (red solid line) the duplicated track removal method.

Using the information from matched and unmatched particles, it was possible to find that this issue is coming from the possibility that the two V^0's used in the correlation shares exactly the same daughter, called *duplicated track effect*. Such contamination appears because all positive tracks are combined with all negative ones during the V^0 reconstruction in order to increase statistics, making it possible to use more than one track from different mothers. In most cases, those V^0's reconstructed using duplicated tracks only contribute to increase the combinatorial background, but, because of the sensitivity of the femtoscopic correlations, it directly affects the region of interest (low-q_{inv}) and needs to be discarded. To remove the contamination, all V^0's are combined and the difference between the χ^2/ndf (from track fit)[9], $|\Delta\chi^2/\text{ndf}|$, used for the reconstruction of the daughters with the same and opposite charge were checked. If the V^0's shared the same daughter a $|\Delta\chi^2/\text{ndf}| = 0$ is expected for same-sign tracks, which was observed in both data and MC RECO. Based on this information, if these particles has exactly the same χ^2/ndf, both mothers are removed (not used in the correlations), to obtain a clean data sample. To be consistent, this selection was also studied and applied for $K_S^0\Lambda \oplus K_S^0\overline{\Lambda}$ and $\Lambda\overline{\Lambda}$ decay products.

The same-sign (SS) and opposite-sign (OS) daughters $|\Delta\chi^2/\text{ndf}|$ histograms for data and `EPOS-LHC` MC are shown in Figs. 5.10 and 5.11, respectively. The difference in magnitude happens because the matched-matched case also removes the combinatorial background (matched-unmatched and unmatched-unmatched contributions), which still remain in data after the duplicated track removal. An efficiency estimate for this selection was defined as the ratio between the q_{inv} distribution from matched V^0's with the duplicated removal and without the removal, resulting in more than 98% for all of the cases.

The effect of the duplicated tracks removal on q_{inv} can be seen in Fig. 5.9, comparing the cases without (red solid line) and with (black dashed line) employing the method for all the V^0 particle combinations. The spurious bump is then completely removed for the identical V^0's. For $K_S^0\Lambda \oplus K_S^0\overline{\Lambda}$ and $\Lambda\overline{\Lambda}$ the duplicated track effect is also present, however, because of the kinematics of the daughter particles involved, it does not affect significantly the low-q_{inv} region. To evaluate the systematic uncertainties for this selection, instead of removing both V^0's, the following conditions are used: i) remove one mother with the mass value far away from the V^0 PDG value; ii) remove one V^0 randomly; and iii) remove the particle with the worst χ^2/ndf quality fit.

---

[9]The χ^2/ndf was chosen because this quantity comes only from the reconstruction.

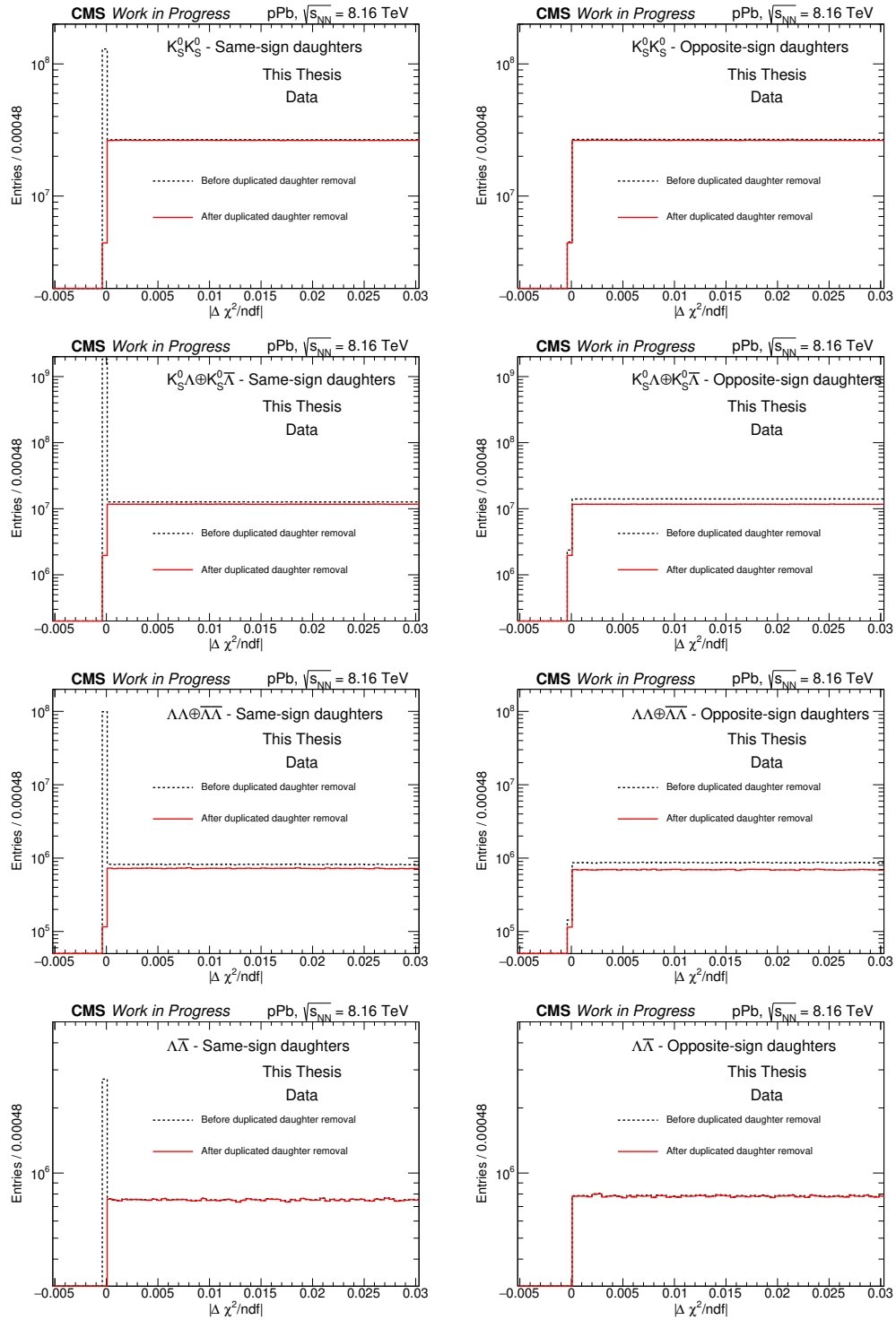Figure 5.10: $\left|\Delta\chi^2/\text{ndf}\right|$ distributions, for data, between V^0 same-sign (left panel) and opposite-sign (right panel) daughters for $K_S^0 K_S^0$ (top panel), $K_S^0\Lambda \oplus K_S^0\overline{\Lambda}$ (top-middle panel), $\Lambda\Lambda \oplus \overline{\Lambda}\overline{\Lambda}$ (middle-bottom panel) and $\Lambda\overline{\Lambda}$ (bottom panel).

Figure 5.11: $\left|\Delta\chi^2/\text{ndf}\right|$ distributions, for EPOS-LHC simulations, between V^0 same-sign (left panel) and opposite-sign (right panel) daughters for $K_S^0 K_S^0$ (top panel), $K_S^0\Lambda \oplus K_S^0\overline{\Lambda}$ (top-middle panel), $\Lambda\Lambda \oplus \overline{\Lambda\Lambda}$ (middle-bottom pa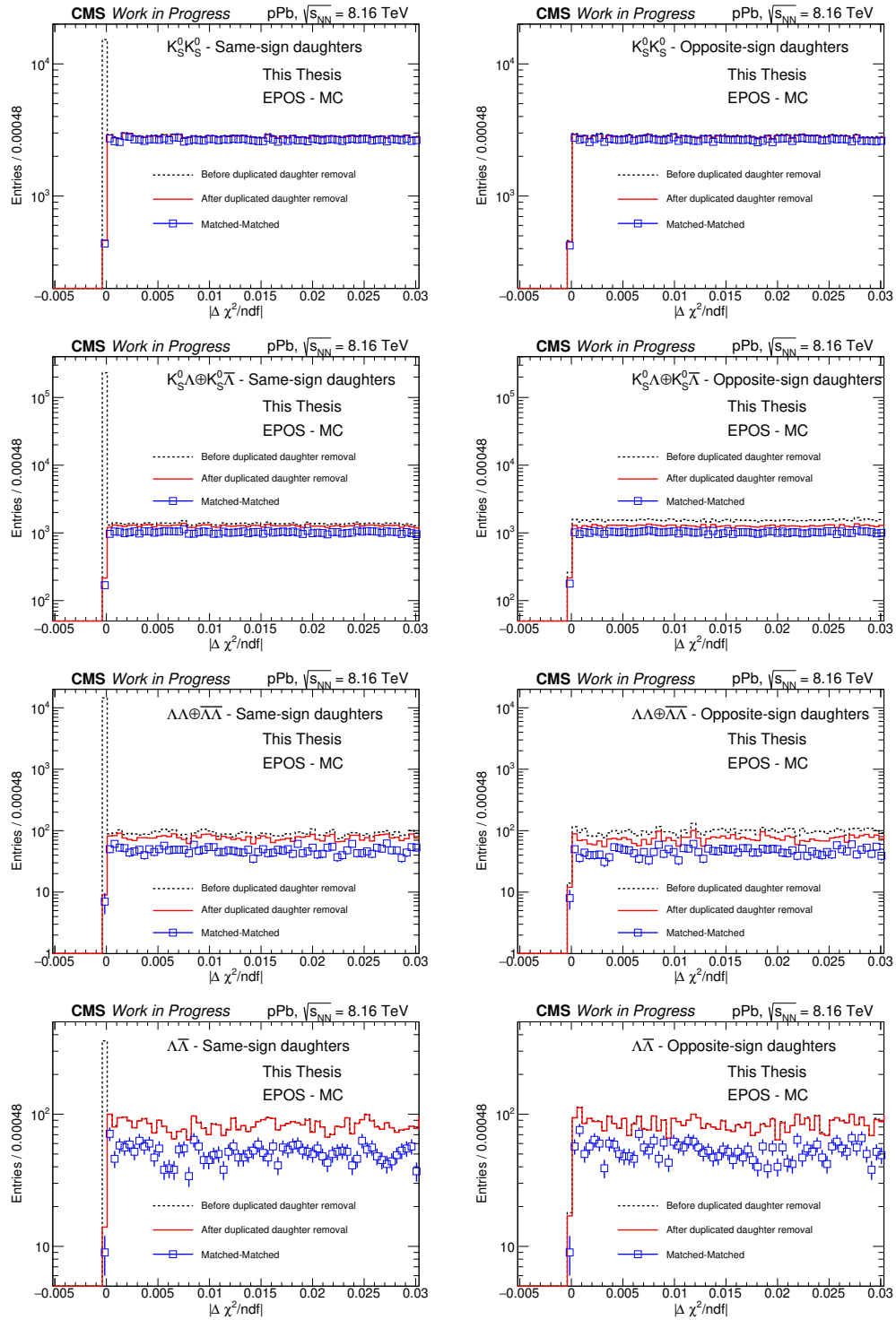nel) and $\Lambda\overline{\Lambda}$ (bottom panel). The black dashed line and red solid line shows the distributions before and after the duplicated track removal. The blue open square shows the distribution for daughters of two matched particles.

5.2.3   Invariant mass distributions

After removing all unwanted tracks used to reconstruct the V^0 particles (from misidentified or duplicated track effects), it is possible to recalculate the invariant mass of the remain daughters and check the candidate identity. Examples of reconstructed V^0 invariant mass for all events in pPb dataset are shown on Fig. 5.12, integrated in $0 < q_{inv} < 3$ GeV, $0 < N_{trk}^{offline} < 400$ and in the average momentum of the pair ($0 < k_T < 2$ GeV). The top panel shows the invariant mass for K_S^0's used in $K_S^0 K_S^0$ (left), $K_S^0 \Lambda$ (middle) and $K_S^0 \overline{\Lambda}$ (right) correlations, while the middle panel displays Λ's measured in $\Lambda \Lambda$ (left), $\Lambda \overline{\Lambda}$ (middle) and $K_S^0 \Lambda$ (right) correlations; and the bottom panel exhibits the $\overline{\Lambda}$'s for $\overline{\Lambda}\,\overline{\Lambda}$ (left), $\Lambda \overline{\Lambda}$ (middle) and $K_S^0 \overline{\Lambda}$ (right) correlations. In all those plots the V^0 peak can be easily identified. The V^0 invariant mass distribution is parametrized by a double Gaussian[10] function with a common mean, m, to describe the signal peak, while the background is modeled by a 4th order polynomial function fit:

$$M_{inv}^{Fit}(q_{inv}, N_{trk}^{offline}, k_T) =$$

$$a \exp\left[\left(\frac{x-m}{\sigma_1}\right)^2\right] + b \exp\left[\left(\frac{x-m}{\sigma_2}\right)^2\right] \quad \text{(signal)} \qquad (5.1)$$

$$+ c + dx + ex^2 + fx^3 + gx^4 \qquad \text{(background)},$$

where x is the invariant mass of the two V^0 daughters, whereas $a, b, c, d, e, f, g, m, \sigma_1$ and σ_2 are the free fitting parameters. The fit is performed using the `ROOT` TMinuit fitting package[11] [293, 324] with χ^2/ndf minimization. In the fit procedure, first the combinatorial background (c, d, e, f, g) is estimated using a region outside the invariant mass peak (called sideband), and later the total fit is performed. The mean, m, observed for the neutral strange particles is close to the mass value from PDG. The parameters σ_1 and σ_2 are the widths of first and second Gaussian, respectively. The total fit is shown for each plot as the red solid line, the combinatorial background is shown as the red dashed line, the ratio data/fit and the pull distributions $\left(\frac{\text{data}-\text{fit}}{\text{data error}}\right)$ can also be seen. The signal fraction, $s/(s+b)$, signal significance, $s/\sqrt{s+b}$, signal yield, mean and χ^2/ndf are also shown. The mass window of $\pm 2\sigma$ ($\pm 1.5\sigma$ and $\pm 2.5\sigma$ are adopted for systematic estimates)

---

[10]For the signal region, multiple Gaussians are used to cover different resolutions for distinct kinematic regions (mainly from different pseudorapidity regions).

[11]The TMinuit is a tool that explores the parameter space searching for the minimum of the function for a set of given free parameters.

around the center of the peak is defined as the "peak region" (vertical blue lines), where σ (show in the figure) represents the root mean square of the two standard deviations of the double Gaussian functions weighted by the yields (Y_1 from the first and Y_2 from the second Gaussian), given by

$$\sigma = \sqrt{\frac{Y_1}{Y_1 + Y_2}\sigma_1^2 + \frac{Y_2}{Y_1 + Y_2}\sigma_2^2}. \tag{5.2}$$

This peak region is used for the present analysis/thesis to measure the femtoscopic correlations. We obtain $\sigma_{K_S^0} \sim 0.005$ and $\sigma_\Lambda \sim \sigma_{\overline{\Lambda}} \sim 0.002$ and for all the particle species, in the peak region, the signal fraction is greater than 95%. To estimate the contribution of background candidates which still present in the peak region, a "sideband region" is chosen that includes V^0 candidates from outside the $\pm 3\sigma$ ($\pm 2.5\sigma$ and $\pm 3.5\sigma$ for systematics) mass range around the V^0 mass to the limit of the mass distributions. The method using the sideband region to remove the combinatorial background is described at Sec. 5.3.1. The fluctuations in the pull distributions (and consequently high χ^2/ndf) comes from the integrated samples, that show small errorbars (most for high-q_{inv}) and merge detector regions with different resolutions. The small discontinuity observed for K_S^0 (~ 0.4777 GeV and ~ 0.5177 GeV), Λ and $\overline{\Lambda}$ (for both ~ 1.106 GeV and ~ 1.126 GeV) invariant mass plots in the case of $K_S^0 \Lambda$ and $K_S^0 \overline{\Lambda}$ correlations (plots on the right panel of Fig. 5.12) are related with the cut applied to remove the misidentified V^0 (see Sec. 5.2.1).

To perform the systematic studies from these fits, both the signal and background functions were changed. For combinatorial background it was also used: i) 3rd order polynomial (or $g = 0$); ii) 2nd order polynomial (or $f = g = 0$); and iii) 4th order Chebychev polynomial, ($c + dx + e(2x^2 - 1) + f(4x^3 - 3x) + g(8x^4 - 8x^2 + 1)$). For the signal, the double Gaussian was replaced by: i) a triple Gaussian; and ii) a quadruple Gaussian.
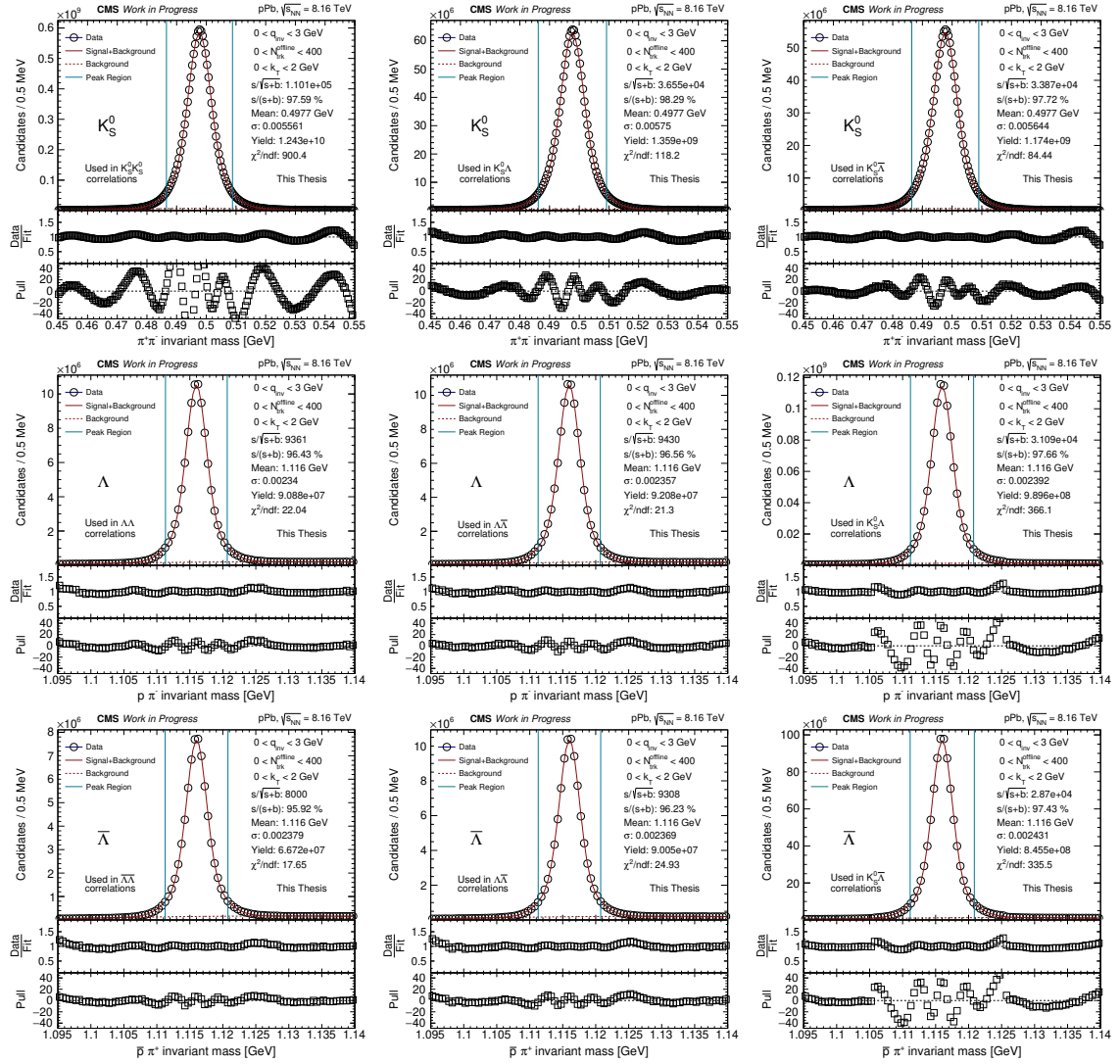
Figure 5.12: Examples of invariant mass distributions (including fits) integrated in q_{inv} ($0 < q_{inv} < 3\,\mathrm{GeV}$), k_T ($0 < k_T < 2\,\mathrm{GeV}$) and multiplicity ($0 < N_{trk}^{offline} < 400$), for K_S^0 (top panel), Λ's (middle panel) and $\overline{\Lambda}$'s (bottom panel) used in different correlations. More informations in the text.

5.2.4 V^0 efficiency

The performance (or efficiency) to reconstruct the strange particles can be evaluated based on MC simulations in two different ways:

- *matched V^0's*: where the efficiency is defined as the ratio between distribution (p_T, η, ...) from matched V^0's divided by the distribution from generated V^0's;

- *fitting and counting*: the number of reconstructed V^0 candidates is obtained from the invariant mass peak (fit) in different bins and than divided by the number of generated V^0 particles in the same bin.

Both methods return similar results and the second is used in the present analysis, because is close to what is usually done to the data to measure the observables. Figure 5.13 shows the three dimentional histogram of the efficiency to reconstruct V^0's as function of η and p_T, produced by using the EPOS-LHC MC generator for K_S^0 (left) and $\Lambda/\overline{\Lambda}$ (right). These efficiencies are similar to the ones obtained in a previous CMS analysis for V^0 production [322]. A comparison between the efficiencies calculated in EPOS-LHC and HIJING as function of p_T is performed returning alike behaviors as show at Fig. 5.14. Also, the dependence with multiplicity was investigated by comparing the p_T distributions in the ranges $0 < N_{trk}^{offline} < 40$ (red open circles) and $80 < N_{trk}^{offline} < 120$ (black open squares), as shown in Fig. 5.15. The efficiencies agrees with each other in different multiplicity regions.

In femtoscopic correlations it is expected that the effect of efficiency correction[12] should be small because both signal and reference samples are corrected and in the single ratios it may cancel each other. Because of that the efficiency effect is studied as a systematic source and in the MC closure[13] test only.

---

[12]The correction is performed by applying a weight defined as 1/efficiency (given by Fig. 5.13) calculated for each particle in different p_T and η bins. For two particle correlations this weight is 1/(efficiency$_1$*efficiency$_2$).

[13]The MC closure is a test performed comparing the variables of interest using RECO (after and before the efficiency correction) and GEN levels, using different MC models.
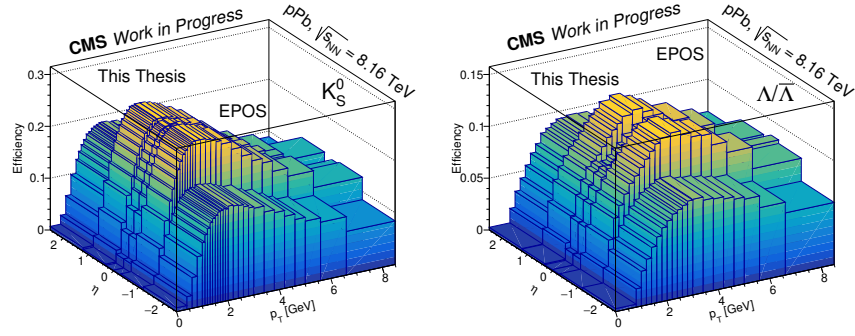
Figure 5.13: Efficiency of reconstruction for K_S^0 (left) and $\Lambda/\overline{\Lambda}$ (right) calculated from `EPOS-LHC` simulations as function of η and p_T.
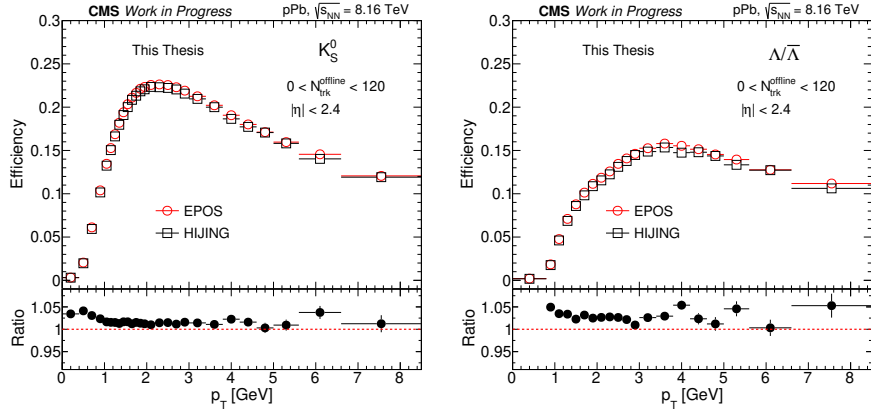
Figure 5.14: Efficiencies calculated from `EPOS-LHC` (red circles) and `HIJING` (black squares) as function of p_T for K_S^0 (left) and $\Lambda/\overline{\Lambda}$ (right). The ratio plot is also show.
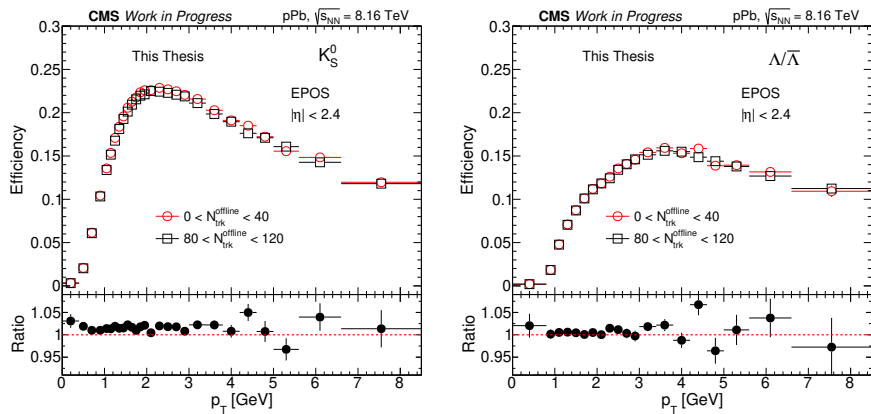
Figure 5.15: Efficiencies calculated using `EPOS-LHC` from different multiplicities: $0 < N_{trk}^{offline} < 40$ (red circles) and $80 < N_{trk}^{offline} < 120$ (black squares) as function of p_T for K_S^0 (left) and $\Lambda/\overline{\Lambda}$ (right). The ratio plot is also show.

5.3 Femtoscopic analysis

The theoretical framework of femtoscopy was described in Chapter 3 employing the source and wave functions. However, in the high energy experiments, these quantities cannot be directly accessed. The experimental procedure leading the correlation function measurement starts by constructing the signal, i.e., the sample that contains the desired femtoscopic effects, and the so-called reference samples. Ideally, the reference sample should contain all the non-femtoscopic information, so that, by taking the ratio of the two, only the signal of interest remains. This technique is known as single ratio (SR) and is largely applied experimentally to measure two particle correlations. Mathematically, the SR is written as [214, 188]

$$\text{SR}\,(q_{\text{inv}}) = C(q_{\text{inv}}) = \left(\frac{N_{\text{ref}}}{N_{\text{sig}}}\right)\left(\frac{dN_{\text{sig}}/dq_{\text{inv}}}{dN_{\text{ref}}/dq_{\text{inv}}}\right), \tag{5.3}$$

where N_{sig} is the integral of the signal content, whereas N_{ref} is the equivalent for the reference sample, both obtained by integrating the pair distributions for all the events in the sample.

For each event, the signal containing femtoscopy correlations is formed by pairing V^0 particles from the same event originating from the primary vertex, in the invariant mass peak region[14], after applying the reconstruction and selections discussed in Sec. 5.2. The histograms are stored in terms of the relative momentum of the pair, $q_{\text{inv}}^2 = -q^\mu q_\mu = -\left(p_1 - p_2\right)^2 = m_{\text{inv}}^2 - 2m_{V_1^0}^2 - 2m_{V_2^0}^2$ (using bins of 40 MeV for all the V^0 pairs), and are divided in bins of the reconstructed charged particle multiplicity, $N_{\text{trk}}^{\text{offline}}$, and/or the pair average transverse momentum, k_T (or transverse mass, $m_T = \sqrt{k_T^2 + m^2}$, where $m = (m_{V_1^0} + m_{V_2^0})/2$).

The reference sample can be constructed in several ways, most commonly formed by mixing V^0's from different events (mixed-event technique). Also this case admits a number of different possibilities. In the standard procedure adopted in this analysis, the reference sample is constructed by pairing particles from different events selected at random in a given event multiplicity range (in bins of width 5: 0-5, 5-10, ..., 395-400) with a similar collision primary vertex coordinate along the beam axis, v_z, in the interval $|\Delta v_z| < 2$ cm. The maximum number of events to mix (N_{mix}) is fixed equal to 20. For estimating the systematic uncertainties

---

[14]The combinations using sideband region are also saved to remove the combinatorial background fraction which remain in the peak region, as will be shown on Sec. 5.3.1.

associated with this choice of reference sample, N_{mix} was considered to be equal to 10 and 30, investigating also $|\Delta v_z| < 0.5$ cm and no $|\Delta v_z|$ selection. The histograms are stored in a similar way as done for the signal.

Examples of normalized q_{inv} distributions for signal (red solid line) and reference (black dotted line) samples are shown on the left panel of Fig. 5.16, while the single ratios are presented in the right panel (using different markers), for $K_S^0 K_S^0$ (top panel), $K_S^0 \Lambda \oplus K_S^0 \overline{\Lambda}$ (middle-top panel), $\Lambda \Lambda \oplus \overline{\Lambda}\,\overline{\Lambda}$ (middle-bottom panel) and $\Lambda \overline{\Lambda}$ (bottom panel), in the range $0 < q_{\text{inv}} < 3$ GeV, with $0 < k_T < 2$ GeV and $0 < N_{\text{trk}}^{\text{offline}} < 400$, including the entire sample available in CMS for pPb collisions at 8.16 TeV. As expected, the correlation function in the low-q_{inv} region is above unity for $K_S^0 K_S^0$ and below unity for $\Lambda \Lambda \oplus \overline{\Lambda}\,\overline{\Lambda}$ due to the quantum statistical nature of the particles involved: K_S^0's are bosons, so follow the Bose-Einstein statistics, and $\Lambda/\overline{\Lambda}$ are fermions, following the Fermi-Dirac statistics. Also, these correlation functions are sensitive to strong final state interactions (FSI) and non-femtoscopic background (see Sec. 5.3.2). For $K_S^0 \Lambda \oplus K_S^0 \overline{\Lambda}$ and $\Lambda \overline{\Lambda}$ two effects are present: strong FSI and non-femtoscopic interactions. According to previous measurements from the ALICE collaboration in PbPb collisions at $\sqrt{s_{\text{NN}}} = 2.76$ GeV [212, 232], the effect of strong FSI seems to push the correlation down to values below unity in both cases. However, in pPb collisions, the effect of non-femtoscopic background seems to push the correlation up to values greater than unity. In all cases the SR goes to unity for high-q_{inv} (> 3 GeV).
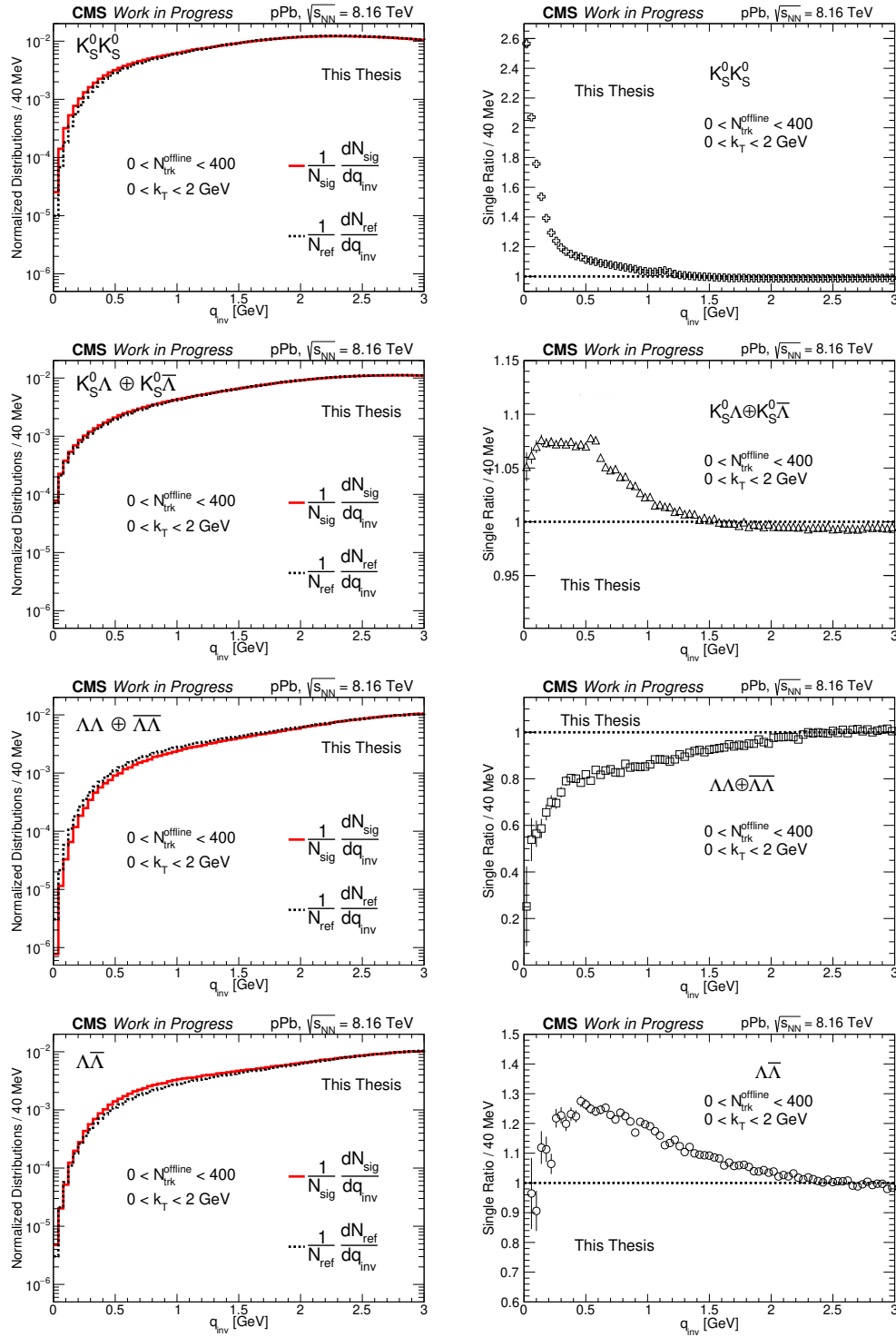
Figure 5.16: Normalized distributions for signal and reference sample (left panel) and single ratio (right panel) as function of q_{inv} integrated in k_T ($0 < k_T < 2$ GeV) and multiplicity ($0 < N_{\text{trk}}^{\text{offline}} < 400$), for $K_S^0 K_S^0$ (top panel), $K_S^0 \Lambda \oplus K_S^0 \overline{\Lambda}$ (middle-top panel), $\Lambda\Lambda \oplus \overline{\Lambda}\,\overline{\Lambda}$ (middle-bottom panel) and $\Lambda\overline{\Lambda}$ (bottom panel). The SR plots are shown in different scales in the y-axis to emphasize the different effects.

5.3.1 Purity correction

After the V^0 reconstruction, the correlation function can be measured with single ratios. However, possible unwanted effects from combinatorial background may remain in the invariant mass peak region and need to be taken into account, since our signal fraction is not 100%. To handle this, a method for purity correction using the sideband region in invariant mass was developed, called *sideband method*. In this method, the measured q_{inv} distribution at the peak region, denoted by $\mathcal{D}(q_{inv}^{meas})$, can be written in terms of the combinations of signal-signal, $\mathcal{D}(q_{inv}^{ss})$, background-background, $\mathcal{D}(q_{inv}^{bb})$, and signal-background, $\mathcal{D}(q_{inv}^{sb})$, distributions as

$$f_{meas}\mathcal{D}(q_{inv}^{meas}) = f_{ss}\mathcal{D}(q_{inv}^{ss}) + f_{bb}\mathcal{D}(q_{inv}^{bb}) + f_{sb}\mathcal{D}(q_{inv}^{sb}). \qquad (5.4)$$

The parameters f_{ss}, f_{bb} and f_{sb} are the fractions of signal-signal, background-background and signal-background in the invariant mass peak region, respectively. The q_{inv} distributions are normalized to unity, so that $f_{ss} + f_{bb} + f_{sb} = f_{meas} = 1$. The fractions can be calculated using the combinatorial analysis, as

$$f_{ss} = \frac{\binom{s}{2}}{\binom{s+b}{2}}, \quad f_{bb} = \frac{\binom{b}{2}}{\binom{s+b}{2}} \text{ and } f_{sb} = 1 - f_{ss} - f_{bb}, \qquad (5.5)$$

where $s = s_{V_1^0} + s_{V_2^0}$ and $b = b_{V_1^0} + b_{V_2^0}$ are the total number of particles in the peak region for signal and background, respectively, extracted by fitting the invariant mass distributions. The term $\binom{x}{2}$ stands for the combinatorial relation

$$\binom{x}{2} = \frac{x!}{2!(x-2)!} = \frac{1}{2}(x-1)x \quad (x \in \mathbb{Z} \text{ and } x > 1), \qquad (5.6)$$

where x is the number of particles (signal, background or total) for a 2 by 2 particles combination, since we are working with two particle correlations.

The parameters, f_{ss} (red circles), f_{sb} (green squares) and f_{bb} (blue crosses), obtained as function of q_{inv} (integrated in $N_{trk}^{offline}$ and k_T) are shown on Fig. 5.17 for $K_S^0 K_S^0$ (top left), $K_S^0 \Lambda \oplus K_S^0 \overline{\Lambda}$ (top right), $\Lambda\Lambda \oplus \overline{\Lambda}\,\overline{\Lambda}$ (bottom left) and $\Lambda\overline{\Lambda}$ (bottom

right). A small dependence (less than 3% for all the cases) on q_{inv} was observed[15], so that, we assume that these factors can be extracted by fitting constant functions (showed by the lines). As expected, $f_{ss} > f_{sb} > f_{bb}$ because of the high signal fraction measured (usually more than 95%) for all the strange particles used in this thesis (K_S^0, Λ and $\overline{\Lambda}$), showing that the effect of combinatorial background is very small. We have also found that $f_{ss}^{K_S^0 K_S^0} > f_{ss}^{K_S^0 \Lambda \oplus K_S^0 \overline{\Lambda}} > f_{ss}^{\Lambda \overline{\Lambda}} > f_{ss}^{\Lambda \Lambda \oplus \overline{\Lambda} \overline{\Lambda}}$, which happens because of the signal fraction from particles used in each correlation. To extract the femtoscopic information, the fits are performed as function of q_{inv} in different intervals of $N_{\text{trk}}^{\text{offline}}$ and/or k_T, where the respective f_{ss}, f_{sb} and f_{bb} are calculated bin-by-bin and applied.
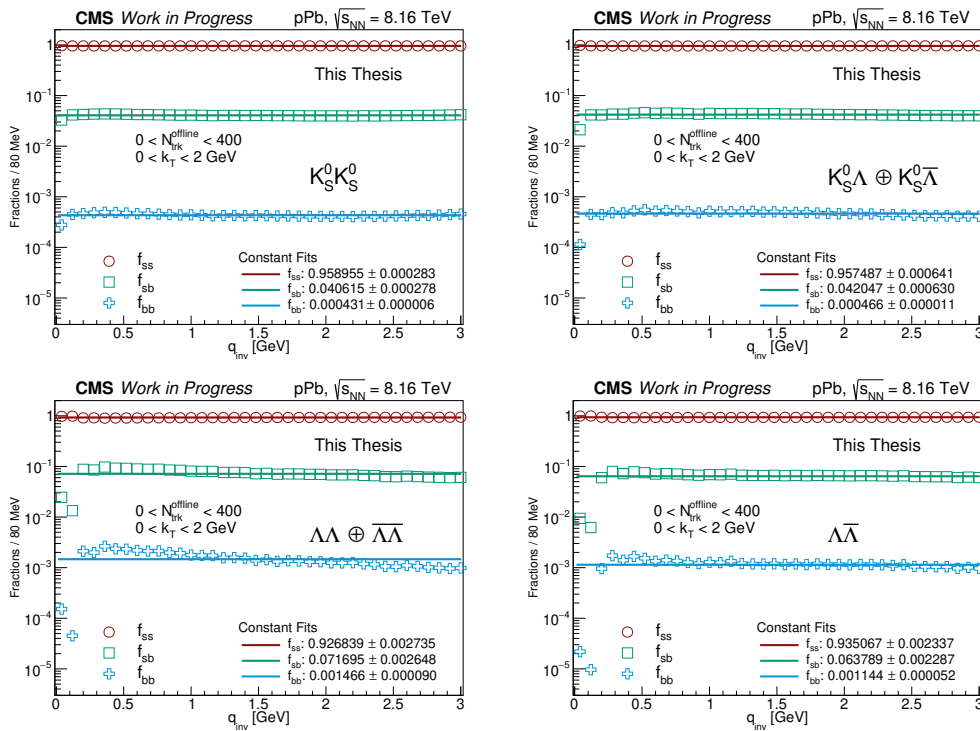
Figure 5.17: Fractions f_{ss} (red circles), f_{bb} (green squares) and f_{sb} (blue crosses) extracted from invariant mass fit as function of q_{inv} for $K_S^0 K_S^0$ (top left), $K_S^0 \Lambda \oplus K_S^0 \overline{\Lambda}$ (top right), $\Lambda \Lambda \oplus \overline{\Lambda} \overline{\Lambda}$ (bottom left) and $\Lambda \overline{\Lambda}$ (bottom right). Lines show constant fits to the factors using the respective colors.

Even after the factors are estimated, the distributions $\mathcal{D}(q_{\text{inv}}^{ss})$, $\mathcal{D}(q_{\text{inv}}^{bb})$ and $\mathcal{D}(q_{\text{inv}}^{sb})$ are still unknown. Then, for background-background and signal-background it is assumed that the shapes of the distributions are the same as in the sideband-

---

[15]The deviation from the first q_{inv} bins comes from the small number of pairs observed in the combinatorial background during the invariant mass fit.

sideband and peak-sideband, respectively. In other words, $\mathcal{D}(q_{\text{inv}}^{bb}) = \mathcal{D}(q_{\text{inv}}^{\text{sideband-sideband}})$ and $\mathcal{D}(q_{\text{inv}}^{sb}) = \mathcal{D}(q_{\text{inv}}^{\text{peak-sideband}})$. This is a good approximation, since in the sideband the signal fraction is negligible. With $\mathcal{D}(q_{\text{inv}}^{\text{meas}})$, $\mathcal{D}(q_{\text{inv}}^{sb})$, $\mathcal{D}(q_{\text{inv}}^{bb})$ and f_{ss}, f_{sb}, f_{bb}, it is possible to obtain the desired signal-signal contribution by re-writting Eq. (5.4) as

$$\mathcal{D}(q_{\text{inv}}^{ss}) = [\mathcal{D}(q_{\text{inv}}^{\text{meas}}) - f_{bb}\mathcal{D}(q_{\text{inv}}^{bb}) - (1 - f_{ss} - f_{bb})\,\mathcal{D}(q_{\text{inv}}^{sb})]/f_{ss}. \qquad (5.7)$$

Now, the single ratio can be measured in terms of the pure signal-signal (q_{inv}^{ss}) distribution and the same procedure is applied for the reference sample. Figure 5.18 shows an example (integrated in $N_{\text{trk}}^{\text{offline}}$ and k_T) of each contribution times the respective fraction as in Eq. (5.4): $\mathcal{D}(q_{\text{inv}}^{\text{meas}})$ as black open square, $f_{ss}\mathcal{D}(q_{\text{inv}}^{ss})$ as red solid line, $f_{sb}\mathcal{D}(q_{\text{inv}}^{sb})$ as green dotted line and $f_{bb}\mathcal{D}(q_{\text{inv}}^{bb})$ as blue dashed line. The plot shows how much background is removed by using this method and, as mentioned earlier, the contribution from combinatorial background is small, so the signal fraction (f_{ss}) is dominant.

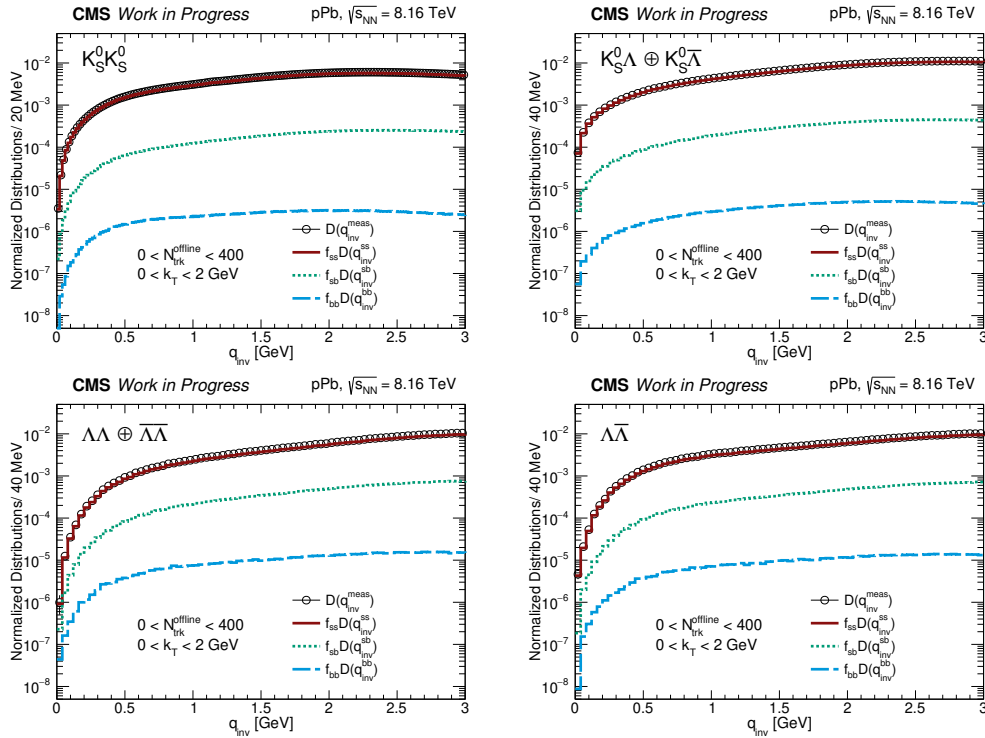Figure 5.18: The q_{inv} distributions of each term from Eq. (5.4) for $K_S^0 K_S^0$ (top left), $K_S^0 \Lambda \oplus K_S^0 \overline{\Lambda}$ (top right), $\Lambda\Lambda \oplus \overline{\Lambda}\,\overline{\Lambda}$ (bottom left) and $\Lambda\overline{\Lambda}$ (bottom right), integrated in the ranges $0 < N_{\text{trk}}^{\text{offline}} < 400$ and $0 < k_T < 2\,\text{GeV}$.

The effect of the sideband method in the correlation function (integrated in $N_{trk}^{offline}$ and k_T) is shown at Fig. 5.19 for $K_S^0 K_S^0$ (top left), $K_S^0 \Lambda \oplus K_S^0 \overline{\Lambda}$ (top right), $\Lambda \Lambda \oplus \overline{\Lambda}\overline{\Lambda}$ (bottom left) and $\Lambda \overline{\Lambda}$ (bottom right). It is possible to observe that the effect of the method is more pronounced in the low-q_{inv} region. The sideband method is employed for all correlations measured in this analysis, and from now on we will use the notation q_{inv} for q_{inv}^{ss}. To evaluate systematic uncertainties from this method, the signal fraction is varied in $\pm 5\%$.
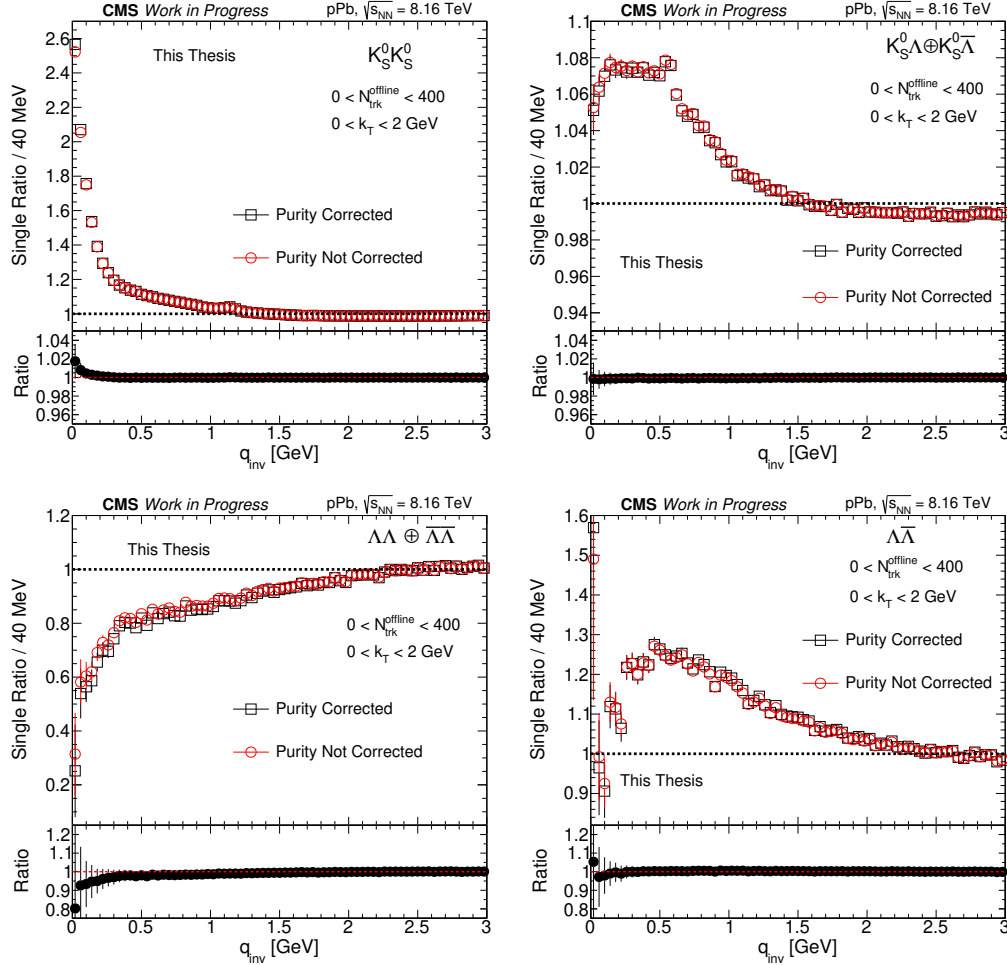
Figure 5.19: Comparison between the single ratios with (black squares) and without (red circles) the purity correction from the sideband method for $K_S^0 K_S^0$ (top left), $K_S^0 \Lambda \oplus K_S^0 \overline{\Lambda}$ (top right), $\Lambda \Lambda \oplus \overline{\Lambda}\overline{\Lambda}$ (bottom left) and $\Lambda \overline{\Lambda}$ (bottom right), integrated in the ranges $0 < N_{trk}^{offline} < 400$ and $0 < k_T < 2$ GeV. The ratios of the single ratios with and without correction are also show.

5.3.2   Non-femtoscopic background

Ideally, the single ratios technique should remove all the non-femtoscopic effects present in the correlation function. However, distortions[16] were observed in measurements and in MC simulations across the entire $q_{\rm inv}$ range, making $SR(q_{\rm inv}) > 1$ (in most of the cases), even where the correlation must go flat to unity ($q_{\rm inv} \gtrsim 0.5$ GeV). This shows that only the SR is not enough to remove the entire background present and the remaining effect is called *non-femtoscopic background* or *cluster*, which increases with $k_{\rm T}$ and decreases with multiplicity, becoming more pronounced in small colliding systems, such as pPb or pp. The origin of this non-femtoscopic background could come from different sources: jet fragmentation (or minijets), energy-momentum conservation, flow, resonances, among others. This distortions must be estimated in order to obtain a precise measurement [214, 189, 188, 232, 210, 191].

According to the literature [189, 191, 242, 190], the observed cluster behavior suggests that these "fake" correlations arise mainly from minijet effects as a consequence of the parton fragmentation and hadronization. To obtain a better understanding (or a hint) of the physical process behind it, investigations using PYTHIA8 simulations (for pp collisions) in two different hard parton-parton scattering configurations ($p_{\rm T}^{\rm parton} > 2$ GeV and $p_{\rm T}^{\rm parton} > 20$ GeV) were performed. PYTHIA8 does not contain the femtoscopic (or flow) effects and allows us to check the complete particle history, thus, becoming possible to access the initial parton responsible to generate the hadrons. When the collision happens, many partons are produced, which later hadronize. Therefore, the V^0 pairs can be produced in two different ways [325]: i) by the same parton fragmentation; or ii) by the fragmentation of different partons, as shown in the sketch on Fig. 5.20. These processes can be tested by comparing the usual V^0 correlations (black open stars), that includes the cluster-like behavior, with the cases where the particles correlated comes from same (red open circles) or different (green open squares) partons, as shown at Fig. 5.21. In most of the cases it is possible to observe the non-femtoscopic background ($SR(q_{\rm inv}) > 1$) behavior in low-$q_{\rm inv}$ coming from the V^0's that are produced by the same parton, while correlations with particles from different partons show a depletion in the opposite direction ($SR(q_{\rm inv}) < 1$), that could be due effect of

---

[16]This effect can be clearly observed in the study of correlations between oppositely charged hadrons in data, where only the Coulomb interaction (present at very low-$q_{\rm inv}$) is expected. And this contribution is also found in the SR using MC GEN level, that not includes detector effects, quantum statistics or any FSI. See, for example, Ref. [188].

energy-momentum conservation. Apparently, there is a competition between these effects, however the non-femtoscopic background wins the competition and that is why we observe such an effect in he $K_S^0 K_S^0$, $K_S^0 \Lambda \oplus K_S^0 \overline{\Lambda}$ and $\Lambda \overline{\Lambda}$ correlation data. The only exception is the $\Lambda \Lambda \oplus \overline{\Lambda} \overline{\Lambda}$ correlation (in $p_T^{parton} > 2$ GeV sample) that will be discussed later in this section. An interesting observation is that the non-femtoscopic background increases for simulations with high energetic partons ($p_T^{parton} > 20$ GeV). In this case, there is a higher probability to produce two (or more) hadrons from the same parton, thus increasing the cluster-like effect. For particles originated from different partons, the behavior observed in correlations (anticorrelation) is slightly reduced, probably because the hadrons formed from high-p_T partons tend to have a larger angular separation in the phase-space reducing the magnitude of depletion in low-q_{inv}. This results leads to an interpretation that the cluster effect mostly comes from the single parton contribution as shown in Fig. 5.21 (left). However, further studies are still needed, maybe by using sophisticated MC models (not developed yet), that includes all the effects (femtoscopy, flow, FSI, ...) that are necessary for a complete understanding of the physics present in the non-femtoscopic background.
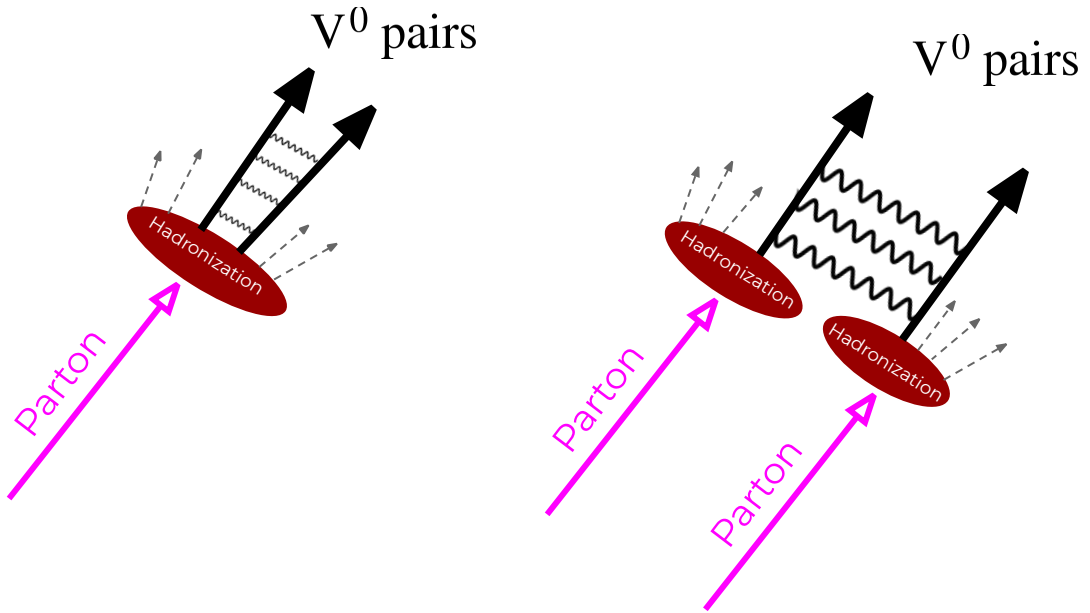
Figure 5.20: Schematic view of the V^0 pair production from a single parton (left) and from two partons (right). See more details in the text.
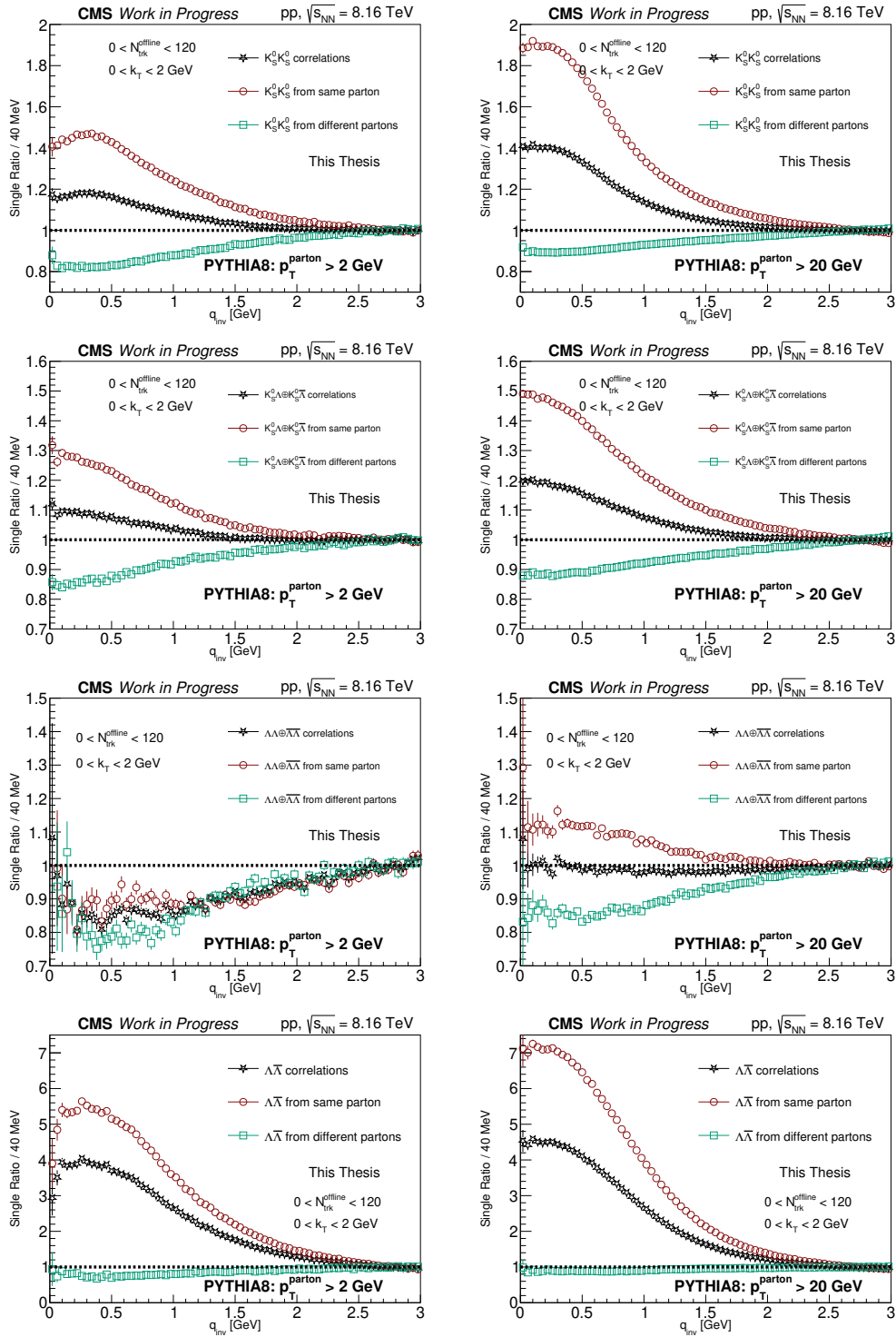
Figure 5.21: Single ratios as function of q_{inv} calculated using `PYTHIA8`, in two different regimes: $p_{\text{T}}^{\text{parton}} > 2\,\text{GeV}$ (left panel) and $p_{\text{T}}^{\text{parton}} > 20\,\text{GeV}$ (right panel); for $K_S^0 K_S^0$ (top panel), $K_S^0 \Lambda \oplus K_S^0 \overline{\Lambda}$ (middle-top panel), $\Lambda\Lambda \oplus \overline{\Lambda}\,\overline{\Lambda}$ (middle-bottom panel) and $\Lambda\overline{\Lambda}$ (bottom panel). The usual correlations (black open star) are compared with the cases where V^0 comes from same (open green circles) and different (open green squares) partons.

Modeling the cluster effect

Cluster effects have been investigated over the years and different methods were employed to correct and/or estimate such undesirable correlations. Some of those methods found on the literature are briefly described bellow:

- *Double ratios* (DR) [214, 189, 188]: is defined as a ratio where the numerator is the SR constructed from data and the denominator is the SR computed in exactly the same way using MC simulations. This can be done if the MC simulation do not contain femtoscopic effects implemented, but describe the overall behavior of the data well, then the DR should return the pure femtoscopic correlation. The DR showed good results for charged hadrons in proton-proton collisions, however, the choise of the MC model (see Sec. 5.1.2) is one of the biggest source of systematics. This method was tested and shows some limitations for V^0 correlations in pPb collisions: i) there are no HM MC samples available and the production becomes unfeasible, therefore, this method can be applied to MB events only; ii) the MC models in pPb collisions tend to underestimate or overestimate the behavior observed in data; iii) none of the official MC generators (see Sec. 5.1.2) can describe the cluster patern present in $\Lambda\Lambda \oplus \overline{\Lambda}\overline{\Lambda}$ correlations (see more informations later in this section) .

- *Fully data-driven* or *cluster subtraction* [189, 188]: this method, based only on data, was developed by the CMS collaboration for the analysis of $\pi\pi$ and *KK* correlations in pp, pPb and peripheral PbPb collisions. Initially, the correlation between opposite-sign pairs is fitted by using a Gaussian-like function (including the attractive Coulomb correction) whose parameters (height and width), are adjusted in bins of average transverse momentum and multiplicity. Both height and width are then parametrized, as function of k_T and $N_{trk}^{offline}$, and fixed. Later, the form of the non-femtoscopic contribution obtained from OS pairs is used to fit the SS correlation functions (with repulsive Coulomb corrections), but multiplied by an amplitude factor, given by the ratio of measured OS to SS contributions, and including the quantum statistics term. Because of the limited data sample and the fact that the K_S^0 is its own antiparticle, this method cannot be applied for V^0's.

- *Hybrid-cluster subtraction* [188, 191]: it was idealized by ATLAS collaboration in pPb collisions at $\sqrt{s_{NN}} = 5.02$ TeV and he concept is similar to the fully data-driven, however it has a small number of parameters. In this method, both single ratios for SS and OS pairs are calculated from MC simulations (without femtoscopic effects) and the cluster is fitted by a Gaussian-shape function in different bins of k_T and $N_{trk}^{offline}$. The height and width obtained from the MC SR fits are then used to parametrize convertion functions between SS and OS. The parameters found when fitting the conversion functions are fixed and depend on the specific MC model used. Once this is done, the OS correlations from data are fitted using the same Gaussian-shape and the cluster structure is transferred from OS to SS using the conversion functions with the MC parameters. Studies were carried out to apply such method by using relations between the different V^0 pairs, instead of SS and OS. However, the differences between data and MC observed in the shapes of $\Lambda\Lambda \oplus \overline{\Lambda}\overline{\Lambda}$ correlations, made it unreliable to apply the method.

- *Transverse sphericity* [326]: according to the ALICE collaboration studies, the induced jet-like structures associated with the hard parton-parton scatterings has influence in the event-shape. The event can be categorized by a variable called transverse sphericity, S_T, that is defined as a momentum space variable, commonly classified as an event shape observable [326], with values between 0 and 1. Events with $S_T < 0.3$ are called jet-like (back-to-back) and events with $0.7 < S_T < 1$ are called spherical. It was observed that $0.7 < S_T < 1$ reduces significantly the cluster contribution for $\pi\pi$ (and later for other pairs) correlations in pp collisions. This selection has been tested in the current analysis in pPb collisions for both charged hadron and V^0 correlations, however it proved to be inefficient in the case of this collision system.

In a recent analysis performed by CMS collaboration [188], the charged particle correlations were measured in pp collisions at $\sqrt{s} = 13$ TeV using three different methods (double ratios, fully data-driven and hybrid-cluster subtraction) and the results showed a good agreement among each method for R_{inv}, however, a discrepancy in the λ parameter was observed when using the fully data-driven method.

Due to the limitations of the methods mentioned above, the present thesis employs a new method developed based on MC studies. According to the GEN level MC simulations, that do not include femtoscopic effects, the correlations for all the pairs analized show a Gaussian-like shape, as shown in Fig. 5.22. In those plots, the single ratios calculated using EPOS-LHC for $K_S^0 K_S^0$ (top left), $K_S^0 \Lambda \oplus K_S^0 \overline{\Lambda}$ (top right), $\Lambda\Lambda \oplus \overline{\Lambda}\,\overline{\Lambda}$ (bottom left), and $\Lambda\overline{\Lambda}$ (bottom right), integrated in the ranges $0 < k_T < 2$ GeV and $0 < N_{trk}^{offline} < 120$ are shown and fitted (see Sec. 5.3.4 for more details about the fitting) by Eq. (5.8). The fits show good agreement with the simulations for all the pairs. Note that, $K_S^0 K_S^0$ correlations from EPOS-LHC show a bump around 0.2 GeV that is an overestimation of the ϕ resonance signal, so the q_{inv} interval from 0.15 to 0.3 was not used in the fit (see Sec. 5.3.3). In addition, the region of $q_{inv} < 0.1$ GeV is also excluded because this region may contain contributions from multi-body decays.

The general fit form used to estimate the non-femtoscopic background is parametrized, based on the hybrid-cluster subtraction method, by the function:

$$\Omega\left(q_{inv}\right) = N\left[1 + \beta \exp\left(-\left|\frac{q_{inv}}{\sigma}\right|^2\right)\right]\left(1 + \delta q_{inv}\right), \tag{5.8}$$

where N is the normalization, the term $1 + \delta q_{inv}$ take into acount deviations from the unity at high q_{inv} (long q_{inv} range term), and the parameters β and σ are related to the cluster. The advantages of this method is that it is applicable directly to the data (not depending on MC nor opposite-sign correlations) by fitting a region where the femtoscopic signal is not expected (usually considerig the region $q_{inv} >$ 0.5 GeV). Then the parameters are fixed and Eq. (5.8) is used as an additional term in the full femtoscopic fitting function, $C_{Femto}(q_{inv}) = C_{Theory}(q_{inv})\Omega(q_{inv})$. This is used to extract the physical quantities from single ratios in the entire q_{inv} range. The method employing Eq. (5.8) offers greater flexibility and is valid for $K_S^0 K_S^0$, $K_S^0 \Lambda \oplus K_S^0 \overline{\Lambda}$ and $\Lambda\overline{\Lambda}$ correlations. However, in the $\Lambda\Lambda \oplus \overline{\Lambda}\,\overline{\Lambda}$ case, the Gaussian behavior is not observed in data and this needs to be studied in a different way as discussed next.
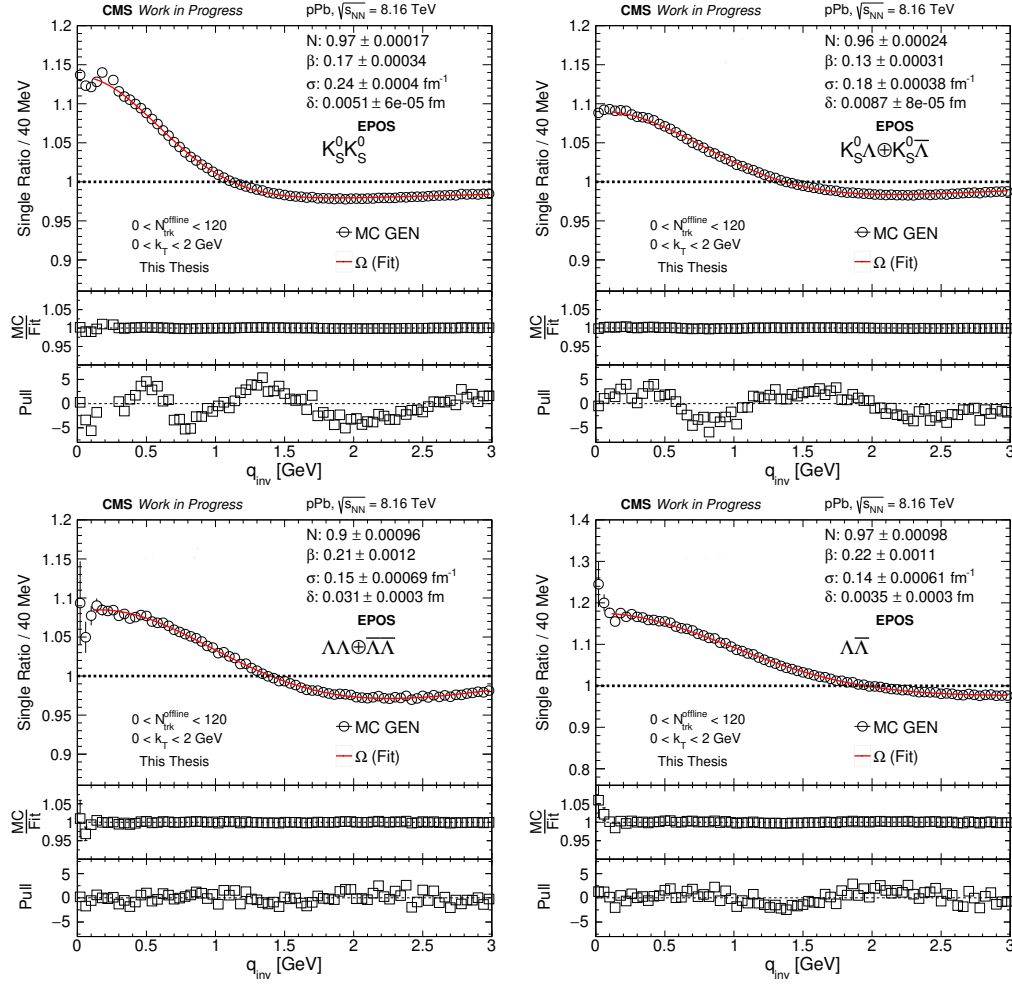
Figure 5.22: Single ratios as function of q_{inv} for $K^0_S K^0_S$ (top left), $K^0_S \Lambda \oplus K^0_S \overline{\Lambda}$ (top right), $\Lambda\Lambda \oplus \overline{\Lambda}\,\overline{\Lambda}$ (bottom left) and $\Lambda\overline{\Lambda}$ (bottom right) calculated using `EPOS-LHC` GEN level of simulations and fitted by Eq. (5.8).

Baryon-baryon and antibaryon-antibaryon

Correlations involving two baryons or two antibaryons (e.g., $\Lambda\Lambda$, $p\Lambda$, $\overline{p}\overline{\Lambda}$, ...) has shown a different behavior as compared to meson-meson, meson-baryon or baryon-antibaryon measurements in small colliding systems. In that case, the Gaussian-like non-femtoscopic background was absent and anticorrelations[17] (single ratio < 1) are seen in the low- and high-q_{inv} ranges, as shown for $\Lambda\Lambda \oplus \overline{\Lambda}\,\overline{\Lambda}$ SR in Fig. 5.16 (middle-bottom), and also in measurements of pp, $p\Lambda \oplus \overline{p}\overline{\Lambda}$ and $\Lambda\Lambda \oplus \overline{\Lambda}\,\overline{\Lambda}$ correlations performed by ALICE collaboration in pp and pPb collisions in different center-of-mass energies [210, 242].

---

[17]Similar to the correlations of strange hadrons coming from different partons at Fig. 5.21.

This effect was first observed in two-particle rapidity correlations performed by TPC/Two-Gamma collaboration in e^+e^- annihilations with $\sqrt{s}$ = 29 GeV at SLAC [327] and later in two particle angular correlations of identified particles (π, K, p and Λ) by ALICE collaboration in pp collisions with $\sqrt{s}$ = 7 TeV [328], where the influence of the known physical effects (quantum statistics and/or Coulomb FSI and/or strong FSI) were investigated using all the combinations between protons and lambdas. In both analyses, this behavior was interpreted in the context of (anti)baryon production mechanism in the fragmentation process (see next), but still is an open question [328].

One possible interpretation of the abscense of the cluster-like structure and the depletion (anticorrelation) observed, as argued in [327], is related to local baryon number conservation, where "local" refers to the total baryon number produced from a single parton, while "global" baryon number refers to all the particles in the event, which should be conserved. In hadronization models, the local mechanism usually requires that two baryons produced from a single fragmentation are separated by at least one hadron with a different baryon number [327, 328]. Assuming that this hypotheses holds and that these particles can be produced by the same or by different partons (from Fig. 5.20), the non-femtoscopic enhancement from a baryon-baryon (antibaryon-antibaryon) correlation must originate from the same parton contribution and, to conserve the local baryon number, this parton should produce an additional antibaryon-antibaryon (baryon-baryon) pair as well. The lightest known baryon is the proton with mass around 0.938 GeV, which indicates that this fragmented parton must have at least $\sim$4 GeV to produce both pairs[18] (2 particles + 2 antiparticles). Thus, if the energy of this parton is not enought, the cluster effect is suppressed and this is probably what we see in our $\Lambda\Lambda \oplus \overline{\Lambda}\,\overline{\Lambda}$ correlations, Fig. 5.16 (middle-bottom). At SLAC energies this can be understood by the constraint from the center-of-mass energy, $\sqrt{s} = 29$ GeV, while at LHC energies (order of TeV), this constraint should have less impact, since this parton energies can be more easily achieved. However, the probability to generate low-p_T partons (or minijets) is higher, being dominant over the high-p_T partons, so that the absence of non-femtoscopic correlations is still present at higher energies. This behavior is confirmed in simulations using `PYTHIA8`, as shown in Fig. 5.21 (middle-bottom panel), where the cluster-like structure is not present for the sample with $p_T^{\text{parton}} > 2$ GeV (left), while for simulations with $p_T^{\text{parton}} > 20$ GeV (right) the non-femtoscopic background arises again. Nevertheless, more investigations are

---

[18]Assuming the most ideal case, in which one pion is produced to separate the (anti)baryons.

needed, to better understand the observed effects.

The depletion seen in simulations, performed using PYTHIA8, can be described by using the Eq. (5.8), with negative β, or by the following expression

$$\Omega\left(q_{\mathrm{inv}}\right) = N\left[\alpha + \frac{\beta - \alpha}{1 + \left(\frac{q_{\mathrm{inv}}}{\sigma}\right)^{\gamma}}\right]\left(1 + \delta q_{\mathrm{inv}}\right). \tag{5.9}$$

This can be used as a systematic effect where, N is the overall normalization, $1 + \delta q_{\mathrm{inv}}$ the long range term, α, β, γ and σ are the free fit parameters used to describe the anticorrelations. The procedure to obtain the physical quantities is exactly the same as explained earlier for the other pairs, but replacing the Eq. (5.8) by Eq. (5.9). Figure 5.23 shows the $\Lambda\Lambda \oplus \overline{\Lambda}\overline{\Lambda}$ single ratio as function of q_{inv} from PYTHIA8 simulations (black open stars): $p_{\mathrm{T}}^{\mathrm{parton}} > 2$ GeV (left) and $p_{\mathrm{T}}^{\mathrm{parton}} > 20$ GeV (right), considering that the V^0's are produced by different partons and fitted by Eqs. (5.8) (red solid line) and (5.9) (blue dashed line), integrated in k_{T} and $N_{\mathrm{trk}}^{\mathrm{offline}}$(MB). The fits can describe the data behavior well. Figure 5.24 presents the fit using both Eq. (5.9) (red solid line) and Eq. (5.8) (blue dashed line) applied direct to the full dataset (integrated in k_{T} and $N_{\mathrm{trk}}^{\mathrm{offline}}$) for $\Lambda\Lambda \oplus \overline{\Lambda}\overline{\Lambda}$ correlations (black open stars) in the region where the femtoscopic signal is not expected ($q_{\mathrm{inv}} > 0.5$ GeV) and extrapolated to low-q_{inv}, to show the behavior. The fits agrees with the data in the high-q_{inv} range for both functions and, as expected, they do not describe the data in the low-q_{inv} because the femtoscopic part is not included.
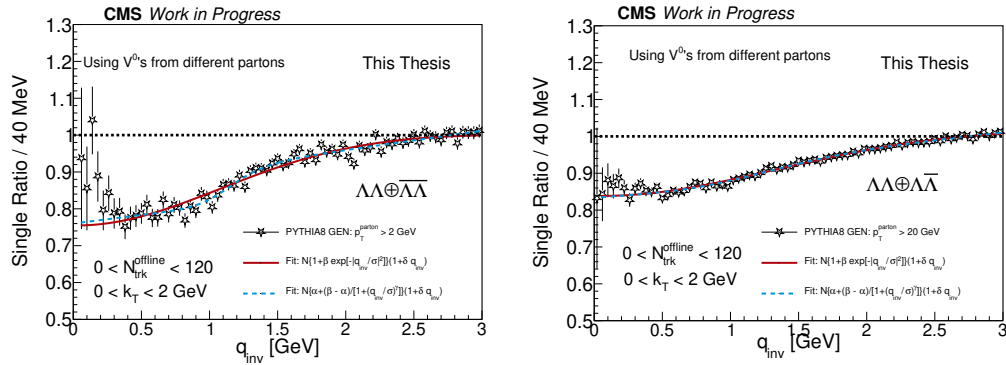
Figure 5.23: Correlation as function of q_{inv} from PYTHIA8 using $p_{\mathrm{T}}^{\mathrm{parton}} > 2$ GeV (left) and $p_{\mathrm{T}}^{\mathrm{parton}} > 20$ GeV (right). In both plots only the contribution of V^0 coming from different partons are taken into account. More informations in the text.
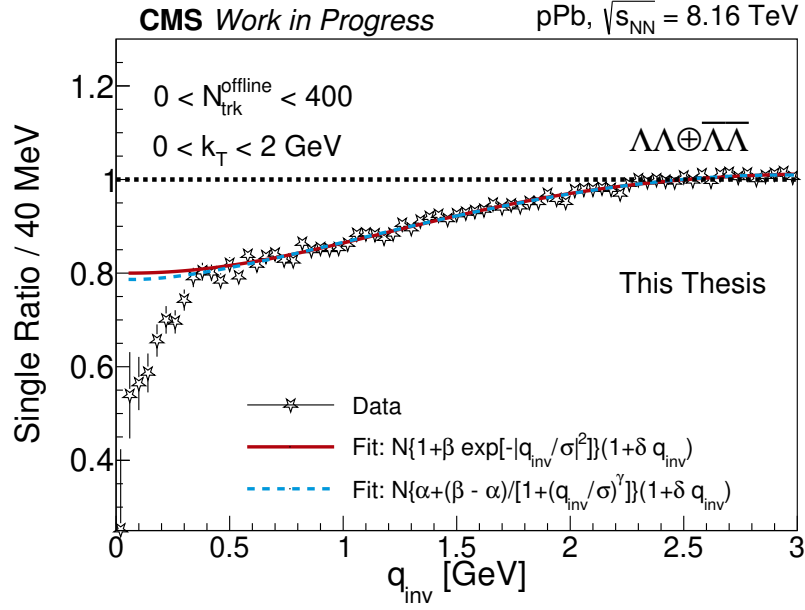
Figure 5.24: Single ratios for $\Lambda\,\Lambda \oplus \overline{\Lambda}\,\overline{\Lambda}$ correlations using full statistics pPb dataset (black open stars), fitted by using Eq. 5.8 (red solid line) and Eq. 5.9. The fits are performed in the region where the femtoscopic signal is not expected ($q_{\mathrm{inv}} > 0.5\,\mathrm{GeV}$).

5.3.3 Non-prompt contribution

After corrections and the non-femtoscopic background estimation, there is still one last effect that can distort our measurement coming from correlations of non-prompt V^0's from heavier decay. Such an effect is known as residual or feed-down correlations and can be better understood by using the schematic view shown in Fig. 5.25. In the sketch, the total correlation function between two particles, A and B, is given by the sum of the contributions from the correlation between the desired prompt particles, directly emitted from the source, and the non-prompt ones which may contribute in three different ways: i) particle B comes from the decay of particle C; and/or ii) particle A is the daughter of D; and/or iii) both particles, A and B, come from the decay of D and C, respectively.

From the experimental point of view, it is difficult to distinguish between prompt and non-prompt V^0's, especially because the variables used to reconstruct these particles have a similar behavior, which implies that simple cuts may not be sufficient to remove those contributions. However, with the help of MC simulations, it is possible to estimate the fraction of particles from decays that is used in our correlations.
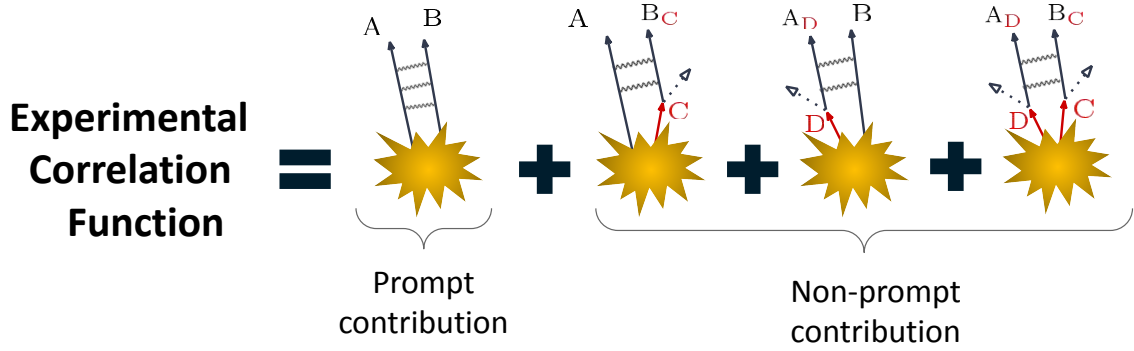
Figure 5.25: Sketch of the total correlation function as the sum of the prompt and non-prompt contributions. See details in the text.

According to MC thermal model calculations [204], most of the neutral kaons are prompt ($\sim 60\%$) while the non-prompt contributions are dominated by K^* ($\sim 25\%$), ϕ ($\sim 5\%$) and higher mass resonances ($\sim 10\%$). Using the official MC simulations available for pPb collisions, the fraction of prompt K_S^0 particles estimated by `EPOS-LHC` was around 69%, while for `HIJING` it was $\sim 47\%$, demonstrating a strong modeling dependence. For avoiding bias from the MC model dependence and since it is not possible to access directly the K_S^0's coming from decays in data, we will follow the procedure adopted in previous measurements and not correct neutral kaons for residual correlations, i.e., assume all K_S^0's as prompt.

For Λ's and $\overline{\Lambda}$'s, the contribution from non-prompt particles are expected to play an important role in femtoscopic measurements [241, 329]. In thermal model studies from STAR collaboration [257, 240] in AuAu collisions at $\sqrt{s_{NN}} = 200$ GeV, $\sim 45\%$ of the lambda baryons are primary and the non-prompt fraction is dominated by $\Sigma^0 \to \Lambda\gamma$ (BR: $\sim 100\%$) and $\Xi \to \Lambda\pi$ (BR: $99.887 \pm 0.035\%$) decays. In pPb collisions at 8.16 TeV, we have estimated the Λ and $\overline{\Lambda}$ prompt fractions to be $\sim 30\%$ for `EPOS-LHC` and $\sim 50\%$ for `HIJING`, also showing a non-negligible dependence on MC. The effect of residual Λ's was first studied in $p\Lambda$ [330] and $\Lambda\Lambda \oplus \overline{\Lambda}\overline{\Lambda}$ [240] correlations using the Gaussian residual method, in which a Gaussian term was included in the final correlation function fit based on phenomenological (hydrodynamics) studies. This method was originally created to explain the difference observed in the measured R_{inv} between baryon-baryon and baryon-antibaryon (by a factor 2) in $p\Lambda$ correlations [257]. Later, the transformed residual method was developed by A. Kisiel et. al. [329], using a two dimensional q_{inv} matrix generated from MC thermal models, based on the desired

residual correlation. Therefore, to calculate a genuine AB correlation (see sketch in Fig. 5.25) removing, for example, the contribution of B coming from C decays, the matrix q_{inv}^{AB} vs $q_{\mathrm{inv}}^{A(C \to B)}$ is generated. The decayed particle contributes to a q_{inv} shift, which is then corrected by using the matrix. This method is adopted by ALICE collaboration, for PbPb collisions[19] only, while in pp and pPb, they estimate the prompt and non-prompt fractions, based on MC simulations, and assume that the feed-down contribution is flat at unit due to the scarcity of knowledge about this type of interaction [210, 242].

Based on the discrepancies observed between the MC models to describe the fraction of prompt V^0's, this thesis study the effect of residual contribution in a data-driven way, by using Λ baryons from the decays of Ξ and Ω particles, which are also reconstructed and stored in our data samples. The reconstruction of $\Xi \to \Lambda\pi$ (BR: $99.887 \pm 0.035\%$) and $\Omega \to \Lambda K$ (BR: $67.8 \pm 0.7\%$) are performed by combining all the lambdas in the sample with one extra track (excluding K_S^0, Λ and $\overline{\Lambda}$ daughters) with selection similar to used in previous CMS studies [331]. In this analysis, the fraction of residual lambdas coming from Ξ was estimated to be less than 4%, while the Ω contamination was neglegible. Here, we are interested in studying the effect of these decayed particles on the correlation function. To perform such study, first the Λ's and $\overline{\Lambda}$'s in our sample are combined with the daughters coming from Ξ and/or Ω (and respective antiparticles) decays. If both particles have exactly the same characteristics (p_{T}, η, ϕ, ...), these lambdas are considered to be non-prompt and are not used to measure the single ratios. Figure 5.26 (left panel) shows the SR measured for $K_S^0\Lambda \oplus K_S^0\overline{\Lambda}$ (top), $\Lambda\Lambda \oplus \overline{\Lambda}\,\overline{\Lambda}$ (middle) and $\Lambda\overline{\Lambda}$ (bottom) for the following cases: i) no particle is removed (black open stars); ii) remove $\Lambda/\overline{\Lambda}$ from $\Xi/\overline{\Xi}$ (red open circles); iii) remove $\Lambda/\overline{\Lambda}$ from $\Omega/\overline{\Omega}$ (green open squares); and iv) remove $\Lambda/\overline{\Lambda}$ from both $\Xi/\overline{\Xi}$ and $\Omega/\overline{\Omega}$ (blue open cross). The ratio plots shows the single ratios for the cases ii) (red), iii) (green) and iv) (blue) divided by the single ratio from case i), showing that the fraction removed affects the correlation function in less than 2%. The case removing Λ's from both $\Xi/\overline{\Xi}$ and $\Omega/\overline{\Omega}$ is chosen as default in our analysis, while the other options are used as systematics.

The single ratios measured using prompt+non-prompt particles were further investigated, as shown in Fig. 5.26 (right panel) for $K_S^0\Lambda \oplus K_S^0\overline{\Lambda}$ (top), $\Lambda\Lambda \oplus \overline{\Lambda}\,\overline{\Lambda}$ (middle) and $\Lambda\overline{\Lambda}$ (bottom). In all the plots one lambda used in the correlations is

---

[19]This happen because the MC code used to generate the matrices employed input from hydrodynamic simulations, for which results from small colliding systems are not yet available.

coming from decays of $\Xi/\overline{\Xi}$ and $\Omega/\overline{\Omega}$ (blue open cross), $\Xi/\overline{\Xi}$ (red open circles) and $\Omega/\overline{\Omega}$ (green open squares). The behavior of the correlation functions for $K_S^0 \Lambda \oplus K_S^0 \overline{\Lambda}$ and $\Lambda\overline{\Lambda}$ is similar to the non-femtoscopic background (Gaussian-like), while for $\Lambda\Lambda \oplus \overline{\Lambda}\,\overline{\Lambda}$ an almost flat distribution is seen. Both $K_S^0 \Lambda \oplus K_S^0 \overline{\Lambda}$ and $\Lambda\Lambda \oplus \overline{\Lambda}\overline{\Lambda}$ SR show a bump around $q_{\text{inv}} \sim 0.5$ GeV: for $K_S^0 \Lambda \oplus K_S^0 \overline{\Lambda}$ it can be seen for all the studied cases, consistent with the q_{inv} region where a peak (probably from a resonance) was found (see Fig. 5.16); while the peak seen in $\Lambda\Lambda \oplus \overline{\Lambda}\,\overline{\Lambda}$ correlations could come from the Ξ contamination, and it could also be due to an unknown resonance or could simply be statistical fluctuations; therefore more data is needed to draw final conclusions. Correlations involving two lambdas ($\Lambda\Lambda \oplus \overline{\Lambda}\overline{\Lambda}$ or $\Lambda\overline{\Lambda}$) where both particles are non-prompt were not shown because of the small number of Ξ's and Ω's in our data sample.

In addition, there is also another possibility, not shown in the sketch, in which both particles used in the SR come from the same particle, i.e., particle $E \rightarrow AB$. In that case a peak (bump) in the correlation function is expected because of the relation between q_{inv} and m_{inv}. Here, the non-prompt effect is easily removed by excluding the q_{inv} range around the resonance during the femtoscopic fit.

5.3.4 Fitting the correlation function

To extract the information about quantum statistics and/or strong final state interactions, the correlation function measured using the SR technique is fitted by the combined function

$$C_{\text{Femto}}(q_{\text{inv}}) = \mathcal{N} \left\{ 1 + \lambda \left[C_{\text{QS}}(q_{\text{inv}}) + C_{\text{SI}}(q_{\text{inv}}) \right] \right\} \Omega(q_{\text{inv}}) \tag{5.10}$$

where $\mathcal{N}$ is an overall normalization, λ is the intensity parameter, C_{QS} is the Gaussian quantum statistic term used for identical particles ($K_S^0 K_S^0$ and $\Lambda\Lambda \oplus \overline{\Lambda}\,\overline{\Lambda}$, see Sec. 3.2 of Chapter 3) and C_{SI} is the Lednicky-Lyubolshitz theory-based model for strong final state interaction applicable for all pairs (see Sec. 3.3 of Chapter 3). The $\Omega(q_{\text{inv}})$ is the function used to estimate the non-femtoscopic background (see Sec. 5.3.2). The fit is performed with `ROOT` TMinuit fitting package [293, 324] using a χ^2/ndf minimization and performed in two steps:

- first, the non-femtoscopic background function, $\Omega(q_{\text{inv}})$, is adjusted using the q_{inv} region where the femtoscopic effects are not expected, i.e., $0.5 < q_{\text{inv}} < 3$ GeV, and the parameters $(N, \beta, \sigma, \delta)$ are obtained and fixed. For the
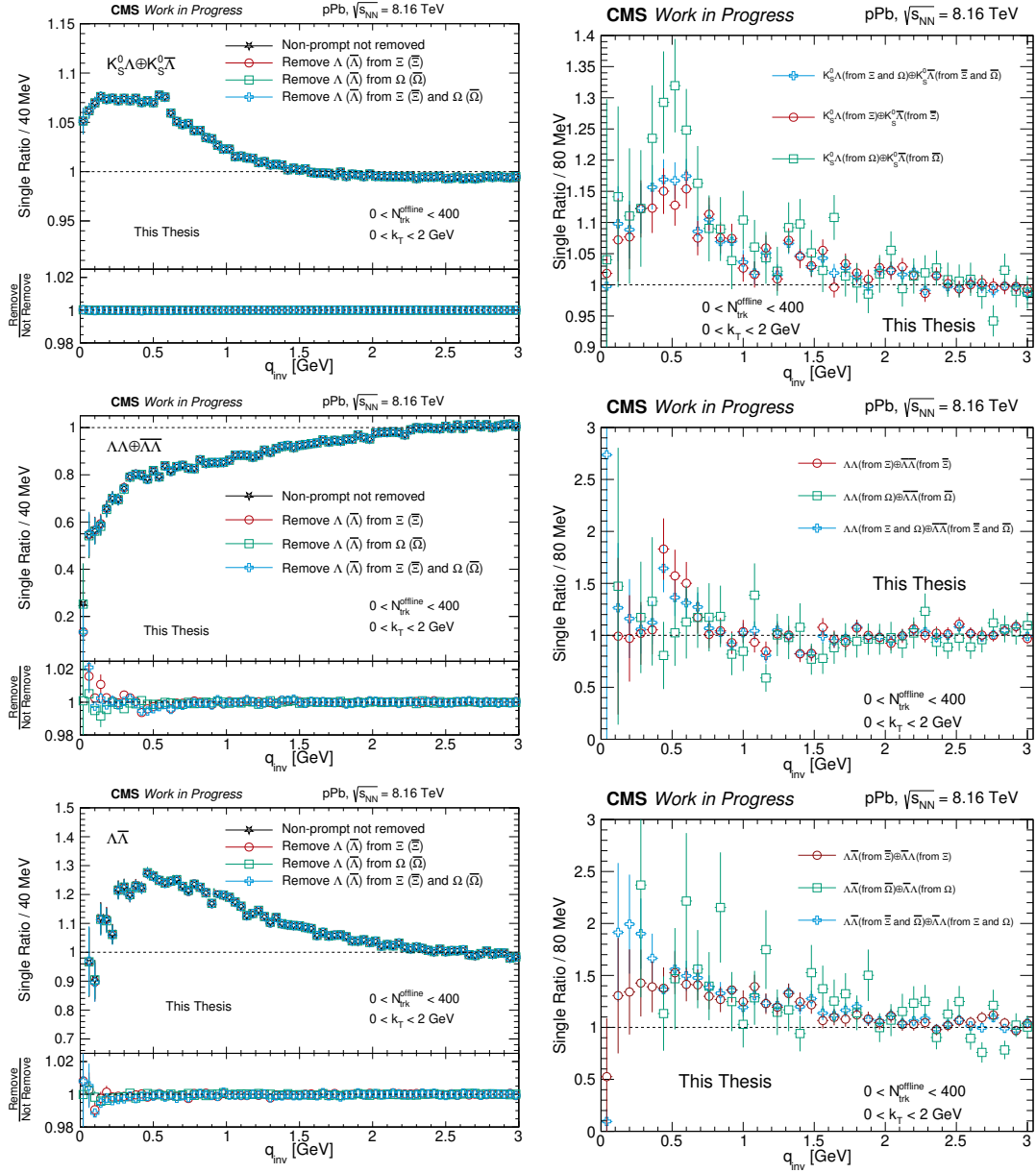
Figure 5.26: Single ratio plots for $K_S^0\Lambda \oplus K_S^0\overline{\Lambda}$ (top panel), $\Lambda\Lambda \oplus \overline{\Lambda\Lambda}$ (middle panel) and $\Lambda\overline{\Lambda}$ (bottom panel) integrated in k_T and $N_{trk}^{offline}$. Left panel: comparison of the correlations with (in different cases) and without the non-prompt removal. In the lower plot, the ratio between the distribution removing, cases ii), iii) and iv), and not removing, case i), the non-prompt contribution are shown. Right panel: correlation between prompt particles and non-prompt lambdas (from Ξ, Ω and $\Xi + \Omega$). The SR is rebinned to 80 MeV because of the lack of statistics. More informations at the text.

systematic studies, the minimum q_{inv} values are changed to 0.4 and 0.6 GeV and the maximum to 4 and 5 GeV;

- once the non-femtoscopic background is fixed the fit is performed again, but now in the full q_{inv} range ($0.04 < q_{inv} < 3$ GeV), to extract the physical quantities. Note that, the fit does not start in $q_{inv} = 0$ GeV because in that region the detector resolution can interfere in our measurement, thus the first bin is not used during the fit. For systematics, the maximum q_{inv} values was also varied to be 2.5 and 3.5 GeV.

The result of the fits using this procedure are shown in Chapter 6, including the desired femtoscopic information for $K_S^0 K_S^0$, $\Lambda\Lambda \oplus \overline{\Lambda}\,\overline{\Lambda}$ and $\Lambda\overline{\Lambda}$ correlations. For $K_S^0\Lambda \oplus K_S^0\overline{\Lambda}$, the signal observed is very small when compared to the background, making it difficult to stabilize the fit, returning non-physical results (high effective range, d_0), demanding further studies.

5.4 Systematic uncertainties

The systematic uncertainties in this analysis are defined by variations of event selections, single particle reconstruction, methods used in the two particle correlation measurements and fitting procedure. Most of systematic sources were presented along the text and can be gathered in the following topics:

- *Trigger reweighting*: as mentioned in Sec. 5.1, the multiplicity distributions are reweighted because of the effect of prescales applied to the triggers during the Run. To treat this effect, "From Bits" method is employed as default. To evaluate the systematic uncertainties, weights from the "From Lumi" method are used and also the case without reweighting, but only to correlations where data from different triggers are not merged.

- v_z *selection*: as default, the vertex longitudinal distance v_z is selected as $|v_z| < 15$ cm. To evaluate systematic uncertainties, the following selection was used: $|v_z| < 3$ cm and $3 < |v_z| < 15$ cm. This systematic only can be used for $K_S^0 K_S^0$ correlations due the small number of events for the other pairs.

- *Pileup filters*: the selections developed to remove events with PU contamination are described in Sec. 5.1.3. The olvFilter_pPb8TeV_dz1p07 is adopted

as default, while the other filters and the case without PU filter are also investigated as systematic uncertainty.

- V^0 *reconstruction*: a set of tighter and looser reconstruction selections are applied to the data to estimate the uncertainty from the V^0 candidates. For the tight cuts, both daughter transverse and longitudinal impact parameter significance > 1.25, $\cos \theta_p > 0.9999$ and the candidate decay length significance > 7.5 were used. For the loose cuts, the daughter transverse and longitudinal impact parameter significance > 1, $\cos \theta_p > 0.99$ and the candidate decay length significance > 2.5 were applied. The effect of V^0 efficiency is also included in this systematic study.

- *Misidentified V^0's*: the effect of misidentified candidates, presented in Sec. 5.2.1, are evaluated by varying the cuts from π-π, p-π and *e-e* hypotheses in ± 5 MeV.

- *Duplicated track removal*: systematic study for the duplicated track effect, Sec. 5.2.2, was performed by removing one mother instead of the two, based on the following criteria: i) by randomly selecting the mother to be eliminated; ii) mass value of the candidate far away from the V^0 PDG value; and iii) the worst $\chi^2/$ndf quality fit.

- *Invariant mass fit and purity correction*: To test the robustness of the invariant mass fit, a 2nd, a 3rd and a Chebychev 4th order polynomial combinatorial background shapes were used, instead of the standard 4th order polynomial. For the signal, the triple and quadruple Gaussians were employed, instead of the double Gaussian distribution. Those fits are also a good check for our purity correction method, but, in addition, the signal and background fraction was changed in $\pm 5\%$.

- *Peak and sideband definition*: a systematic study related to the definition of the peak and the sideband regions are used by changing the acceptance region in $\pm 0.5 \sigma$.

- *Mixing reference sample*: the systematic uncertainties associated with the choice of the reference sample are performed by varying the N_{mix} from 20 to 10 and 30 events. Also, the selection using $|\Delta v_z| < 2$ cm between the events used in the mixing was varied to $|\Delta v_z| < 0.5$ cm and no $|\Delta v_z|$ requirement.

- *Non-prompt contamination*: as default, the $\Lambda/\overline{\Lambda}$ contamination from $\Xi/\overline{\Xi}$ and $\Omega/\overline{\Omega}$ baryons are removed using the data-driven method. Here, the systematic studies were considered as the cases of Λ's/$\overline{\Lambda}$'s from $\Xi/\overline{\Xi}$ only or from $\Omega/\overline{\Omega}$ only are removed, and also the case where any $\Lambda/\overline{\Lambda}$ is removed (considering all prompt).

- *Fitting procedure*: during the femtoscopic fit some regions were choosen to obtain the physical parameters, which were varied to performe a systematic study. In the first part of the fit, where the non-femtoscopic background is fitted, the minimum value of q_{inv} is 0.5 GeV, this value was varied in ± 0.1 GeV and the maximum q_{inv} region as also been changed between 3, 4 and 5 GeV. In the second part of fit, in which the femtoscopic parameter are fitted, the maximum q_{inv} region is varied in $\pm$ 0.5 GeV. In the case of $\Lambda\Lambda \oplus \overline{\Lambda}\,\overline{\Lambda}$ correlations, the usage of Eq. (5.9) to parametrize the cluster contribution is included as systematic uncertainty here.

- *FSI parameters*: for $K_S^0 K_S^0$ correlations, the strong FSI paramaters coming from the $f_0(980)$ and $a_0(980)$ near threshold resonances can be used from measurements performed by low-energy experiments, as shown in Sec. 3.3 of Chapter 3. One of the parameter set is used as default while all the others are used as systematic uncertainties.

For each source of systematic effects investigated, the full femtoscopic fit is performed and we evaluate how much the parameters of interest changes by using:

$$\text{Systematics (in \%)} = 100 \times \left| \frac{X_{\text{std}} - X_{\text{sys}}}{X_{\text{std}}} \right|, \tag{5.11}$$

where, X_{std} and X_{sys} are the parameters obtained by using the standard selection and the ones from systematic variation, respectively. The maximum variation is taken as the final systematic from each source and the total systematic uncertainties are evaluated by adding all the listed sources in quadrature, considering that they are all independent.

Due to the small sample size for $\Lambda\overline{\Lambda}$ and $\Lambda\Lambda \oplus \overline{\Lambda}\,\overline{\Lambda}$ correlations, and the larger uncertainties, the systematic uncertainties are calculated by integrating the data in k_T and $N_{\text{trk}}^{\text{offline}}$, while in $K_S^0 K_S^0$ correlations each $N_{\text{trk}}^{\text{offline}}$ and k_T bin has a systematic uncertainty associated. As mentioned before, due the small signal observed for $K_S^0 \Lambda \oplus K_S^0 \overline{\Lambda}$ correlations, the fits are unstable and it is hard to draw

any conclusion. Because of that, no fit and systematic uncertainty is evaluated for that case. The final systematic uncertainties are shown in Table 5.3 for $\Lambda\overline{\Lambda}$, Table 5.4 for $\Lambda\Lambda \oplus \overline{\Lambda}\overline{\Lambda}$, and Tables 5.5, 5.6, 5.7 and 5.8 for $K_S^0 K_S^0$ correlations. In all the tables the NA means "not applicable" (e.g., cases with not enought number of pairs).

Table 5.3: Summary of systematic uncertainties (in %) for $\Lambda\overline{\Lambda}$ correlations

Source	λ	R_{inv}	$\Re f_0$	$\Im f_0$	d_0
Trigger reweighting	0	0	0	3	1
v_z selection	NA	NA	NA	NA	NA
Pileup filters	21	10	8	36	5
V^0 reconstruction	30	13	8	14	5
Misidentified V^0's	5	3	4	21	8
Duplicated track removal	2	1	1	1	1
Invariant mass fit and purity correction	2	1	1	1	1
Peak and sideband definition	24	9	17	18	2
Reference sample	7	6	5	22	6
Non-prompt contamination	3	2	1	1	2
Fitting procedure	7	10	5	10	18
Strong FSI parameters	NA	NA	NA	NA	NA
Total	45	22	22	53	22

Table 5.4: Summary of systematic uncertainties (in %) for $\Lambda\Lambda \oplus \overline{\Lambda}\overline{\Lambda}$ correlations

Source	λ	R_{inv}	f_0	d_0
Trigger reweighting	0	0	1	0
v_z selection	NA	NA	NA	NA
Pileup filters	18	4	14	2
V^0 reconstruction	58	24	40	24
Misidentified V^0's	11	2	4	0
Duplicated track removal	25	5	15	4
Invariant mass fit and purity correction	1	0	1	1
Peak and sideband definition	36	4	40	5
Reference sample	9	2	5	5
Non-prompt contamination	17	4	6	10
Fitting procedure	33	0	5	25
Strong FSI parameters	NA	NA	NA	NA
Total	85	26	60	37

Table 5.5: Summary of systematic uncertainties (in %) for R_{inv} and λ with k_T dependence (integrated in $0 < N_{trk}^{offline} < 400$), measured in $K_S^0 K_S^0$ femtoscopic correlations.

Source	k_T range in GeV									
	0 to 0.8		0.8 to 1.0		1.0 to 1.2		1.2 to 1.5		1.5 to 2.0	
	R_{inv}	λ	R_{inv}	λ	R_{inv}	λ	R_{inv}	λ	R_{inv}	λ
Trigger reweighting	1	0	0	0	0	0	0	1	0	1
v_z selection	2	6	1	3	1	2	3	3	8	3
Pileup filters	1	4	0	0	0	0	1	0	0	1
V^0 reconstruction	4	11	2	6	1	5	4	5	2	7
Misidentified V^0's	0	0	0	0	0	0	1	0	0	1
Duplicated track removal	2	4	1	4	0	5	1	5	1	7
Invariant mass fit and purity correction	1	1	1	1	0	0	3	4	0	1
Peak and sideband definition	1	1	2	2	1	2	0	1	0	2
Reference sample	1	2	1	1	1	1	1	1	1	1
Non-prompt contamination	NA	NA	NA	NA	NA	NA	NA	NA	NA	NA
Fitting procedure	2	1	3	1	5	4	5	4	6	3
Strong FSI parameters	0	0	0	0	0	0	0	0	4	4
Total	6	14	5	8	5	9	8	10	10	11

Table 5.6: Summary of systematic uncertainties (in %) for R_{inv} and λ, with $N_{trk}^{offline}$ dependence (integrated in $0 < k_T < 2$ GeV), from 0 to 90, measured in $K_S^0 K_S^0$ femtoscopic correlations.

Source	$N_{trk}^{offline}$ range									
	0 to 30		30 to 40		40 to 60		60 to 80		80 to 90	
	R_{inv}	λ	R_{inv}	λ	R_{inv}	λ	R_{inv}	λ	R_{inv}	λ
Trigger reweighting	1	0	1	0	0	0	1	1	1	2
v_z selection	12	6	3	2	4	5	2	4	3	6
Pileup filters	1	1	0	0	0	1	0	1	1	2
V^0 reconstruction	14	7	2	10	1	9	2	10	2	8
Misidentified V^0's	0	0	0	0	0	1	0	1	0	0
Duplicated track removal	4	4	1	4	1	5	0	6	0	5
Invariant mass fit and purity correction	1	1	1	1	0	1	0	1	0	1
Peak and sideband definition	1	2	2	1	0	1	1	2	2	1
Reference sample	1	1	1	1	0	1	0	1	0	1
Non-prompt contamination	NA	NA	NA	NA	NA	NA	NA	NA	NA	NA
Fitting procedure	8	3	14	8	5	2	2	3	4	1
Strong FSI parameters	9	18	0	1	2	1	0	2	0	0
Total	22	21	15	14	7	12	4	13	6	12

Table 5.7: Summary of systematic uncertainties (in %) for R_{inv} and λ, with $N_{trk}^{offline}$ dependence (integrated in $0 < k_T < 2$ GeV), from 90 to 185, measured in $K_S^0 K_S^0$ femtoscopic correlations.

Source	$N_{trk}^{offline}$ range									
	90 to 100		100 to 110		110 to 120		120 to 150		150 to 185	
	R_{inv}	λ	R_{inv}	λ	R_{inv}	λ	R_{inv}	λ	R_{inv}	λ
Trigger reweighting	0	1	0	0	2	2	0	2	4	2
v_z selection	1	3	1	3	1	3	5	2	3	3
Pileup filters	1	1	1	1	2	2	0	1	1	2
V^0 reconstruction	5	5	6	6	8	5	3	7	5	10
Misidentified V^0's	0	0	0	0	0	1	0	0	1	1
Duplicated track removal	1	5	0	5	1	5	2	4	2	5
Invariant mass fit and purity correction	1	1	0	1	1	1	1	1	1	1
Peak and sideband definition	0	3	2	4	3	5	2	1	2	1
Reference sample	1	1	1	1	1	1	1	2	1	1
Non-prompt contamination	NA	NA	NA	NA	NA	NA	NA	NA	NA	NA
Fitting procedure	3	1	3	1	3	2	1	1	0	0
Strong FSI parameters	0	0	0	0	0	0	0	0	0	0
Total	6	9	7	9	10	10	7	9	8	12

Table 5.8: Summary of systematic uncertainties (in %) for R_{inv} and λ, with $N_{\text{trk}}^{\text{offline}}$ dependence (integrated in $0 < k_T < 2$ GeV), from 185 to 400, measured in $K_S^0 K_S^0$ femtoscopic correlations.

| Source | $N_{\text{trk}}^{\text{offline}}$ range | | | | | | | | | |
| | 185 to 200 | | 200 to 215 | | 215 to 230 | | 230 to 250 | | 250 to 400 | |
	R_{inv}	λ	R_{inv}	λ	R_{inv}	λ	R_{inv}	λ	R_{inv}	λ
Trigger reweighting	0	1	1	1	0	1	3	3	0	0
v_z selection	4	6	2	1	1	4	9	18	4	5
Pileup filters	0	1	5	2	6	4	3	4	4	6
V^0 reconstruction	5	6	5	4	10	4	7	3	13	9
Misidentified V^0's	0	0	1	1	0	1	1	2	2	4
Duplicated track removal	3	5	0	5	4	2	5	2	5	1
Invariant mass fit and purity correction	0	2	2	1	1	2	1	3	1	2
Peak and sideband definition	1	2	1	2	2	2	5	7	2	5
Reference sample	1	1	2	1	2	2	2	2	1	3
Non-prompt contamination	NA	NA	NA	NA	NA	NA	NA	NA	NA	NA
Fitting procedure	1	1	1	0	0	0	1	0	0	1
Strong FSI parameters	0	0	1	3	0	0	0	0	0	1
Total	7	10	8	8	13	8	14	20	15	14

Chapter 6

Experimental Results

This chapter shows the preliminary results obtained by using the data analysis methods and tool employed, including the systematic uncertainties evaluation described in Chapter 5, using the data collected by the CMS experiment in pPb collisions at $\sqrt{s_{NN}} = 8.16$ TeV for minimum bias and high multiplicity event samples. The measurements of meson-meson ($K_S^0 K_S^0$), meson-baryon ($K_S^0 \Lambda \oplus K_S^0 \overline{\Lambda}$), baryon-antibaryon ($\Lambda \overline{\Lambda}$) and baryon-baryon ($\Lambda \Lambda \oplus \overline{\Lambda} \, \overline{\Lambda}$) correlations are performed to study effects from quantum statistics, strong final state interactions and non-femtoscopic background. Most of the results are presented in terms of the source size (R_{inv}), the correlation intensity parameter (λ) and scattering observables ($\Re f_0$, $\Im f_0$, d_0). Comparisons with data from previous measurements and theory are also shown. All results presented in this thesis correspond to an analysis that is going through an internal CMS publication process and will became public as a paper later.

6.1 $K_S^0 K_S^0$ correlations

The neutral kaon correlations provide information from Bose-Einstein quantum statistic correlations ($\left|K^0 K^0\right\rangle$ and $\left|\overline{K}^0 \overline{K}^0\right\rangle$) and strong final state interactions (mainly from $\left|K^0 \overline{K}^0\right\rangle$ and $\left|\overline{K}^0 K^0\right\rangle$) the latter dominated by $f_0(980)$ and $a_0(980)$ resonances. In the $K_S^0 K_S^0$ case, the parameters of strong FSI can be fixed, as discussed in Chapter 3, and the correlations used to investigate the source size, R_{inv}, and intensity parameter, λ. Due to the large number of $K_S^0 K_S^0$ pairs available in our data sample, it is possible to study the dependence of R_{inv} and λ with charged particle multiplicity, $N_{trk}^{offline}$, and average transverse momentum, k_T, of the K_S^0 pairs. In each of such bins, the femtoscopic fit, Eq. (5.10), is performed, where observables and cluster parameters are extracted. An example of such fit is shown in Fig. 6.1, for $185 < N_{trk}^{offline} < 200$ and $0 < k_T < 2$ GeV as illustration. An example of the cluster parameters extracted in this same multiplicity range, for three different

pair relative momentum intervals is shown at Table 6.1.
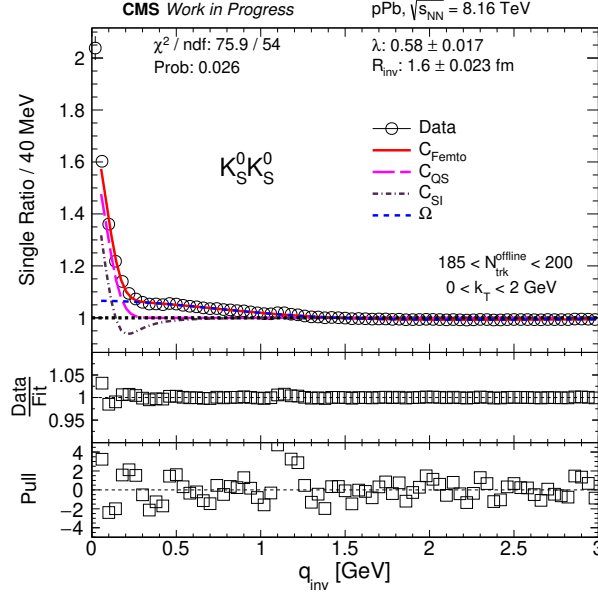
Figure 6.1: Single ratio of $K_S^0 K_S^0$ pairs as a function of q_{inv} (black open circles) integrated in k_T ($0 < k_T < 2$ GeV) and multiplicity range ($185 < N_{trk}^{offline} < 200$). The fit is performed using Eq. (5.10), where the full fit (red solid line), the Bose-Einstein quantum statistic term (pink long dashed line), the strong FSI (purple dash-dotted line) and the non-femtoscopic backgrond (blue short dashed line) are shown. The parameters extracted from the fit, including only statistic uncertainties, fit quality (χ^2/ndf), data/fit ratio and pull distributions are shown in the plot. More informations in the text.

Table 6.1: Non-femtoscopic parameters obtained with the fit in the multiplicity range [185, 200], as shown in Fig. 6.1 using Eq. (5.8), for different low-q_{inv} regions. The statistical uncertainties are given by `ROOT` TMinuit.

Parameter	$q_{inv} > 0.5$ GeV	$q_{inv} > 0.4$ GeV	$q_{inv} > 0.6$ GeV
N	0.9851 ± 0.0018	0.9842 ± 0.0018	0.9853 ± 0.0019
β	0.0816 ± 0.0014	0.0813 ± 0.0014	0.0816 ± 0.0146
σ [fm^{-1}]	0.1929 ± 0.0041	0.1902 ± 0.0036	0.1936 ± 0.0045
δ [fm]	0.0158 ± 0.0036	0.0176 ± 0.0036	0.0155 ± 0.0038

The dependence on multiplicity of tracks, $N_{trk}^{offline}$, and on the pair average transverse momentum, k_T, of R_{inv} and λ are shown in Figs. 6.2 and 6.3, respectively. Figure 6.2 (left) shows that the apparent source size, R_{inv}, steadily increases for multiplicities ranging from MB to HM events, an effect that can also be seen in

the plot showing the k_T dependence, in Fig. 6.3 (left), by comparing the two sets of values of R_{inv} in the MB and HM ranges. On the other hand, the λ parameter decreases in lower multiplicities and for $N_{trk}^{offline} > 50$ it shows a constante behavior, within the uncertainties. In terms of the pair average transverse momentum, the radius parameter decreases for increasing k_T, showing that the a smaller portion of the source is accessible to femtoscopy for larger values of k_T and is an indication of the expansion of the system due dynamical effects. In the case of λ, the parameter slightly increases with k_T.
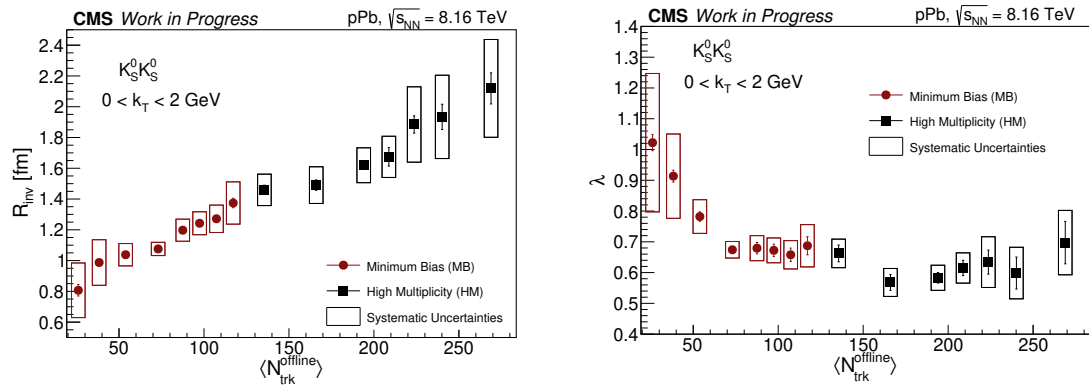
Figure 6.2: Multiplicity dependence of R_{inv} (left) and λ (right) from minimum bias (red circles) and high multiplicity (black squares) data samples extracted from femtoscopic fits. The boxes represents the systematic uncertainties.
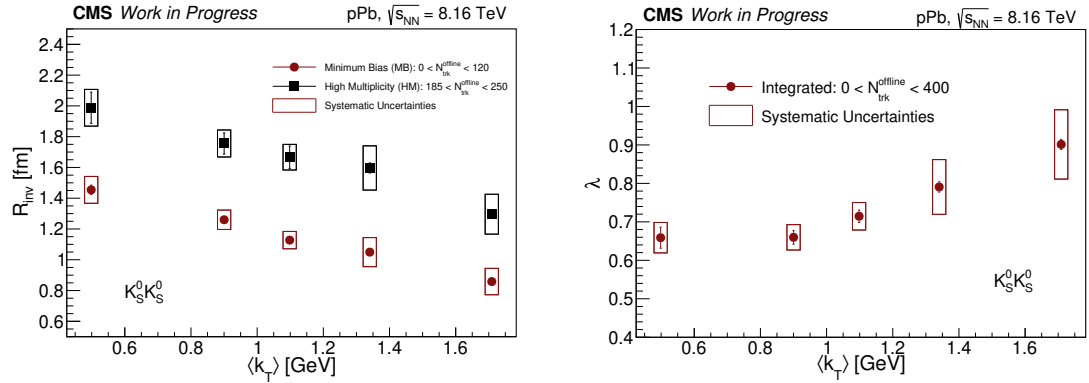
Figure 6.3: Pair average transverse momentum dependence of R_{inv} (left) and λ (right), integrated in $N_{trk}^{offline}$ (0 to 400), extracted from femtoscopic fits. The boxes represents the systematic uncertainties.

6.2 $K_S^0 \Lambda \oplus K_S^0 \overline{\Lambda}$ correlations

The measured single ratio for the $K_S^0 \Lambda \oplus K_S^0 \overline{\Lambda}$ interaction is dominated by the non-femtoscopic Gaussian-like behavior and the observed effect of strong FSI signal is very small (less than 3%, including the statistic uncertainties), as can be seen at Fig. 6.4 (black open circles), integrate in k_T ($0 < k_T < 2$ GeV) and $N_{trk}^{offline}$($0 < N_{trk}^{offline} < 400$ GeV). Such small effect makes the femtoscopic fit of the correlation function becomes unstable and the Lednicky-Lyubolshitz model fails to obtain the scattering and source parameters, returning unphysical results. One possible interpretation for these non-physical results could be the non-applicability of the effective range expansion (which is an approximation) for the $K_S^0 \Lambda \oplus K_S^0 \overline{\Lambda}$ system and than a more complex theoretical development would be needed [233]. Therefore, no femtoscopic fit is considered in this case for avoiding possible mistaken interpretation of the data.
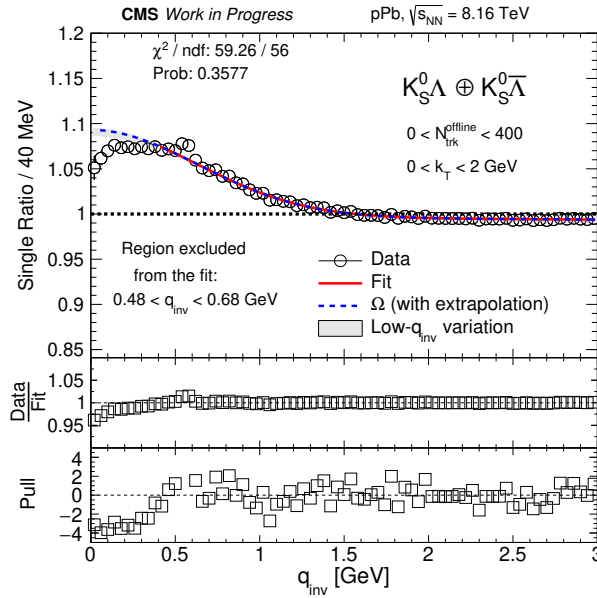
Figure 6.4: Single ratio of $K_S^0 \Lambda \oplus K_S^0 \overline{\Lambda}$ pairs as a function of q_{inv} integrated in k_T ($0 < k_T < 2$ GeV) and multiplicity ($0 < N_{trk}^{offline} < 400$). The data is represented by the black open circles, the standard non-femtoscopic fit by the red solid line (for $q_{inv} > 0.4$ GeV), the low-q_{inv} extrapolation by the blue dashed line and the gray band corresponds to the q_{inv} variation. The range $0.48 < q_{inv} < 0.68$ is removed from the fit to remove the effect of resonances. The ratio data/fit and the pull are also shown. More informations in the text.

However, as shown in Fig. 6.4, is still possible, in addition to the data points (black open circles), to extract additional information related to the non-femtoscopic

background. In the first step of the correlation fit, the $\Omega(q_{\text{inv}})$ function is adjusted from a region outside of the femtoscopic signal, usually $q_{\text{inv}} > 0.5\,\text{GeV}$, and extract the cluster parameters using Eq. (5.8). Here, the same procedure is employed for three different cases: $q_{\text{inv}} > 0.4\,\text{GeV}$ (standard), $q_{\text{inv}} > 0.2\,\text{GeV}$ and $q_{\text{inv}} > 0.7\,\text{GeV}$, the last two are studied as systematic effects; as shown in Table 6.2, that includes the cluster parameters obtained in each range. The fit[1] of the non-femtoscopic background is shown at Fig. 6.4 as the red solid line (for standard), together with the extrapolation for low-q_{inv} that is represented by the dashed-dotted purple line and the systematic variation that can be seen as the gray band. It is interesting to observe that even applying a large variation as systematics studies, the effect is still small in all the q_{inv} range. Note that, the standard choise corresponding to $q_{\text{inv}} > 0.4\,\text{GeV}$ is used because the range from 0.48 to 0.68 must be removed from the fit for avoiding a possible resonance effect. Therefore, both the data points and the non-femtoscopic background (including the systematic uncertainties) will be available to test theoretical models.

Table 6.2: Non-femtoscopic parameters obtained with the fit, as shown in Fig. 6.4 using Eq. (5.8), for different low-q_{inv} regions. The statistical uncertainties are given by ROOT TMinuit.

Parameter	$q_{\text{inv}} > 0.4\,\text{GeV}$	$q_{\text{inv}} > 0.2\,\text{GeV}$	$q_{\text{inv}} > 0.7\,\text{GeV}$
N	0.9972 ± 0.0015	0.9952 ± 0.0015	0.9980 ± 0.0016
β	0.0962 ± 0.0021	0.0917 ± 0.0016	0.0996 ± 0.0037
$\sigma\,[\text{fm}^{-1}]$	0.2197 ± 0.0040	0.2108 ± 0.0032	0.2246 ± 0.0058
$\delta\,[\text{fm}]$	-0.0055 ± 0.0030	-0.0020 ± 0.0030	-0.0076 ± 0.0030

6.3 $\Lambda\Lambda \oplus \overline{\Lambda}\,\overline{\Lambda}$ correlations

Correlations between identical lambdas are particularly interesting because they contain effects from Fermi-Dirac quantum statistics and strong final state interactions; these correlations (baryon-baryon in general) also break the standard Gaussian non-femtoscopic behavior (above unity), showing an anticorrelation (below unity) in q_{inv} values between 0.5 and 3 GeV (see Sec. 5.3.2 of Chapter 5). Furthermore, the lack of experimental measurements about the behavior of the correlation function (attractive or repulsive), makes this analysis even more interesting.

---

[1]The χ^2/ndf presented in Fig. 6.4 is related with the range $q_{\text{inv}} > 0.4\,\text{GeV}$ (red solid line).

Figure 6.5 shows the single ratio measured for $\Lambda\Lambda \oplus \overline{\Lambda}\overline{\Lambda}$ pairs as function of q_{inv} (black open circles), integrated in $0 < k_T < 2$ GeV (with $\langle k_T \rangle \approx 1.14$ GeV) and $0 < N_{trk}^{offline} < 400$ (with $\left\langle N_{trk}^{offline} \right\rangle \approx 103$). The full femtoscopic fit is performed using Eq. (5.10) (red solid line), counting with the contributions from: Fermi-Dirac quantum statistic (pink long dashed line), strong FSI (purple dash-dotted line) and non-femtoscopic backgrond (blue short dashed line). The fit performance is very good, with a $\chi^2/\mathrm{ndf} \approx 0.933$, resulting in the physical observables shown in Table 6.3 and cluster parameters in Table 6.4. One of the most interesting results here is that a positive f_0 was obtained, indicating that the strong part of the $\Lambda\Lambda \oplus \overline{\Lambda}\overline{\Lambda}$ femtoscopic correlation has an "attractive" behavior (repulsive strong interaction potential), being consistent with most of the theoretical/phenomenological models [241] and experimental results from other (anti)baryon-(anti)baryon correlations (see compiled results in Ref. [210]). This result also suggests that an exotic H-dibaryon bound state does not exist, since this would be possible in case of negative f_0 values. The R_{inv} measured is similar to the value obtained by ALICE collaboration[2] in pPb collisions at 5.02 GeV, $R_{inv}^{ALICE} = 1.427 \pm 0.007$ (stat.)$^{+0.001}_{-0.014}$ (syst.) fm. Due to the big uncertainties it is not possible to draw any clear conclusion about the λ parameter.

In addition, the measured scattering observables for $\Lambda\Lambda \oplus \overline{\Lambda}\overline{\Lambda}$ correlations, are compared with other results available in the literature. Figure 6.6 shows the d_0 versus $\Re f_0$ plot for $\Lambda\Lambda \oplus \overline{\Lambda}\overline{\Lambda}$ correlations in pPb collisions (red marker) at $\sqrt{s_{NN}} = 8.16$ TeV, compared with Lattice QCD results from the HAL QCD collaboration [210, 332], previous measurements from STAR in AuAu collisions at $\sqrt{s_{NN}} = 200$ GeV [240] (black marker), STAR reanalysis (gray area) performed by K. Morita et. al. [241] and NAGARA[3] events [238, 239] (blue markers). Our results show good agreement, within the uncertainties, with lattice QCD and with all experimental measurements, except for the 2015 STAR results.

---

[2]In this analysis, R_{inv} was fixed based on previous measurements in pp femtoscopic correlations.
[3]In the papers from NAGARA events [238, 239], only the central values are available (without uncertainties).
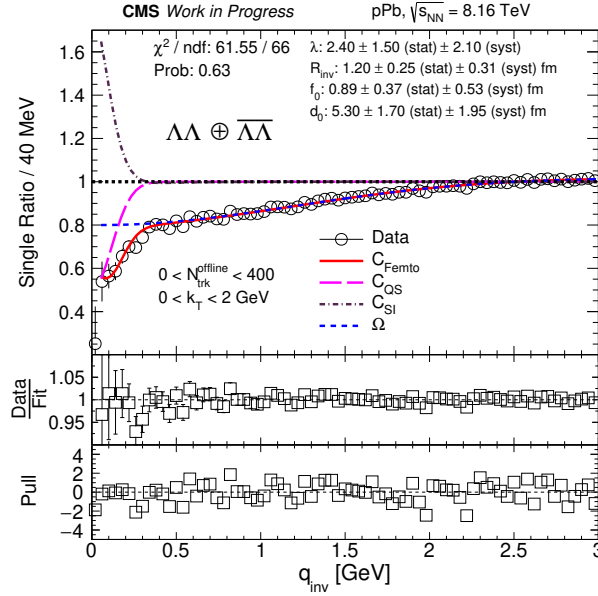
Figure 6.5: Single ratio of $\Lambda\Lambda \oplus \overline{\Lambda}\overline{\Lambda}$ pairs as a function of q_{inv} (black open circles) integrated in k_T ($0 < k_T < 2$ GeV) and multiplicity ($0 < N_{\text{trk}}^{\text{offline}} < 400$). The fit is performed using Eq. (5.10), where the full fit (red solid line), the Fermi-Dirac quantum statistic term (pink long dashed line), the strong FSI (purple dash-dotted line) and the non-femtoscopic backgrond (blue short dashed line) are shown. The parameters extracted from the fit, including statistic and systematic uncertainties, the fit quality (χ^2/ndf), data/fit ratio and pull distributions are shown in the plot. More informations in the text.

Table 6.3: Physical parameters extracted using the femtoscopic fit, Eq. (5.10), for $\Lambda\Lambda \oplus \overline{\Lambda}\overline{\Lambda}$ correlations. The statistical uncertainties are given by `ROOT` TMinuit and the systematic uncertainties are those discussed in Chapter 5.

Parameter	Fitted value
λ	2.40 ± 1.50 (stat) ± 2.10 (syst)
R_{inv}	1.20 ± 0.25 (stat) ± 0.31 (syst) fm
f_0	0.86 ± 0.37 (stat) ± 0.53 (syst) fm
d_0	5.30 ± 1.70 (stat) ± 1.95 (syst) fm

Table 6.4: Non-femtoscopic parameters obtained with the fit, as shown at Fig. 6.5, using Eq. (5.8), for different low-q_{inv} regions. The statistical uncertainties are given by `ROOT` TMinuit.

Parameter	$q_{inv} > 0.5$ GeV	$q_{inv} > 0.4$ GeV	$q_{inv} > 0.6$ GeV
N	1.066 ± 0.0861	1.0288 ± 0.0659	1.08386 ± 0.1048
β	-0.2492 ± 0.0502	-0.2293 ± 0.0404	-0.2586 ± 0.0170
σ [fm^{-1}]	0.1141 ± 0.0113	0.1203 ± 0.0107	0.1115 ± 0.0129
δ [fm]	-0.0660 ± 0.1088	-0.0133 ± 0.1006	-0.08960 ± 0.1375
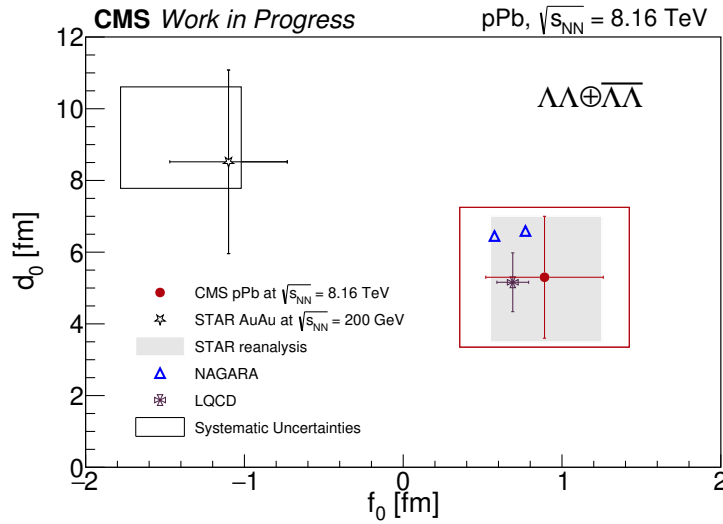
Figure 6.6: Scattering observables, d_0 versus f_0, extracted using Lednicky-Lyubolshitz model for $\Lambda\Lambda \oplus \overline{\Lambda}\,\overline{\Lambda}$ pairs in pPb collisions at $\sqrt{s_{NN}} = 8.16$ TeV (red marker), compared with Lattice QCD results [210, 332] (purple marker) and previous measurements from STAR at AuAu collisions at $\sqrt{s_{NN}} = 200$ GeV [240] (black marker), STAR reanalysis [241] (gray area) and NAGARA events [238, 239] (blue markers).

6.4 $\Lambda\overline{\Lambda}$ correlations

In the case of $\Lambda\overline{\Lambda}$ correlation, the effect of quantum statistics is not present, but the LL model can still be used to estimate the scattering observables related to the strong final state interactions ($\Re f_0$, $\Im f_0$, d_0), besides the R_{inv} and λ parameters. In this case, the f_0 can be divided in real and imaginary parts, corresponding to elastic and inelastic interactions, respectively, thus giving more information about the processes involved.

The single ratio measured for $\Lambda\overline{\Lambda}$ pairs as function of q_{inv} (black open circles)

integrated in $0 < k_T < 2$ GeV (with $\langle k_T \rangle \approx 1.15$ GeV) and $0 < N_{trk}^{offline} < 400$ (with $\left\langle N_{trk}^{offline} \right\rangle \approx 101$) is shown at Fig. 6.7. Being non-identical particles, the femtoscopic fit (red solid line) contains contribution from strong FSI (purple dash-dotted line) and non-femtoscopic backgrond (blue dashed line). The χ^2/ndf of the fit is ≈ 1.19 and the values of extracted physical parameters are shown in Table 6.5, while the cluster parameters are shown in Table 6.6.
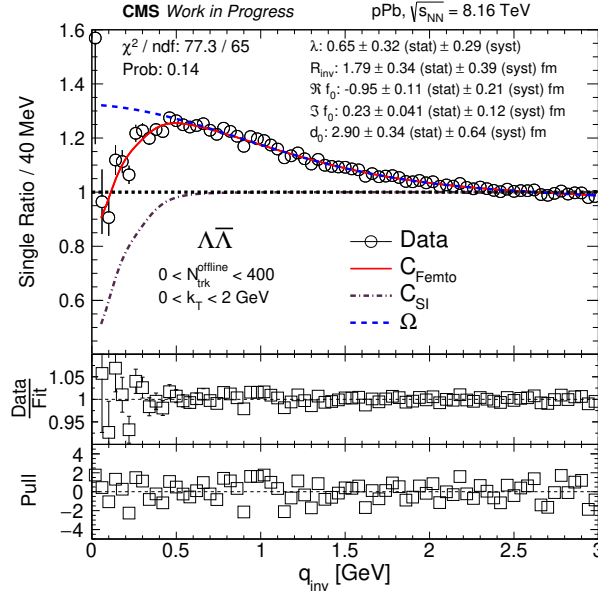
Figure 6.7: Single ratio of $\Lambda\overline{\Lambda}$ pairs as function of q_{inv} (black open circles) integrated in k_T ($0 < k_T < 2$ GeV) and multiplicity ($0 < N_{trk}^{offline} < 400$). The fit is performed using Eq. (5.10) without the quantum statistic term (non-identical particles); the full fit (red solid line), the strong FSI (purple dash-dotted line) and the non-femtoscopic background (blue dashed line) are shown. The parameters extracted from the fit including statistic and systematic uncertainties, the fit quality (χ^2/ndf), data/fit ratio and pull distributions are also shown in the plot. More informations in the text.

Table 6.5: Physical parameters extracted using the femtoscopic fit, Eq. (5.10), for $\Lambda\overline{\Lambda}$ correlations. The statistical uncertainties are given by `ROOT` TMinuit and the systematic uncertainties are those discussed in Chapter 5.

Parameter	Fitted value
λ	0.63 ± 0.32 (stat) ± 0.29 (syst)
R_{inv}	1.79 ± 0.34 (stat) ± 0.39 (syst) fm
$\Re f_0$	-0.95 ± 0.11 (stat) ± 0.21 (syst) fm
$\Im f_0$	0.23 ± 0.04 (stat) ± 0.12 (syst) fm
d_0	2.90 ± 0.34 (stat) ± 0.64 (syst) fm

Table 6.6: Non-femtoscopic parameters obtained with the fit, as shown in Fig. 6.5, using Eq. (5.8), for different low-q_{inv} regions. The statistical uncertainties are given by `ROOT` TMinuit.

Parameter	$q_{\text{inv}} > 0.5$ GeV	$q_{\text{inv}} > 0.4$ GeV	$q_{\text{inv}} > 0.6$ GeV
N	1.065 ± 0.0227	1.0529 ± 0.0246	1.0768 ± 0.0213
β	0.2426 ± 0.0197	0.2481 ± 0.0224	0.2403 ± 0.0170
σ [fm^{-1}]	0.1546 ± 0.0072	0.1498 ± 0.0066	0.1605 ± 0.0081
δ [fm]	-0.1242 ± 0.0355	-0.1059 ± 0.038	-0.1420 ± 0.0330

Differently from the case of identical lambda's, here $\Re f_0 < 0$, which indicates a "repulsive" femtoscopic behavior (attractive strong interaction potential) or a possible bound state formation. This can be checked using the effective range, where $d_0 > |f_0|/2$ (see Chapter 3) stands for a repulsive effect. Furthermore, the present result is even more interesting because it shows that strong FSI (for baryons) follow a pattern: baryon-baryon femtoscopic correlations presents an "attractive" behavior, while baryon-antibarion femtoscopic correlations show a "repulsive" behavior.

A non-zero imaginary part of f_0 ($\Im f_0 > 0$) was measured, indicating that inelastic interactions are happening between those hadrons, i.e. $\Lambda\overline{\Lambda}$ interaction indeed corresponding to a particle-antiparticle annihilation process. In terms of the radii, there is no other experimental measurement in pPb for $\Lambda\overline{\Lambda}$, however, it is possible to compare this result with the R_{inv} from $\Lambda\Lambda \oplus \overline{\Lambda}\overline{\Lambda}$ correlations (previous section), once these particles have the same mass and similar $\langle k_T \rangle$ and $\left\langle N_{\text{trk}}^{\text{offline}} \right\rangle$. Comparing the results from Fig. 6.5 and Fig. 6.7, it can be seen that the measured R_{inv} values are in agreement within the uncertainties for $\Lambda\Lambda \oplus \overline{\Lambda}\overline{\Lambda}$ and $\Lambda\overline{\Lambda}$ correlations.

6.4.1 Multiplicity dependence

The data sample available for $\Lambda\overline{\Lambda}$ correlations allows to perform the study of scattering quantities as function of multiplicity. This is the first time that such a dependence is measured in small colliding systems for the case of correlations involving Λ's. The measured values of the $\Re f_0$, $\Im f_0$, d_0 observables come from interactions happening after the emission, therefore those parameters should not depend on $N_{\text{trk}}^{\text{offline}}$, which could be used as an additional check/result.

Figure 6.8 shows the $\Lambda\overline{\Lambda}$ single ratios as function of q_{inv}, for minimum bias

(left), $0 < N_{trk}^{offline} < 120$ with $\left\langle N_{trk}^{offline} \right\rangle \approx 79$, and high multiplicity (right), $185 < N_{trk}^{offline} < 250$ with $\left\langle N_{trk}^{offline} \right\rangle \approx 205$, (black open circles) datasets. The data is fitted using the LL model together with the effect of the non-femtoscopic background, as discussed in the previous section. The R_{inv} increases for events with higher $N_{trk}^{offline}$($R_{inv} = 1.76 \pm 0.35$ fm for MB and $R_{inv} = 2.192 \pm 0.95$ fm for HM), as expected, while the values of the scattering observables are in agreement within the uncertainties, for both MB and HM. The λ parameter also increases, however the uncertainty in the case of HM is large, making it difficult to draw any conclusion. Figure 6.9 shows the $N_{trk}^{offline}$dependence of $\Re f_0$ (top), $\Im f_0$ (middle) and d_0 (bottom). As previously mentioned, the MB and HM are consistent and can be fitted by a constant fit[4], with the results in agreement, within the uncertanties. Therefore, the scattering parameters obtained in different multiplicities are consistent within uncertainties, as expected from final state interactions.
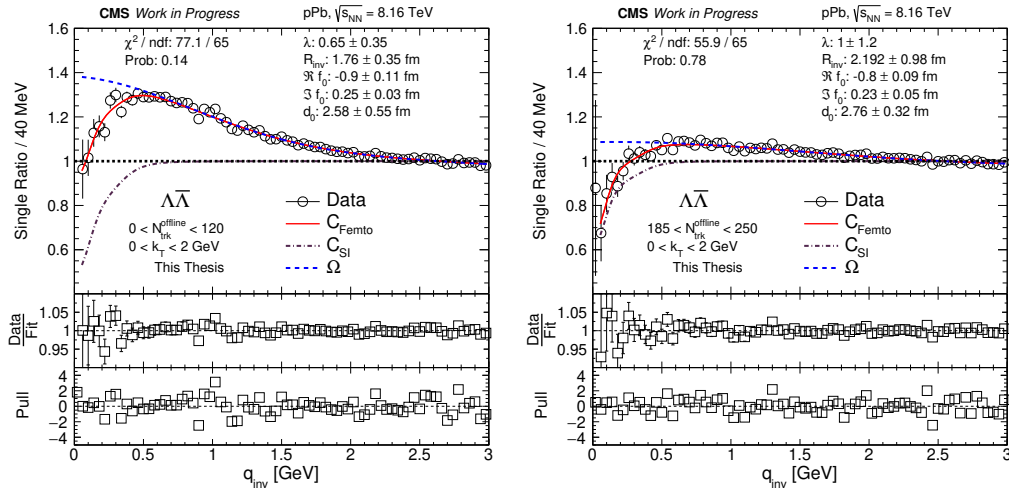
Figure 6.8: Single ratio of $\Lambda\overline{\Lambda}$ pairs as a function of q_{inv} (black open circles) in two multiplicity bins: $0 < N_{trk}^{offline} < 120$ (left) and $185 < N_{trk}^{offline} < 250$ (right), both cases integrated in k_T ($0 < k_T < 2$ GeV). The fit is shown with the lines representing the same contributions as in Fig. 6.7. More informations in the text.

---

[4]In the constant fit only statistical uncertainties are considered. The systematic uncertainties shown are the ones obtained with the multiplicity integrated sample (see Sec. 5.4 of Chapter 5).
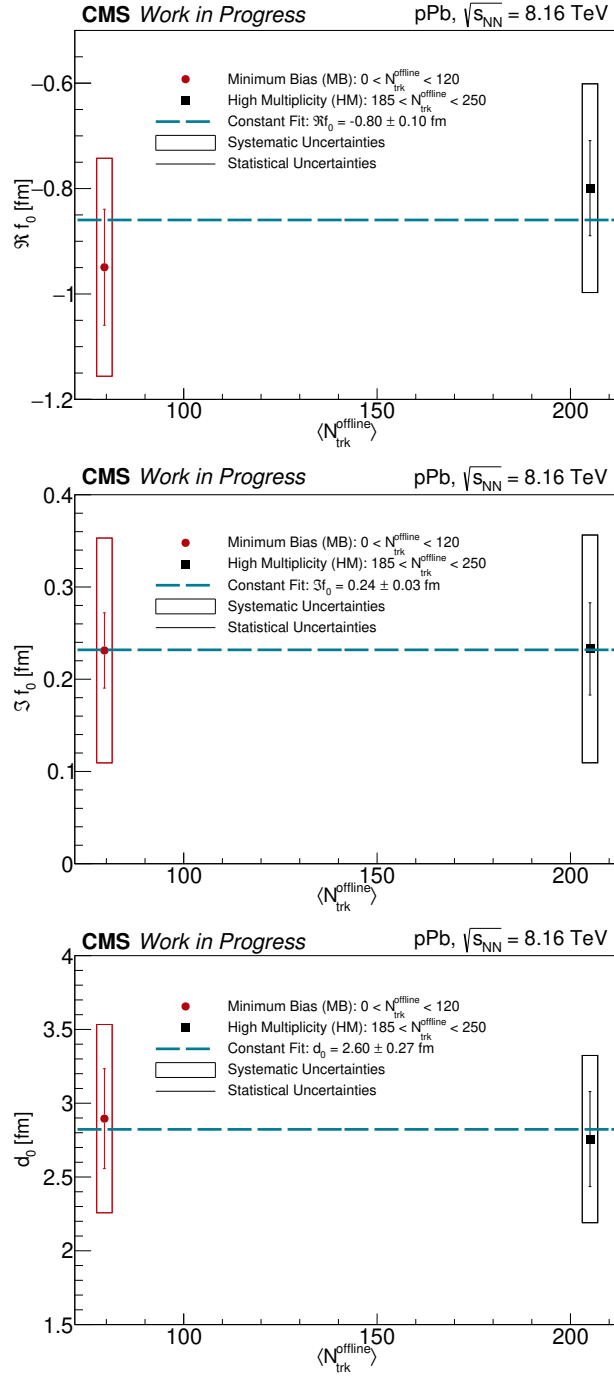
Figure 6.9: Scattering parameters $\Re f_0$ (top), $\Im f_0$ (middle) and d_0 (bottom), as a function of multiplicity, for minimum bias (red circle), $0 < N_{trk}^{offline} < 120$, and high multiplicity (black square), $185 < N_{trk}^{offline} < 250$, samples. The blue-dashed line represents a constant fit. Both statistical (lines) and systematic uncertainties (boxes) are shown. More informations in the text.

6.4.2 Comparison with other experiments

The observables obtained in the current $\Lambda\overline{\Lambda}$ analysis are compared with several experimental results available in the literature, for baryon-antibaryon interactions, that were measured using different apparatus and different energy scales.

Figure 6.10 shows the d_0 versus $\Re f_0$ plot, where our $\Lambda\overline{\Lambda}$ result, in pPb collisions (red marker) at $\sqrt{s_{\text{NN}}} = 8.16$ TeV, is compared with $p\overline{\Lambda} \oplus \overline{p}\Lambda$ (green marker) and $\Lambda\overline{\Lambda}$ (black marker) measurements by ALICE collaboration in PbPb collisions at $\sqrt{s_{\text{NN}}} = 2.76$ and 5.02 TeV [212], and $p\bar{p}$ interactions (blue marker) from a lower energy experiment [251]. Figure 6.11 shows the $\Im f_0$ versus $\Re f_0$ plot, also comparing our results with the measurements from ALICE [212] and additional low energy scattering experiments [251, 253, 254]. For all observables in Figs. 6.10 and 6.11 the same behavior is present and a good agreement is seen, between CMS and ALICE collaborations for $\Lambda\overline{\Lambda}$ correlations, which is expected, since final state interaction should not depend on the multiplicities/centralities related to the different colliding systems investigated. In addition, it is interesting to see that even for baryon-antibaryon pairs formed by different particle species, a similar "repulsive" behavior (attractive strong interaction potential) is seen, including similar scattering parameter values.

These results indicate that the strong FSI observables do not depend on multiplicity/centrality or on the particle species used in baryon-antibaryon correlation studies. In addition, a behavior practically energy independent is suggested from Fig. 6.10 and 6.11.
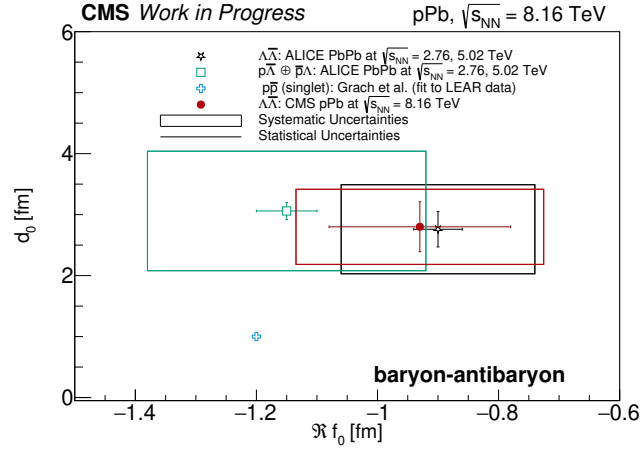
Figure 6.10: Scattering observables, d_0 versus f_0, extracted using Lednicky-Lyubolshitz model for $\Lambda\overline{\Lambda}$ pairs in pPb collisions at $\sqrt{s_{\mathrm{NN}}} = 8.16$ TeV (red solid circle), compared with $p\overline{\Lambda} \oplus \overline{p}\Lambda$ and $\Lambda\overline{\Lambda}$ measurements from ALICE collaboration in PbPb collisions at $\sqrt{s_{\mathrm{NN}}} = 2.76$ and 5.02 TeV [212] and $p\bar{p}$ (singlet) interaction from lower energy experiments [251]. Statistical (lines) and systematic (boxes) uncertainties are shown.
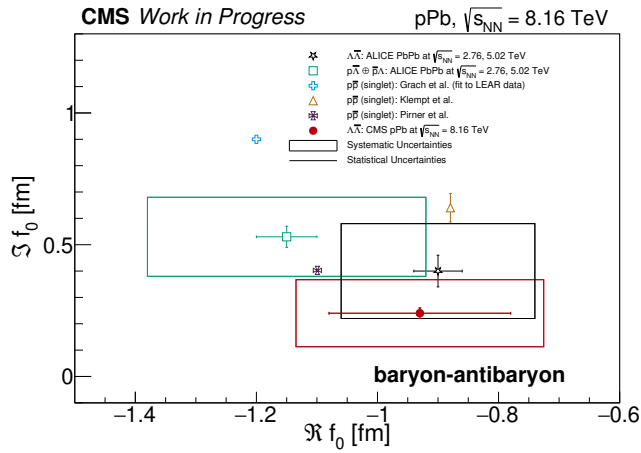
Figure 6.11: Scattering observables, $\Im f_0$ versus $\Re f_0$, extracted using Lednicky-Lyubolshitz model for $\Lambda\overline{\Lambda}$ pairs in pPb collisions at $\sqrt{s_{\mathrm{NN}}} = 8.16$ TeV (red solid circle), compared with $p\overline{\Lambda} \oplus \overline{p}\Lambda$ and $\Lambda\overline{\Lambda}$ measurements from ALICE collaboration in PbPb collisions at $\sqrt{s_{\mathrm{NN}}} = 2.76$ and 5.02 TeV [212] and $p\bar{p}$ (singlet) interaction from lower energy experiments [251, 253, 254]. Statistical (lines) and systematic (boxes) uncertainties are shown.

Chapter 7

Summary and Outlook

A femtoscopic analysis performed in one spatial dimension is presented using all pair combinations of neutral strange particles, K_S^0, Λ and $\overline{\Lambda}$. The studies are performed for the first time in a wide range of charged particle multiplicities with data from proton-lead collisions at $\sqrt{s_{NN}} = 8.16$ TeV collected by the CMS experiment in 2016.

This thesis starts with an overview of strongly interacting particles, quantum chromodynamics and the quark-gluon plasma. Then, a historical and theoretical overview of femtoscopy is presented, discussing the contributions from quantum statistics and final state interactions effects. Next, a brief description of the CMS experiment is shown and details about the data analysis techniques are described. Finally, the results obtained in this analysis are presented and discussed.

The correlation between identical neutral kaons ($K_S^0 K_S^0$) is important because it contains effects from both Bose-Einstein correlations ($\left|K^0 K^0\right\rangle$ and $\left|\overline{K}^0 \overline{K}^0\right\rangle$ contribution) and strong final state interactions (from $\left|K^0 \overline{K}^0\right\rangle$ and $\left|\overline{K}^0 K^0\right\rangle$). In this case, the femtoscopic correlations can be measured to investigate the source size dependence on charged particle multiplicity and on the pair average transverse momentum, since the effect of strong FSI is dominated by $f_0(980)$ and $a_0(980)$ resonances and the strong FSI parameters can be fixed by results from lower energy experiments. Due to the large number of $K_S^0 K_S^0$ pairs available in our data sample, this analysis was performed with a large number of multiplicity bins (15, in total). The obtained R_{inv} values increase with charged particle multiplicity and decreases for increasing k_T values, showing that a smaller portion of the source is accessible to femtoscopy for larger values of k_T, which is an indication of the expansion of the system formed in the collision.

For $K_S^0 \Lambda \oplus K_S^0 \overline{\Lambda}$ correlations, the signal of strong final state interactions at low q_{inv} is small, less than 3%, when compared with the non-femtoscopic background, which causes instabilities in the method used to fit the correlation function. In consequence, the Lednicky-Lyubolshitz model fails to obtain the physical fit parameters. To avoid misleading interpretations, no femtoscopic fit is considered

for these correlations. However, the single ratio data points and estimation of non-femtoscopic background are provided to test theoretical models.

In the case of identical lambda correlations ($\Lambda\Lambda \oplus \overline{\Lambda}\,\overline{\Lambda}$), a system size of $R_{\mathrm{inv}} = 1.20 \pm 0.25$ (stat) ± 0.31 (syst) fm was measured considering effects from both Fermi-Dirac quantum statistics and strong final state interactions. The scattering observables measured were the scattering length, $f_0 = 0.86 \pm 0.37$ (stat) ± 0.53 (syst) fm, and the effective range, $d_0 = 5.30 \pm 1.70$ (stat) ± 1.95 (syst) fm. The fact that f_0 is positive indicates an "attractive" femtoscopic behavior, corresponding to a repulsive strong interaction potential, which is consistent with previous (anti)baryon-(anti)baryon theoretical/phenomenological and experimental studies. This result also suggests the non-existence of an exotic H-dibaryon bound state that could exist only for negative values of f_0. Our measurements was also compared with $\Lambda\Lambda \oplus \overline{\Lambda}\overline{\Lambda}$ results from other experiments, showing a good agreement.

For baryon-antibaryon ($\Lambda\overline{\Lambda}$) correlations, our measurements indicate a "repulsive" femtoscopic behavior, corresponding to an attractive strong interaction potential, with $\Re f_0 = -0.95 \pm 0.11$ (stat) ± 0.21 (syst) fm, showing an opposite behavior as that seen in $\Lambda\Lambda \oplus \overline{\Lambda}\,\overline{\Lambda}$. The presence of a non-zero imaginary part of the scattering length, $\Im f_0 = 0.23 \pm 0.04$ (stat) ± 0.12 (syst) fm, can be related to an annihilation process of $\Lambda\overline{\Lambda}$ pairs. The source size measured, $R_{\mathrm{inv}} = 1.79 \pm 0.34$ (stat) ± 0.39 (syst) fm, is compatible with the value measured in $\Lambda\Lambda \oplus \overline{\Lambda}\overline{\Lambda}$ correlations. In addition, these measurements were performed in a wide range of charged particle multiplicity, showing a constant behavior of the scattering parameters. Comparison with experimental data from other experiments was also performed, showing a similar behavior among all baryon-antibaryon pairs.

Further extensions of this work can be performed in the near future. For example, by means of a multidimensional analysis using neutral kaons. In addition, it is possible to extend the femtoscopy measurements using data obtained in pPb collisions, by studying the correlations between the K_S^0, Λ and $\overline{\Lambda}$ particles with heavier particles, such as Ξ's or Ω's, in order to obtain a better understanding of the strong final state interactions involving these particles.

Appendices

Appendix A

Definitions and Concepts

In this appendix some definitions and concepts used in the body of this thesis are discussed in more detail.

A.1 Beam collision energy

In high-energy experiments the center-of-mass collision energy is defined by the Lorentz-invariant quantity $\sqrt{s}$, where $s = (p_t^\mu + p_p^\mu)^2$ with p_t and p_p are the four-momentum of the two particles in each beam, the target and the projectile, respectively.

In the case of fixed-targed experiments, this quantity (for a target particle at rest in the laboratory frame) is given by [333]

$$\sqrt{s} = \sqrt{m_p^2 + m_t^2 + 2m_t E_p}, \tag{A.1}$$

where m_p, E_p and m_t are the rest mass and energy or the projectile particle in the laboratory frame and the target particle mass, respectively.

In collider experiments, both target and projectile are moving toward each other and the center-of-mass energy is defined as [333]

$$\sqrt{s} = \sqrt{(E_p + E_t)^2 - (|\vec{p}_t| - |\vec{p}_p|)^2} \approx 2\sqrt{E_p E_t}, \tag{A.2}$$

where, E_t is the energy of the target particle and $\vec{p}$ the tri-momentum of the target and projectile. The approximation assumed is valid when $E_p, E_t \gg m_p, m_t$. Using Eq. (A.2) for proton-proton collisions and assuming that each proton beam has 6.5 TeV, the collision center-of-mass energy is $\sqrt{s} = 13$ TeV.

In heavy ion collisions Eq. (A.2) is also valid, however, the energy needs to be scaled by the ratio between the atomic number (Z) and the mass number (A) for both target and projectile, in order to obtain the nucleon-nucleon center-of mass

energy, $\sqrt{s_{\mathrm{NN}}}$. The corresponding relation can be written as

$$\sqrt{s_{\mathrm{NN}}} \approx 2\sqrt{\frac{Z_p}{A_p}E_p\frac{Z_t}{A_t}E_t} \approx \sqrt{s}\sqrt{\frac{Z_pZ_t}{A_pA_t}}, \tag{A.3}$$

where E is the energy of the protons accelerated at the LHC. This equation is valid in all cases: in pp collisions, $A_p = Z_p = A_t = Z_t = 1$, going back to Eq. (A.2). At top lead-lead collision energy, $A_p = A_t = 208$, $Z_p = Z_t = 82$ and $\sqrt{s} \approx 13$ TeV, leading to $\sqrt{s_{\mathrm{NN}}} \approx 5.02$ TeV. For xenon-xenon, $A_p = A_t = 129$, $Z_p = Z_t = 54$ and $E_t = E_p = 6.5$ TeV, thus $\sqrt{s_{\mathrm{NN}}} \approx 5.44$ TeV. In the case of top proton-lead energy, used in this thesis, the proton has energy of ≈ 6.5 TeV and $A_p = Z_p = 1$, while the lead nucleus has $A_t = 208$ and $Z_t = 82$, leading to $\sqrt{s_{\mathrm{NN}}} = 8.16$ TeV.

A.2 Matrices and properties

In Chapter 2, the Dirac and Gell-Mann matrices were cited. In this section, the explicity form of this matrices as well as some properties are presented.

A.2.1 Dirac matrices

One of the representations of the Dirac matrices are [9]:

$$\gamma^0 = \begin{pmatrix} 1 & 0 & 0 & 0 \\ 0 & 1 & 0 & 0 \\ 0 & 0 & -1 & 0 \\ 0 & 0 & 0 & -1 \end{pmatrix} = \begin{pmatrix} I & 0 \\ 0 & -I \end{pmatrix},$$

$$\gamma^1 = \begin{pmatrix} 0 & 0 & 0 & 1 \\ 0 & 0 & 1 & 0 \\ 0 & -1 & 0 & 0 \\ -1 & 0 & 0 & 0 \end{pmatrix} = \begin{pmatrix} 0 & \sigma^1 \\ -\sigma^1 & 0 \end{pmatrix},$$

$$\gamma^2 = \begin{pmatrix} 0 & 0 & 0 & -i \\ 0 & 0 & i & 0 \\ 0 & i & 0 & 0 \\ -i & 0 & 0 & 0 \end{pmatrix} = \begin{pmatrix} 0 & \sigma^2 \\ -\sigma^2 & 0 \end{pmatrix},$$

$$\gamma^3 = \begin{pmatrix} 0 & 0 & 1 & 0 \\ 0 & 0 & 0 & -1 \\ -1 & 0 & 0 & 0 \\ 0 & 1 & 0 & 0 \end{pmatrix} = \begin{pmatrix} 0 & \sigma^3 \\ -\sigma^3 & 0 \end{pmatrix},$$

where I is the 2×2 identity matrix and σ^i the Pauli matrices

$$I = \begin{pmatrix} 1 & 0 \\ 0 & 1 \end{pmatrix}, \quad \sigma^1 = \begin{pmatrix} 0 & 1 \\ 1 & 0 \end{pmatrix}, \quad \sigma^2 = \begin{pmatrix} 0 & -i \\ i & 0 \end{pmatrix}, \quad \sigma^3 = \begin{pmatrix} 1 & 0 \\ 0 & -1 \end{pmatrix}.$$

The Pauli matrices present the following commutation and anticommutation relations: $[\sigma^i, \sigma^j] = 2i\varepsilon_{ijk}\sigma^k$ and $\{\sigma^i, \sigma^j\} = 2\delta^{ij}I$, respectively. ε_{ijk} is the Levi-Civita symbol (+1 for even permutations of 123, −1 for odd permutations and 0 otherwise) and δ^{ij} is the Kronecker delta (1 for $i = j$ and 0 for $i \neq j$).

In the case of Dirac matrices, they satisfy the following relations:

$$\begin{aligned} \{\gamma^\mu, \gamma^\nu\} &= \gamma^\mu\gamma^\nu + \gamma^\nu\gamma^\mu = 2g^{\mu\nu}; \\ \gamma^\mu\gamma_\mu &= 4I; \\ \gamma^0 &= \gamma_0; \\ \gamma^i &= -\gamma_i (\text{for } i = 1, 2, 3); \\ (\gamma^0)^2 &= -(\gamma^i)^2 = 1; \\ [\gamma^\mu\gamma^\nu, \gamma^\alpha] &= 2[\gamma^\mu g^{\nu\alpha} - \gamma^\nu g^{\mu\alpha}]; \\ \gamma^\mu\gamma_\nu\gamma_\mu &= -2\gamma_\nu; \\ \gamma^\mu\gamma_\nu\gamma_\alpha\gamma_\mu &= 4g_{\nu\alpha}; \end{aligned}$$

where $g^{\mu\nu}$ is the metric tensor

$$g^{\mu\nu} = \begin{pmatrix} 1 & 0 & 0 & 0 \\ 0 & -1 & 0 & 0 \\ 0 & 0 & -1 & 0 \\ 0 & 0 & 0 & -1 \end{pmatrix}.$$

The spin tensor can be than written in terms of the Dirac matrices as

$$\sigma^{\mu\nu} = (i/2)[\gamma^\mu, \gamma^\nu] = i(\gamma^\mu\gamma^\nu - g^{\mu\nu}), \tag{A.4}$$

where $[\sigma^{\mu\nu}, \gamma^\alpha] = (\gamma^\mu g^{\nu\alpha} - \gamma^\nu g^{\mu\alpha})$. An additional combination results in the pseudo-scalar γ^5, a matrix given by

$$\gamma^5 = i\gamma^0\gamma^1\gamma^2\gamma^3 = \begin{pmatrix} 0 & 0 & 1 & 0 \\ 0 & 0 & 0 & 1 \\ 1 & 0 & 0 & 0 \\ 0 & 1 & 0 & 0 \end{pmatrix} = \begin{pmatrix} 0 & I \\ I & 0 \end{pmatrix},$$

so that $\left(\gamma^5\right)^2 = I$, $\gamma^5 = \gamma_5$ and $\{\gamma^5, \gamma^\mu\} = 0$.

A.2.2 Gell-Mann matrices

The Gell-Mann λ-matrices are related with the generators of the SU(3) symmetry group ($T^a = \lambda^a/2$) and are written as

$$\lambda^1 = \begin{pmatrix} 0 & 1 & 0 \\ 1 & 0 & 0 \\ 0 & 0 & 0 \end{pmatrix}, \quad \lambda^2 = \begin{pmatrix} 0 & -i & 0 \\ i & 0 & 0 \\ 0 & 0 & 0 \end{pmatrix}, \quad \lambda^3 = \begin{pmatrix} 0 & 1 & 0 \\ -1 & 0 & 0 \\ 0 & 0 & 0 \end{pmatrix},$$

$$\lambda^4 = \begin{pmatrix} 0 & 0 & 1 \\ 0 & 0 & 0 \\ 1 & 0 & 0 \end{pmatrix}, \quad \lambda^5 = \begin{pmatrix} 0 & 0 & -i \\ 0 & 0 & 0 \\ i & 0 & 0 \end{pmatrix}, \quad \lambda^6 = \begin{pmatrix} 0 & 0 & 0 \\ 0 & 0 & 1 \\ 0 & 1 & 0 \end{pmatrix},$$

$$\lambda^7 = \begin{pmatrix} 0 & 0 & 0 \\ 0 & 0 & -i \\ 0 & i & 0 \end{pmatrix}, \quad \lambda^8 = \frac{1}{\sqrt{3}} \begin{pmatrix} 1 & 0 & 0 \\ 0 & 1 & 0 \\ 0 & 0 & -2 \end{pmatrix},$$

and satisfy the following proprierties,

$$\begin{aligned} \text{tr}\left(\lambda^a\right) &= 0, \\ \text{tr}\left(\lambda^a\lambda^b\right) &= 2\delta^{ab}, \\ \left[\lambda^a, \lambda^b\right] &= 2if^{abc}\lambda^c, \end{aligned}$$

where tr stands for trace and f^{abc} are the structure factors, $f^{abc} = (4i)^{-1}\text{tr}(\lambda^c[\lambda^a, \lambda^b])$. Using the Gell-Mann matrices, it is possible to write the non-null structure constants as:

$$f^{123} = 1, f^{147} = -f^{156} = f^{246} = f^{257} = f^{345} = -f^{367} = 1/2 \text{ and } f^{458} = f^{678} = \sqrt{3}/2.$$

A.3 Collision geometry

One important aspect to characterize heavy ion collisions is the collision geometry. It is possible to describe such collisions by several individual nucleon-nucleon (binary) collisions between the nucleus' constituents. Figure A.1, illustrates a nucleus-nucleus collision: on the left, two nuclei contracted by the Lorentz factor accelerated with velocities close to c, are shown moments before the collision. The so-called impact parameter[1], b, is the distance between the center of the two nuclei and defines the interaction region; on the right, it shows a moment just after the collision; the so-called participants are the nucleons that interact in the collision, whereas spectators are the nucleons that remain unchanged. In this way, it is possible to define the number of participants, denoted by N_{part}, and the number of spectators, N_{spec}. The number of participants is inversely proportional to b, i.e., for small b, N_{spec} is small and N_{part} is large, producing a more central collision, and vice versa. In high energy heavy ion collisions, the classes of centralities are given in terms of percentages, that is, the higher (lower) the percentage, the more peripheral (central) the collision is. In a simple way, for identical nuclei, the centrality can be written as $C = b^2/(2R)^2$, where R is the nuclei radius. The collisions are classified as central (largest N_{part}), semi-central, semi-peripheral and peripheral (smaller N_{part}).
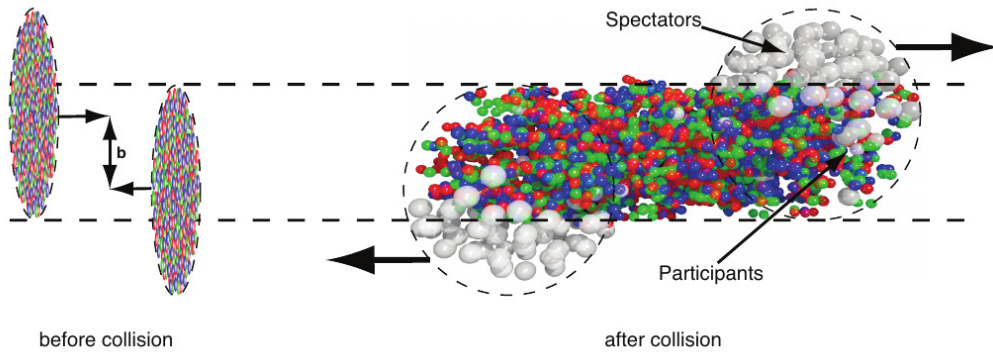
Figure A.1: Schematic view of a heavy ion collision before (left) and after (right) the interaction. The impact parameter b is shown on the left. Participants and spectators are shown on the right, where the colored region represents the system formed in the collision. Extracted from [94].

---

[1] It is important to note that this impact parameter is not the same as presented before also called distance of closest approach.

Experimentally, b and N_{part} cannot be accessed, and other measureable quantities are used to determine the nuclei overlap region. This quantity is directly related with the event multiplicity (higher multiplicity, more central events), as illustrated by the cartoon in Fig. A.2 (left), showing the multiplicity distribution and its "dependence" on average b and average N_{part}. In CMS, the centrality is studied by the Heavy Ion Global Observables (GO) Group and is obtained using the sum of the transverse energy ($E_T = E/\cosh\eta$, where E is the energy tower) deposited in the HF detector ($3 < |\eta| < 5$), as show by Fig. A.2 (right), for minimum bias lead-lead collisions; a very similar behavior to the cartoon in the left plot can be seen. The black line is the data and the red dashed lines show the centrality windows, which are defined by comparing the distribution with results from the Glauber model [107, 108]. In pPb collisions at 8.16 TeV, the centrality has not yet been defined by CMS GO group, however our interest in this thesis is to observe the dependence with multiplicity, which is done as described in Chapter 5.
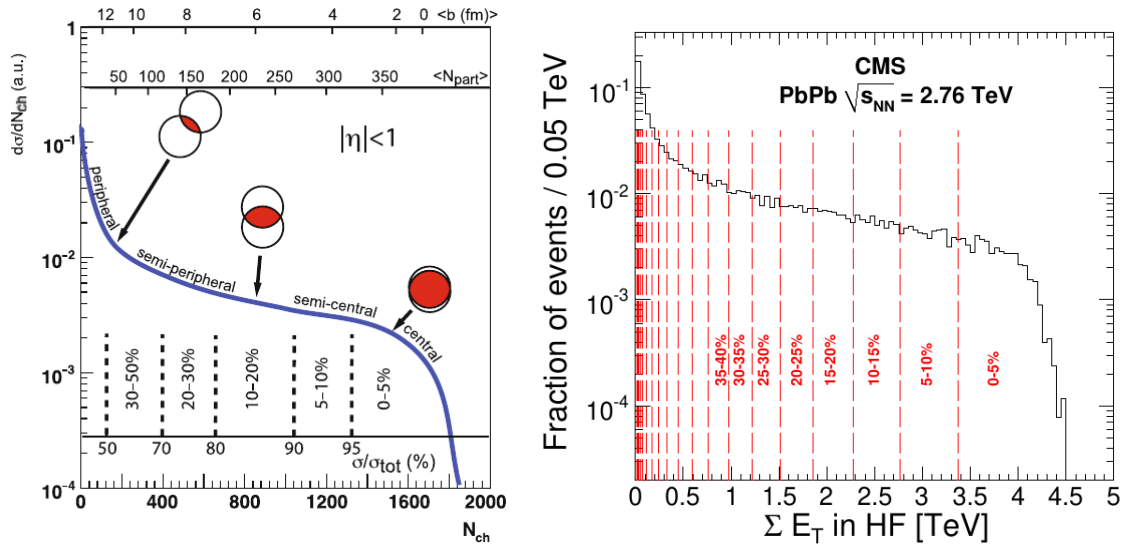
Figure A.2: Left: schematic cartoon of the multiplicity distribution from central to peripheral collisions showing the dependence with the average b and the average N_{part}. Extracted from [334]. Right: centrality determination measuread with the CMS detector, based on the sum of the transverse energy deposited at the HF calorimeter, for PbPb collisions at $\sqrt{s_{NN}} = 5.02$ TeV. The black line shows the data and the red dashed lines correspond to the centrality windows. Extracted from [335].

A.4 Luminosity

The accelerator capatibility to deliver collisions/events to a detector is characterized by a quantity called luminosity ($\mathcal{L}$), usually given in $\text{cm}^{-2}\text{s}^{-1}$. The event rate (events per second or dN/dt), $\mathcal{R}$, is proportional to the physics process, given by the cross-section (σ), multiplied by $\mathcal{L}$ as $\mathcal{R} = dN/dt = \sigma \cdot \mathcal{L}$.

The luminosity is given by [333]

$$\mathcal{L} = f N_B \frac{n_1 n_2}{\mathcal{A}} \tag{A.5}$$

where, f is the revolution frequency, N_B is the number of bunches, n_1 and n_2 are the number of particles in each bunch and $\mathcal{A}$ is the cross-sectional area of the beams. The total number of events can be obtained (assuming that σ does not depend on time) by integrating $\mathcal{R}$ in a time interval, as $N_{\text{tot}} = \sigma \cdot L_{\text{int}}$, where $L_{\text{int}} = \int \mathcal{L} dt$ is the integrated luminosity in units of 1/barn (b^{-1}). The integrated luminosity for pPb collisions at $\sqrt{s_{\text{NN}}} = 8.16$ TeV (used in this thesis) recorded by CMS was $L_{\text{int}} \approx 180$ nb^{-1}. Figure A.3 shows L_{int} increasing during the heavy ion data-taking in 2016, the blue histogram shows the luminosity delivered by LHC and the yellow one shows the fraction of collisions recorded by CMS.
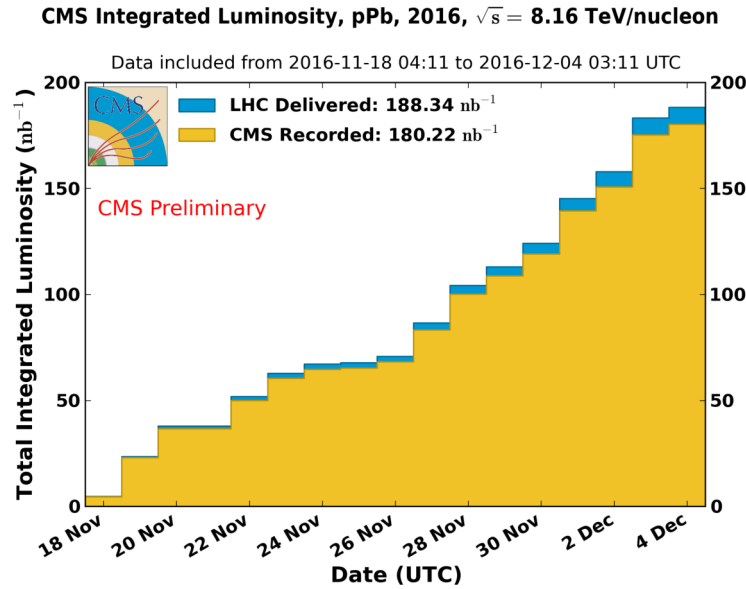
Figure A.3: Total integrated luminosity delivered for 2016 proton-lead data. Blue is the delivered luminosity by LHC and yellow is the collected luminosity. Extracted from https://twiki.cern.ch/twiki/bin/view/CMSPublic/LumiPublicResults#2016_proton_lead_collisions [last access on 13/Mar/2021].

Appendix B

QGP: Thermodynamics and Hydrodynamics

In this appendix, the equation of state considering a first order phase transition, mentioned in Sec. 2.3.2 of Chapter 2, is derived by using statitical mechanics in Sec. B.1. In Sec. B.2, a brief description of the relativistic hydrodynamic model that is applied to describe the QGP evolution is presented.

B.1 Equation of state with first order phase transition

In the 1970s and many years afterwards, it was believed that there would be a first order phase transition between the quark-gluon plasma (QGP) and hadron gas (HG) phases. This equation of state (EoS) englobes three different regions in the evolution of matter: the initial phase, at high temperatures, in which the entire matter is formed by the QGP only; the final phase, that the matter is formed by a HG only; and the intermediate phase, where QGP and HG coexist, called mixed phase.

B.1.1 QGP phase

At high temperatures and high energy densities, the interactions between quarks and gluons are weak practically neglegible due to the assymptotic freedom property of QCD. Based on that, the QGP was first imagined as an ideal gas in thermal equilibrium, composed of free quarks (u, d, s), antiquarks ($\overline{u}, \overline{d}, \overline{s}$) and gluons [88]. To obtain the equation of state for the QGP phase, it is necessary to calculate the contributions for quarks, antiquarks and gluons individually. For a gas made of quarks the energy density is written using the Fermi-Dirac distribution, as

$$\varepsilon_q(T) = \frac{g_q}{2\pi^2} \int_0^\infty \frac{p^3 dp}{1 + e^{p/T}}. \tag{B.1}$$

where g_q is the quark degeneracy factor, p the momentum and T the temperature. The integral in Eq. (B.1) can be solved using

$$\int_0^\infty \frac{z^{a-1}dz}{e^z + 1} = (1 - 2^{1-a})\zeta(a)\Gamma(a) \qquad (a > 0), \tag{B.2}$$

where Γ is the Euler gamma function (see Chapter 8 of Ref. [166]) and ζ is the Riemann zeta function (see Chapter 5 of Ref. [166]). Replacing Eq. (B.2) in Eq. (B.1) and using the values: $\Gamma(4) = 6$ e $\zeta(4) = \pi^4/90$; then the energy density of a quark gas is

$$\varepsilon_q(T) = \frac{7}{8}g_q\frac{\pi^2}{30}T^4. \tag{B.3}$$

Similarlly, the energy density of an antiquark gas is given by

$$\varepsilon_{\bar{q}}(T) = \frac{7}{8}g_{\bar{q}}\frac{\pi^2}{30}T^4, \tag{B.4}$$

where $g_{\bar{q}}$ is the antiquark degeneracy. Summing Eqs. (B.3) and (B.4), it is possible to obtain the total energy density of an ideal gas formed by quarks and antiquarks,

$$\varepsilon_{q\bar{q}}(T) = \frac{7}{8}(g_q + g_{\bar{q}})\frac{\pi^2}{30}T^4. \tag{B.5}$$

Once the ε of a gas composed of quarks and antiquarks are obtained, the gluon contribution still needs to be calculated. In this case, the energy density is written following the Bose-Einstein distribution, as

$$\varepsilon_g(T) = \frac{g_g}{(2\pi^2)}\int_0^\infty \frac{p^3dp}{e^{p/T} - 1}, \tag{B.6}$$

where g_g is the gluon degeneracy factor. The integral in Eq. (B.6) can be solved using

$$\int_0^\infty \frac{z^{a-1}dz}{e^z - 1} = \zeta(a)\Gamma(a) \qquad (a > 1). \tag{B.7}$$

Replacing the Eq. (B.7) in Eq. (B.6) and $\zeta(4)$, $\Gamma(4)$ values, we have the energy density of a gluon gas,

$$\varepsilon_g(T) = g_g\frac{\pi^2}{30}T^4, \tag{B.8}$$

Using Eqs. (B.5), (B.8), and the relation between pressure and energy density for an ultrarelativistic Fermi (for quarks) or Boson (for gluons) gas [73, 336], $P = \varepsilon/3$,

we have

$$P_{q\bar{q}}(T) = \frac{7}{8}(g_q + g_{\bar{q}})\frac{\pi^2}{90}T^4,$$ (B.9)

$$P_g(T) = g_g\frac{\pi^2}{90}T^4.$$ (B.10)

Adding the Eq. (B.9) and the Eq. (B.10), the pressure for a gas composed of gluons, quarks and antiquarks is given by

$$P(T) = \left[g_g + \frac{7}{8}(g_q + g_{\bar{q}})\right]\frac{\pi^2}{90}T^4.$$ (B.11)

The Eq. (B.11) is valid only in the high temperature regime. However, the interactions and the confinement of quarks and gluons at lower temperatures should also be taken into account, which can be done by means of the MIT bag model [89]. According to this model, it is postulated a constant energy density $\mathcal{B}$ representing the pressure from the vacuum that balances the pressure from the quarks inside the bag. Based on this, it is possible to determine the energy density of the QGP by adding the densities given by Eq. (B.5), Eq. (B.8) and the bag constant as

$$\varepsilon_{\text{QGP}}(T) = g_{\text{QGP}}\frac{\pi^2}{30}T^4 + \mathcal{B},$$ (B.12)

where the plasma degeneracy factor is $g_{\text{QGP}} = \left[g_g + \frac{7}{8}(g_q + g_{\bar{q}})\right]$, that depends on the following quantum numbers: spin (N_{spin}), flavor (N_{flavor}) and color (N_{color})[1].

Using the balance between the vacuum pressure and the thermodynamic pressure of the gas made of quarks and gluons inside the MIT bag, from Eq. (B.11), the QGP pressure can be written as

$$P_{\text{QGP}}(T) = \frac{1}{3}\left(\varepsilon_{\text{QGP}} - 4\mathcal{B}\right) = g_{\text{QGP}}\frac{\pi^2}{90}T^4 - \mathcal{B}.$$ (B.13)

With Eqs. (B.12), (B.13) and the thermodynamic relation $s = (\varepsilon + P)/T$, the QGP entropy density also can be calculated, as

$$s_{\text{QGP}}(T) = 4g_{\text{QGP}}\frac{\pi^2}{90}T^3.$$ (B.14)

---

[1]The quark and antiquark degeneracy are $g_q = g_{\bar{q}} = N_{spin} \times N_{flavor} \times N_{color}$, while the gluon degeneracy is $g_g = N_{spin}(N_{color}^2 - 1)$.

B.1.2 Hadron gas phase

In the high energy regime, as is the case of the LHC experiments, it is possible to approximate the hadronic phase by an ideal gas formed by different hadrons [337]. This hypothesis is valid in this limit, because the thermal energy is sufficiently high compared to the interaction energy between the hadrons. Thus, the total pressure of an ideal hadron gas, P_{HG}, is given by the sum of the pressures of each hadron species, that is,

$$P_{\text{HG}}(T, \mu) = \sum_i P_i(T, \mu_i), \tag{B.15}$$

where μ is the hadron gas chemical potential, P_i and μ_i are the pressure and chemical potential of the ith hadron, respectively.

The hadrons that compose the gas can be either fermions (baryons) or bosons (mesons). Thus, it is possible to write the pressure for each type of hadron as [88]:

$$P_i(T, \mu_i) = \pm \frac{g_i}{2\pi^2} T \int dk k^2 \ln \left[1 \pm e^{-\left(\sqrt{k^2 + m_i^2} - \mu_i\right)/T} \right], \tag{B.16}$$

where $\varepsilon_k = \sqrt{k^2 + m_i^2}$, the signal $+(-)$ refers to fermions (bosons), k is the wave number, g_i and m_i, are the degeneracy and the mass of the ith hadron, respectively. Using a Taylor expansion, $\ln(1+x) = \sum_0^\infty \frac{(-1)^n}{n+1} x^{n+1}$ for $x < 1$, we can rewrite Eq. (B.16) as:

$$P_i(T, \mu_i) = \pm \frac{g_i}{2\pi^2} T \sum_{n=1}^\infty \frac{(\mp 1)^{n-1}}{n} e^{\frac{n\mu_i}{T}} \int_0^\infty dk k^2 e^{\frac{-n\sqrt{k^2 + m_i^2}}{T}}. \tag{B.17}$$

The integral in Eq. (B.17) can be solved, resulting in

$$\int_0^\infty dk k^2 e^{\frac{-n\sqrt{k^2 + m_i^2}}{T}} = \frac{m_i^2 T}{n} K_2 \left(\frac{n m_i}{T} \right), \tag{B.18}$$

where the K_ν is the modifield Bessel function, defined as

$$K_\nu(z) = \frac{\sqrt{\pi}}{\Gamma(\nu + \frac{1}{2})} \left(\frac{z}{2} \right)^\nu \int_0^\infty dx \frac{x^{2\nu}}{1 + x^2} e^{-z\sqrt{1+x^2}}. \tag{B.19}$$

Thus,

$$P_i(T, \mu_i) = \pm \frac{g_i}{2\pi^2} T^2 m_i^2 \sum_{n=1}^\infty \frac{(\mp 1)^{n-1}}{n^2} e^{\frac{n\mu_i}{T}} K_2 \left(\frac{n m_i}{T} \right). \tag{B.20}$$

The serie in Eq. (B.20) converges quickly in the Boltzmann limit, where there is no difference between bosons and fermions and the first term of the series gives us a good approximation. Therefore, it is possible to rewrite Eq. (B.20) as

$$P_i(T, \mu_i) \approx \frac{g_i}{2\pi^2} m_i^2 T^2 e^{\frac{\mu_i}{T}} K_2\left(\frac{m_i}{T}\right). \tag{B.21}$$

Using Eqs. (B.21) and (B.16), the total pressure of the hadronic gas is then

$$P_{\text{HG}}(T, \mu) \approx \sum_i \frac{g_i}{2\pi^2} m_i^2 T^2 e^{\frac{\mu_i}{T}} K_2\left(\frac{m_i}{T}\right). \tag{B.22}$$

Once the pressure is calculated, it is possible to obtain the thermodynamical quantites[2]: energy density, ε_{HG}, particle number density, n_{HG}, and entropy density, s_{HG}, as

$$\varepsilon_{\text{HG}}(T, \mu_i) \approx \sum_i \frac{g_i}{2\pi^2} m_i^3 T e^{\frac{\mu_i}{T}} \left[K_1\left(\frac{m_i}{T}\right) + \frac{3T}{m_i} K_2\left(\frac{m_i}{T}\right) \right], \tag{B.23}$$

$$n_{\text{HG}}(T, \mu_i) \approx \sum_i \frac{g_i}{2\pi^2} m_i^2 T e^{\frac{\mu_i}{T}} K_2\left(\frac{m_i}{T}\right), \tag{B.24}$$

$$s_{\text{HG}}(T, \mu_i) \approx \sum_i \frac{g_i}{2\pi^2} m_i^3 T e^{\frac{\mu_i}{T}} \left[K_1\left(\frac{m_i}{T}\right) + \frac{(4T - \mu_i)}{m_i} K_2\left(\frac{m_i}{T}\right) \right]. \tag{B.25}$$

This set of thermodynamic quantities gives us the equation of state of the hadronic phase. However, according to G. D. Yen, W. Greiner, and S. Yang [338] the ideal gas model returns extremely large values for the total particle number density in heavy ion collisions, exceeding the results from experimental measurements of particle multiplicity and also exceeds the estimate of the volume of the system at freeze-out as measured by pion femtoscopy. To obtain the desired particle number density valeus it is necessary to introduce the repulsive interaction between hadrons at short distances, which is done by using the excluded volume correction (more information about this can be found at Refs. [73, 339, 338]). After the correction it is possible to calculate the phase transition.

---

[2]To calculate that quantities, the following recurrence relation of the modifield Bessel function was used: $\frac{d}{dz}\left[z^{-n} K_\nu(z)\right] = -z^{-n} K_{\nu+1}(z)$.

B.1.3 Phase transition

The transition region between the QGP and the HG can be defined as the region where the pressure between the two states is identical,

$$P_{\text{HG}}(T_c, \mu_c) = P_{\text{QGP}}(T_c, \mu_c), \tag{B.26}$$

where T_c e μ_c are the critical temperature and chemical potential, respectively. When $T < T_c$, $P_{\text{HG}}(T, \mu) > P_{\text{QGP}}(T, \mu)$, the matter is in the hadronic phase; while for $T > T_c$, $P_{\text{HG}}(T, \mu) < P_{\text{QGP}}(T, \mu)$, the matter is in the QGP phase. For $\mathcal{B} = 380$ MeV and $\mu_c = 0$ (LHC energies), the critical temperature is $T_c \approx 162\text{MeV}$ [88].

B.2 Relativistic Hydrodynamics

The application of hydrodynamics to study the evolution of particle collisions was idealized and derived by L. Landau [71] in the fifties. Along the years, the hydrodynamical model proved to be a good tool for reproducing some of the experimental observables in relativistic heavy ion collisions [179, 337] and a brief description of this model is presented below.

In the hydrodynamical description of a relativistic heavy ion collision (or of small colliding systems), we assume that matter in local thermal equilibrium is formed and its evolution is governed by the conservation of energy-momentum and of other quantum numbers (baryonic number, strangeness, electric charge, etc.). This model is valid when the mean free path is very small compared to the system size[3]. Then, the hydrodynamic evolution equations can be written as

$$\partial_{;\nu} T^{\mu\nu} \equiv \partial_\nu T^{\mu\nu} + \Gamma^\mu_{\nu\lambda} T^{\nu\lambda} + \Gamma^\nu_{\nu\lambda} T^{\mu\lambda} = 0 \tag{B.27}$$

$$\partial_{;\nu} j^\nu_i \equiv \partial_\nu j^\nu_i + \Gamma^\nu_{\nu\lambda} j^\lambda_i = 0, \tag{B.28}$$

where $\Gamma^\mu_{\nu\lambda}$ the Christoffel symbols, defined as $\Gamma^\alpha_{\mu\nu} = \frac{1}{2} g^{\alpha\beta} \left(\partial_\mu g_{\beta\nu} + \partial_\nu g_{\beta\mu} - \partial_\beta g_{\mu\nu} \right)$, and $g^{\alpha\beta}$ being the metric. This definition is usefull, since the hydrodynamical equations are usually solved using the Milne (or hyperbolic) coordinate system, where t and z are replaced by $\tau = \sqrt{t^2 + z^2}$ and $\eta_s = \frac{1}{2} \ln \left(\frac{t+z}{t-z} \right)$. In this case, the

---

[3]This can be also understood by means of Knudsen number. This number is defined as the ratio between the mean free path and the system size, the application of hydrodynamics is valid when Knudsen number $\ll 1$.

invariant interval is $ds^2 = dt^2 - dx^2 - dy^2 - \tau^2 d\eta_s^2$ and the metric tensor is

$$g_{\mu\nu} = \begin{pmatrix} 1 & 0 & 0 & 0 \\ 0 & -1 & 0 & 0 \\ 0 & 0 & -1 & 0 \\ 0 & 0 & 0 & -\tau^2 \end{pmatrix} \text{ and } g^{\mu\nu} = \begin{pmatrix} 1 & 0 & 0 & 0 \\ 0 & -1 & 0 & 0 \\ 0 & 0 & -1 & 0 \\ 0 & 0 & 0 & -1/\tau^2 \end{pmatrix}. \tag{B.29}$$

$T^{\mu\nu}$ and j_i^ν are the energy-momentum tensor and ith conserved charge current in the system, respectivelly. Given by [340]

$$T^{\mu\nu} = \epsilon u^\mu u^\nu - (P + \Pi)\Delta^{\mu\nu} + \pi^{\mu\nu} \tag{B.30}$$

$$j_i^\nu = n_i u^\nu + V_i^\nu, \tag{B.31}$$

where, Π, $\pi^{\mu\nu}$ e V_i^ν are the bulk viscosity, the shear viscosity tensor and the charge diffusion currents, respectively. In this definition, the vorticity is not considered and, at LHC energies, $V_i^\nu = 0$ (assuming zero baryon density) [340]. If $\Pi = \pi^{\mu\nu} = 0$, we obtain the ideal fluid case. The 4-velocity of the fluid is defined as $u^\mu = \gamma(1, \mathbf{v})$, where $\gamma = 1/\sqrt{1 - \mathbf{v}^2}$ is the Lorentz factor and $\mathbf{v}$ is the fluid velocity vector in the laboratory frame and satisfies $u^\mu u_\mu = 1$. The $\Delta^{\mu\nu} = g^{\mu\nu} - u^\mu u^\nu$ is the projector orthogonal to u^μ.

Replacing Eq. (B.30) in Eq. (B.27), and using the second law of thermodynamics in the covariant form, $\partial_\nu S^\nu = \partial_\nu(su^\nu) \geq 0$ (S^ν is the entropy current and s is the entropy density), we obtain the so-called first order or Navier-Stokes viscous hydrodynamic equations for both shear and bulk viscosities:

$$\pi_{\text{NS}}^{\mu\nu} = \eta_v \left(\Delta^{\mu\lambda}\partial_{;\lambda}u^\nu + \Delta^{\nu\lambda}\partial_{;\lambda}u^\mu \right) - \frac{2}{3}\eta_v \Delta^{\mu\nu}\partial_{;\lambda}u^\lambda \tag{B.32}$$

and

$$\Pi_{\text{NS}} = -\zeta_v \partial_{;\lambda}u^\lambda. \tag{B.33}$$

where η_v and ζ_v are the shear and bulk coefficients, respectivelly. These coefficients are used as input in the hydrodynamical simulations and are discussed with more details at Sec. B.2.1. The calculations in the Navier-Stokes formalism violate causality, returning velocities higher than c and causing instabilities in the solutions of these equations, therefore it cannot be applied [341, 342].

To restore causality, a proposal was first studied by I. Müller [343], in 1967,

and later by W. Israel and J. M. Stewart [344], in the 1970's, and is known as second order theory. In this studies, they suggested that, for a system out of the equilibrium, S^ν would have contributions coming from shear and bulk viscosities. Therefore, S^ν is expanded in term of the relaxion times (τ's) as [73]

$$S^\nu = su^\nu - \frac{1}{2T}u^\nu\left(\frac{\tau_\Pi}{\zeta_v}\Pi^2 + \frac{\tau_\pi}{2\eta_v}\pi_{\alpha\beta}\pi^{\alpha\beta}\right). \tag{B.34}$$

If $\tau_\pi, \tau_\Pi \to 0$, the Navier-Stokes formalism is recovered.

Using Eqs. (B.30), (B.27) and the second law of thermodynamics, with S^ν from Eq. (B.34), the second order viscous hydrodynamic equations are calculated for both shear and bulk viscosities as

$$u^\gamma\partial_{;\gamma}\pi^{\alpha\beta} = -\frac{1}{\tau_\pi}\left[\pi^{\alpha\beta} - \pi^{\alpha\beta}_{\mathrm{NS}}\right] - \frac{4}{3}\pi^{\alpha\beta}\partial_{;\gamma}u^\gamma \tag{B.35}$$

and

$$u^\gamma\partial_{;\gamma}\Pi = -\frac{1}{\tau_\Pi}\left[\Pi - \Pi_{\mathrm{NS}}\right] - \frac{4}{3}\Pi\partial_{;\gamma}u^\gamma. \tag{B.36}$$

These equations are the so-called Israel-Stewart framework [73, 344], written in terms of the Navier-Stokes quantities from Eqs. (B.32) and (B.33). In Eqs. (B.35) and (B.36), the causality is reestablished, then the hydrodynamic model is stable again and can be calculated numerically [342].

In addition, this model requires three ingredients as input to calculate the entire collision evolution:

- Initial conditions (IC): gives us information about the state of matter formed in the collisions at the instant it reaches local thermal equilibrium;

- Equation of state (EoS): relates the thermodynamic quantities and brings information about the phase transition of the matter created in the collisions;

- Decoupling mechanism (freeze-out): the stage in which the mean free path becomes of the order of the system size, and consequently the hydrodynamic model is no longer valid (the particles decouple by traveling in straight lines to the detector).

Numerically, these ingredients are calculated by separate codes, as for IC and freeze-out, or using parametrizations/calculations, as in the EoS. A detailed study, including the derivation of these equations, can be found in my M.Sc. thesis [73].

B.2.1 Transport coefficients

The transport/viscosity coefficients (η_v and ζ_v), from the Israel-Stewart equations, are intensively studied (theoretically and phenomenologically) in the field of heavy ion physics. These coefficients enter as input parameters in the hydrodynamic model and can be dependent or not on the temperature. Calculations performed using the AdS/CFT correspondence[4] [345, 346] demonstrated that the fractions η_v/s and ζ_v/s have an inferior limit, called Kovtun-Son-Starinets (KSS) bound:

$$\frac{\eta_v}{s} \geq \frac{1}{4\pi} \quad \text{and} \quad \frac{\zeta_v}{s} \geq 2\frac{\eta_v}{s}\left(\frac{1}{3} - c_s^2\right), \tag{B.37}$$

where c_s is the sound speed. Figure B.1 shows a comparison of η_v/s for different fluids: water (blue solid circle), helium (grey solid crosses), dinitrogen (green solid triangles) and QGP (red solid and open squares). For the QGP, the red open squares represents the results calculated from LQCD, while the red solid squares are the constant (temperature independent) values used across the years in hydrodynamical simulations. The KSS limit is shown as the black dashed line, Eq. (B.37). In this figure, is possible to observe that the QGP has the smallest η_v/s when compared to the other fluids, being an almost perfect fluid.

Recently, the dependence of the viscosity coefficients with temperature has being largelly investigated by using modern techniques (bayesian analysis), comparing the simulations with a large number of available experimental measurements for different observables, energies and experiments [347]. Nevertheless further studies are still needed.

---

[4]The AdS/CFT correspondence establishes a relationship between the four-dimensional supersymmetric gauge theory (Conformal Field Theory - CFT) and the gravitational theory in an anti-de Sitter space (AdS) of five dimensions. More information in [345, 346].
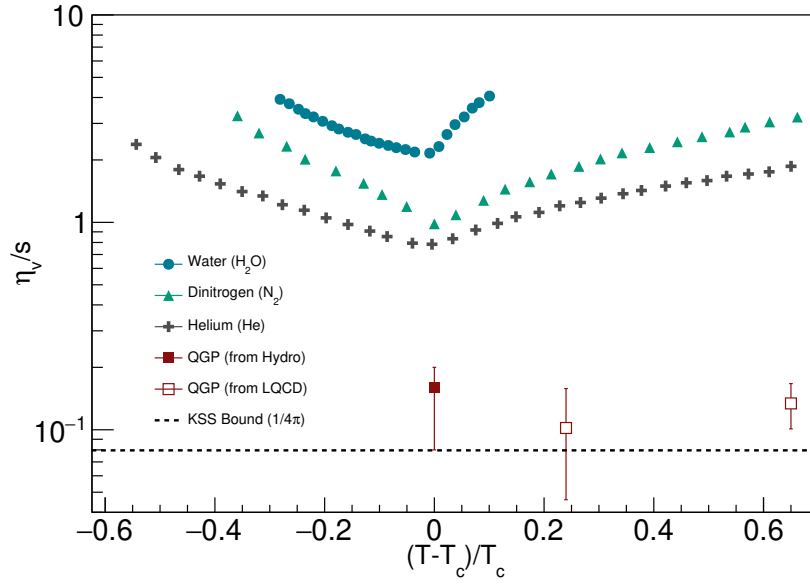
Figure B.1: Shear viscosity coeficient (η_v) to entropy density (s) ratio versus the reduced temperature $(T - T_c)/T_c$ (T_c is the critical phase transition temperature) for water, helium, dinitrogen and QGP. Plot adapted from the references [93, 348].

B.2.2 The hydrodynamical code CHESS

The Complete Hydrodynamical Evolution SyStem (CHESS) is a phenomenological package created in parallel to this thesis, to compare the calculation results with experimental data. This code is designed to be used for both heavy ion collisions and small colliding systems. The structure of the package is given by the three public codes T_RENTo [349, 350], vHLLE [340, 344] and THERMINATOR 2 [351, 352] connected by scripts in python language. Besides, a large number of equation of state (e. g. first order, LQCD based, ...) are included and can be studied. A brief description of each code that composes CHESS is given below:

- T_RENTo is a Monte Carlo (MC) generator that gives the entropy density in the transverse plane for many colliding systems: pp, pA, dA, AA, and so on. This code produces results in good agreement with data in pp, pPb, PbPb collisions at the LHC and AuAu at RHIC [349, 350].

- vHLLE is a code based on the Godunov-type relativistic HLLE approximate Riemann solver that solves the equations of relativistic viscous hydrodynamics in the Israel-Stewart framework, Eqs. (B.35) and (B.36) [340, 344]. In default version of this code the viscosity coefficients are considered constant,

but it is also possible to include the temperature dependence;

- THERMINATOR 2 is a MC event generator dedicated to study the statistical production of particles in relativistic heavy-ion collisions (and small colliding systems) that calculate the decoupling and the observables based on the Cooper-Frye method [351, 352]. In the public version, only the contribution from ideal fluid is considered, however, the version implemented in CHESS also includes viscosity corrections.

Currently, the CHESS code is parallelized and runs for all collision systems (proton-proton, proton-nucleus and nucleus-nucleus) in 2+1 dimensions, i. e., for cases assuming boost invariance. The first results were presented at the Quark Matter conference in 2018 [75]. Another result was presented at the XLI National Meeting on Nuclear Physics, in Maresias, SP, in September 2018. In this calculation the effect of viscosity in central AuAu collisions at RHIC energies were investigated. The corresponding contribution to the proceedings was published in [74].

A version in 3+1 dimensions was tested and was shown to work well, however the simulation time is large, therefore requiring further improvements of the code. The α version of CHESS code in 2+1 dimensions is available for download at Github: github.com/denerslemos/CHESS. Improvements are expected soon, for example, the inclusion of parton fluctuations in the initial conditions. With this code it is possible to calculate many observables and compare with data, as for example, rapidity distributions, invariant momentum distribution, flow harmonics and femtoscopy correlations (for charged pions and kaons).

Appendix C

Lednicky-Lyubolshitz model

A derivation of the Lednicky-Lyubolshitz (LL) model used to fit the strong final state interaction component in the correlation function is presented. The starting point in the building of this model is the Koonin-Pratt equation,

$$C(q) = \int S(r) \left| \Psi(q,r) \right|^2 dr, \tag{C.1}$$

where $q = |\mathbf{q}| = |\mathbf{p}_1 - \mathbf{p}_2|$, $r = |\mathbf{r}| = |\mathbf{x}_1 - \mathbf{x}_2|$, $S(r)$ and $\Psi(q,r)$ are the source and wave functions, respectively. In the LL model derivation, the source function is assumed to have a Gaussian shape, spherically symmetric (i.e. $S(\mathbf{r}) = S(r)$), and normalized in such a way that $\int S(\mathbf{r}) \, d\mathbf{r} = 1$, given by

$$S(r) = \frac{e^{-r^2/4R^2}}{\left(4\pi R^2\right)^{3/2}}. \tag{C.2}$$

The other important ingredient is the wave function that contains the information about the strong final state interaction (FSI), which is described below for all cases of interest.

C.1 Non-identical particles

The two-particle wave function, for the strong FSI, can be described by a partial wave decomposition as [353]

$$\Psi(q,r) = \sum_{l=0}^{\infty} \psi_l(q,r) P_l \left(\cos\theta\right), \tag{C.3}$$

where $P_l \left(\cos\theta\right)$ is the Legendre polynomial [166] associated with the orbital angular momentum l. For simplicity, we start to work with pairs composed by non-identical and neutral particles and assume that only the s-wave (i.e., $l = 0$)

part is affected by the interaction, thus

$$
\begin{aligned}
\Psi(q,r) &= \psi_0(q,r) + \sum_{l=1}^{\infty} \psi_l^{\text{free}}(q,r) P_l(\cos\theta) \\
&= \psi_0(q,r) + \sum_{l=0}^{\infty} \psi_l^{\text{free}}(q,r) P_l(\cos\theta) - \psi_0^{\text{free}}(q,r). \quad \text{(C.4)}
\end{aligned}
$$

where $\psi_0(q,r)$ and $\psi_l^{\text{free}}(q,r)$ are the scattered and free-particle wave functions, respectively. The sum in the second term of the Eq. (C.4) can be written as $\sum_{l=0}^{\infty} \psi_l^{\text{free}}(q,r) P_l(\cos\theta) = e^{i\frac{\mathbf{q}\cdot\mathbf{r}}{2}}$. The last term is the s-wave free-particle wave function that can be described by the spherical Bessel function [166, 353] as $\psi_0^{\text{free}}(q,r) = j_0(qr) = 2\sin(qr/2)/qr$. Therefore, the total wave function is given by

$$
\begin{aligned}
\Psi(q,r) &= e^{i\frac{\mathbf{q}\cdot\mathbf{r}}{2}} + \psi_0(q,r) - j_0(qr) \\
&= e^{i\frac{\mathbf{q}\cdot\mathbf{r}}{2}} + \phi(q,r), \quad \text{(C.5)}
\end{aligned}
$$

where $\phi(q,r) = \psi_0(q,r) - j_0(qr)$. Replacing Eq. (C.5) in Eq. (C.1), we obtain

$$
C(q) = \underbrace{\int d\mathbf{r}\, S(\mathbf{r})}_{\text{I}} + \underbrace{\int d\mathbf{r}\, S(\mathbf{r})\left[e^{-i\frac{\mathbf{q}\cdot\mathbf{r}}{2}}\phi(q,r) + e^{i\frac{\mathbf{q}\cdot\mathbf{r}}{2}}\phi^*(q,r)\right]}_{\text{II}} + \underbrace{\int d\mathbf{r}\, S(\mathbf{r})|\phi(q,r)|^2}_{\text{III}}.
$$

$$\text{(C.6)}$$

Substituting $\phi(q,r)$ and integrating term by term in Eq. 9 (C.6), we have

$$
\mathbf{I} = \int d\mathbf{r}\, S(\mathbf{r}) = 1, \quad \text{(C.7)}
$$

$$
\mathbf{II} = 4\pi \int dr\, r^2 S(r) j_0(kr)\left[\psi_0(q,r) + \psi_0^*(q,r) - 2j_0(kr)\right], \quad \text{(C.8)}
$$

$$
\mathbf{III} = 4\pi \int dr\, r^2 S(r)\left[|\psi_0(q,r)|^2 - j_0(kr)\left(\psi_0(q,r) + \psi_0^*(q,r)\right) + j_0^2(qr)\right]. \quad \text{(C.9)}
$$

Consequently, the correlation function for non-identical particles is given by

$$
C(q) = 1 + 4\pi \int_0^{\infty} dr\, r^2 S(r)\left[|\psi_0(q,r)|^2 - j_0^2(qr)\right]. \quad \text{(C.10)}
$$

The s-wave scattered wave function, $\psi_0(q,r)$, can be written similarly to the free-particle wave function component, but adding a phase shift δ_0 [201, 200], i.e., $\psi_0(q,r) = 2\sin(qr/2 + \delta_0)/qr$. The δ_0 cannot be measured in our experiment and to obtain information about the scattering quantities the S-matrix definition is

used [200]

$$S_l = e^{2i\delta_l} = 1 + iqf_l(q), \tag{C.11}$$

thus, the s-wave scattered wave function can be rewritten as

$$
\begin{aligned}
\psi_0(q,r) &= \frac{1}{iqr}\left(e^{i\left(\frac{qr}{2}+\delta_0\right)} - e^{-i\left(\frac{qr}{2}+\delta_0\right)}\right) \\
&= \frac{2e^{-i\delta_0}}{qr}\left(\sin\frac{qr}{2} + \frac{q}{2}fe^{i\frac{qr}{2}}\right),
\end{aligned} \tag{C.12}
$$

where $f = f(q)$ is the scattering amplitude[1] that depends on the physical observables of interest (see later in this section) and, at the limit of $q \to 0$, can give us information about the total cross-section of the interaction: $\sigma = 4\pi|f(q)|^2$ [200].

Using the Eqs. (C.12) and (C.10), the correlation function becomes

$$C(q) = 1 + \underbrace{4\pi|f|^2\int_0^\infty dr\, S(r)}_{\text{I}} + \underbrace{4\pi\int_0^\infty dr\, S(r)\frac{2}{q}\sin\frac{qr}{2}\left[f^*e^{-i\frac{qr}{2}} + fe^{i\frac{qr}{2}}\right]}_{\text{II}}. \tag{C.13}$$

Assuming the Gaussian distribution from Eq. (C.2), it is possible to calculate **I** and **II** as follows

$$\mathbf{I} = 4\pi|f|^2\int_0^\infty dr\, S(r) = 4\pi|f|^2\int_0^\infty dr\, \frac{e^{-r^2/4R^2}}{(4\pi R^2)^{\frac{3}{2}}} = \frac{|f|^2}{2R^2}, \tag{C.14}$$

and

$$
\begin{aligned}
\mathbf{II} &= 4\pi\int_0^\infty dr\, S(r)\frac{2}{q}\sin\frac{qr}{2}\left[f^*e^{-i\frac{qr}{2}} + fe^{i\frac{qr}{2}}\right] \\
&= \frac{8\pi}{q}\int_0^\infty dr\, S(r)\sin\frac{qr}{2}\left[(f^*+f)\cos\frac{qr}{2} - i(f^*-f)\sin\frac{qr}{2}\right] \\
&= \frac{8\pi}{q}\int_0^\infty dr\, S(r)\sin\frac{qr}{2}\left[2\Re f\cos\frac{qr}{2} - 2\Im f\sin\frac{qr}{2}\right] \\
&= \underbrace{\frac{16\pi}{q}\int_0^\infty dr\, S(r)\sin\frac{qr}{2}\Re f\cos\frac{qr}{2}}_{\text{II}^a} - \underbrace{\frac{16\pi}{q}\int_0^\infty dr\, S(r)\sin\frac{qr}{2}\Im f\sin\frac{qr}{2}}_{\text{II}^b}.
\end{aligned}
$$
$$\tag{C.15}$$

---

[1] Here, we use $f(q) = f_0(q)$ to avoid confusions with the fitted scattering length parameter, usually called f_0 (see later in this section).

where $\Re f$ and $\Im f$ are the real and imaginary part of f. Solving $\mathbf{II}^a$ and $\mathbf{II}^b$:

$$
\begin{aligned}
\mathbf{II}^a &= \frac{16\pi}{q} \int_0^\infty dr\, S(r) \sin \frac{qr}{2} \Re f \cos \frac{qr}{2} \\
&= \frac{16\pi \Re f}{q} \int_0^\infty dr \frac{e^{-r^2/4R^2}}{(4\pi R^2)^{\frac{3}{2}}} \sin \frac{qr}{2} \cos \frac{qr}{2} \\
&= \frac{2\Re f}{\sqrt{\pi}R} F_1(qR),
\end{aligned}
\tag{C.16}
$$

and

$$
\begin{aligned}
\mathbf{II}^b &= \frac{16\pi}{q} \int_0^\infty dr\, S(r) \sin \frac{qr}{2} \Im f \sin \frac{qr}{2} \\
&= \frac{16\pi \Im f}{q} \int_0^\infty dr \frac{e^{-r^2/4R^2}}{(4\pi R^2)^{\frac{3}{2}}} \sin^2 \frac{qr}{2} \\
&= \frac{\Im f}{R} F_2(qR),
\end{aligned}
\tag{C.17}
$$

where

$$
F_1(qR) = \int_0^{qR} dx \frac{e^{x^2-(qR)^2}}{qR} \quad \text{and} \quad F_2(qR) = \frac{1 - e^{(qR)^2}}{qR}.
\tag{C.18}
$$

With the Eqs. (C.13), (C.14), (C.15), (C.16), (C.17) and writting $f = f(q)$, the correlation function is

$$
C(q) = 1 + \frac{|f(q)|^2}{2R^2} + \frac{2\Re f(q)}{\sqrt{\pi}R} F_1(qR) - \frac{\Im f(q)}{R} F_2(qR).
\tag{C.19}
$$

The scattering amplitude, $f(q)$, present in Eq. (C.19) can be written in terms of the phase-shift as $f(q) = \left[\frac{q}{2}\cot\delta_0 - i\frac{q}{2}\right]^{-1}$. However, as previous mentioned, the δ_0 is not the observable that we are interested (since it depends on q). One way to obtain measurable quantities is by using the *effective range expansion*[2] [201], which leads to

$$
f(q) \approx \left[\frac{1}{f_0} + \frac{1}{8}d_0 q^2 - i\frac{q}{2}\right]^{-1},
\tag{C.20}
$$

where f_0 and d_0 are called *scattering lenght* and *effective range*, respectively, and these are the physical observables that can be extracted from the femtoscopic fit.

---

[2]This can be used for most of the cases in this thesis ($K_S^0\Lambda \oplus K_S^0\overline{\Lambda}$, $\Lambda\Lambda \oplus \overline{\Lambda}\overline{\Lambda}$ and $\Lambda\overline{\Lambda}$ correlations), except in the case of $K_S^0 K_S^0$ correlations, which is discussed at Sec. 3.3 of Chapter 3, and will be discussed later in this Appendix.

The physics interpretation of these parameters are detailed in Sec. 3.3 of Chapter 3.

In addition, the effect of pair of particles that are produced from the non-zero potential (non-asymptotic) region, i.e. $V(r) \neq 0$, should be taken into account in the correlations. According to the Lednicky and Lyubolshitz [175], this contribution is calculated assuming the distance of the pair to be equal to 0, that implies in $S(r=0) = 1/(4\pi R^2)^{3/2}$, and the correction, using the Eq. (C.20), is given by

$$\Delta C(q) = 4\pi S(r=0) \frac{|f(q)|^2}{q} \frac{d}{dq}\left(\frac{1}{\Re f(q)}\right) = \frac{d_0}{4\sqrt{\pi}R^3}|f(q)|^2. \qquad (C.21)$$

Than the LL model for non-identical particles is

$$
\begin{aligned}
C_{\mathrm{LL}}(q) &= C(q) - \Delta C(q) = 1 + C_{\mathrm{SI}}(q) \\
&= 1 + \sum_S \rho_S\left[\frac{|f^S(q)|^2}{2R^2}\left(1 - \frac{d_0^S}{2\sqrt{\pi}R}\right) + \frac{2\Re f^S(q)}{\sqrt{\pi}R}F_1(qR) - \frac{\Im f^S(q)}{R}F_2(qR)\right],
\end{aligned}
$$
$$(C.22)$$

where the spin dependence, $\rho_S = \frac{(2S+1)}{(2s_1+1)(2s_2+1)}$, for the case of unpolarized emission is introduced as shown at Chapter 3. The sum runs over the possible spin states. The correction from the non-zero potencial implies in an extra constraint to avoid negative (unphysical) correlations, specially for negative values of f_0, which is $d_0 \leq 2\sqrt{\pi}R$. For $\Lambda\overline{\Lambda}$ the sum must run over both singlet ($S = 0$) and triple ($S = 1$) states, however due the limited statistics only the average spin-dependency is taken into account, while for $K_S^0\Lambda \oplus K_S^0\overline{\Lambda}$, there is only one possible spin state. From Eq. (C.22), the strong final state interaction term can be identified as

$$C_{\mathrm{SI}}(q) = \sum_S \rho_S\left[\frac{|f^S(q)|^2}{2R^2}\left(1 - \frac{d_0^S}{2\sqrt{\pi}R}\right) + \frac{2\Re f^S(q)}{\sqrt{\pi}R}F_1(qR) - \frac{\Im f^S(q)}{R}F_2(qR)\right],$$
$$(C.23)$$

where in the experimental fit it is used $q = q_{\mathrm{inv}}$ and $R = R_{\mathrm{inv}}$.

C.2 Identical particles

In the case of identical particles, the effect of the wave function symmetrization for bosons (Bose-Einstein correlations) or antisymmetrization for fermions (Fermi-

Dirac correlations), due to the quantum statistics, must be taken into account. The derivation below considers the correlations of interest: i) spin half baryons, for $\Lambda\Lambda \oplus \overline{\Lambda}\,\overline{\Lambda}$; and ii) spin zero mesons, for $K_S^0 K_S^0$.

Pair of spin half baryons

In the case of $\Lambda\Lambda \oplus \overline{\Lambda}\,\overline{\Lambda}$ correlations (identical spin half baryons), the contributions from both singlet and triplet states must be studied (as shown in Chapter 3). The total two-particle wave function for the singlet can be written as a product of the terms from the symmetric spatial wave function, $\Psi_{\text{sym}}(\mathbf{q}, \mathbf{r})$, and the antisymmetric spin (S) part, χ_{antisym}, as

$$\Psi_{\text{tot}}(\mathbf{q}, \mathbf{r}) = \Psi_{\text{sym}}(\mathbf{q}, \mathbf{r}) \cdot \chi_{\text{antisym}}(S). \tag{C.24}$$

The symmetrization of the spatial wave function can be done applying $\mathbf{r} \to -\mathbf{r}$ [199], thus

$$
\begin{aligned}
\Psi_{\text{sym}}(\mathbf{q}, \mathbf{r}) &= \frac{1}{\sqrt{2}} \left[\Psi(\mathbf{q}, \mathbf{r}) + \Psi(\mathbf{q}, -\mathbf{r}) \right] \\
&= \sqrt{2} \left[\cos\left(\frac{\mathbf{q} \cdot \mathbf{r}}{2} \right) + \psi_0(q, r) - j_0(qr) \right].
\end{aligned}
\tag{C.25}
$$

Replacing Eq. (C.25) in Eq. (C.1), and using the Gaussian source function from Eq. (C.2), the correlation function for the singlet state is given by

$$C_{S=0}(q) = 1 + e^{-q^2 R^2} + 8\pi \int dr\, r^2 S(r) \left[|\psi_0(q, r)|^2 - j_0^2(qr) \right]. \tag{C.26}$$

For the triplet state, the wave function is written in terms of the symmetric spin part, χ_{sym}, and antisymmetric spatial wave function, $\Psi_{\text{antisym}}(\mathbf{q}, \mathbf{r})$, as

$$\Psi(\mathbf{q}, \mathbf{r}) = \Psi_{\text{antisym}}(\mathbf{q}, \mathbf{r}) \cdot \chi_{\text{sym}}(S, M), \tag{C.27}$$

where

$$
\begin{aligned}
\Psi_{\text{antisym}}(\mathbf{q}, \mathbf{r}) &= \frac{1}{\sqrt{2}} \left[\Psi(\mathbf{q}, \mathbf{r}) - \Psi(\mathbf{q}, -\mathbf{r}) \right] \\
&= \frac{1}{\sqrt{2}} \left[e^{i \frac{\mathbf{q} \cdot \mathbf{r}}{2}} - e^{-i \frac{\mathbf{q} \cdot \mathbf{r}}{2}} \right],
\end{aligned}
\tag{C.28}
$$

which does not have strong FSI contributions since it does not have s-wave inter-

action. Therefore, only the quantum statistic term remain: $C_{S=1}(k) = 1 - e^{-q^2R^2}$.

Using the contributions from singlet and triplet and the respective statistical weight for each spin state (see Chapter 3), the correlation function for identical spin half baryons is given by

$$
\begin{aligned}
C(q) &= \frac{1}{4}C_{S=0}(q) + \frac{3}{4}C_{S=1}(q) \\
&\quad 1 - \frac{1}{2}e^{-q^2R^2} + 2\pi \int_0^\infty dr r^2 S(r) \left[|\psi_0(q,r)|^2 - j_0^2(qr) \right],
\end{aligned} \quad \text{(C.29)}
$$

where the strong final state interaction contribution can be identified as

$$
C_{SI}(q) = 2\pi \int_0^\infty dr r^2 S(r) \left[|\psi_0(q,r)|^2 - j_0^2(kq) \right], \quad \text{(C.30)}
$$

which only differs from the Eq. (C.10) by a factor of $1/2$. Using the result from Eq. (C.23), the equation above can be rewritten as

$$
C_{SI}(k) = \frac{1}{2} \left[\frac{|f(q)|^2}{2R^2} \left(1 - \frac{d_0}{2\sqrt{\pi}R} \right) + \frac{2\Re f(q)}{\sqrt{\pi}R} F_1(qR) - \frac{\Im f(q)}{R} F_2(qR) \right]. \quad \text{(C.31)}
$$

Pair of spin zero mesons

In the case of two identical mesons with spin zero ($\rho_S = 1$), as in $K_S^0 K_S^0$ correlations, the total wave function is written only in terms of the symmetrical spatial wave function, $\Psi_{\text{sym}}(\mathbf{q}, \mathbf{r})$, since there is no spin part, thus

$$
\begin{aligned}
\Psi_{\text{sym}}(\mathbf{q}, \mathbf{r}) &= \frac{1}{\sqrt{2}} \left[\Psi(\mathbf{q}, \mathbf{r}) + \Psi(\mathbf{q}, -\mathbf{r}) \right] \\
&= \sqrt{2} \left[\cos\left(\frac{\mathbf{q} \cdot \mathbf{r}}{2} \right) + \psi_0(q,r) - j_0(kr) \right].
\end{aligned} \quad \text{(C.32)}
$$

Similarly as done for identical baryons, the correlation function can be derived using Eqs. (C.32), (C.1), Eq. (C.2), and the respective statistical weight as

$$
C(q) = 1 + e^{-q^2R^2} + 2\pi \int_0^\infty dr r^2 S(r) \left[|\psi_0(q,r)|^2 - j_0^2(qr) \right], \quad \text{(C.33)}
$$

where the strong FSI term can be identified as

$$
C_{SI}(q) = 2\pi \int_0^\infty dr r^2 S(r) \left[|\psi_0(q,r)|^2 - j_0^2(qr) \right], \quad \text{(C.34)}
$$

which only differs from the Eq. (C.10) by a factor of 2. Using again the result from Eq. (C.23), we have

$$C_{\text{SI}}(q) = \left[\left| \frac{f(q)}{R} \right|^2 + \frac{4\Re f(q)}{\sqrt{\pi}R} F_1(qR) - \frac{2\Im f(q)}{R} F_2(qR) \right] \tag{C.35}$$

Note that, the Eqs. (C.29) and (C.33), show that the strong FSI is addictive to the quantum statistic term and than the correlation function becomes: $C_{\text{Theory}}(q) = 1 + C_{\text{QS}}(q) + C_{\text{SI}}(q)$. This behavior is also valid in the case of non-identical particles, but with $C_{\text{QS}}(q) = 0$.

In the case of $K_S^0 K_S^0$ correlations, the scattering amplitude is written in terms of $f_0(980)$ and $a_0(980)$, as shown at Chapter 3. Also, an additional constant, usually called $B = (1 - \epsilon)/2$, multiplies C_{SI} in order to take into account possible effects from the assymetry in the kaon production. In CMS, the ratio K^+/K^- [354] is basically at unity, thus, assuming the same for neutral kaons, we obtain $\epsilon = 0$ (1-K^+/K^-) and $B = 1/2$.

Appendix D

Service Work and Run Activities

All CMS members are required to perform services for the collaboration, these services are called Experimental Physics Responsibilities (EPR) and are taken into account using months of work (called EPR months). The EPR is basically all the work needed to collect the data and can be done in the hardware or software part (improvements on softwares, detector upgrades, ...)[1]. These services are directly related with authorship, each institute is requested to contribute a certain amount of EPR per year, which is calculated based on the number of authors from that institute. To became an author of CMS papers, 6 EPR months of work are needed and to continue in the author list each person of the group (e. g. SPRACE) needs 4 EPR months during the year. The service works performed from 2018[2] to 2020 are described below[3].

D.1 2018

During 2018, two service work were the performed: i) Computing Shifts (CSP); and ii) Recontruction algorithms with the Heavy Ion (HI) Tracking Group;

D.1.1 Computing Shifts

First, I joined the computing team for helping to monitor the data generation and transfer among CMS Grid Tiers-1 and Tiers-2 around the world. This is called Computing shifts (CSP). This task is a common service work activity performed by the SPRACE team. This activity is considered central (equivalent to those done on site) by CMS, but can be performed remotely, from the SPRACE CMS Center in São Paulo. In total, 41 CSP shifts day were concluded, from February to December of 2018.

---

[1] Analysis are not counted as service work.
[2] In 2017 the main focus was the PhD courses and to learn CMSSW.
[3] Since these results are not public, they cannot be included here.

D.1.2   CMS Heavy Ion Tracking Group

In parallel, studies were performed together with the CMS HI Tracking Group in order to implement a new algorithm to reconstruct the tracks for the new detector geometry (including pixel tracks with 4 layers), used in the HI Run (PbPb collisions) at the end of 2018. This reconstruction was done in the same way as it was done in xenon-xenon collisions in 2017. One of the tasks was focused on reducing the track reconstruction time and the fake tracks, and increasing efficiency. Tests using different versions of CMSSW were performed for minimum bias events using Monte Carlo simulations.

D.2   2019

In 2019, I joined the Heavy Ion Global Observables (or Centrality) Group and continued to work together with the Heavy Ion Tracking Group.

D.2.1   CMS Heavy Ion Tracking Group

In the tracking group, two tasks were performed in 2019, using the data collected in 2018 PbPb Run:

- Estimate the offline track selection to obtain the high efficiency and low fake rate by comparing results of the official Monte Carlo simulation with data samples. Later, this efficiency and fake rates are used as corrections to the analyses. This study was performed for investigate the p_{T}, η and centrality dependences. Systematic variations of the track selection were also studied.

- Optimize the V^0 cut-based reconstruction and compare with the results using Boosted Decision Trees performed by Kansas University Group. In the cut-based, the selections (similar to presented at Sec. 5.2 of Chapter 5) was optimized using Monte Carlo to reduce the combinatorial background as much as possible, and then applied to data. A similar efficiency between cut based and BDT was observed. In the non-central collisions (centrality $> 10\%$ for K_{S}^0 and $> 20\%$ for $\Lambda/\overline{\Lambda}$) the cut-based showed similar (and sometimes better) signal fraction $\left(\frac{s}{s+b}\right)$ than the BTD. However, for central events (0-10% for K_{S}^0 and 0-20% for $\Lambda/\overline{\Lambda}$), the BDT showed better results.

D.2.2 CMS Heavy Ion Global Observables Group

In the GO group, the task addressed was the validation of centrality quantities, e. g. multiplicity, in different releases of CMSSW, Monte Carlo checks and the consistency of reconstructions.

D.3 2020

In 2020, I worked with GO group for producing MC simulations to investigate contaminations for the next Run period and also in `CMSSW` implementations to store important information (filters) in a new data format adopted by the HI group. Also, I joined to CMS High-Level Trigger Group to study the online track reconstruction (connecting the tracking and HLT groups) by using GPU's.

D.3.1 CMS Heavy Ion Global Observables Group

In the centrality group, two tasks were concluded in 2020.

- The first one was to simulate two MC samples for STARLight [355] generator for the 2022 heavy ion run with 1 million events each. The STARLight MC simulates PbPb ultra-peripheral collisions (the nuclei do not touch each other), and only photon-nucleus interactions (in this case the nucleus is broken by the photon, similarly to a deep inelastic scattering process and this generates the signal) happen and this can be used to estimate the electromagnetic contamination in peripheral events for the next HI Run. The samples were generated in two different configurations: i) single diffraction: one nucleus emit a single photon that interacts with the other nucleus; and ii) double diffraction: each nucleus emit a photon that interacts with the opposite nucleus.

- The second task was related with the fact that the CMS HI group is migrating from AOD data format to MiniAOD data format. This should reduce the data size significantly (at least by a factor of 10). Originally, this MiniAOD is used for pp collisions and the format does not include important information which are useful for some HF centrality filters[4]. To solve that, those filters should be stored in MiniAOD format only for HI runs and could not affect

---

[4]Centrality filters are applied to eliminate events with some contamination (for example: electromagnetic).

pp runs. This implementation was done by saving a C++ "struct" type with a minimum number of towers between the positive ($3 < \eta < 5$) side and negative side ($-5 < \eta < -3$) of HF for different thresholds (2, 3, 4 and 5 GeV). This quantities were also added in the HiForest framework (basically converts CMS heavy ion data into ROOT Trees). The usage of these filters by analyzers was also studied. At the end, validations and cross-checks were performed in order to check the consistency between AOD and MiniAOD. The comparison showed total agreement.

D.3.2 CMS Heavy Ion High-Level Trigger Group

I was designated as the CMS contact person of the Graphics Processing Units (GPU) implementation of HLT for 2022 heavy ion run. The proposal of this task is to implement the HLT in the GPU structure[5]. Originally, the GPU implementation of the codes was developed for pp collisions (see patatrack.web.cern.ch/), called patatrack. This implementation is already working for pixel detectors (most internal part of the tracker), electromagnetic calorimeter (ECAL) and hadronic calorimeter (HCAL). A website including pie charts for different modules was created in order to check the timing performance (test-pie.web.cern.ch/test-pie/circles/web/piechart.html). These pie charts were produced by running the HLT in `CMSSW` on real machine and the timing studies were performed for different 2018 PbPb datasets, with different configurations. The GPU speed-up the individual modules: pixels in ∼35%, ECAL ∼38% and HCAL in ∼85%. The total time difference was ∼13%. Since this is an ongoing task, more studies are needed yet, for example the efficiency studies for PbPb data comparing CPU's and GPU's, as done for pp.

D.4 2021

In 2021, I have continued to work together with the CMS GO group to study possible electromagnetic (and other) contaminations in the centrality determination. Also, I was nominated group leader of the Heavy Ion High-Level Trigger Group, position that started in September, and continue the efforts with the GPU implementation.

---

[5]The idea is to used the multicores from GPU's instead of CPU's.

D.5   2018 Heavy Ion Run (PbPb)

As the HI Group in CMS counts with a small number of people, besides the services, usually the students are required to help during the data-taking activities. During the 2018 heavy ion Run, which happened in November and December, I have actively participated in the lead-lead (PbPb) data-taking activities together with the HI Group, at CERN, during which:

- I attended all daily run meetings and all the meetings of the flow/correlations group.

- Tracking studies: compared tracking quantities from 2018 lead-lead collisions with the corresponding variables from 2015 lead-lead data-taking. Considered data events and Monte Carlo simulations to check their consistency and the effects of the new tracker geometry.

- Low-multiplicity triggers: I've participated in the implementation and monitoring of the efficiency (turn-on curves) of low charged particles multiplicity triggers during the run. These triggers were designed to study different collision systems, for example, to compare lead-lead and proton-proton physics.

Such period constitute a very intense and unique learning experience. As mention in D.3.1 and D.3.2, our group has worked for the improvements for the next Heavy Ion Run, in softwares, and hopefully we will join the HI group at CERN for the next data-taking period (probably in 2022).

D.6   Publications

The list of publications containing the experimental and phenomenological papers can be found in Inpire published HEP website, in the link:

https://inspirehep.net/authors/1589924

Bibliography

[1] T. Ludlam and S. Aronson. Hunting the quark gluon plasma. *BNL-73847-2005*, 2005. doi:10.2172/15015225.

[2] CMS Collaboration. Observation of Long-Range Near-Side Angular Correlations in Proton-Proton Collisions at the LHC. *JHEP*, **09**:091, 2010. doi:10.1007/JHEP09(2010)091, arXiv:1009.4122.

[3] G. Goldhaber et al. Influence of Bose-Einstein statistics on the anti-proton proton annihilation process. *Phys. Rev.*, **120**:300, 1960. doi:10.1103/PhysRev.120.300.

[4] CMS Collaboration. The CMS experiment at the CERN LHC. The Compact Muon Solenoid experiment. *JINST*, **3**:S08004, 2008. doi:10.1088/1748-0221/3/08/S08004, cds.cern.ch/record/1129810, CMS Website.

[5] J. J. Thomson. Xl cathode rays. *Phil. Mag.*, **44**:293, 1897. doi:10.1080/14786449708621070.

[6] M. K. Gaillard et al. The Standard model of particle physics. *Rev. Mod. Phys.*, **71**:S96, 1999. doi:10.1103/RevModPhys.71.S96, arXiv:hep-ph/9812285.

[7] S. F. Novaes. Standard model: An Introduction. In *10th Jorge Andre Swieca Summer School: Particle and Fields*, 1999. arXiv:hep-ph/0001283.

[8] S. Weinberg. The making of the standard model. *Eur. Phys. J. C*, **34**:5, 2004. doi:10.1140/epjc/s2004-01761-1, arXiv:hep-ph/0401010.

[9] C. Quigg. *Gauge Theories of the Strong, Weak, and Electromagnetic Interactions: Second Edition*. Princeton University Press, USA, 2013.

[10] Particle Data Group. Review of Particle Physics. *Progress of Theoretical and Experimental Physics*, 2020. doi:10.1093/ptep/ptaa104, pdg.lbl.gov.

[11] S. L. Glashow. The renormalizability of vector meson interactions. *Nuclear Physics*, **10**:107, 1959. doi:10.1016/0029-5582(59)90196-8.

[12] A. Salam. Weak and Electromagnetic Interactions. *Conf. Proc. C*, **680519**:367, 1968. doi:10.1142/9789812795915_0034.

[13] S. Weinberg. A model of leptons. *Phys. Rev. Lett.*, **19**:1264, 1967. doi:10.1103/PhysRevLett.19.1264.

[14] Peter W. Higgs. Broken symmetries and the masses of gauge bosons. *Phys. Rev. Lett.*, **13**:508, 1964. doi:10.1103/PhysRevLett.13.508.

[15] F. Englert and R. Brout. Broken Symmetry and the Mass of Gauge Vector Mesons. *Phys. Rev. Lett.*, **13**:321, 1964. doi:10.1103/PhysRevLett.13.321.

[16] CMS Collaboration. Observation of a New Boson at a Mass of 125 GeV with the CMS Experiment at the LHC. *Phys. Lett. B*, **716**:30, 2012. doi:10.1016/j.physletb.2012.08.021, arXiv:1207.7235.

[17] ATLAS Collaboration. Observation of a new particle in the search for the Standard Model Higgs boson with the ATLAS detector at the LHC. *Phys. Lett. B*, **716**:1, 2012. doi:10.1016/j.physletb.2012.08.020, arXiv:1207.7214.

[18] E. Rutherford. Collision of α particles with light atoms. IV. An anomalous effect in nitrogen. *Phil. Mag.*, **90**:31, 1919. doi:10.1080/14786431003659230.

[19] J. Chadwick. The existence of a neutron. *Proc. R. Soc. Lond. A*, **136**:692, 1932. doi:10.1098/rspa.1932.0112.

[20] C. M. G. Lattes et al. Processes Involving Charged Mesons. *Nature*, **159**:694, 1947. doi:10.1038/159694a0.

[21] G. D. Rochester and C. C. Butler. Evidence for the Existence of New Unstable Elementary Particles. *Nature*, **160**:855, 1947. doi:10.1038/160855a0.

[22] R. Armenteros et al. The properties of neutral V-particles. *Phil. Mag.*, **42**:1113, 1951. doi:10.1080/14786445108561358.

[23] R. Armeteros et al. Decay of V-Particles. *Nature*, **167**:501, 1951. doi:10.1038/167501a0.

[24] S. Sakata. On a Composite Model for the New Particles. *Progress of Theoretical Physics*, **16**:686, 12 1956. doi:10.1143/PTP.16.686.

[25] Z. Maki et al. A Unified Model for Elementary Particles: . *Progress of Theoretical Physics*, **23**:1174, 1960. doi:10.1143/PTP.23.1174.

[26] Z. Maki et al. Remarks on the Unified Model of Elementary Particles. *Progress of Theoretical Physics*, **28**:870, 1962. doi:10.1143/PTP.28.870.

[27] M. Gell-Mann. A Schematic Model of Baryons and Mesons. *Phys. Lett.*, **8**:214–215, 1964. doi:10.1016/S0031-9163(64)92001-3.

[28] G. Zweig. An SU(3) model for strong interaction symmetry and its breaking. 1964. cds.cern.ch/record/352337.

[29] O. W. Greenberg. Spin and unitary-spin independence in a paraquark model of baryons and mesons. *Phys. Rev. Lett.*, **13**:598, 1964. doi:10.1103/PhysRevLett.13.598.

[30] M. Y. Han and Y. Nambu. Three-triplet model with double SU(3) symmetry. *Phys. Rev.*, **139**:B1006, 1965. doi:10.1103/PhysRev.139.B1006.

[31] A. Ali and G. Kramer. Jets and QCD: A Historical Review of the Discovery of the Quark and Gluon Jets and its Impact on QCD. *Eur. Phys. J. H*, **36**:245, 2011. doi:10.1140/epjh/e2011-10047-1, arXiv:1012.2288.

[32] E598 Collaboration. Experimental observation of a heavy particle J. *Phys. Rev. Lett.*, **33**:1404, 1974. doi:10.1103/PhysRevLett.33.1404.

[33] SLAC-SP-017 Collaboration. Discovery of a Narrow Resonance in e^+e^- Annihilation. *Phys. Rev. Lett.*, **33**:1406, 1974. doi:10.1103/PhysRevLett.33.1406.

[34] S. W. Herb et al. Observation of a dimuon resonance at 9.5 GeV in 400-GeV proton-nucleus collisions. *Phys. Rev. Lett.*, **39**:252, 1977. doi:10.1103/PhysRevLett.39.252.

[35] PLUTO Collaboration. Evidence for gluon bremsstrahlung in e^+e^- annihilations at high energies. *Physics Letters B*, **86**:418, 1979. doi:10.1016/0370-2693(79)90869-4.

[36] MARK-J Collaboration. Discovery of three-jet events and a test of quantum chromodynamics at PETRA. *Phys. Rev. Lett.*, **43**:830, 1979. doi:10.1103/PhysRevLett.43.830.

[37] TASSO Collaboration. Evidence for planar events in e^+e^- annihilation at high energies. *Physics Letters B*, **86**:243, 1979. doi:10.1016/0370-2693(79)90830-X.

[38] F. Halzen and A. Martin. *Quarks & Leptons: An introductory course in modern particle physics*. John Wiley & Sons, New York, USA, 1984.

[39] DØ Collaboration. Observation of the top quark. *Phys. Rev. Lett.*, **74**:2632, 1995. doi:10.1103/PhysRevLett.74.2632, arXiv:hep-ex/9503003.

[40] CDF Collaboration. Observation of top quark production in $\bar{p}p$ collisions. *Phys. Rev. Lett.*, **74**:2626, 1995. doi:10.1103/PhysRevLett.74.2626, arXiv:hep-ex/9503002.

[41] CMS Collaboration. Observation of top quark production in proton-nucleus collisions. *Phys. Rev. Lett.*, **119**:242001, 2017. doi:10.1103/PhysRevLett.119.242001, arXiv:1709.07411.

[42] CMS Collaboration. Evidence for Top Quark Production in Nucleus-Nucleus Collisions. *Phys. Rev. Lett.*, **125**:222001, 2020. doi:10.1103/PhysRevLett.125.222001, arXiv:2006.11110.

[43] Belle Collaboration. Observation of two charged bottomonium-like resonances in Y(5S) decays. *Phys. Rev. Lett.*, **108**:122001, 2012. doi:10.1103/PhysRevLett.108.122001, arXiv:1110.2251.

[44] BESIII Collaboration. Observation of a Charged Charmoniumlike Structure in $e^+e^- \to \pi^+\pi^- J/\psi$ at $\sqrt{s}$ =4.26 GeV. *Phys. Rev. Lett.*, **110**:252001, 2013. doi:10.1103/PhysRevLett.110.252001, arXiv:1303.5949.

[45] LHCb Collaboration. Observation of the resonant character of the $Z(4430)^-$ state. *Phys. Rev. Lett.*, **112**:222002, 2014. doi:10.1103/PhysRevLett.112.222002, arXiv:1404.1903.

[46] LHCb Collaboration. Amplitude analysis of $B^+ \to J/\psi\phi K^+$ decays. *Phys. Rev. D*, **95**:012002, 2017. doi:10.1103/PhysRevD.95.012002, arXiv:1606.07898.

[47] LHCb Collaboration. Observation of $J/\psi\phi$ structures consistent with exotic states from amplitude analysis of $B^+ \to J/\psi\phi K^+$ decays. *Phys. Rev. Lett.*, **118**:022003, 2017. doi:10.1103/PhysRevLett.118.022003, arXiv:1606.07895.

[48] LHCb Collaboration. LHCb measurements of the exotic tetraquark candidate $\chi_{c1}(3872)$ in high-multiplicity pp and pPb collisions. *Nucl. Phys. A*, **1005**:121918, 2021. arXiv:2002.01551.

[49] LHCb Collaboration. Observation of $J/\psi p$ Resonances Consistent with Pentaquark States in $\Lambda_b^0 \rightarrow J/\psi K^- p$ Decays. *Phys. Rev. Lett.*, **115**:072001, 2015. doi:10.1103/PhysRevLett.115.072001, arXiv:1507.03414.

[50] LHCb Collaboration. Observation of structure in the J/ψ-pair mass spectrum. *Sci. Bull.*, **65**:1983, 2020. doi:10.1016/j.scib.2020.08.032, arXiv:2006.16957.

[51] H. Fritzsch et al. Advantages of the Color Octet Gluon Picture. *Phys. Lett. B*, **47**:365, 1973. doi:10.1016/0370-2693(73)90625-4.

[52] D. J. Gross and F. Wilczek. Ultraviolet Behavior of Non-abelian Gauge Theories. *Phys. Rev. Lett.*, **30**:1343, 1973. doi:10.1103/PhysRevLett.30.1343.

[53] S. Weinberg. Nonabelian Gauge Theories of the Strong Interactions. *Phys. Rev. Lett.*, **31**:494, 1973. doi:10.1103/PhysRevLett.31.494.

[54] G. 't Hooft and M. J. G. Veltman. Regularization and Renormalization of Gauge Fields. *Nucl. Phys. B*, **44**:189, 1972. doi:10.1016/0550-3213(72)90279-9.

[55] M. E. Peskin and D. V. Schroeder. *An introduction to quantum field theory*. Westview, Boulder, CO, 1995.

[56] J. L. Kneur and A. Neveu. $\Lambda_{\text{MS}}^{\text{QCD}}$ from Renormalization Group Optimized Perturbation. *Phys. Rev. D*, **85**:014005, 2012. 10.1103/PhysRevD.85.014005, arXiv:1108.3501.

[57] Y. V. Kovchegov and E. Levin. *Quantum chromodynamics at high energy*. Cambridge University Press, 2012.

[58] S. Durr et al. Ab-Initio Determination of Light Hadron Masses. *Science*, **322**:1224, 2008. doi:10.1126/science.1163233, arXiv:0906.3599.

[59] C. Liu. Recent results from Lattice QCD. *Int. J. Mod. Phys. Conf. Ser.*, **31**:1460282, 2014. doi:10.1142/S2010194514602828, arXiv:1403.1645.

[60] Mark Thomson. *Modern particle physics*. Cambridge University Press, New York, 2013.

[61] CMI Website – Yang–Mills and Mass Gap. https://www.claymath.org/millennium-problems/yang%E2%80%93mills-and-mass-gap. [last access on 13/Mar/2021].

[62] H. D. Politzer. Reliable perturbative results for strong interactions? *Phys. Rev. Lett.*, **30**:1346, 1973. doi:10.1103/PhysRevLett.30.1346.

[63] E. V. Shuryak. *The QCD vacuum, hadrons and the superdense matter*. World Scientific Publishing Company, 2004.

[64] J. Rafelski. Discovery of Quark-Gluon-Plasma: Strangeness Diaries. *Eur. Phys. J. ST*, **229**:1, 2020. doi:10.1140/epjst/e2019-900263-x, arXiv:1911.00831.

[65] Report of the workshop on BeV/nucleon collisions of heavy ions – how and why, Bear Mountain, New York, Nov. 29 – Dec. 1, 1974 (BNL-AUI, 1975). www.osti.gov/biblio/4061527.

[66] T. D. Lee. A Possible New Form of Matter at High Density. *AIP Conf. Proc.*, **28**:65, 1976. doi:10.1142/9789814434973_0005.

[67] M. Gyulassy and L. McLerran. New forms of QCD matter discovered at RHIC. *Nuc. Phys. A*, **750**:30, 2005. doi:10.1016/j.nuclphysa.2004.10.034, arXiv:nucl-th/0405013.

[68] W. Scheid and others. Nuclear Shock Waves in Heavy-Ion Collisions. *Phys. Rev. Lett.*, **32**:741, 1974. doi:10.1103/PhysRevLett.32.741.

[69] J. C. Collins and M. J. Perry. Superdense matter: Neutrons or asymptotically free quarks? *Phys. Rev. Lett.*, **34**:1353, 1975. doi:10.1103/PhysRevLett.34.1353.

[70] J. D. Bjorken. Highly Relativistic Nucleus-Nucleus Collisions: The Central Rapidity Region. *Phys. Rev. D*, **27**:140, 1983. doi:10.1103/PhysRevD.27.140.

[71] L. D. Landau. On the multiparticle production in high-energy collisions. *Izv. Akad. Nauk Ser. Fiz.*, **17**:51, 1953.

[72] L. D. Landau and E. M. Lifshitz. *Fluid Mechanics. Landau and Lifshitz: Course of Theoretical Physics*. Butterworth-Heinemann Ltd., 1987.

[73] D. S. Lemos. Efeitos da Hidrodinâmica Dissipativa e da Equação de Estado sobre o Fluxo Elíptico e a Interferometria HBT (in portuguese): https://sucupira.capes.gov.br/sucupira/public/consultas/coleta/trabalho Conclusao/viewTrabalhoConclusao.jsf?popup=true&id_trabalho=4998386. Master's thesis, Universidade Federal do Rio Grande (FURG), 2017.

[74] D. S. Lemos and O. Socolowski. Effects of dissipative hydrodynamics on elliptic flow and HBT interferometry in central collisions at RHIC. *J. Phys. Conf. Ser.,* **1291**:012033, 2019. doi:10.1088/1742-6596/1291/1/012033.

[75] D. S. Lemos. Complete Hydrodynamical Evolution SyStem (CHESS). *Github page: github.com/denerslemos/CHESS/ (α version),* Results for pp collisions presented at QM2018: indico.cern.ch/event/656452/contributions/2859548/, [last access on 13/Mar/2021].

[76] O. Socolowski et al. Fluctuations of the initial conditions and the continuous emission in the hydrodynamical description of two-pion interferometry. *Phys. Rev. Lett.,* **93**:182301, 2004. doi:10.1103/PhysRevLett.93.182301, arXiv:hep-ph/0405181.

[77] Y. Hama et al. NeXSPheRIO Results on Elliptic-Flow Fluctuations at RHIC. *Phys. Atom. Nucl.,* **71**:1558, 2008. doi:10.1134/S106377880809010X, arXiv:0711.4544.

[78] B. Schenke et al. (3+1)D hydrodynamic simulation of relativistic heavy-ion collisions. *Phys. Rev. C,* **82**:014903, 2010. doi:10.1103/PhysRevC.82.014903, arXiv:1004.1408.

[79] B. Schenke et al. Elliptic and triangular flow in event-by-event (3+1)D viscous hydrodynamics. *Phys. Rev. Lett.,* **106**:042301, 2011. doi:10.1103/PhysRevLett.106.042301, arXiv:1009.3244.

[80] M. Habich et al. Particle spectra and HBT radii for simulated central nuclear collisions of C + C, Al + Al, Cu + Cu, Au + Au, and Pb + Pb from $\sqrt{s_{NN}} = 62.4$ - 2760 GeV. *Eur. Phys. J. C,* **75**:15, 2015. doi:10.1140/epjc/s10052-014-3206-7, arXiv:1409.0040.

[81] C. Shen et al. The iEBE-VISHNU code package for relativistic heavy-ion collisions. *Comput. Phys. Commun.,* **199**:61, 2016. doi:10.1016/j.cpc.2015.08.039, arXiv:1409.8164.

[82] J. Barale. Performance of the Bevalac. *IEEE Trans. Nucl. Sci.,* **22**:1672, 1975. doi:10.1109/TNS.1975.4327963.

[83] E. J. Lofgren. Accelerator division annual reports. 1975. doi:10.2172/937059.

[84] CERN Website. New State of Matter created at CERN. https://home.cern/news/press-release/cern/new-state-matter-created-cern [last access on 13/Mar/2021], 2000.

[85] A. Aboot. CERN claims first experimental creation of quark-gluon plasma. *Nature*, **403**:6770, 2000. doi:10.1038/35001196.

[86] NA61/SHINE Collaboration. NA61/SHINE facility at the CERN SPS: beams and detector system. *JINST*, **9**:P06005, 2014. doi:10.1088/1748-0221/9/06/P06005, arXiv:1401.4699.

[87] R. Hagedorn. Statistical thermodynamics of strong interactions at high-energies. *Nuovo Cim. Suppl.*, **3**:147, 1965. cds.cern.ch/record/346206.

[88] C.-Y. Wong. *Introduction to high-energy heavy-ion collisions*. World Scientific, 1994.

[89] A. Chodos, R. L. Jaffe, K. Johnson, C. B. Thorn, and V. F. Weisskopf. New extended model of hadrons. *Phys. Rev. D*, **9**:3471, 1974. doi:10.1103/PhysRevD.9.3471.

[90] A. Bazavov et al. The equation of state in (2+1)-flavor QCD. *Phys. Rev. D*, **90**:094503, 2014. doi:10.1103/PhysRevD.90.094503, arXiv:1407.6387.

[91] J Buchler. Properties of the neutron gas and application to neutron stars. *Nucl. Phys. A*, **170**:1, 1971. doi:10.1016/0375-9474(71)90678-6.

[92] M. G. Alford et al. Color superconductivity in dense quark matter. *Rev. Mod. Phys.*, **80**:1455, 2008. doi:10.1103/RevModPhys.80.1455, arXiv:0709.4635.

[93] DOE/NSF Nuclear Science Advisory Committee. The Frontiers of Nuclear Science, A Long Range Plan. 2008. arXiv:0809.3137.

[94] R. Snellings. Elliptic Flow: A Brief Review. *New J. Phys.*, **13**:055008, 2011. doi:10.1088/1367-2630/13/5/055008, arXiv:1102.3010.

[95] STAR Collaboration. Azimuthal anisotropy in Au+Au collisions at $\sqrt{s_{\mathrm{NN}}} = 200$ GeV. *Phys. Rev. C*, **72**:014904, 2005. doi:10.1103/PhysRevC.72.014904, arXiv:nucl-ex/0409033.

[96] M. D. Oldenburg. Scaling of anisotropic flow in the picture of quark coalescence. *J. Phys. G*, **31**:S437, 2005. doi:10.1088/0954-3899/31/4/054, arXiv:nucl-ex/0412001.

[97] N. van der Kolk. *To flow or not to flow: A study of elliptic flow and nonflow in proton-proton collisions in ALICE*. PhD thesis, Utrecht University, 2012. cds.cern.ch/record/1432220.

[98] J. Rafelski and B. Muller. Strangeness Production in the Quark-Gluon Plasma. *Phys. Rev. Lett.*, **48**:1066, 1982. doi:10.1103/PhysRevLett.48.1066.

[99] E802 Collaboration. Centrality dependence of K^+ and π^+ multiplicities from Si+A collisions at 14.6-A-GeV/c. *Phys. Lett. B*, **291**:341, 1992. doi:10.1016/0370-2693(92)91056-F.

[100] WA97 Collaboration. Production of strange and multistrange hadrons in nucleus nucleus collisions at the SPS. *Nucl. Phys. A*, **661**:130, 1999. doi:10.1016/S0375-9474(99)85015-5.

[101] STAR Collaboration. Enhanced strange baryon production in Au+Au collisions compared to p+p at $\sqrt{s_{\mathrm{NN}}}$ = 200 GeV. *Phys. Rev. C*, **77**:044908, 2008. doi:10.1103/PhysRevC.77.044908, arXiv:0705.2511.

[102] ALICE Collaboration. Enhanced production of multi-strange hadrons in high-multiplicity proton-proton collisions. *Nature Phys.*, **13**:535, 2017. doi:10.1038/nphys4111, arXiv:1606.07424.

[103] J. D. Bjorken. Energy Loss of Energetic Partons in Quark - Gluon Plasma: Possible Extinction of High p(t) Jets in Hadron - Hadron Collisions. 1982. FERMILAB-PUB-82-059-THY.

[104] STAR Collaboration. Evidence from d+Au measurements for final-state suppression of high-p_T hadrons in Au + Au collisions at rhic. *Phys. Rev. Lett.*, **91**:072304, 2003. doi:10.1103/PhysRevLett.91.072304, arXiv:nucl-ex/0306024.

[105] ATLAS Collaboration. Observation of a Centrality-Dependent Dijet Asymmetry in Lead-Lead Collisions at $\sqrt{s_{\mathrm{NN}}}$ = 2.76 TeV with the ATLAS Detector at the LHC. *Phys. Rev. Lett.*, **105**:252303, 2010. doi:10.1103/PhysRevLett.105.252303, arXiv:1011.6182.

[106] CMS Collaboration. Observation and studies of jet quenching in PbPb collisions at nucleon-nucleon center-of-mass energy = 2.76 TeV. *Phys. Rev. C*, **84**:024906, 2011. doi:10.1103/PhysRevC.84.024906, arXiv:1102.1957.

[107] B. Alver et al. The PHOBOS Glauber Monte Carlo. 2008. arXiv:0805.4411.

[108] C. Loizides et al. Improved version of the PHOBOS Glauber Monte Carlo. *SoftwareX*, **1-2**:13, 2015. doi:10.1016/j.softx.2015.05.001, arXiv:1408.2549.

[109] ALICE Collaboration. Centrality dependence of high-p_T D meson suppression in Pb-Pb collisions at $\sqrt{s_{NN}}$ = 2.76 TeV. *JHEP*, **11**:205, 2015. doi:10.1007/JHEP11(2015)205, arXiv:1506.06604.

[110] T. Matsui and H. Satz. J/ψ Suppression by Quark-Gluon Plasma Formation. *Phys. Lett. B*, **178**:416, 1986. doi:10.1016/0370-2693(86)91404-8.

[111] NA50 Collaboration. Results from the NA50 experiment on J/ψ suppression in $Pb - Pb$ collisions at the cern sps. *Nuclear Physics B - Proceedings Supplements*, **92**:43, 2001. doi:10.1016/S0920-5632(00)01018-5.

[112] PHENIX Collaboration. J/ψ Production in $\sqrt{s_{NN}}$ = 200 GeV Cu+Cu Collisions. *Phys. Rev. Lett.*, **101**:122301, 2008. doi:10.1103/PhysRevLett.101.122301, arXiv:0801.0220.

[113] CMS Collaboration. Suppression of Excited Y States Relative to the Ground State in Pb-Pb Collisions at $\sqrt{s_{NN}}$ =5.02 TeV. *Phys. Rev. Lett.*, **120**:142301, 2018. doi:10.1103/PhysRevLett.120.14230, arXiv:1706.05984.

[114] A. G. Stahl Leiton. *Measurement of W bosons in p-Pb at 8.16 TeV and of charmonia in Pb-Pb at 5.02 TeV with the CMS detector at the LHC.* PhD thesis, University of Paris-Saclay, 2018. cds.cern.ch/record/2655003.

[115] E. V. Shuryak. Quark-Gluon Plasma and Hadronic Production of Leptons, Photons and Pions. *Sov. J. Nucl. Phys.*, **28**:408, 1978. doi:10.1016/0370-2693(78)90370-2.

[116] PHENIX Collaboration. Detailed measurement of the e^+e^- pair continuum in p+p and Au+Au collisions at $\sqrt{s_{NN}}$ = 200 GeV and implications for direct photon production. *Phys. Rev. C*, **81**:034911, 2010. doi:10.1103/PhysRevC.81.034911, arXiv:0912.0244.

[117] R. Rapp. Dilepton Spectroscopy of QCD Matter at Collider Energies. *Adv. High Energy Phys.*, **2013**:148253, 2013. doi:10.1155/2013/148253, arXiv:1304.2309.

[118] S. J. Freedman. *Nuclear Physics: Exploring the Heart of Matter*. The National Academies Press, Washington - DC, 2013.

[119] CMS Collaboration. Study of Z production in PbPb and pp collisions at $\sqrt{s_{NN}}$ = 2.76 TeV in the dimuon and dielectron decay channels. *JHEP*, **03**:022, 2015. doi:10.1007/JHEP03(2015)022, arXiv:1410.4825.

[120] CMS Collaboration. New constraints of initial states in PbPb collisions with Z boson yields and azimuthal anisotropy at $\sqrt{s_{NN}}$ = 5.02 TeV. 2020. CMS-PAS-HIN-19-003: cds.cern.ch/record/2719526.

[121] G. Baym. The Physics of Hanbury Brown-Twiss intensity interferometry: From stars to nuclear collisions. *Acta Phys. Polon. B*, **29**:1839, 1998. arXiv:nucl-th/9804026.

[122] G. Alexander. Bose-Einstein and Fermi-Dirac interferometry in particle physics. *Rept. Prog. Phys.*, **66**:481, 2003. doi:10.1088/0034-4885/66/4/202, arXiv:hep-ph/0302130.

[123] M. Lisa et al. Femtoscopy in relativistic heavy ion collisions: Two Decades of Progress. *Ann. Rev. Nucl. Part. Sci.*, **55**:357, 2005. doi:10.1146/annurev.nucl.55.090704.151533, arXiv:nucl-ex/0505014.

[124] M. Lisa. Femtoscopy in heavy ion collisions: Wherefore, whence, and whither? *AIP Conf. Proc.*, **828**:226, 2006. doi:10.1063/1.2197421, arXiv:nucl-ex/0512008.

[125] STAR Collaboration. Minijet deformation and charge-independent angular correlations on momentum subspace (η, ϕ) in Au − Au collisions at $\sqrt{s_{NN}}$ = 130 GeV. *Phys. Rev. C*, **73**:064907, 2006. doi:10.1103/PhysRevC.73.064907, arXiv:nucl-ex/0411003.

[126] PHOBOS Collaboration. High p_T Triggered $\Delta\eta$, $\Delta\phi$ Correlations over a Broad Range in $\Delta\eta$. *J. Phys. G*, **35**:104080, 2008. doi:10.1088/0954-3899/35/10/104080, arXiv:0804.3038.

[127] CMS Collaboration. Observation of Long-Range Near-Side Angular Correlations in Proton-Lead Collisions at the LHC. *Phys. Lett. B*, **718**:795, 2013. doi:10.1016/j.physletb.2012.11.025, arXiv:1210.5482.

[128] CMS Collaboration. Evidence for collectivity in pp collisions at the LHC. *Phys. Lett. B*, **765**:193, 2017. doi:10.1016/j.physletb.2016.12.009, arXiv:1606.06198.

[129] CMS Collaboration. Studies of charm and beauty hadron long-range correlations in pp and pPb collisions at LHC energies. *Phys. Lett. B*, **813**:136036, 2021. doi:10.1016/j.physletb.2020.136036, arXiv:2009.07065.

[130] ATLAS Collaboration. Measurements of long-range azimuthal anisotropies and associated Fourier coefficients for pp collisions at $\sqrt{s}$ = 5.02 and 13 TeV and p+Pb collisions at $\sqrt{s_{\mathrm{NN}}}$ = 5.02 TeV with the ATLAS detector. *Phys. Rev. C*, **96**:024908, 2017. doi:10.1103/PhysRevC.96.024908, arXiv:1609.06213.

[131] ALICE Collaboration. Investigations of Anisotropic Flow Using Multiparticle Azimuthal Correlations in pp, p-Pb, Xe-Xe, and Pb-Pb Collisions at the LHC. *Phys. Rev. Lett.*, **123**:142301, 2019. doi:10.1103/PhysRevLett.123.142301, arXiv:1903.01790.

[132] ALICE Collaboration. Long- and short-range correlations and their event-scale dependence in high-multiplicity pp collisions at $\sqrt{s}$ = 13 TeV. *JHEP*, **05**:290, 2021. doi:10.1007/JHEP05(2021)290, arXiv:2101.03110.

[133] LHCb Collaboration. Measurements of long-range near-side angular correlations in $\sqrt{s_{\mathrm{NN}}}$ = 5 TeV proton-lead collisions in the forward region. *Phys. Lett. B*, **762**:473, 2016. doi:10.1016/j.physletb.2016.09.064, arXiv:1512.00439.

[134] LHCb Collaboration. Dihadron correlations in pp and pPb collisions with LHCb. *PoS*, **ICHEP2018**:600, 2019. doi:10.22323/1.340.0600, cds.cern.ch/record/2702682.

[135] PHENIX Collaboration. Creation of quark–gluon plasma droplets with three distinct geometries. *Nature Phys.*, **15**:214, 2019. doi:10.1038/s41567-018-0360-0, arXiv:1805.02973.

[136] STAR Collaboration. Azimuthal Harmonics in Small and Large Collision Systems at RHIC Top Energies. *Phys. Rev. Lett.*, **122**(17):172301, 2019. doi:10.1103/PhysRevLett.122.172301, arXiv:1901.08155.

[137] C. A. Bertulani et al. Physics of ultra-peripheral nuclear collisions. *Ann. Rev. Nucl. Part. Sci.*, **55**:271, 2005. doi:10.1146/annurev.nucl.55.090704.151526, arXiv:nucl-ex/0502005.

[138] J. G. Contreras and J. D. Tapia Takaki. Ultra-peripheral heavy-ion collisions at the LHC. *Int. J. Mod. Phys. A*, **30**:1542012, 2015. doi:10.1142/S0217751X15420129, cds.cern.ch/record/2711536.

[139] ATLAS Collaboration. Two-particle azimuthal correlations in photonuclear ultraperipheral Pb+Pb collisions at 5.02 TeV with ATLAS. *Phys. Rev. C*, **104**:014903, 2021. doi:10.1103/PhysRevC.104.014903, arXiv:2101.10771.

[140] CMS Collaboration. Search for elliptic azimuthal anisotropies in γp interactions within ultra-peripheral pPb collisions at $\sqrt{s_{\mathrm{NN}}} = 8.16$ TeV. Technical report, CERN, 2020. cds.cern.ch/record/2725477.

[141] A. Badea et al. Measurements of two-particle correlations in e^+e^- collisions at 91 GeV with ALEPH archived data. *Phys. Rev. Lett.*, **123**(21):212002, 2019. doi:10.1103/PhysRevLett.123.212002, arXiv:1906.00489.

[142] ZEUS Collaboration. Two-particle azimuthal correlations as a probe of collective behaviour in deep inelastic *ep* scattering at HERA. *JHEP*, **04**:070, 2020. doi:10.1007/JHEP04(2020)070, arXiv:1912.07431.

[143] Wenbin Z. et al. Hydrodynamic collectivity in proton$-$proton collisions at 13 TeV. *Phys. Lett. B*, **780**:495, 2017. doi:10.1016/j.physletb.2018.03.022,arXiv:1801.00271.

[144] L. D. McLerran. The Color glass condensate and small$-$x physics: Four lectures. *Lect. Notes Phys.*, **583**:291, 2002. doi:10.1007/3-540-45792-5_8, arXiv:hep-ph/0104285.

[145] L. McLerran. A Brief Introduction to the Color Glass Condensate and the Glasma. 2009. doi:10.3204/DESY-PROC-2009-01/26, arXiv:0812.4989.

[146] F. Gelis et al. The Color Glass Condensate. *Ann. Rev. Nucl. Part. Sci.*, **60**:463, 2010. doi:10.1146/annurev.nucl.010909.083629, arXiv:1002.0333.

[147] T. Sjöstrand et al. An introduction to PYTHIA 8.2. *Comput. Phys. Commun.*, **191**:159, 2015. doi:10.1016/j.cpc.2015.01.024, arXiv:1410.3012.

[148] T. Pierog et al. EPOS LHC: Test of collective hadronization with data measured at the CERN Large Hadron Collider. *Phys. Rev. C*, **92**:034906, 2015. doi:10.1103/PhysRevC.92.034906, arXiv:1306.0121.

[149] C. Bierlich et al. Effects of Overlapping Strings in pp Collisions. *JHEP*, **03**:148, 2015. doi:10.1007/JHEP03(2015)14, arXiv:1412.6259.

[150] ALICE Collaboration. Inclusive J/ψ production at forward and backward rapidity in p-Pb collisions at $\sqrt{s_{NN}}$ = 8.16 TeV. *JHEP*, **07**:160, 2018. doi:10.1007/JHEP07(2018)160, arXiv:1805.04381.

[151] CMS Collaboration. Nuclear modification of Υ states in pPb collisions at $\sqrt{s_{NN}}$ = 5.02 TeV. Technical report, CERN, Geneva, 2019. cds.cern.ch/record/2699566.

[152] PHENIX Collaboration. Centrality-dependent modification of jet-production rates in deuteron-gold collisions at $\sqrt{s_{NN}}$=200 GeV. *Phys. Rev. Lett.*, **116**:122301, 2016. doi:10.1103/PhysRevLett.116.122301, arXiv:1509.04657.

[153] ALICE Collaboration. Constraints on jet quenching in p-Pb collisions at $\sqrt{s_{NN}}$ = 5.02 TeV measured by the event-activity dependence of semi-inclusive hadron-jet distributions. *Phys. Lett. B*, **783**:95, 2018. doi:10.1016/j.physletb.2018.05.059, arXiv:1712.05603.

[154] ATLAS Collaboration. Collective behavior of high-p_T particles in 8.16 TeV p+Pb collisions with ATLAS. Technical report, CERN, 2020. cds.cern.ch/record/2709069.

[155] ALICE Collaboration. *D*-meson production in p-Pb collisions at $\sqrt{s_{NN}}$ =5.02 TeV and in pp collisions at $\sqrt{s}$ =7 TeV. *Phys. Rev. C*, **94**:054908, 2016. doi:10.1103/PhysRevC.94.054908, arXiv:1605.07569.

[156] E. Shuryak and I. Zahed. High-multiplicity pp and pA collisions: Hydrodynamics at its edge. *Phys. Rev. C*, **88**:044915, 2013. doi:10.1103/PhysRevC.88.044915, arXiv:1301.4470.

[157] R. D. Weller and P. Romatschke. One fluid to rule them all: viscous hydrodynamic description of event-by-event central p+p, p+Pb and Pb+Pb collisions at $\sqrt{s}$ = 5.02 TeV. *Phys. Lett. B*, **774**:351, 2017. doi:10.1016/j.physletb.2017.09.07, arXiv:1701.07145.

[158] M. Strickland. Small system studies: A theory overview. *Nucl. Phys. A*, **982**:92, 2019. doi:10.1016/j.nuclphysa.2018.09.071, arXiv:1807.07191.

[159] J. L. Nagle and W. A. Zajc. Small System Collectivity in Relativistic Hadronic and Nuclear Collisions. *Ann. Rev. Nucl. Part. Sci.*, **68**:211, 2018. doi:10.1146/annurev-nucl-101916-123209, arXiv:1801.03477.

[160] U. W. Heinz and J. S. Moreland. Hydrodynamic flow in small systems or: "How the heck is it possible that a system emitting only a dozen particles can be described by fluid dynamics?". *J. Phys. Conf. Ser.*, **1271**:012018, 2019. doi:10.1088/1742-6596/1271/1/012018, arXiv:1904.06592.

[161] J. Adolfsson et al. QCD challenges from pp to AA collisions. *Eur. Phys. J. A*, **56**:288, 2020. doi:10.1140/epja/s10050-020-00270-1, arXiv:2003.10997.

[162] R. Hanbury Brown. *The Intensity Interferometer*. Taylor & Francis, London, 1974.

[163] R. H. Brown and R. Q. Twiss. Correlation between Photons in two Coherent Beams of Light. *Nature*, **177**:27, 1956. doi:10.1038/177027a0.

[164] R. H. Brown and R. Q. Twiss. A Test of a new type of stellar interferometer on Sirius. *Nature*, **178**:1046, 1956. doi:10.1038/1781046a0.

[165] E. M. Purcell. The Question of Correlation between Photons in Coherent Light Rays. *Nature*, **178**:1449, 1956. doi:10.1038/1781449a0.

[166] G. B. Arfken and H. J. Weber. *Mathematical Methods for Physicists: Sixth Edition*. Elsevier, 2005.

[167] P. Kervella et al. The interferometric diameter and internal structure of Sirius A. *Astron. Astrophys.*, **408**:681, 2003. doi:10.1051/0004-6361:20030994, arXiv:astro-ph/0306604.

[168] R. Hanbury Brown et al. The Angular Diameters of 32 Stars. *Monthly Notices of the Royal Astronomical Society*, **167**:121, 1974. doi:10.1093/mnras/167.1.121.

[169] J.-P. Rivet et al. Optical long baseline intensity interferometry: prospects for stellar physics. *Experimental Astronomy*, **46**:531, 2018. doi:10.1007/s10686-018-9595-0, arXiv:1805.06078.

[170] F. Vakili-Christensen et al. Intensity interferometry revival on the côte d'azur. *Optical and Infrared Interferometry and Imaging VI*, 2018. doi:10.1117/12.2309491, arXiv:1810.08023.

[171] W. Guerin et al. Spatial intensity interferometry on three bright stars. *Monthly Notices of the Royal Astronomical Society*, **480**:245, 2018. doi:10.1093/mnras/sty1792, arXiv:1805.06653.

[172] CTA Website. www.cta-observatory.org/. [last access on 13/Mar/2021].

[173] M. A. Lisa et al. Femtoscopy in relativistic heavy ion collisions: Two decades of progress. *Annual Review of Nuclear and Particle Science*, **55**:357, 2005. doi:10.1146/annurev.nucl.55.090704.151533, arXiv:nucl-ex/0505014.

[174] Sandra S. Padula. HBT interferometry: Historical perspective. *Braz. J. Phys.*, **35**:70, 2005. doi:10.1590/S0103-97332005000100005, arXiv:nucl-th/0412103.

[175] R. Lednicky and V. L. Lyuboshits. Final State Interaction Effect on Pairing Correlations Between Particles with Small Relative Momenta. *Sov. J. Nucl. Phys.*, **35**:770, 1982. [Yad. Fiz. **35**:1316, 1981].

[176] R. Lednicky. Progress in correlation femtoscopy. In *32nd International Symposium on Multiparticle Dynamics*, 2002. doi:10.1142/9789812704962_0005, arXiv:nucl-th/0212089.

[177] R. Lednicky. Finite-size effects on two-particle production in continuous and discrete spectrum. *Phys. Part. Nucl.*, **40**:307, 2009. doi:10.1134/S1063779609030034, arXiv:nucl-th/0501065.

[178] M. Fox. *Quantum optics: an introduction*. Oxford Univ. Press, 2006.

[179] W. Florkowski. *Phenomenology of Ultra-relativistic Heavy-ion Collisions*. World Scientific, (2010).

[180] D. Anchishkin et al. Final state interactions in two particle interferometry. *Phys. Rev. C*, **57**:1428, 1998. doi:10.1103/PhysRevC.57.1428, arXiv:nucl-th/9710051.

[181] J. Buxton. ΛK and $\Xi K^{\pm}$ *Femtoscopy in Pb-Pb Collisions at* $\sqrt{s_{NN}}$ = 2.76 TeV *from the LHC ALICE Collaboration*. PhD thesis, Ohio State University, 2019. cds.cern.ch/record/2739399.

[182] R Lednicky. Femtoscopic correlations of nonidentical particles. *Acta Phys. Polon. B*, **40**:1145, 2009. www.actaphys.uj.edu.pl/R/40/4/1145/pdf.

[183] U. A. Wiedemann and U. W. Heinz. Particle interferometry for relativistic heavy ion collisions. *Phys. Rept.*, **319**:145, 1999. doi:10.1016/S0370-1573(99)00032-0, arXiv:nucl-th/9901094.

[184] F. B. Yano and S. E. Koonin. Determining Pion Source Parameters in Relativistic Heavy Ion Collisions. *Phys. Lett. B*, **78**:556, 1978. doi:10.1016/0370-2693(78)90638-X.

[185] S. Pratt. Pion Interferometry for Exploding Sources. *Phys. Rev. Lett.*, **53**:1219, 1984. doi:10.1103/PhysRevLett.53.1219.

[186] T. Csorgo et al. Bose-Einstein correlations for Levy stable source distributions. *Eur. Phys. J. C*, **36**:67, 2004. doi:10.1140/epjc/s2004-01870-9, arXiv:nucl-th/0310042.

[187] CMS Collaboration. Measurement of Bose-Einstein Correlations in pp Collisions at $\sqrt{s} = 0.9$ and 7 TeV. *JHEP*, **05**:029, 2011. doi:10.1007/JHEP05(2011)029, arXiv:1101.3518.

[188] CMS Collaboration. Bose-Einstein correlations of charged hadrons in proton-proton collisions at $\sqrt{s} = 13$ TeV. *JHEP*, **03**:014, 2020. doi:10.1007/JHEP03(2020)014, arXiv:1910.08815.

[189] CMS Collaboration. Bose-Einstein correlations in pp, pPb, and PbPb collisions at $\sqrt{s_{NN}} = 0.9 - 7$ TeV. *Phys. Rev. C*, **97**:064912, 2018. doi:10.1103/PhysRevC.97.064912, arXiv:1712.07198.

[190] M. Clark. *Femtoscopic signatures of small QGP droplets in proton-lead collisions at the Large Hadron Collider*. PhD thesis, Columbia University, 2019. doi:10.7916/d8-t50g-tn57.

[191] ATLAS Collaboration. Femtoscopy with identified charged pions in proton-lead collisions at $\sqrt{s_{\mathrm{NN}}} = 5.02$ TeV with ATLAS. *Phys. Rev. C*, **96**:064908, 2017. doi:10.1103/PhysRevC.96.064908, arXiv:1704.01621.

[192] T. Csorgo et al. Stable Bose-Einstein correlations. *Nukleonika*, **49**:s7, 2004. arXiv:nucl-th/0402035.

[193] PHENIX Collaboration. Lévy-stable two-pion Bose-Einstein correlations in $\sqrt{s_{\text{NN}}}$ = 200 GeV Au+Au collisions. *Phys. Rev. C*, **97**:064911, 2018. doi:10.1103/PhysRevC.97.064911, arXiv:1709.05649.

[194] PHENIX Collaboration. Three dimensional Lévy HBT results from PHENIX. *Acta Phys. Pol. B Proc. Suppl.*, **12**, 2018. doi:10.5506/APhysPolBSupp.12.477, arXiv:1809.09392.

[195] STAR Collaboration. Shape analysis of HBT correlations at STAR. Presented at WPCF2019: theor.jinr.ru/ wpcf2019/files/talks/03/12.%20kincsesd_wpcf2019_v3.pdf, [last access on 26/Jul/2021].

[196] Barnabás Pórfy. Lévy HBT Results at NA61/SHINE. *Universe*, **5**, 2019. doi:10.3390/universe5060154.

[197] M. Deutschmann et al. A Study of Second Order Interference for Pions Produced in Various Hadronic Interactions. *Nucl. Phys. B*, 204:333, 1982. doi:10.1016/0550-3213(82)90193-6, cds.cern.ch/record/137216.

[198] T. Csorgo and B. Lorstad. Bose-Einstein correlations for expanding finite systems. *Nucl. Phys. A*, **590**:465C, 1995. doi:10.1016/0375-9474(95)00255-Y, arXiv:hep-ph/9503494.

[199] ExHIC Collaboration. Exotic hadrons from heavy ion collisions. *Prog. Part. Nucl. Phys.*, **95**:279, 2017. doi:10.1016/j.ppnp.2017.02.002, arXiv:1702.00486.

[200] J. J. Sakurai and J. J. Napolitano. *Modern Quantum Mechanics (2nd Edition)*. Addison Wesley, 2010.

[201] H. A. Bethe. Theory of the effective range in nuclear scattering. *Phys. Rev.*, **76**:38, 1949. doi:10.1103/PhysRev.76.38.

[202] L. K. Graczykowski. *Femtoscopic analysis of hadron-hadron correlations in ultrarelativistic collisions of protons and heavy-ions registered by ALICE at the LHC*. PhD thesis, Warsaw University of Technology, 2014. cds.cern.ch/record/2066992.

[203] STAR Collaboration. Neutral kaon interferometry in Au+Au collisions at $\sqrt{s_{\text{NN}}}$ = 200-GeV. *Phys. Rev. C*, **74**:054902, 2006. doi:10.1103/PhysRevC.74.054902, arXiv:nucl-ex/0608012.

[204] M. Steinpreis. *Neutral Kaon Femtoscopy in Pb-Pb Collisions at* $\sqrt{s_{NN}}$ = *2.76 TeV at the LHC with ALICE*. PhD thesis, Ohio State University, 2014. cds.cern.ch/record/2677618.

[205] M. Gell-Mann and A. Pais. Behavior of neutral particles under charge conjugation. *Phys. Rev.*, **97**:1387, 1955. doi:10.1103/PhysRev.97.1387.

[206] N. N. Achasov and V. V. Gubin. Analysis of the nature of the phi —> gamma pi eta and phi —> gamma pi0 pi0 decays. *Phys. Rev. D*, **63**:094007, 2001. doi:10.1103/PhysRevD.63.094007, arXiv:hep-ph/0101024.

[207] N. N. Achasov and A. V. Kiselev. The New analysis of the KLOE data on the phi —> eta pi0 gamma decay. *Phys. Rev.*, **D68**:014006, 2003. doi:10.1103/PhysRevD.68.014006, arXiv:hep-ph/0212153.

[208] A.D. Martin and E.N. Ozmutlu. Analyses of kk production and scalar mesons. *Nuclear Physics B*, **158**:520, 1979. doi:10.1016/0550-3213(79)90180-9.

[209] A. (KLOE Collaboration) Antonelli. Radiative phi decays. *eConf*, **C020620**:THAT06, 2002. arXiv:hep-ex/0209069.

[210] ALICE Collaboration. Study of the Λ-Λ interaction with femtoscopy correlations in pp and p-Pb collisions at the LHC. *Phys. Lett. B*, **797**:134822, 2019. doi:10.1103/PhysRevLett.114.02230, arXiv:1905.07209.

[211] S. Gongyo et al. Most Strange Dibaryon from Lattice QCD. *Phys. Rev. Lett.*, **120**:212001, 2018. doi:10.1103/PhysRevLett.120.212001, arXiv:1709.00654.

[212] ALICE Collaboration. Measurement of strange baryon–antibaryon interactions with femtoscopic correlations. *Phys. Lett. B*, **802**:135223, 2020. doi:10.1016/j.physletb.2020.135223, arXiv:1903.06149.

[213] ALICE Collaboration. Kaon-proton strong interaction at low relative momentum via femtoscopy in Pb-Pb collisions at the LHC. 2021. arXiv:2105.05683.

[214] CMS Collaboration. First measurement of bose-einstein correlations in proton-proton collisions at $\sqrt{s}$ =0.9 and 2.36 tev at the lhc. *Phys. Rev. Lett.*, **105**:032001, 2010. doi:10.1103/PhysRevLett.105.032001, arXiv:1005.3294.

[215] M. G. Bowler. Coulomb corrections to Bose-Einstein corrections have greatly exaggerated. *Phys. Lett. B*, **270**:69, 1991. doi:10.1016/0370-2693(91)91541-3.

[216] Yu. M. Sinyukov et al. Coulomb corrections for interferometry analysis of expanding hadron systems. *Physics Letters B*, **432**:248, 1998. doi:10.1016/S0370-2693(98)00653-4.

[217] R. Maj and S. Mrowczynski. Coulomb Effects in Femtoscopy. *Phys. Rev. C*, **80**:034907, 2009. doi:10.1103/PhysRevC.80.034907, arXiv:0903.0111.

[218] M. A. Janik. Overview of recent femtoscopy measurements with ALICE. In *13th Workshop on Particle Correlations and Femtoscopy*, 2018. arXiv:1811.02828.

[219] A. M. Cooper et al. A study of $K\overline{k}$ correlations in $p\overline{p}$ annihilations at 0.76 gev/c. *Nuclear Physics B*, **139**:45, 1978. doi:10.1016/0550-3213(78)90178-5.

[220] OPAL Collaboration. A Study of $K_S^0 K_S^0$ Bose-Einstein correlations in hadronic Z^0 decays. *Phys. Lett. B*, **298**:456, 1993. doi:10.1016/0370-2693(93)91851-D.

[221] ALEPH Collaboration. Production of K^0 and Λ in hadronic Z decays. *Z. Phys. C*, **64**:361, 1994. doi:10.1007/BF01560096.

[222] DELPHI Collaboration. Interference of neutral kaons in the hadronic decays of the Z^0. *Physics Letters B*, **323**:242, 1994. doi:10.1016/0370-2693(94)90298-4.

[223] WA97 Collaboration. Di-V0 events in PbPb collisions at 158-A-GeV/c. *J. Phys. G*, **25**:423, 1999. doi:10.1088/0954-3899/25/2/032.

[224] EXCHARM Collaboration. Correlation femtoscopy of neutral kaons in the EXCHARM experiment. *Phys. Atom. Nuc.*, **70**:1208, 2007. doi:10.1134/S1063778807070101.

[225] E. F. Troyanov. Status of the U70 accelerator at the institute of high-energy physics. *Atomic Energy*, **93**:923, 2002. doi:10.1023/A:1022968727103.

[226] ALICE Collaboration. $K_S^0 K_S^0$ correlations in pp collisions at $\sqrt{s} = 7$ TeV from the LHC ALICE experiment. *Phys. Lett. B*, **717**:151, 2012. doi:10.1016/j.physletb.2012.09.013, arXiv:1206.2056.

[227] ALICE Collaboration. One-dimensional pion, kaon, and proton femtoscopy in Pb-Pb collisions at $\sqrt{s_{NN}}$ =2.76 TeV. *Phys. Rev. C*, **92**:054908, 2015. doi:10.1103/PhysRevC.92.054908, arXiv:1506.07884.

[228] ALICE Collaboration. Kaon femtoscopy in Pb-Pb collisions at $\sqrt{s_{NN}} = 2.76$ TeV. *Phys. Rev. C*, **96**:064613, 2017. doi:10.1103/PhysRevC.96.064613.

[229] CERES Collaboration. Pion-pion and pion-proton correlations: New results from CERES. *Braz. J. Phys.*, **37**:979, 2007. doi:10.1590/S0103-97332007000600015, arXiv:hep-ph/0702219.

[230] STAR Collaboration. Pion-proton correlations and asymmetry measurement in Au+Au collisions at $\sqrt{s_{NN}} = 200$ *GeV* data. *Phys. Part. Nucl. Lett.*, **8**:924, 2011.

[231] STAR Collaboration. Meson-baryon femtoscopy in Au + Au collisions at 200-GeV measured by STAR experiment. *Indian J. Phys.*, **85**:1051, 2011. doi:10.1007/s12648-011-0146-z.

[232] ALICE Collaboration. ΛK femtoscopy in Pb-Pb collisions at $\sqrt{s_{NN}} = 2.76$ TeV. *Phys. Rev. C*, **103**:055201, 2021. doi:10.1103/PhysRevC.103.055201, arXiv:2005.11124.

[233] S. K. Adhikari. Improved effective-range expansions for small and large values of scattering length. *Eur. J. Phys.*, **39**:055403, 2018. doi:10.1088/1361-6404/aad620, arXiv:1807.05208.

[234] ALICE Collaboration. Experimental evidence for an attractive p-ϕ interaction. 2021. arXiv:2105.05578.

[235] ALICE Collaboration. Scattering studies with low-energy kaon-proton femtoscopy in proton-proton collisions at the LHC. *Phys. Rev. Lett.*, **124**:092301, 2020. doi:10.1103/PhysRevLett.124.092301, arXiv:1905.13470.

[236] G. Wolf and W. (ALEPH Collaboration) Wiedenmann. Fermi-Dirac-correlations in ΛΛ and $\overline{\Lambda\Lambda}$ pairs in hadronic Z decays. Technical report, CERN, Geneva, 1999. cds.cern.ch/record/404157.

[237] H. Takahashi et al. Observation of a (Lambda Lambda)He-6 double hypernucleus. *Phys. Rev. Lett.*, **87**:212502, 2001. doi:10.1103/PhysRevLett.87.212502.

[238] E. Hiyama, M. Kamimura, T. Motoba, T. Yamada, and Y. Yamamoto. Four-body cluster structure of A = 7 -10 double Lambda hypernuclei. *Phys. Rev. C*, **66**:024007, 2002. doi:10.1103/PhysRevC.66.024007, arXiv:nucl-th/0204059.

[239] I. N. Filikhin and A. Gal. Faddeev-Yakubovsky calculations for light lambda lambda hypernuclei. *Nucl. Phys. A*, **707**:491, 2002. doi:10.1016/S0375-9474(02)01008-4, arXiv:nucl-th/0203036.

[240] STAR Collaboration. $\Lambda\Lambda$ Correlation Function in Au+Au collisions at $\sqrt{s_{\mathrm{NN}}}$ = 200 GeV. *Phys. Rev. Lett.*, **114**:022301, 2015. doi:10.1103/PhysRevLett.114.02230, arXiv:1408.4360.

[241] K. Morita et al. $\Lambda\Lambda$ interaction from relativistic heavy-ion collisions. *Phys. Rev. C*, **91**:024916, 2015. doi:10.1103/PhysRevC.91.024916, arXiv:1408.6682.

[242] ALICE Collaboration. p-p, p-Λ and Λ-Λ correlations studied via femtoscopy in pp reactions at $\sqrt{s}$ = 7 TeV. *Phys. Rev. C*, **99**:024001, 2019. doi:10.1103/PhysRevC.99.024001, arXiv:1805.12455.

[243] Robert L. Jaffe. Perhaps a Stable Dihyperon. *Phys. Rev. Lett.*, **38**:195, 1977. doi:10.1103/PhysRevLett.38.195, [Erratum: Phys.Rev.Lett. 38, 617 (1977)].

[244] NPLQCD Collaboration. Evidence for a Bound H-dibaryon from Lattice QCD. *Phys. Rev. Lett.*, **106**:162001, 2011. doi:10.1103/PhysRevLett.106.162001, arXiv:1012.3812.

[245] HAL QCD Collaboration. Bound H-dibaryon in Flavor SU(3) Limit of Lattice QCD. *Phys. Rev. Lett.*, **106**:162002, 2011. doi:10.1103/PhysRevLett.106.162002, arXiv:1012.5928.

[246] KEK-PS E224 Collaboration. Enhanced $\lambda\lambda$ production near threshold in the $^{12}c(\mathrm{K}^-, \mathrm{K}^+)$ reaction. *Physics Letters B*, **444**:267, 1998. doi:10.1016/S0370-2693(98)01416-6.

[247] KTeV Collaboration. Search for the weak decay of a lightly bound h^0 dibaryon. *Phys. Rev. Lett.*, **84**:2593, Mar 2000. doi:10.1103/PhysRevLett.84.2593.

[248] E836 Collaboration. Search for the H-dibaryon in $^3he(K^-, K^+)Hn$. *Phys. Rev. Lett.*, **78**:3646, May 1997. doi:10.1103/PhysRevLett.78.3646.

[249] Belle Collaboration. Search for an h-dibaryon with a mass near $2m_\Lambda$ in $\Upsilon(1s)$ and $\Upsilon(2s)$ decays. *Phys. Rev. Lett.*, **110**:222002, 2013. doi:10.1103/PhysRevLett.110.222002.

[250] ALICE Collaboration. Search for weakly decaying $\Lambda\mathrm{n}^-$ and $\Lambda\Lambda$ exotic bound states in central Pb-Pb collisions at $\sqrt{s_{\mathrm{NN}}}$ = 2.76 TeV. *Phys. Lett. B*, **752**:267, 2016. doi:10.1016/j.physletb.2015.11.048, arXiv:1506.07499.

[251] I. L. Grach et al. Effective range analysis of low-energy nucleon-antinucleon interaction. *Physics Letters B*, **208**:309, 1988. doi:10.1016/0370-2693(88)90436-4.

[252] C. J. Batty. Antiprotonic-hydrogen atoms. *Reports on Progress in Physics*, **52**:1165, oct 1989. doi:10.1088/0034-4885/52/10/001.

[253] H. J. Pirner et al. Updating the effective range expansion of low-energy N anti-N scattering. *Z. Phys. A*, **338**:111, 1991. doi:10.1007/BF01279121.

[254] E. Klempt et al. Antinucleon–nucleon interaction at low energy: scattering and protonium. *Physics Reports*, **368**:119, 2002. doi:10.1016/S0370-1573(02)00144-8, cds.cern.ch/record/571796.

[255] STAR Collaboration. Two-proton femtoscopy at STAR. *PoS*, **WPCF2011**, 2011. doi:10.22323/1.154.0006, arXiv:1403.0462.

[256] ALICE Collaboration. Baryon femtoscopy in heavy-ion collisions at ALICE. *EPJ Web Conf.*, **71**, 2014. doi:10.1051/epjconf/20147100130, arXiv:1403.0462.

[257] STAR Collaboration. Proton - Λ correlations in central Au+Au collisions at $\sqrt{s_{\mathrm{NN}}}$ = 200 GeV. *Phys. Rev. C*, **74**:064906, 2006. doi:10.1103/PhysRevC.74.064906, arXiv:0511003.

[258] S. A. Bass et al. Microscopic models for ultrarelativistic heavy ion collisions. *Prog. Part. Nucl. Phys.*, **41**:255, 1998. doi:10.1016/S0146-6410(98)00058-1, arXiv:nucl-th/9803035.

[259] M. Bleicher et al. Relativistic hadron hadron collisions in the ultrarelativistic quantum molecular dynamics model. *J. Phys. G*, **25**:1859, 1999. doi:10.1088/0954-3899/25/9/308, arXiv:hep-ph/9909407.

[260] LHC Website. https://home.cern/science/accelerators/large-hadron-collider. [last access on 13/Mar/2021].

[261] LHC Machine. *JINST*, **3**:S08001, 2008. doi:10.1088/1748-0221/3/08/S08001, cds.cern.ch/record/1129806.

[262] W. Berz, M. Wan and K. Makino. *An Introduction to Beam Physics (1st edition)*. 2015.

[263] Linac-4 − CERN Website. https://home.cern/science/accelerators/linear-accelerator-4. [last access on 13/Mar/2021].

[264] Linac-2 − CERN Website. https://home.cern/science/accelerators/linear-accelerator-2. [last access on 13/Mar/2021].

[265] Karlheinz Schindl. The PS Booster as Preinjector for LHC. *Part. Accel.*, **58**:63, 1997. cds.cern.ch/record/1120300.

[266] R. Cappi. The PS in the LHC injector chain. *Part. Accel.*, **58**:79, 1997. cds.cern.ch/record/323933.

[267] T. Linnecar. Preparing the SPS for LHC. *Part. Accel.*, **58**:91, 1997. cds.cern.ch/record/327491.

[268] C. E. Hill. Ion and electron sources. *CERN Accelerator School:Cyclotrons, Linacs and Their Applications, La Hulpe, Belgium.*, 1994. cds.cern.ch/record/276893.

[269] Linac-3 − CERN Website. https://home.cern/science/accelerators/linear-accelerator-3. [last access on 13/Mar/2021].

[270] ALICE Collaboration. The ALICE experiment at the CERN LHC. *JINST*, **3**:S08002, 2008. doi:10.1088/1748-0221/3/08/S08002, cds.cern.ch/record/1129812.

[271] ATLAS Collaboration. The ATLAS Experiment at the CERN Large Hadron Collider. *JINST*, **3**:S08003, 2008. doi:10.1088/1748-0221/3/08/S08003, cds.cern.ch/record/1129811.

[272] LHCb Collaboration. The LHCb Detector at the LHC. *JINST*, **3**:S08005, 2008. doi:10.1088/1748-0221/3/08/S08005, cds.cern.ch/record/1129809.

[273] TOTEM − CERN Website. https://home.cern/science/experiments/totem. [last access on 13/Mar/2021].

[274] LHCf − CERN Website. https://home.cern/science/experiments/lhcf. [last access on 13/Mar/2021].

[275] MOEDAL − CERN Website. https://home.cern/science/experiments/moedal. [last access on 13/Mar/2021].

[276] FCC Collaboration. HE-LHC: The High-Energy Large Hadron Collider. Technical report, CERN, Geneva, 2018. doi:10.1140/epjst/e2019-900088-6, cds.cern.ch/record/2651305.

[277] FCC Collaboration. FCC-ee: The Lepton Collider. Technical report, CERN, 2018. doi:10.1140/epjst/e2019-900045-4, cds.cern.ch/record/2651299.

[278] N. Arkani-Hamed et al. Physics Opportunities of a 100 TeV Proton-Proton Collider. *Phys. Rept.*, **652**:1, 2015. 10.1016/j.physrep.2016.07.004, cds.cern.ch/record/2104388, arXiv:1511.06495.

[279] A. Dainese et al. Heavy ions at the Future Circular Collider. 2016. doi:10.23731/CYRM-2017-003.635, arXiv:1605.01389.

[280] O. Bruening and M. Klein. The Large Hadron Electron Collider. 2013. cds.cern.ch/record/1546382.

[281] CERN Website. https://home.cern/science/accelerators/future-circular-collider. [last access on 13/Mar/2021].

[282] M. Benedikt et al. Future Circular Colliders succeeding the LHC. *Nature Phys.*, **16**:402, 2020. doi:10.1038/s41567-020-0856-2.

[283] NICA Website. https://nica.jinr.ru/. [last access on 13/Mar/2021].

[284] V. Kekelidze et al. Heavy ion collision experiments at NICA. *PoS*, **ICHEP2018**:493, 2019. doi:0.22323/1.340.0493.

[285] FAIR Website. https://fair-center.eu/. [last access on 13/Mar/2021].

[286] BNL Website. https://www.bnl.gov/eic/. [last access on 13/Mar/2021].

[287] J. Tang et al. Concept for a Future Super Proton-Proton Collider. 2015. arXiv:1507.03224.

[288] CEPC Website. http://cepc.ihep.ac.cn/intro.html. [last access on 13/Mar/2021].

[289] P. Gunnellini. The CASTOR calorimeter at the CMS experiment. Technical report, CERN, 2013. cds.cern.ch/record/1537336.

[290] CMS Collaboration. Status of Zero Degree Calorimeter for CMS Experiment. Technical report, 2006. doi:10.1063/1.2396962, cds.cern.ch/record/981111, hrefhttps://arxiv.org/abs/nucl-ex/0608052arXiv:nucl-ex/0608052.

[291] CMS-TOTEM Collaboration. CMS-TOTEM Precision Proton Spectrometer. Technical Report CERN-LHCC-2014-021, 2014. cds.cern.ch/record/1753795.

[292] CMSSW Github page. https://cms-sw.github.io/. [last access on 13/Mar/2021].

[293] R. Brun and F. Rademakers. ROOT − an object oriented data analysis framework. *Nuclear Instruments and Methods in Physics Research Section A: Accelerators, Spectrometers, Detectors and Associated Equipment*, **389**:81, 1997. doi:10.1016/S0168-9002(97)00048-X.

[294] N. Parashar. CMS Pixel Detector Upgrade. In *Meeting of the APS Division of Particles and Fields*, 10 2011. arXiv:1110.2125.

[295] A. Dominguez et al. CMS Technical Design Report for the Pixel Detector Upgrade. Technical Report CERN-LHCC-2012-016. CMS-TDR-11, 2012. cds.cern.ch/record/1481838.

[296] C. Biino. The CMS electromagnetic calorimeter: overview, lessons learned during run 1 and future projections. *Journal of Physics: Conference Series*, **587**:012001, 2015. doi:10.1088/1742-6596/587/1/012001.

[297] CMS Collaboration. *CMS Physics: Technical Design Report Volume 1: Detector Performance and Software*. Technical design report. CMS. CERN, 2006. cds.cern.ch/record/922757.

[298] C. A. Bernardes. *Search for narrow high-mass resonances in proton-proton collisions at $\sqrt{s}$ = 8 TeV decaying to a Z and a Higgs bosons in the CMS detector at LHC*. PhD thesis, Universidade Federal do ABC (UFABC), 2018. https://sucupira.capes.gov.br/sucupira/public/consultas/coleta/trabalho Conclusao/viewTrabalhoConclusao.jsf?popup=true&id_trabalho=3314116.

[299] CMS Collaboration. Precise Mapping of the Magnetic Field in the CMS Barrel Yoke using Cosmic Rays. *JINST*, **5**:T03021, 2010. doi:10.1088/1748-0221/5/03/T03021,arXiv:0910.5530.

[300] G. Abbiendi. The CMS muon system in Run2: preparation, status and first results. *PoS*, **EPS-HEP2015**:237, 2015. doi:10.22323/1.234.0237,arXiv:1510.05424.

[301] CMS Collaboration. Commissioning of the CMS high-level trigger with cosmic rays. *Journal of Instrumentation*, **5**:T03005, 2010. doi:10.1088/1748-0221/5/03/t03005, arXiv:0911.4889.

[302] S. Agostinelli et al. GEANT4 − a simulation toolkit. *Nuclear Instruments and Methods in Physics Research Section A: Accelerators, Spectrometers, Detectors and Associated Equipment*, **506**:250, 2003. doi:10.1016/S0168-9002(03)01368-8, cds.cern.ch/record/602040.

[303] SPRACE Website. https://sprace.org.br/. [last access on 13/Mar/2021].

[304] CMS Collaboration. A MIP Timing Detector for the CMS Phase-2 Upgrade. Technical Report CERN-LHCC-2019-003. CMS-TDR-020, CERN, Geneva, 2019. cds.cern.ch/record/2667167.

[305] P. Billoir and S. Qian. Fast vertex fitting with a local parametrization of tracks. *Nuclear Instruments and Methods in Physics Research Section A: Accelerators, Spectrometers, Detectors and Associated Equipment*, **311**:139, 1992. doi:10.1016/0168-9002(92)90859-3.

[306] CMS Collaboration. Description and performance of track and primary-vertex reconstruction with the CMS tracker. *JINST*, **9**:P10009, 2014. doi:10.1088/1748-0221/9/10/P10009, arXiv:1405.6569.

[307] R. Fruhwirth. Application of Kalman filtering to track and vertex fitting. *Nucl. Instrum. Meth. A*, **262**:444, 1987. doi:10.1016/0168-9002(87)90887-4.

[308] P. Billoir and S. Qian. Simultaneous pattern recognition and track fitting by the Kalman filtering method. *Nucl. Instrum. Meth. A*, **294**:219, 1990. doi:10.1016/0168-9002(90)91835-Y.

[309] M. Swartz et al. A new technique for the reconstruction, validation, and simulation of hits in the CMS pixel detector. *PoS*, **VERTEX2007**:035, 2007. doi:10.22323/1.057.0035, cds.cern.ch/record/1073691.

[310] M. Swartz. CMS pixel simulations. *Nucl. Instrum. Meth. A*, **511**:88, 2003. doi:10.1016/S0168-9002(03)01757-1, cds.cern.ch/record/726082.

[311] E. Brondolin. *Track reconstruction in the CMS experiment for the High Luminosity LHC*. PhD thesis, Technical University of Vienna, 2017. cds.cern.ch/record/2308020.

[312] J. C. Butcher. *Numerical Methods for Ordinary Differential Equations*. J. Wiley, England, 2003.

[313] H. Drucker and C. Cortes. Boosting Decision Trees. In *Advances in Neural Information Processing Systems*. MIT Press, 1996. proceedings.neurips.cc/paper/1995/file/4a08142c38dbe374195d41c04562d9f8-Paper.pdf.

[314] A. Hocker et al. TMVA - Toolkit for Multivariate Data Analysis. 2007. root.cern/manual/tmva/, arXiv:physics/0703039.

[315] A. A. Baty. *Study of Parton Energy Loss in Heavy Ion Collisions using Charged Particle Spectra Measured with CMS*. PhD thesis, Massachusetts Institute of Technology (MIT), 2019. dspace.mit.edu/handle/1721.1/123355.

[316] K. Rose. Deterministic annealing for clustering, compression, classification, regression, and related optimization problems. *Proceedings of the IEEE*, **86**:2210, 1998. doi:10.1109/5.726788.

[317] R Frühwirth et al. Adaptive Vertex Fitting. Technical Report CMS-NOTE-2007-008, CERN, 2007. cds.cern.ch/record/1027031.

[318] CMS Open Data Website. cms-opendata-workshop.github.io/workshop-lesson-luminosity/02-installing-brilcalc/index.html. [last access on 13/Mar/2021].

[319] M. Gyulassy and X.-N. Wang. HIJING 1.0: A Monte Carlo program for parton and particle production in high-energy hadronic and nuclear collisions. *Comput. Phys. Commun.*, **83**:307, 1994. doi:10.1016/0010-4655(94)90057-4, arXiv:nucl-th/9502021.

[320] Z.-W. Lin et al. A Multi-phase transport model for relativistic heavy ion collisions. *Phys. Rev. C*, **72**:064901, 2005. doi:10.1103/PhysRevC.72.064901, arXiv:nucl-th/0411110.

[321] CMS Collaboration. Observation of Correlated Azimuthal Anisotropy Fourier Harmonics in pp and $p + Pb$ Collisions at the LHC. *Phys. Rev. Lett.*, **120**:092301, 2018. doi:10.1103/PhysRevLett.120.092301, arXiv:1709.09189.

[322] CMS Collaboration. Multiplicity and rapidity dependence of strange hadron production in pp, pPb, and PbPb collisions at the LHC. *Phys. Lett. B*, **768**:103, 2017. doi:10.1016/j.physletb.2017.01.075, arXiv:1605.06699.

[323] CMS Collaboration. Elliptic flow of charm and strange hadrons in high-multiplicity pPb collisions at $\sqrt{s_{\mathrm{NN}}}$ = 8.16 TeV. *Phys. Rev. Lett.*, **121**:082301, 2018. doi:10.1103/PhysRevLett.121.082301, arXiv:1804.09767.

[324] F. James and M. Winkler. MINUIT User's Guide. 2004. User's Guides: First Version, Version 94.1, ROOT TMinuit.

[325] O. W. Arnold. *Study of the hyperon-nucleon interaction via femtoscopy in elementary systems with HADES and ALICE*. PhD thesis, Technical University of Munich, 2017. cds.cern.ch/record/2654293.

[326] ALICE Collaboration. Event-shape and multiplicity dependence of freeze-out radii in pp collisions at $\sqrt{s}$ = 7 TeV. *JHEP*, **09**:108, 2019. doi:10.1007/JHEP09(2019)108, arXiv:1901.05518.

[327] TPC/Two Gamma Collaboration. Study of baryon correlations in e^+e^- annihilation at 29-GeV. *Phys. Rev. Lett.*, **57**:3140, 1986. doi:10.1103/PhysRevLett.57.3140.

[328] ALICE Collaboration. Insight into particle production mechanisms via angular correlations of identified particles in pp collisions at $\sqrt{s}$ = 7 TeV. *Eur. Phys. J. C*, **77**:569, 2017. doi:10.1140/epjc/s10052-017-5129-6, arXiv:1612.08975. [Erratum: Eur.Phys.J.C 79, 998 (2019)].

[329] A. Kisiel et al. Extracting baryon-antibaryon strong interaction potentials from $p\overline{\Lambda}$ femtoscopic correlation functions. *Phys. Rev. C*, **89**:054916, 2014. doi:10.1103/PhysRevC.89.054916, arXiv:1403.0433.

[330] V. M. Shapoval et al. Extracting $p\Lambda$ scattering lengths from heavy ion collisions. *Phys. Rev. C*, **92**:034910, 2015. doi:10.1103/PhysRevC.92.034910, arXiv:1405.3594.

[331] CMS Collaboration. Strange hadron production in pp and pPb collisions at $\sqrt{s_{\mathrm{NN}}}$ = 5.02 TeV. *Phys. Rev. C*, **101**:064906, 2020. doi:10.1103/PhysRevC.101.064906, arXiv:1910.04812.

[332] S. Aoki and T. Doi. Lattice QCD and baryon-baryon interactions: HAL QCD method. *Front. in Phys.*, **8**:307, 2020. doi:10.3389/fphy.2020.00307, arXiv:2003.10730.

[333] D. H. Perkins. *Introduction to high energy physics (4th edition)*. Cambridge University Press, 2000.

[334] S. Sarkar, H. Satz, and B. Sinha. *The physics of the quark-gluon plasma: Introductory Lectures*. Springer Science, 2010.

[335] CMS Collaboration. Dependence on pseudorapidity and centrality of charged hadron production in PbPb collisions at a nucleon-nucleon centre-of-mass energy of 2.76 TeV. *JHEP*, **08**:141, 2011. doi:10.1007/JHEP08(2011)141, arXiv:1107.4800.

[336] W. Greiner, L. Neise and H. Stocker. *Thermodynamics and Statistical Mechanics*. Springer-Verlag New York, 1997.

[337] Y. Hama et al. Topics on hydrodynamic model of nucleus-nucleus collisions. *Braz. J. Phys.*, **35**:24, 2005. doi:10.1590/S0103-97332005000100003, arXiv:hep-ph/0407264.

[338] G. D. Yen et al. Excluded volume hadron gas model for particle number ratios in A+A collisions. *Phys. Rev. C*, **56**:2210, 1997. doi:10.1103/PhysRevC.56.2210, arXiv:nucl-th/9711062.

[339] D. H. Rischke et al. Excluded volume effect for the nuclear matter equation of state. *Z. Phys. C*, **51**:485, 1991. doi:10.1007/BF01548574.

[340] Iu. Karpenko et al. A 3+1 dimensional viscous hydrodynamic code for relativistic heavy ion collisions. *Comput. Phys. Commun.*, **185**:3016, 2014. 10.1016/j.cpc.2014.07.010, arXiv:1312.4160.

[341] W. A. Hiscock and L. Lindblom. Generic instabilities in first-order dissipative relativistic fluid theories. *Phys. Rev. D*, **31**:725, 1985. doi:10.1103/PhysRevD.31.725.

[342] P. Romatschke. New Developments in Relativistic Viscous Hydrodynamics. *Int. J. Mod. Phys. E*, **19**:1, 2010. doi:10.1142/S0218301310014613, arXiv:0902.3663.

[343] I. Muller. On the paradox of heat conduction theory (translated). *Z. Phys.*,
198:329, 1967. doi:10.1007/BF01326412.

[344] W. Israel and J.M. Stewart. Transient relativistic thermodynamics and kinetic
theory. *Annals of Physics*, **118**:341, 1979. doi:10.1016/0003-4916(79)90130-1.

[345] P. Kovtun et al. Viscosity in strongly interacting quantum field
theories from black hole physics. *Phys. Rev. Lett.*, **94**:111601, 2005.
doi:10.1103/PhysRevLett.94.111601, arXiv:hep-th/0405231.

[346] A. Buchel. Bulk viscosity of gauge theory plasma at strong coupling. *Phys.
Lett. B*, **663**:286, 2008. doi:10.1016/j.physletb.2008.03.069, arXiv:0708.3459.

[347] J. E. Bernhard. *Bayesian parameter estimation for relativistic heavy-ion collisions*.
PhD thesis, Duke University, 2018. arXiv:1804.06469.

[348] A. Adams et al. Strongly Correlated Quantum Fluids: Ultracold Quan-
tum Gases, Quantum Chromodynamic Plasmas, and Holographic Dual-
ity. *New J. Phys.*, **14**:115009, 2012. doi:10.1088/1367-2630/14/11/115009,
arXiv:1205.5180.

[349] J. Scott Moreland et al. Alternative ansatz to wounded nucleon and binary
collision scaling in high-energy nuclear collisions. *Phys. Rev. C*, **92**:011901,
2015. doi:10.1103/PhysRevC.92.011901, arXiv:1412.4708.

[350] J. E. Bernhard et al. Applying Bayesian parameter estimation to rela-
tivistic heavy-ion collisions: simultaneous characterization of the initial
state and quark-gluon plasma medium. *Phys. Rev. C*, **94**:024907, 2016.
doi:10.1103/PhysRevC.94.024907, arXiv:1605.03954.

[351] M. Chojnacki et al. THERMINATOR 2: THERMal heavy IoN generATOR
2. *Comput. Phys. Commun.*, **183**:746, 2012. doi:10.1016/j.cpc.2011.11.018,
arXiv:1102.0273.

[352] F. Cooper and G. Frye. Single-particle distribution in the hydrodynamic and
statistical thermodynamic models of multiparticle production. *Phys. Rev. D*,
10:186, 1974. doi:10.1103/PhysRevD.10.186.

[353] R. H. Landau. *Quantum Mechanics II: A Second Course in Quantum Theory,
2nd Edition*. John Wiley & Sons, USA, 2008.

[354] CMS Collaboration. Identified particles in pPb collisions at $\sqrt{s_{NN}} =$ 5.02 TeV measured with the CMS detector. *Nucl. Phys. A*, 926:**128**, 2014. doi:10.1016/j.nuclphysa.2014.02.018.

[355] S. R. Klein et al. STARLight: A Monte Carlo simulation program for ultra-peripheral collisions of relativistic ions. *Comput. Phys. Commun.*, **212**:258, 2017. doi:10.1016/j.cpc.2016.10.016, arXiv:1607.03838.